amU
Aix Marseille Université

NNT : 2024AIXM0001

THÈSE DE DOCTORAT

Soutenue à AMU — Aix-Marseille Université
le 16 décembre 2024 par

Basheer KALBOUNEH

A Model-Independent Analysis of Local Cosmic Spacetime via a Novel Observable: The Expansion Rate Fluctuation Field

Discipline
Physique et sciences de la matière

Spécialité
Astrophysique et cosmologie

École doctorale
ED 352

Laboratoire
Centre de Physique Théorique

Composition du jury

R. Brent TULLY Inst. Astron., Honolulu	Rapporteur
Subir SARKAR Oxford U., Theor. Phys. Oxford	Rapporteur
Hélène COURTOIS IP2I, Lyon	Examinatrice
Dominique FOUCHEZ CPPM, Marseille	Président du jury
Elena PIERPAOLI USC, Los Angeles	Examinatrice
Christian MARINONI CPT, Marseille	Directeur de thèse
Julien Bel CPT, Marseille	Co-directeur de thèse

CPT
Centre de Physique Théorique

Je soussigné, Basheer Kalbouneh, déclare par la présente que le travail présenté dans ce manuscrit est mon propre travail, réalisé sous la direction scientifique de Christian Marinoni et Julien Bel, dans le respect des principes d'honnêteté, d'intégrité et de responsabilité inhérents à la mission de recherche. Les travaux de recherche et la rédaction de ce manuscrit ont été réalisés dans le respect à la fois de la charte nationale de déontologie des métiers de la recherche et de la charte AMU relative à la lutte contre le plagiat.

Ce travail n'a pas été précédemment soumis en France ou à l'étranger dans une version identique ou similaire à un organisme examinateur.

Fait à Marseille le 21 Octobre 2024.

Basheer Kalbouneh

Cette œuvre est mise à disposition selon les termes de la Licence Creative Commons Attribution - Pas d'Utilisation Commerciale - Pas de Modification 4.0 International.

Liste de publications et participation aux conférences

Liste des publications:

1. Multipole expansion of the local expansion rate. Basheer Kalbouneh, Christian Marinoni, and Julien Bel. Phys. Rev. D, 107(2):023507, 2023. arXiv:2210.11333v3.

2. Covariant cosmography: the observer- dependence of the Hubble parameter. Roy Maartens, Jessica Santiago, Chris Clarkson, Basheer Kalbouneh, and Christian Marinoni. JCAP 09, 070, 2024. arXiv:2312.09875.

3. Cosmography of the local universe by multipole analysis of the expansion rate fluctuation field. Basheer Kalbouneh, Christian Marinoni, and Roy Maartens. JCAP 09, 069, 2024. arXiv:2312.09875.

4. Expanding covariant cosmography of the local Universe: incorporating the snap and axial symmetry. Basheer Kalbouneh, Jessica Santiago, Christian Marinoni, Roy Maartens, Chris Clarkson, and Maharshi Sarma. JCAP submitted, 2024. arXiv:2408.04333.

Participation aux conférences et écoles d'été au cours de la période de thèse:

1. Colloque National Action Dark Energy 2021 - 5ème édition. Marseille, France, 2021.

2. MaNiTou Summer School on Gravitational Waves: A new window to the Universe. Marseille, France, 2022.

3. Colloque National Action Dark Energy 2022 - 6ème édition. Marseille, France, 2022.
Contribution: Oral presentation titled: The multipole expansion of the local expansion rate. Authors: Basheer Kalbouneh, Christian Marinoni, and Julien Bel.

4. Progress on Old and New Themes in cosmology - PONT 2023. Avignon, France, 2023.
Contribution: Oral presentation titled: Multipole Expansion of the Local Expansion Rate. Authors: Basheer Kalbouneh, Christian Marinoni, and Julien Bel.

5. Cosmology Workshop: A multipolar universe?. Thessaloniki, Greece, 2023.
Contribution: Oral presentation titled: The Multipoles of the Cosmographic Parameters in Cosmicflows-4 and Pantheon+. Authors: Basheer Kalbouneh, Christian

Marinoni, Julien Bel, and Roy Maartens.
Proceedings:

- The Multipolar Structure of the Local Expansion Rate. Basheer Kalbouneh, Christian Marinoni and Julien Bel. Springer, in press.
- Covariant Cosmography of the Local Universe. Basheer Kalbouneh, Christian Marinoni and Roy Maartens. Springer, in press.

6. Corfu Summer Institute: Workshop on Tensions in Cosmology. Corfu, Greece, 2023.
   Contribution: Oral presentation titled: The multipolar structure of the local universe. Authors: Basheer Kalbouneh, Christian Marinoni, Julien Bel, and Roy Maartens.

7. Colloque national Action Dark Energy 2023 - 7ème édition. Annecy, France, 2023.

8. Relativistic Effects and Novel Observables in Cosmology. Geneva, Switzerland, 2024.
   Contribution: Oral presentation titled: Estimating covariant cosmographic parameters in the local universe. Authors: Basheer Kalbouneh, Christian Marinoni, Julien Bel, Roy Maartens, Jessica Santiago, and Chris Clarkson.

Abstact

This thesis introduces a novel, model-independent approach to investigate the local cosmic spacetime by analyzing fluctuations in the expansion rate, represented through a new observable: the expansion rate fluctuation field, η. The η field, constructed from redshift and luminosity distance data, provides a model-agnostic way to detect anisotropies in the local expansion rate without assuming a specific spacetime metric. By developing spherical harmonic expansions of η, this work investigates local deviations from isotropy and assesses their consistency with the Standard Model of cosmology. Through analyses of observational datasets such as Cosmicflows-3, Cosmicflows-4, and Pantheon, I find persistent and significant anisotropies in the expansion rate at redshifts up to $z = 0.1$ which challenge the assumption of a homogeneous and isotropic universe in a patch centered on the observer and of radius $R \sim 400$ Mpc. Furthermore, I explore the covariant cosmographic framework, deriving multipoles for key cosmological parameters (e.g., covariant Hubble, deceleration, jerk) to probe the structure of spacetime. The results indicate that the local universe exhibits persistent deviations from the Standard Model of cosmology on scales larger than previously anticipated. This suggests the possibility of an unexpected structuring of matter, or perhaps even intriguing new physics at play in the cosmic framework.

Résumé

Cette thèse introduit une nouvelle approche, indépendante du modèle, pour étudier l'espace-temps cosmique local par le biais d'une nouvelle observable : le champ de fluctuation du taux d'expansion, η. Le champ η, construit à partir des données de distances de luminosité et de décalages spectraux vers le rouge, fournit un moyen de détection des anisotropies dans le taux d'expansion local de l'univers et ce, sans supposer une métrique spécifique de l'espace-temps. En développant η en harmoniques sphériques, ce travail étudie les déviations locales de l'isotropie et évalue leur cohérence avec le Modèle Standard de la cosmologie. En analysant les données observées dans les catalogues Cosmicflows-3, Cosmicflows-4 et Pantheon, je trouve des anisotropies persistantes et significatives dans le taux d'expansion à des *redshifts* allant jusqu'à $z = 0.1$. Celles-ci, remettent en question l'hypothèse d'un univers homogène et isotrope dans un volume de rayon de $R \sim 400$ Mpc centré sur l'observateur. En outre, j'étudie comment cette nouvelle observable permet de placer des contraintes sur les multipoles des parametres cosmographiques covariants. Les résultats indiquent que l'univers local présente des écarts persistants par rapport au modèle standard de la cosmologie à des échelles plus grandes que prévues. Cela suggère la possibilité d'une structuration inattendue de la matière, ou peut-être même d'une nouvelle physique.

Résumé long

Les récents programmes d'observations extragalactiques sont devenus de plus en plus précis, mais peinent encore à contraindre les paramètres fondamentaux du modèle standard de la cosmologie d'une manière stable et non contradictoire. Notamment, des tensions existent dans les estimations du paramètre de Hubble (H_0), des fluctuations quadratiques moyennes du champ de densité de matière (σ_8), et de la courbure spatiale de l'Univers.

Ces tensions suggèrent la nécessité de réévaluer les hypothèses de base de la cosmologie, en particulier celles concernant la structure de l'espace-temps cosmique. Un exemple est la divergence entre les déterminations locales de H_0 et les estimations du fond diffus comologique (FDC), qui peut indiquer une rupture du principe cosmologique (PC), c'est-à-dire une nature non triviale, moins symétrique, de l'élément de ligne associé à la métrique cosmique.

Par définition, le PC ne s'applique pas aux petites échelles cosmiques ($r < 150\ h^{-1}$ Mpc), ce qui peut affecter la détermination du paramètre de Hubble. Traditionnellement, les déviations de l'uniformité spatiale à ces échelles sont traitées à l'aide de techniques perturbatives. Cependant, cette approche présente certains inconvénients : elle dépend fondamentalement du modèle, car elle nécessite l'hypothèse que la métrique est de type Friedmann-Lemaître-Robertson-Walker (FLRW), ce qui implique l'existence de variables cosmologiques "lisses", qui ne dépendent que du temps. En outre, elle suppose que les fluctuations de densité sont faibles, ce qui limite son applicabilité aux structures cosmiques plus complexes dont la dynamique est fortement non-linéaire.

Je cherche donc à savoir s'il est possible d'utiliser des mesures de décalage spectral vers le rouge (*redshift*) et de distances pour représenter l'espace-temps cosmique de manière nonperturbative, sans s'appuyer sur la notion de vitesses propres, et de manière indépendante du modèle, sans référence préalable à des principes ou à des hypothèses de symétrie. Le but ultime est de caractériser le taux d'expansion à des échelles cosmiques locales ($z \lesssim 0.1$ ou $r \lesssim 300\ h^{-1}$ Mpc) de manière plus significative et plus complète qu'en utilisant uniquement le paramètre H_0 du Modèle Standard. Ce programme comporte deux étapes essentielles. Tout d'abord, on doit identifier et classer les déviations de l'isotropie dans la relation redshift-distance observée, de manière robuste et indépendante du modèle choisi pour la metrique cosmique. Ensuite, on doit relier ces distorsions angulaires à des quantités géométriques, définies de manière covariante dans des espaces-temps arbitraires, afin de mieux comprendre la structure effective de l'élément de ligne cosmique dans l'environnement local de l'observateur.

Le premier défi a été relevé en introduisant le *champ de fluctuation du taux d'expansion* η. Cette observable est définie comme suit

$$\eta = \log\left(\frac{z}{d_L}\right) - \mathcal{M} \tag{1}$$

où z est le redshift, d_L est la distance de luminosité et $\mathcal{M}$ est le facteur de normalisation pour rendre le monopôle de η égal à zéro. Par conséquent, η n'est sensible qu'à la structure angulaire de la composante fluctuante et à son évolution possible avec le redshift. Ce n'est qu'en présence d'anisotropies angulaires de la distance de luminosité, à un redshift donné, que η s'écarte de zéro. Par exemple, dans un modèle cosmologique FLRW idéalisé, $\eta = 0$ à chaque époque.

En tant qu'indicateur scalaire gaussien, η présente plusieurs avantages statistiques et se prête assez facilement à une décomposition sur la base des harmoniques sphériques, ce qui facilite l'interprétation directe du signal. Premièrement, η, n'ayant pas de monopôle ($\mathcal{M}$), est complètement indépendant de la normalisation de la relation redshift-distance, ce qui permet de comparer le signal extrait de différents ensembles de données de distances lumineuses, indépendamment de leur étalonnage au point zéro. Cela ne signifie pas que l'observable η est insensible à la constante de Hubble. L'information sur H_0 est enfermée dans le terme de normalisation $\mathcal{M}$ apparaissant dans 1. L'avantage supplémentaire est que les erreurs systématiques potentielles dans les mesures des distances de luminosité en fonction du redshift n'affectent pas le signal de η.

Le deuxième défi consiste à généraliser la notion de « taux d'expansion cosmique ». Il s'agit de répondre à la question de savoir ce que signifie le mot « expansion » pour un observateur arbitraire dans un espace-temps générique. Cette idée remonte à l'article fondateur de Kristian et Sachs, « Observations in Cosmology », publié en 1966, dans lequel ils ont analysé le taux d'expansion non-standard (anisotropes) par le biais de l'expansion tensorielle de la distance lumineuse en fonction du redshift. Cette approche permet d'obtenir les *paramètres cosmographiques covariants*, $\mathbb{H}(\boldsymbol{n})$ (Hubble covariant), $\mathbb{Q}(\boldsymbol{n})$ (décélération), $\mathbb{J}(\boldsymbol{n})$ (jerk) et $\mathbb{R}(\boldsymbol{n})$ (courbure). Ces paramètres sont des fonctions dépendant de la direction de la ligne de visée $\boldsymbol{n}$ et caractérisent la structure métrique autour de l'observateur, et en même temps, ils sont liés aux termes d'expansion de la distance de luminosité en fonction du redshift, ce qui les rend observables. Bien qu'ils soient initialement inconnus (aucune théorie gravitationnelle n'est supposée dans cette approche), ils sont charactérisés par un nombre fini d' harmoniques sphériques. Par conséquent, les paramètres cosmographiques covariants peuvent être entièrement reconstruits observationellement en ajustant un sous-ensemble limité de leurs multipoles aux données.

Dans cette thèse, je présente les résultats que j'ai obtenus en explorant ces deux voies.

Dans le premier chapitre, je passe en revue le modèle standard de la cosmologie, en commençant par sa physique fondamentale, y compris les équations de champs d'Einstein et les équations de Friedmann. Les concepts cosmologiques clés tels que le redshift, les mesures de distance et l'approche cosmographique dans le cadre du modèle standard sont introduits. Je présente également les principales techniques d'observation utilisées pour estimer la distance de luminosité. En outre, je présente synthétiquement la théorie des perturbations linéaires et discute des propriétés statistiques du champ de densité de matière perturbé, y compris le spectre de puissance et la fonction de corrélation, qui sont nécessaires tout au long de la thèse. Enfin, je passe brièvement en revue les tensions au sein du modèle standard de la cosmologie qui motivent des recherches supplémentaires, en mettant particulièrement l'accent sur la tension de Hubble. En effet, à long terme, je propose d'aborder cette question en utilisant l'approche développée dans cette thèse.

Dans le deuxième chapitre, je définis le champ de fluctuation du taux d'expansion η et je décris comment cette nouvelle observable peut être estimée à partir de données discrètes. Je montre ensuite comment développer ce champ en harmoniques sphériques et je présente

les méthodes utilisées pour estimer l'expansion multipolaire de η, en commençant par HEALPix (Hierarchical Equal Area isoLatitude Pixelization of a 2-sphere). Cette méthode consiste à lisser le champ de η en faisant la moyenne des valeurs mesurées à chaque pixel et à estimer les multipoles sur la base de ces données pixellisées. La seconde méthode consiste à minimiser directement le χ^2 pour toutes les mesures sans appliquer de lissage. Je discute également des propriétés statistiques, des biais et des incertitudes associés à chaque méthode.

Enfin, puisque η est une quantité indépendante du modèle, je démontre comment elle est liée à la composante radiale du champ de vitesses propres dans le cadre du Modèle Standard. Cette relation me permet également de montrer comment le spectre de puissance des multipoles de η (ou la variance cosmique de des coefficients de son expansion en harmoniques sphériques) est lié au spectre de puissance de la matière prédit par le modèle ΛCDM. Ce spectre de puissance est crucial pour évaluer si les multipoles observés s'alignent ou s'écartent des prédictions théoriques.

Dans le troisième chapitre, je présente la carte de η sur tout le ciel, ainsi que son expansion multipolaire, dérivée des données locales ($z < 0.05$) : les catalogues Cosmicflows-3 (CF3) et Pantheon. Pour le catalogue Panthéon, le signal est confiné au dipôle ($\sim 2 \times 10^{-2}$), alors que les données CF3 révèlent des signaux dans le quadripôle ($\sim 1 \times 10^{-2}$) et l'octupôle ($\sim 1 \times 10^{-2}$). Je calcule la probabilité d'observer ces multipôles dans le cadre du modèle standard à un redshift donné et je constate qu'ils sont compatibles avec les prévisions. En outre, j'ai divisé l'échantillon CF3 en deux sous-échantillons : CF4sn, qui contient des mesures de distance utilisant des supernovae de type Ia (SNIa), et CF4g, qui comprend les données restantes. Les résultats des deux sous-échantillons se sont avérés compatibles.

Je trouve une preuve intrigante que la direction du dipôle ($(l, b) \approx (290°, 8°)$) s'aligne avec le maximum du quadrupole, l'octupole présentant également un maximum dans cette direction. J'examine ensuite l'expansion multipolaire sous l'hypothèse simplificatrice d'une symétrie axiale le long de cet axe préféré et je trouve que cela est compatible avec les données. En développant sur une base de Legendre au lieu d'harmoniques sphériques, chaque multipôle est déterminé par un seul degré de liberté, ce qui rend l'interprétation des observations plus simple. Enfin, puisque le dipôle de η est lié à la vitesse globale (*bulk velocity*) v_b du volume sondé, je l'estime pour chaque échantillon, et je trouve $v_b \approx 330 \pm 25$ km/s pour le volume considéré ($z < 0.05$ ou $r < 150\ h^{-1}Mpc$). Cette valeur est cohérente avec d'autres résultats de la littérature obtenus par des techniques indépendantes.

Dans le quatrième chapitre, je présente des estimations actualisées du champ η obtenues à partir de nouvelles compilations publiques de distances indépendantes du redshift : les catalogues Cosmicflows-4 (CF4) et Pantheon+. Le catalogue CF4 permet d'étendre les estimations des anisotropies dans le champ du taux d'expansion à des redshifts plus élevés, jusqu'à $z = 0.1$. Je trouve que les cartes de η pour des redshifts allant jusqu'à $z = 0.05$ sont quantitativement cohérentes avec celles de CF3 et Pantheon.

Je divise ensuite cet échantillon plus riche (~ 4 fois son prédécesseur) en trois sous-échantillons : CF4SN (contenant les mesures de distance utilisant les SNIa), CF4TF (contenant les mesures de distance utilisant la relation de Tully-Fisher pour les galaxies spirales), et CF4FP (contenant les mesures de distance utilisant la méthode du plan fondamental pour les galaxies elliptiques). Les résultats de ces sous-échantillons sont cohérents dans les limites des incertitudes données.

Dans l'intervalle de redshifts le plus profond exploré, $0.05 < z < 0.1$, nous détectons également des preuves statistiquement significatives de signaux dipolaires et quadrupo-

laires, chacun avec une amplitude de $\sim 1 \times 10^{-2}$. Ces amplitudes sont en tension avec les prédictions du modèle standard de la cosmologie à ce redshift. L'anomalie observée dans le dipôle est cohérente avec les résultats indépendants d'autres chercheurs qui ont analysé le même échantillon CF4 en utilisant le modèle FLRW. Ces analyses dépendantes du modèle suggèrent que qu'une vitesse apparente sur un volume aussi grand et profond n'est pas conforme aux attentes du modèle standard. En plus de la composante quadrupolaire inattendue, nous trouvons également des preuves tout aussi intrigantes que les maximas du dipôle et du quadrupôle restent alignés le long du même axe comme observé dans la tranche de redshift inférieure (CF3). J'ai ensuite examiné si le taux d'expansion dans la région au-delà de la concentration de Shapley $0.05 < z < 0.1$) présentait une symétrie axiale autour de cet axe privilégié. Pour ce faire, j'ai développé une méthode plus sophistiquée qui exploite les propriétés des harmoniques sphériques. Plus précisément, si l'expansion en harmonique sphérique d'un champ à symétrie axiale est faite dans un système de coordonnée aligné avec cette axe de symétrie alors tous les coefficients des harmoniques sphériques s'annulent, à l'exception du mode $m = 0$. Or, j'ai constaté que cette rotation augmente le signal dans les modes $m = 0$ tout en le diminuant dans les autres modes, confirmant ainsi la présence d'une symétrie axiale. Ces résultats suggèrent que le taux d'expansion cosmique est perturbé de façon systématique et cohérente à une échelle dépassant $\sim 400h^{-1}$ Mpc. Il ne s'agit plus seulement de "*bulk motions*" anormaux. C'est toute la structure complexe du champ d'expansion qui nous entoure qui reste inchangée au moins jusqu'à $z = 0.1$, le plus grand redshift étudié.

Dans le chapitre 5, je passe en revue *l'approche cosmographique covariante*. Cette méthode, totalement indépendante du modèle et nonperturbative, permet d'interpréter le signal η sans supposer de métrique spatio-temporelle spécifique $g_{\mu\nu}$. Ses paramètres caractéristiques, les paramètres cosmographiques covariants, sont les coefficients de l'expansion en fonction du redshift de la distance de luminosité dans un espace-temps générique. Ils dépendent des propriétés géométriques de l'espace-temps, mais aussi de la vitesse à laquelle l'observateur se déplace par rapport au référentiel où la matière est au repos. La forme fonctionnelle exacte de cette dépendence n'était connue auparavant que jusqu'au troisième ordre. Motivé par des preuves suggérant que cet ordre d'expansion pourrait être insuffisant pour capturer complètement la cinématique du taux d'expansion dans un univers local fortement inhomogène, j'étend ces résultats au quatrième ordre, en incorporant le paramètre *snap* $\mathbb{S}(\boldsymbol{n})$. Je démontre également que le paramètre de Hubble covariant a des multipoles jusqu'au quadripôle ($\ell = 2$), tandis que les multipoles indépendants du paramètre de décélération s'étendent jusqu'à l'octupôle ($\ell = 3$). Le terme d'expansion de troisième ordre, qui inclut les paramètres jerk et courbure, a des multipoles indépendants jusqu'à $\ell = 4$, et le paramètre snap a des multipoles indépendants jusqu'à $\ell = 5$.

Le nombre total de degrés de liberté est de 86 (chaque multipôle ayant $2\ell + 1$ degrés de liberté), ce qui est trop important pour esperer de le contraindrer à l'aide des données. Cependant, je montre qu'en supposant une symétrie axiale et en considérant que les particules de matière se déplacent le long de géodésiques, le nombre de degrés de liberté est réduit à 17. De plus, certains multipôles comportent des dérivées spatiales, ce qui signifie qu'ils sont amplifiés par un facteur égal au rapport entre l'échelle de l'horizon de Hubble et l'échelle de la perturbation qui les génère. Si nous ne considérons que ces multipôles « boostés », en plus des monopôles, nous nous retrouvons avec seulement 12 degrés de liberté, un nombre assez raisonnable de degrés de liberté pour l'inférence statistique.

J'établis ensuite la relation entre les multipoles de η, qui sont observables, et les multi-

poles des paramètres cosmographiques covariants sous l'hypothèse de symétrie axiale. Ce formalisme pose les bases pour l'analyse des données et les inférence statistiques présentées au chapitre 7 de cette thèse.

Une contribution clé de cette section est la clarification et la quantification analytique des effets induits par le mouvement de l'observateur sur l'amplitude des paramètres cosmographiques. Les observations cosmologiques fournissent souvent des mesures du redshift et de la distance par rapport à des référentiels spécifiques, généralement le référentiel héliocentrique ou le référentiel du FDC, où l'observateur n'observe pas le dipôle du FDC. Cependant, dans les calculs théoriques des paramètres cosmographiques, on suppose que l'observateur se déplace par rapport au fluide de matière cosmologique (ce que l'on appelle le référentiel de matière, qui ne coïncide pas avec le référentiel héliocentrique). Alors que les systemes de réferences de la matière et du FDC sont indiscernables dans un univers parfaitement uniforme tel que décrit par la métrique cosmologique standard, ils diffèrent dans des géométries arbitraires. Pour résoudre ce problème, souvent négligé dans la littérature, j'introduis un nouveau degré de liberté, la vitesse relative locale v_o entre le référentiel de la matière et le référentiel d'observation dans lequel les mesures sont analysées. Je montre comment, en incorporant cette vitesse relative dans l'analyse, nous obtenons des informations supplémentaires sur le mouvement relatif entre les referentiels de la matiére et du FDC.

Au chapitre 6, je teste le formalisme de la cosmographie covariante en utilisant des modèles analytiques à symétrie axiale qui simulent des fluctuations linéaires à grande échelle dans la relation redshift-distance de l'Univers local. À cette fin, je perturbe un modèle cosmologique uniforme d'Einstein-de Sitter avec une surdensité à symétrie sphérique, en considérant deux tailles différentes pour la surdensité et en supposant que l'observateur est excentré par rapport à la perturbation. Ce modèle est choisi de façon à ce que les multipoles observés de η et la vitesse globale soient compatibles avec les valeurs que j'ai déduites des données. J'échantillonne ensuite le modèle en essayant de reproduire à la fois la distribution des redshifts et les erreurs dans les distances attendues par le sondage, en cours de réalisation, Zwicky Transient Facility (ZTF).

Ce modèle réaliste me permet d'évaluer comment la distance de luminosité se compare à celle reconstruite en utilisant les paramètres cosmographiques covariants, évaluant ainsi les limites potentielles de notre méthode. Ces analyses permettent de trouver l'intervalle de redshifts où l'expansion en série de la distance est valide. En outre, elles me permettent de prévoir la précision avec laquelle les paramètres cosmographiques covariants peuvent être estimés. Les résultats montrent que l'estimation de l'octupole de $\mathbb{Q}$ est biaisée si le snap n'est pas inclus dans les analyses. De plus, le multipôle $\ell = 4$ du jerk et $\ell = 5$ du snap sont biaisés, ce qui indique que des termes d'ordre plus élevé sont nécessaires pour récupérer avec précision ces multipôles. Les autres multipoles ne sont pas biaisés, et la vitesse v_o est bien reconstruite.

Dans le dernier chapitre, j'applique finalement le formalisme de la cosmographie covariante pour extraire des informations physiques sur les échantillons CF4 et Pantheon+. J'estime les multipoles des paramètres cosmographiques (à l'exclusion des monopoles) en plus de la vitesse v_o directement à partir des mesures des multipoles du champ de fluctuation du taux d'expansion η (jusqu'au multipôle $\ell = 4$). Je n'ajuste pas le monopôle $\mathcal{M}$, qui est lié à l'étalonnage du point zéro des indicateurs de distance et peut être biaisé compte tenu des résultats contradictoirs présents en littérature. Ceci est possible grâce à la propriété inhérente de l'observable η d'être indépendante de la normalisation des distances. Cependant, cela s'accompagne d'un compromis : une dégénérescence entre le

monopôle du jerk et de la courbure et le dipôle et l'octupôle du snap. Par conséquent, je ne peux qu'estimer des combinaisons de ces paramètres.

Une deuxième mise en garde est que, selon le formalisme, si l'expansion théorique de la distance modélise avec précision les données jusqu'à un redshift spécifié, les paramètres cosmographiques les mieux ajustés devraient rester stables, à l'intérieur de leurs barres d'erreur, lorsque nous faisons varier l'intervalle de redshift de l'analyse, en particulier sa limite inférieure. Cependant, j'ai trouvé que la stabilité se maintient systématiquement pour les différents échantillons analysés, mais seulement jusqu'à une seuil de redshift de $z_{\rm cut} = 0.01$. En dessous de ce seuil, les paramètres deviennent instables en raison de l'influence de structures très locales dans ce volume ($\lesssim 40$ Mpc), telles que l'amas de la Vierge et le vide local, dont la dynamique n'est pas alignée avec la dynamique moyenne montrée par l'ensemble du volume étudié. Cette instabilité suggère que nous ne sommes plus dans la limite des fluides où la cosmographie covariante peut être appliquée. Par conséquent, j'applique cette coupure de redshift inférieur pour assurer la fiabilité des paramètres estimés.

Pour Panthéon+, je détecte un signal statistiquement significatif uniquement pour v_o. Dans CF4, des signaux sont également observés dans le quadripôle de $\mathbb{H}$ ($\sim (3 \pm 0.5)\%$ du monopôle), dans le dipôle ($\sim 2 \pm 1$) et l'octupôle ($\sim 1 \pm 0.5$) de $\mathbb{Q}$. La vitesse v_o est de $\sim 170 \pm 30$ km/s dans la direction du dipôle. Bien qu'aucun signal significatif ne soit trouvé dans les multipôles du jerk, les combinaisons du dipôle et de l'octupôle du snap avec le monopôle du jerk et de la courbure montrent des signaux significatifs. Pour valider davantage ces résultats, j'analyse également les sous-échantillons CF4SN, CF4TF et CF4FP. Les résultats de ces sous-échantillons sont globalement cohérents, CF4SN ne montrant aucun signal dans le quadrupôle du paramètre de Hubble covariant mais confirmant la robustesse des signaux observés dans les autres paramètres.

La valeur positive du quadrupole de $\mathbb{H}$ suggère que le fluide cosmique local est étiré le long de l'axe de symétrie. Je montre qu'un seul "attracteur" sphérique (surdensité) situé dans la direction générale de la concentration de Shapley peut expliquer cet effet. Cependant, je démontre également que ce même modèle à un seul attracteur prédit des signes opposés pour le dipôle et l'octupôle de $\mathbb{Q}$, ce qui contredit les observations. Il est intéressant de noter qu'il existe des preuves dans la littérature de l'existence d'un "répulseur", une grande sous-densité cosmique qui pourrait influencer la dynamique de l'univers locale. Un model impliquant un attracteur et un « répulseur » sphérique n'est viable que s'ils sont alignés avec l'observateur pour préserver la symétrie axiale dans le champ de perturbations du taux d'expansion. Par contre, je n'ai pas trouvé de configurations permettant d'expliquer les multipoles des paramètres cosmographiques covariants observés.

En conclusion, l'approche nonperturbative et indépendante de tout modèle développée dans cette thèse contribue à mettre en lumière la structure complexe du champ local du taux d'expansion de l'univers. Cette complexité ne montre pas de tendance claire à s'estomper avec la distance, et les taux d'expansion à évoluer vers un état isotrope. Cela motive donc les programmes d'observation visant à mesurer des distances des galaxies au-delà de $z = 0.1$, afin d'obtenir des informations physiques sur la nature et l'origine des anisotropies observées.

La méthode presentée fournit également des outils théoriques pour une étude plus approfondie des questions cosmologiques clés. En particulier, les contraintes sur les paramètres cosmographiques covariants dérivées dans cette thèse seront cruciales pour accepter, rejeter ou affiner des modèles métriques de l'espace-temps de l'univers local. De

plus, j'espère que les méthodologies développées ici contribueront finalement à résoudre la tension de Hubble. Relever ces défis sera mon principal objectif dans les années à venir.

Acknowledgments

I would like to begin by sincerely thanking my supervisor, Christian Marinoni. Thank you for being an amazing supervisor, you've taught me so much, and really refined my skills. I will always appreciate how you put your trust and confidence in me, I will never forget your endless support, or our long discussions which I enjoyed every single time. Thank you!
I am also deeply grateful to my co-supervisor, Julien Bel. Thank you for your invaluable contributions and for boosting my research. Your encouragement and insights have been instrumental in my development as a researcher.
Moreover, I would like to thank the entire cosmology group, where I truly feel at home and have had many enriching discussions.
Finally, I would like to extend my gratitude to my collaborators, whom I'm proud that I got an opportunity to work with, Roy Maartens, Jessica Santiago, and Chris Clarkson, whose contributions have been vital in expanding and deepening my research. Their support and collaboration have been indispensable.

Contents

1 Introduction **18**
- 1.1 The Standard Model of cosmology . . . 20
- 1.2 Model independent observables : redshift and distances . . . 23
  - 1.2.1 Redshift . . . 23
  - 1.2.2 The angular diameter distance . . . 24
  - 1.2.3 The luminosity distance . . . 25
- 1.3 Cosmography in FLRW spacetime . . . 26
- 1.4 Linear perturbation theory . . . 28
  - 1.4.1 Perturbed redshift and distance . . . 30
  - 1.4.2 Matter power spectrum . . . 30
- 1.5 Observational evidences in favour of the ΛCDM model . . . 31
  - 1.5.1 Galaxy distance probes . . . 31
  - 1.5.2 CBM radiation probes . . . 34
  - 1.5.3 Galaxy clustering probes . . . 36
- 1.6 Tensions in the standard model . . . 38
- 1.7 Conclusions . . . 44

2 The expansion rate fluctuation field $\boldsymbol{\eta}$ **45**
- 2.1 Definition . . . 46
- 2.2 Spherical harmonic decomposition of $\boldsymbol{\eta}$ . . . 47
  - 2.2.1 Estimation of η and its multipoles using pixelization . . . 49
  - 2.2.2 Maximum Likelihood method for estimating η and its multipoles . . . 54
- 2.3 Standard model predictions for η . . . 55
- 2.4 Conclusion . . . 57

3 The expansion rate fluctuation field in Cosmicflows-3 and Pantheon **59**
- 3.1 Data . . . 60
  - 3.1.1 The Pantheon sample . . . 60
  - 3.1.2 The Cosmicflows-3 data . . . 61
- 3.2 Results . . . 61
  - 3.2.1 Axial symmetry of the multipoles . . . 69
  - 3.2.2 Bulk motion model . . . 73
  - 3.2.3 The scale of anisotropies . . . 74
  - 3.2.4 p-value of the multipoles in ΛCDM . . . 75
  - 3.2.5 Removing peculiar motions from the Hubble diagram by means of the η field . . . 76
- 3.3 Conclusion . . . 79

4 The expansion rate fluctuation field in Cosmicflows-4 and Pantheon+ 82
4.1 Data . . . 83
4.1.1 Cosmicflows-4 sample . . . 83
4.1.2 Pantheon+ sample . . . 84
4.2 Results . . . 85
4.2.1 Axial symmetry . . . 89
4.3 Conclusion . . . 92

5 Covariant Cosmography 94
5.1 Cosmography in a general spacetime . . . 96
5.1.1 Null geodesic congruence . . . 96
5.1.2 Angular diameter distance expansion . . . 97
5.2 Degrees of freedom . . . 100
5.2.1 Boosted observer . . . 102
5.3 Relation between $\boldsymbol{\eta}$ an the covariant cosmographic parameters . . . 103
5.3.1 The $\boldsymbol{\eta}$ field for a boosted observer . . . 105
5.4 Conclusion . . . 108

6 An analytical model for testing the cosmographic reconstruction scheme 109
6.1 The attractor model . . . 109
6.2 Luminosity distance of analytical model: cosmographic approach . . . 111
6.3 Luminosity distance of analytical model: linear perturbation theory . . . 113
6.4 Expansion rate fluctuations field of the analytical model . . . 115
6.5 Forecasting precision on cosmographic parameter estimation . . . 120
6.6 Limits of the cosmographic expansion . . . 126
6.7 Multipoles of the radial peculiar velocity field . . . 128
6.8 Incorporating the snap . . . 129
6.9 Conclusion . . . 132

7 Estimation of the cosmographic parameters of the local universe 134
7.1 Estimating the cosmographic parameters . . . 134
7.2 Results . . . 136
7.3 Conclusion . . . 142

Summary and Outlook 149

A Multipole expansions of $\mathbb{X}^{(3,4)}$ and $\mathbb{Y}^{(1,2)}$ 150

B Light geodesics in Einstein de Sitter spacetime 155

Mathematical conventions

In this thesis, I adopt the Einstein summation convention for repeated indices, with Greek indices (from 0 to 3) and Latin indices (from 1 to 3). The natural units are used ($c = 1$), and the metric signature is $(- + ++)$.

Concerning logarithms, I use log to denote the decimal logarithm (base 10) and ln for the natural logarithm (base e).

Chapter 1

Introduction

Modern cosmology, derived from the Ancient Greek words κόσμος (cosmos, meaning 'world') and λογία (logia, meaning 'study'), is a branch of physics that explores the large-scale structure of cosmic spacetime, including its history, geometry, and mass-energy content. While cosmology originated in theoretical physics, it has evolved into an observationally driven discipline, where many unexpected empirical discoveries help to refine our understanding of fundamental physics.

It all began when Einstein realized that his general relativistic field equations for gravity, which relate the curvature of spacetime to its energy content, could be applied to gain insights into the structure of the entire universe. In 1917, he proposed the first physically consistent cosmological model: a static, uniform (i.e., homogeneous and isotropic) 3D spherical space filled only with matter [1]. However, to maintain the static nature of the universe, he had to introduce an extra term into his gravitational field equations : the cosmological constant.

In the early 1920s, Alexander Friedmann demonstrated that Einstein's field equations, with or without the cosmological constant, allow for an infinite class of homogeneous and isotropic models that can evolve over time [2]. One of these models has since become the standard cosmological model.

In 1926, Edwin Hubble published an influential paper [3], in which he analyzed how the spatial number density of galaxies evolves as a function of their apparent magnitude. He found that the observations were consistent with a uniform spatial distribution thus supporting the Einstein and Friedmann hypotheses regarding the symmetries of spacetime.

In 1927, Georges Lemaître independently derived the Friedmann equations and extended them by predicting that, in these dynamic models, the relative distances between co-moving, freely falling particles—if sufficiently close—should be linearly related to their relative redshift.[1] In 1929, Hubble presented his fundamental paper, where the expansion of the universe was established on observational grounds, and the local rate of this expansion, the Hubble constant, was tentatively estimated.

In those early days, confusion persisted on the theoretical side. Hubble misinterpreted the physics responsible for the distance-redshift relation. The very notion of time and distances employed within the frameworks of general relativity, were not fully understood even by theoreticians. In 1935 [6] and 1936 [7], Howard Robertson and Arthur Walker

[1]Lemaître even calculated the Hubble constant by using galaxy redshifts measured by Slipher and distances estimated from brightness measurements published by Hubble. His paper, originally written in French, was translated into English in 1931 with the help of Eddington. However, Lemaître chose to omit his estimation of the Hubble parameter in the translation, as Hubble had already published more precise data on the expansion of the universe [4, 5].

independently addressed this issue by formulating the general metric that uniquely satisfies the so-called *cosmological principle*. This principle states that there is no privileged spatial position or direction in the universe, which is mathematically expressed by the condition that the spatial sections of the universe are homogeneous and isotropic. This principle is understood not in a strict mathematical sense, but rather in a statistical sense, after the spatial distribution of matter is suitably averaged over large scales.

Since then, the expanding homogeneous and isotropic models—known as the Friedmann-Lemaître-Robertson-Walker (FLRW) models—became the preferred relativistic world models for comparing against the growing body of observational data in an effort to identify the most accurate in capturing the characteristics of our Universe. This progression culminated in the development of the standard model of cosmology, the Λ-Cold-Dark-Matter (ΛCDM) model, which remains the most successful and predictive model for interpreting cosmological data across a wide range of spatial and temporal scales.

However, as observational programs have become increasingly powerful and precise, they seem to have stopped converging toward unambiguous determinations of the fundamental parameters of the standard model. On the contrary, the data seem to highlight certain tensions in the estimates, particularly a significant inconsistency between the locally (and model-independent) measured value of the Hubble constant, based on Cepheids and Type Ia supernovae, and the value determined at early epochs (in a model-dependent way) by Planck's analysis of the Cosmic Microwave Background (CMB).

Proposals to resolve the Hubble tension include new early-universe physics and modified gravity theories. However, several indications suggest that resolving the Hubble tension at least requires new physics in the late universe [8]. These indications include the tension between the locally measured H_0 and the upper limit constrained by the ages of old astrophysical objects, as well as the decreasing trend in H_0 values with increasing distance, in addition to the tension between the CMB dipole and the radio galaxies dipole, as will be discussed later in this chapter.

In this context, my bet is that the very geometrical description of the local universe needs to be put under the "microscope", and, the physical consequences of the observed irregularities fully appreciated if we are to solve these puzzles. The cosmological principle, with its aesthetic appeal and mathematical simplicity, aligns well with the observed isotropic CMB (with fluctuations of order 10^{-5}) and the FLRW metric is extraordinarily effective in explaining the general characteristics of the universe, in particular its expansion and evolution. However, as new exquisitely precise data are flowing in, this description in zero-order approximation no longer seems sufficient: the local universe has increasingly revealed deviations at larger than expected scales, posing a challenge to this principle.

Before introducing the techniques developed to investigate the local structure of cosmic spacetime in a fully model-independent and agnostic way, this chapter reviews the basis of the Standard Model of cosmology, focusing on both the supporting observations and the challenges to its foundations. Since this thesis proposes a novel approach to exploring the local universe without relying on the cosmological principle or symmetry assumptions, I will place particular emphasis on reviewing model-independent physical quantities, i.e. those independent of the FLRW metric.

1.1 The Standard Model of cosmology

The most successful model for understanding the large-scale structure of the universe is founded on two key principles. First is the cosmological principle, second are Einstein's gravitational field equations, These principles are applied not just to the observable universe within our light cone, but are also extrapolated to regions beyond current observational reach.

The cosmological principle. The cosmological principle (CP) states that there is a congruence of time-like world-lines with a tangent vector u^μ (called the fundamental observers) to whom the universe appears spatially homogeneous and isotropic. This principle gives us only three possibilities for the curvature of the spatial hypersurfaces (perpendicular to u^μ), flat space, positively curved space (closed), and negatively curved space (open).

It is crucial to highlight that the CP can only be interpreted in a statistical sense, after convolving the spatial distribution of matter with large smoothing kernels. This makes its empirical confirmation difficult and subject to non-trivial systematicity.

Despite observational hurdles (e.g. [9]), convincing proofs of isotropy are provided by the angular distribution of the temperature fluctuations of the cosmic microwave background (CMB) [10, 11]. Also, 3D supporting evidence continues to grow as spectroscopic studies reveal the structure of ever larger and deeper regions of the Universe [12, 13, 14, 15, 16, 17, 18, 19, 20, 21]. Analysis of the spatial distribution of supernovae, i.e. objects whose distances are estimated using redshift independent techniques, also provides tentative confirmation [22, 23, 24, 25, 26, 27, 28, 29]. The nature of the confirmations remains preliminary, however, there is no shortage of evidence to the contrary [30, 31, 32, 33, 34, 35, 36, 37, 38, 39, 40, 41, 42, 43, 44]. If some of these signals are not statistically significant enough to reject outright the CP, others appear as improbable in the framework of the standard cosmological model.

The CP offers a crucial simplification in that it uniquely determines the form of the metric of the universe. By assuming homogeneity and isotropy on large scales, the principle dictates that the cosmic line element must take the Friedmann-Lemaître-Robertson-Walker (FLRW) form. In comoving coordinates (glued to matter particles and dragged around by their motion) the FLRW line element is represented by

$$\mathrm{d}s^2 = g_{\mu\nu}\,\mathrm{d}x^\mu \mathrm{d}x^\nu = -\mathrm{d}t^2 + a^2(t)\left[\frac{\mathrm{d}r^2}{1-Kr^2} + r^2\Big(\mathrm{d}\vartheta^2 + \sin^2\vartheta\,\mathrm{d}\phi^2\Big)\right], \tag{1.1}$$

where t is the coordinate time (also called cosmic time) and $a(t)$ is the scale factor of the universe. The CP constrain the curvature K of the spatial hypersurfaces (perpendicular to u^μ) to take a constant values. As a consequence, only three configurations are possible: flat space ($K = 0$), closed, and open. By opportunely rescaling K, r and $a(t)$, one can choose K to take one of the values $(-1, 0, 1)$, which are related to open , flat, and closed spaces respectively. In this case, the scale factor will carry the dimension of a length.

Einstein's field equations. The evolution of the metric coefficients $g_{\mu\nu}$, and thus essentially the time evolution of the scale factor, is ruled by the Einstein field equations (EFE)

$$R_{\mu\nu} - \frac{1}{2}g_{\mu\nu}R + \Lambda g_{\mu\nu} = 8\pi G\, T_{\mu\nu} \tag{1.2}$$

where Λ is the cosmological constant, $R_{\nu\beta} = R^\mu{}_{\nu\mu\beta}$ is the Ricci tensor, $R = R^\alpha{}_\alpha$ is the

Ricci scalar and

$$R^{\mu}{}_{\nu\alpha\beta} = \frac{\partial \Gamma^{\mu}{}_{\nu\beta}}{\partial x^{\alpha}} - \frac{\partial \Gamma^{\mu}{}_{\nu\alpha}}{\partial x^{\beta}} + \Gamma^{\mu}{}_{\alpha\rho}\Gamma^{\rho}{}_{\nu\beta} - \Gamma^{\mu}{}_{\nu\rho}\Gamma^{\rho}{}_{\alpha\beta} \tag{1.3}$$

with $\Gamma^{\mu}{}_{\alpha\beta}$ the Christoffel symbols,

$$\Gamma^{\mu}{}_{\alpha\beta} = \frac{1}{2} g^{\mu\lambda} \left(\frac{\partial g_{\lambda\alpha}}{\partial x^{\beta}} + \frac{\partial g_{\lambda\beta}}{\partial x^{\alpha}} - \frac{\partial g_{\beta\alpha}}{\partial x^{\lambda}} \right). \tag{1.4}$$

The source term in EFE is the energy-momentum tensor $T_{\mu\nu}$, which accounts for all the masses and energies that influence and drive the evolution of the cosmic geometry. If one model the cosmic mass-energy distribution as a perfect fluid

$$T_{\mu\nu} = (\rho + p) u_{\mu} u_{\nu} + p g_{\mu\nu} \tag{1.5}$$

where u^{μ} is the 4-velocity of a comoving fluid element, ρ and p are the energy density and pressure as measured by an observer moving locally with the fluid (so they are scalar quantities).

By inserting the FLRW form of the $g_{\mu\nu}$ into the EFE, it is possible to determine the relation between the cosmic scale factor and the cosmic distribution of energy densities and pressures. This is given by the two independent Friedmann equations,

$$H^2 := \left(\frac{\dot{a}}{a} \right)^2 = \frac{8\pi G}{3} \rho + \frac{\Lambda}{3} - \frac{K}{a^2} \tag{1.6}$$

$$\frac{\ddot{a}}{a} = -\frac{4\pi G}{3} (\rho + 3p) + \frac{\Lambda}{3} \tag{1.7}$$

where ρ is the sum of the energy densities of the different mass-energy components of the universe, and the overdot denotes a derivative with respect to cosmic time. The standard components include the non-relativistic fluid (matter) density ρ_{m}, which includes both baryonic and dark matter, and the energy density of relativistic fluids ρ_{r}, which includes radiation and neutrinos. One can simplify the Friedmann equations, by expressing the cosmological constant and the curvature term as being effective sources of energy density, $\rho_{\Lambda} = \Lambda/(8\pi G)$ and $\rho_K = -3K/(8\pi G a^2)$, so

$$H^2 = \frac{8\pi G}{3} \sum_f \rho_f \tag{1.8}$$

$$\frac{\ddot{a}}{a} = -\frac{4\pi G}{3} \left(\sum_f \rho_f + 3 \sum_f p_f \right). \tag{1.9}$$

The continuity equation, which can be derived by combining the two Friedmann equations (1.8) and (1.9), is given by

$$\dot{\rho} + 3H(p + \rho) = 0 \tag{1.10}$$

This equation can also be obtained from the conservation of the energy-momentum tensor, projected along u^{μ} ($u_{\mu} \nabla_{\nu} T^{\mu\nu} = 0$). If the various cosmic fluids do not interact, meaning energy is not transferred between them, then each fluid will independently satisfy eq. (1.10).

To solve Friedmann equations, one requires an additional equation since there are three unknowns (a, ρ and p). The necessary additional equation is the equation of state,

which relates the pressure to the energy density. Under the additional assumption that the perfect fluids are also barotropic, this relation simplifies to $p = w\rho$, and w is a constant that depends on the nature of the fluid. For non-relativistic matter, pressure is proportional to the mean square of the thermal velocity, which is much smaller than the speed of light. Therefore, the pressure can be neglected compared to the mass energy density, which implies $w = 0$.
For the relativistic fluid, the equation of state parameter is $w = 1/3$. The cosmological constant effectively acts as a fluid with $w = -1$ and the curvature term as an hypothetical perfect fluid with $w = -1/3$. Therefore by using eq. (1.10), the time scale of the matter and radiation energy density is

$$\rho_{\rm m} = \rho_{\rm m0}\left(\tfrac{a_0}{a}\right)^3 \quad , \quad \rho_{\rm r} = \rho_{\rm r0}\left(\tfrac{a_0}{a}\right)^4$$

where ρ_{f0} is the energy density today as measured by a comoving observer, and a_0 is the scale factor today. Note that, the acceleration of the universe's expansion can only occur ($\ddot{a} > 0$) if the equation of state for the cosmic fluid satisfies $w < -1/3$.

By defining the critical density as $\rho_{\rm c} = 3H^2/(8\pi G)$, and introducing the adimensional density parameter $\Omega_f = \rho_f/\rho_{\rm c}$ one can rewrite the first Friedmann equation (1.8) as the constraint equation

$$\Omega_{\rm m} + \Omega_{\rm r} + \Omega_\Lambda = 1 - \Omega_K, \tag{1.11}$$

which tell us that the curvature of the spatial sections of the universe is uniquely determined by its energy content. Also, by defining $\Omega_{f0} = \rho_{f0}/\rho_{\rm c0}$, where $\rho_{\rm c0}$ is the critical density today, equation (1.8) takes the form

$$\frac{H^2}{H_0^2} = \Omega_{\rm m0}\left(\frac{a_0}{a}\right)^3 + \Omega_{\rm r0}\left(\frac{a_0}{a}\right)^4 + \Omega_{\Lambda 0} + \Omega_{K0}\left(\frac{a_0}{a}\right)^2. \tag{1.12}$$

For flat space ($K = 0$), the solution of eq. (1.12) if the universe has only one dominant fluid is

$$a(t) = a_0\left(\frac{t}{t_0}\right)^{\frac{2}{3(1+w)}} \tag{1.13}$$

and the age of the universe since the Big Bang (defined as the time $t_{\rm b}$ at which $a(t_{\rm b}) = 0$)) is $t_0 = \frac{2}{3(1+w)H_0}$. Note that this solution (1.13) is not valid for $w = -1$; in the latter case, one has $a(t) = a_0 e^{H_0(t-t_0)}$, and so, the Hubble parameter is independent on time and the universe is eternal. It is also interesting to show the solution in the case the universe contains two fluids, a matter fluid and a fluid that mimics the effects of the cosmological constant:

$$t(a) = \frac{2}{3H_0\sqrt{1-\Omega_{\rm m0}}}\left(\frac{3}{2}\ln\left(\frac{a}{a_0}\right) + \ln\left(\frac{\sqrt{1-\Omega_{\rm m0}} + \sqrt{1-\left(1-\left(\frac{a_0}{a}\right)^3\right)\Omega_{\rm m0}}}{\sqrt{\Omega_{\rm m0}}}\right)\right) \tag{1.14}$$

In this case, the universe transitions from an early decelerated phase to a late epoch accelerated expansion. The age of such an universe is

$$t_0 = \frac{2}{3H_0\sqrt{1-\Omega_{\rm m0}}}\ln\left(\frac{1+\sqrt{1-\Omega_{\rm m0}}}{\sqrt{\Omega_{\rm m0}}}\right) \tag{1.15}$$

and it is larger, for a given value of H_0, than it would be without a cosmological constant. This model is the one that seems preferred by current data. Its best fitting parameter $H_0 \approx 70$ km/s/Mpc and $\Omega_{\mathrm{m}0} \approx 0.3$ implies that the age of the universe is around 13.5×10^9 years.

1.2 Model independent observables : redshift and distances

1.2.1 Redshift

In the beginning of the 19th century, Wollaston and then Fraunhofer independently discovered dark lines (absorption lines) in the solar spectrum and speculated that these lines, that they also later detected in other stars, carry information about the chemical structure of the light sources. [45, 46]. In 1842, Doppler discovered that the frequency of a wave depends on the relative velocity between the source and the observer, and a few years later, Huggins and Fizeau proposed that shifts observed in the absorption lines of stellar spectra reveal the stars' radial velocity relative to us [47, 48]. This spectral shift is determined by measuring the difference between the observed wavelengths (λ_0) in a star's spectrum and the known wavelengths (λ_{e}) of spectral lines of the elements found in the laboratory

$$z \equiv \frac{\lambda_0 - \lambda_{\mathrm{e}}}{\lambda_{\mathrm{e}}} \,. \tag{1.16}$$

When the spectrographs were sufficiently powerful to disperse also the faint light of galaxies, Slipher [49] noticed that most extragalactic objects exhibit a redshift, meaning that the characteristic spectral lines are systematically shifted towards longer wavelengths. Later, Lemaître proposed that this redshift could be a consequence of general relativity and explained it, using the Friedmann equations, as caused by the expansion of space. Indeed, in FLRW models, the the redshift of a photon is related to changes in the scale factor of the universe at the time of emission and reception of the photon. This relation is determined as follows. Since light moves along null geodesics ($\mathrm{d}s^2 = 0$), a light wave crest that travels in the radial direction (ϑ and ϕ are fixed) from a source towards us will travel a distance

$$\frac{\mathrm{d}r}{\sqrt{1-Kr^2}} = -\frac{\mathrm{d}t}{a(t)} = -\frac{\mathrm{d}r}{\sqrt{1-Kr^2}} \tag{1.17}$$

the minus sign denoting that the light ray is coming towards us at $r = 0$. If the wave crest is emitted from the source at $(t_{\mathrm{e}}, r_{\mathrm{e}})$, it will arrive the observer at a time t_0 given by

$$\int_{t_{\mathrm{e}}}^{t_0} \frac{\mathrm{d}t}{a(t)} = \int_0^{r_{\mathrm{e}}} \frac{\mathrm{d}r}{\sqrt{1-Kr^2}}. \tag{1.18}$$

A second wave crest that leaves the source after the very short period δt_{e} will reach the observer with a delay δt_0,

$$\int_{t_{\mathrm{e}}+\delta t_{\mathrm{e}}}^{t_0+\delta t_0} \frac{\mathrm{d}t}{a(t)} = \int_0^{r_{\mathrm{e}}} \frac{\mathrm{d}r}{\sqrt{1-Kr^2}}, \tag{1.19}$$

where the coordinate r_{e}, being comoving, does not change between the emission of the

two wave crests. One thus concludes that

$$\int_{t_e+\delta t_e}^{t_0+\delta t_0} \frac{\mathrm{d}t}{a(t)} - \int_{t_e}^{t_0} \frac{\mathrm{d}t}{a(t)} = 0. \tag{1.20}$$

i.e. in first order approximation,

$$\frac{\delta t_e}{a(t_e)} = \frac{\delta t_0}{a(t_0)}. \tag{1.21}$$

Therefore, the period of the wave at emission is different than the period it has at the observer. As consequence the wavelength will also be different ($\delta t = \lambda$). By eq. (1.16), we conclude that in the FLRW model the redshift is related to the scale factor as

$$1 + z = \frac{a(t_0)}{a(t_e)} \tag{1.22}$$

that is a source will display a redshift if its light was emitted when the size of the universe was smaller.

For the purposes of this thesis, it is more convenient to express the link between the redshift and the physical parameters of the system in a different form. Since the energy E is related to the wavelength of the photon by $E \propto \lambda^{-1}$, and energy can be determined from the photon's 4-momentum p^μ by $p^\mu u_\mu = E$, the redshift z can be expressed in all generally as:

$$1 + z = \frac{p^\mu u_\mu|_e}{p^\mu u_\mu|_0} \tag{1.23}$$

This definition has the merit of highlighting that the redshift is a direct observable whose value depends on the metric $g_{\mu\nu}$ of the spacetime. but not on the coordinate system used to express this metric (the redshift is a scalar quantity). Being general, it is also independent from the specific metric parameter ($a(t)$) that characterize the FLRW cosmological models.

For example in a FLRW spacetime the 4-momentum of a photon, obtaied by solving the geodesic equations $p^\mu \nabla_\mu p^\nu = 0$ is

$$p^\mu = \frac{a_0}{a} E_0 \left(1, \frac{1}{a}\sqrt{1 - Kr^2}, 0, 0\right). \tag{1.24}$$

By substituting this expression into (1.23), one can verify that it yields the same result as given in the equation (1.22).

Redshift is a fundamental concept in astronomy and one of the few observational parameters that can be measured directly with high precision. The uncertainty in a single redshift measurement depends on the spectrograph's resolution, but this error is generally much smaller than the redshift value itself, allowing me to neglect it in this work.

1.2.2 The angular diameter distance

The angular diameter distance d_A is defined in general for a geodesic bundle converging at the point of observation, as the square root of the ratio between the transverse physical area of an object at the emission epoch and the observed solid angle subtended by the

source at the observer position (e.g. [50])

$$d_A \equiv \sqrt{\frac{\mathrm{d}A}{\mathrm{d}\Omega}}. \tag{1.25}$$

Because of this general definition, that holds in any spacetime, the angular distance, as the redshift, is in principle a direct cosmic observable if $\mathrm{d}A$ is a priori known.

In an FLRW spacetime, the angular diameter distance to a source that emitted a photon at $t = t_\mathrm{e}$, is

$$d_A = a(t_\mathrm{e})\, S_K\left(\chi\right), \tag{1.26}$$

where χ is the comoving distance,

$$\chi = \int_{t_\mathrm{e}}^{t_0} \frac{\mathrm{d}t'}{a(t')}, \tag{1.27}$$

and $S_K(\chi)$ is the coordinate distance travelled by the photon, and it is defined for different spatial geometries as:

$$S_K(\chi) = \begin{cases} \sin(\chi) & , \ K = +1 \\ \chi & , \ K = 0 \\ \sinh(\chi) & , \ K = -1. \end{cases} . \tag{1.28}$$

Therefore, we can express the angular diameter distance as a function of the redshift as:

$$d_A(z) = \frac{a_0}{1+z} S_K\left(\frac{1}{a_0}\int_0^z \frac{\mathrm{d}z'}{H(z')}\right) . \tag{1.29}$$

This expression explicitly shows that the amplitude of the angular diameter distance depends on the cosmological parameters of the specific FLRW model. By comparing the observed value (1.25) with this theoretical prediction, one can constrain the values of the standard cosmological parameters and, in principle, identify the best FLRW model that describes the actual Universe.

1.2.3 The luminosity distance

An operationally different definition of distance is that derived by comparing the apparent and intrinsic luminosity of a source. The luminosity distance of an object in a general spacetime is defined as

$$d_L \equiv \sqrt{\frac{L}{4\pi f}} \tag{1.30}$$

where L is the intrinsic luminosity of the object (energy/time), and f is its observed flux (energy/time/area).

It is common to use apparent and absolute magnitudes (m and M, respectively) rather than luminosity and flux to measure luminosity distances. The apparent magnitude of an object is related to its observed flux by the relation[2]: $m = -\frac{5}{2}\log\varphi + const.$ The

[2]The concept of stellar magnitudes began at least with Ptolemy's *Almagest* (circa 137 AD), where he listed 1,024 stars with magnitudes from 1 to 6 (with 1 being the brightest and 6 the faintest) [51]. This system is related to the logarithm of the flux, reflecting the human eye's logarithmic rather than linear

absolute magnitude is defined as the apparent magnitude of the object when observed from a distance of 10 parsecs. Furthermore, using magnitudes, the distance modulus is defined as

$$\mu = m - M = 5\log(d_L) + 25 \tag{1.31}$$

where d_L here must be in Mpc.

Like redshift and distances, the luminosity distance is also a direct observable, meaning it is a cosmological model-independent quantity. In principle, measuring the distance to an object only requires knowledge of its absolute luminosity which might in principle be inferred from its physical or astrophysical properties. Moreover according to the reciprocity theorem [52, 53], the luminosity distance is related to the angular diameter distance as follows

$$d_L = (1+z)^2 d_A. \tag{1.32}$$

This relation is valid for any spacetime as long as the number of the photons is conserved.

Consider now the specific case of a FLRW model. The absolute luminosity $L = \mathrm{d}E/\mathrm{d}t$, at time of observation will differ from that at time of emission for two effects: first because the energy of each observed photon will be lower $\mathrm{d}E_0 = \mathrm{d}E_\mathrm{e}/(1+z)$, and also because the time between two successive photons increases $\mathrm{d}t_0 = (1+z)\mathrm{d}t_\mathrm{e}$. Since the observed flux is equal to the observed energy per unit surface and per unit time, and since the surface of a sphere, centered around the source and passing through the observer position, is $A = 4\pi a_0^2 S_K^2(\chi)$, one obtains

$$f(t_0) = \frac{L(t_\mathrm{e})}{4\pi a_0^2 S_K^2(\chi)(1+z)^2}. \tag{1.33}$$

So, by using the definition in equation (1.30),

$$d_L = a_0 S_K(\chi)(1+z) \tag{1.34}$$

or

$$d_L = a_0(1+z) S_K\left(\frac{1}{a_0}\int_0^z \frac{dz'}{H(z')}\right). \tag{1.35}$$

Note that, in the low redshift limit ($z << 1$), the angular diameter distance and the luminosity distance converge and they both become proportional to the redshift, $z = H_0 d$, which is the Hubble-Lemaître law [3].

1.3 Cosmography in FLRW spacetime

In FLRW cosmological models, angular diameter distances (and luminosity distances) can be predicted by solving the EFE to determine the time evolution of the cosmic scale factor. However, it is also possible, to some extent, to predict the redshift scaling of these distances without assuming a specific gravitational model, relying solely on the symmetry imposed by the CP.

The cosmic scale factor $a(t)$ in the metric (1.1) can be expanded as a power series

response to light.

[3] IAU members voted to recommend renaming the Hubble law $z = H_0 d$ as the Hubble–Lemaître law [54]

around the present time t_0 as

$$a(t) = a(t_0)\Bigg(1 + H_0(t-t_0) - \frac{1}{2}q_0 H_0^2 (t-t_0)^2 + \frac{1}{6}j_0 H_0^3 (t-t_0) + \frac{1}{24}s_0 H_0^4 (t-t_0)^4 + \mathcal{O}\left((t-t_0)^5\right)\Bigg) \tag{1.36}$$

where

$$q_0 \equiv -\frac{\ddot{a}_0}{a_0 H_0^2} \qquad \text{deceleration}^4 \tag{1.37a}$$

$$j_0 \equiv \frac{\dddot{a}_0}{a_0 H_0^3} \qquad \text{jerk} \tag{1.37b}$$

$$s_0 \equiv \frac{\ddddot{a}_0}{a_0 H_0^4} \qquad \text{snap} \tag{1.37c}$$

are the so-called cosmographic parameters in the FLRW spacetime. By expanding relation (1.29) around $z = 0$, one can find [56]

$$d_A(z) = \frac{z}{H_0}\Bigg[1 - \frac{1}{2}(3+q_0)z + \frac{1}{6}\left(11 + 7q_0 + 3q_0^2 + \Omega_{K0} - j_0\right)z^2 + \frac{1}{24}\left(-50 - 10\Omega_{K0} - q_0(46 + 6\Omega_{K0} + 39q_0 + 15q_0^2) + j_0(13 + 10q_0) + s_0\right)z^3\Bigg] + \mathcal{O}(z^5), \tag{1.38}$$

The expansion of the luminosity distance is, instead,

$$d_L(z) = \frac{z}{H_0}\Bigg[1 + \frac{1}{2}(1-q_0)z + \frac{1}{6}\left(3q_0^2 + q_0 - 1 + \Omega_{K0} - j_0\right)z^2 + \frac{1}{24}\left(2 - q_0(2 + 15q_0 + 15q_0^2) + 5j_0(1+2q_0) - 2\Omega_{K0}(1+3q_0) + s_0\right)z^3\Bigg] + \mathcal{O}(z^5)\,. \tag{1.39}$$

Since these relations are derived without invoking the Einstein's field equations, they are independent of any assumptions about the matter-energy content of the universe and rely solely on the FLRW metric (1.1). While fitting these parameters with observations provides information not on the full evolution of the parameter $a(t)$ but only on its scaling near the observer, this approach has the advantage of being completely independent of assumptions about the universe's dynamics. Potential large-scale modifications to gravity, contributions from unknown cosmic fluids, or unconventional equations of state for known cosmic components may alter the functional form of $a(t)$. However, such changes do not affect the cosmographic formalism [57, 58], which remains robust for interpreting observations.

Conversely, once the cosmographic parameters are determined from observations, one can infer information about the Friedmann cosmological models, provided that Einstein's field equations are assumed and a specific energy content for the universe is specified. The relationships between the cosmographic parameters and the density parameters in

[4]The choice of deceleration and the negative sign is historical. When the parameter q_0 was first introduced, it was thought that the universe was decelerating [55].

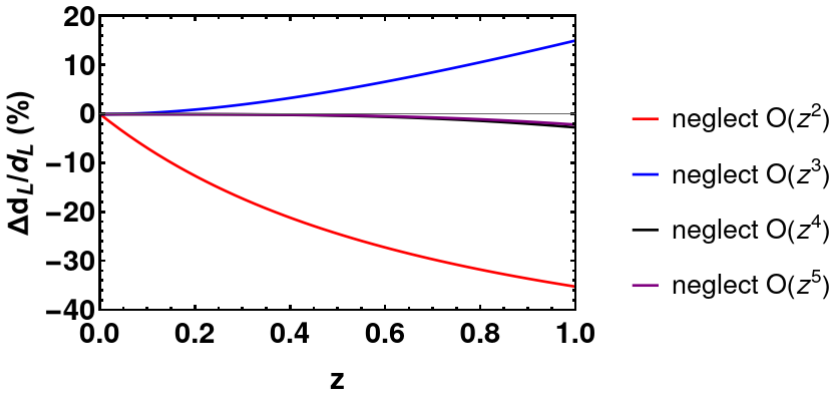


Figure 1.1: The relative error between the expansion of the luminosity distance using cosmographic parameters and the exact distance as given by eq. (1.39) for the case $\Omega_{\mathrm{m0}} = 0.3$, $\Omega_{\Lambda 0} = 0.7$ and $H_0 = 70$ km/s/Mpc.

an FLRW universe (excluding relativistic fluids) are:

$$q_0 = \frac{1}{2}\Omega_{\mathrm{m0}} - \Omega_{\Lambda 0} \tag{1.40a}$$

$$j_0 = \Omega_{\mathrm{m0}} + \Omega_{\Lambda 0} \tag{1.40b}$$

$$s_0 = \frac{1}{2}\Omega_{\mathrm{m0}}(\Omega_{\Lambda 0} - \Omega_{\mathrm{m0}} - 6) + \Omega_{\Lambda 0}^2 \tag{1.40c}$$

In Chapter 5, following an original idea of Kristian and Sachs [59], the cosmographic parameters will be generalized and calculated for a generic spacetime. This approach, called *covariant cosmography*, does not assume any specific symmetry or geometric constraints for the metric. It allows for a general investigation of the spacetime structure around the observer, remaining entirely independent not only of the EFE but also of the CP.

Figure 1.1 shows the relative error between the luminosity distance obtained through the cosmographic expansion and the exact distance as given by eq. (1.39) for the case $\Omega_{\mathrm{m0}} = 0.3$, $\Omega_{\Lambda 0} = 0.7$ and $H_0 = 70$ km/s/Mpc.

1.4 Linear perturbation theory

Cosmological linear perturbation theory offers a framework for describing deviations from perfect uniformity in the universe. By treating perturbations in density or metric coefficients as small, their evolution can be studied using linear approximations. This approach is especially powerful as it simplifies the complex equations of General Relativity, making them more manageable in various cosmological contexts.

According to inflation theory, quantum fluctuations seeded during the early cosmic epochs grew over time under the influence of gravity, eventually forming the large-scale structures we observe today, such as galaxies and galaxy clusters (e.g [60]). For the purposes of this thesis, I focus only on scalar perturbations in a flat FLRW spacetime ($\Omega_K = 0$). By further ignoring anisotropic stresses (assuming Einstein's field equations are valid) and using the Newtonian gauge, the perturbed metric can be expressed to first

order as

$$\mathrm{d}s^2 = -\left(1+2\Phi\right)\mathrm{d}t^2 + a^2(t)(1-2\Phi)\left[\mathrm{d}r^2 + r^2(\mathrm{d}\vartheta^2 + \sin^2\vartheta\,\mathrm{d}\phi^2)\right]. \tag{1.41}$$

The small variations in matter density are described by the adimensional density contrast δ, which represents the difference between the local matter density $\rho(t,\boldsymbol{r})$ and the background density of the universe ρ_{BG}, with the background matter density being a function only of the cosmic time,

$$\delta(t,\boldsymbol{r}) = \frac{\rho(t,\boldsymbol{r}) - \rho_{\mathrm{BG}}(t)}{\rho_{\mathrm{BG}}(t)}. \tag{1.42}$$

In addition to inhomogeneities in the matter distribution, galaxies have peculiar velocities—motions superimposed on the Hubble expansion. Therefore, u^μ becomes

$$u^\mu = (1-\Phi, \frac{\boldsymbol{v}}{a}) \tag{1.43}$$

where $\boldsymbol{v}$ is the peculiar velocity and it is equal to the physical velocity of the matter particle as measured in the inertial frame that locally coincides with the event of observation of an ideal comoving observer in the underlying smooth background model.

In the Newtonian approximation, which neglects time derivatives compared to spatial derivatives, and is applicable in regions much smaller than the Hubble horizon H_0^{-1}, the equations of motion linearized with respect to the perturbation parameters δ, $\boldsymbol{v}$ and Φ are

$$\dot{\delta} + \frac{1}{a}\nabla\cdot\boldsymbol{v} = 0 \tag{1.44}$$

$$\dot{\boldsymbol{v}} + \boldsymbol{v}H = -\frac{\boldsymbol{\nabla}\Phi}{a} \tag{1.45}$$

$$\nabla^2\Phi = 4\pi G a^2 \rho_{\mathrm{BG}}\delta \tag{1.46}$$

These are the linearized continuity, Euler, and Poisson equations, respectively, with operators expressed using comoving coordinates. By taking the time derivative of eq. (1.44) and use equations (1.45) and (1.46), one finds

$$\ddot{\delta} + 2H\dot{\delta} = 4\pi G\rho_{\mathrm{BG}}\delta. \tag{1.47}$$

Since this second-order differential equation has only time derivatives, the density contrast can be separated into the temporal part and spatial part, and it has two independent solutions, one is decaying and the other is growing, as

$$\delta(t,\boldsymbol{r}) = D_1(t)\Delta_1(\boldsymbol{r}) + D_2(t)\Delta_2(\boldsymbol{r}) \tag{1.48}$$

The formal solution of eq. (1.46) is

$$\Phi = G\rho a^2 \int \frac{\delta(t,\boldsymbol{r}')}{|\boldsymbol{r}'-\boldsymbol{r}|}\mathrm{d}\boldsymbol{r}' \tag{1.49}$$

where the integral is over all of the space. If we consider only the growing mode and denote it as D, and we ignore the vorticity of the velocity ($\nabla\times\boldsymbol{v} = \boldsymbol{0}$) since it is proportional to

a^{-1}, and thus decaying as a function of time, the velocity can be expressed as

$$\boldsymbol{v} = -\frac{\nabla\Phi}{4\pi G\rho a}\frac{1}{D}\frac{\mathrm{d}D}{\mathrm{d}t} = -\frac{2f\nabla\Phi}{3aH\Omega_{\mathrm{m}}} \tag{1.50}$$

where f is the growth rate $f = \frac{a}{D}\frac{\mathrm{d}D}{\mathrm{d}a}$, and for matter with the cosmological constant it is $f \approx \Omega_{\mathrm{m}}^{0.6}$ [61].

1.4.1 Perturbed redshift and distance

In a linearly perturbed background, the redshift measured by an observer with peculiar velocity $\boldsymbol{v}_0$ is [62, 63]

$$1 + z = (1 + \bar{z})\left[1 + \boldsymbol{n}\cdot(\boldsymbol{v} - \boldsymbol{v}_0) - (\Phi - \Phi_0) - 2\int_{\lambda_0}^{\lambda_{\mathrm{e}}} \Phi' \mathrm{d}\lambda\right], \tag{1.51}$$

where $\bar{z}$ is the background cosmological redshift

$$1 + \bar{z} = \frac{a_0}{a}, \tag{1.52}$$

and here, the prime denotes the derivative with respect to the conformal time $\mathrm{d}t/a(t)$ and the integral is taken over the affine parameter (λ) describing the null geodesic of light. The angular diameter distance, if we neglect the correction of the gravitational potential Φ, which is second order small, is

$$d_A(z) = \bar{d}_A(\bar{z}(z))\,(1 + \boldsymbol{n}\cdot\boldsymbol{v}_0)\,. \tag{1.53}$$

since the angular size of an object will look smaller if the observer is moving toward it ($\delta\Omega \to \delta\Omega(1 - 2\boldsymbol{n}\cdot\boldsymbol{v}_0)$). The luminosity distance then can be finally found by exploiting the reciprocity relation, [62, 64]

$$d_L(z) = \bar{d}_L(\bar{z}(z))\,(1 + 2\boldsymbol{n}\cdot\boldsymbol{v} - \boldsymbol{n}\cdot\boldsymbol{v}_0)\,. \tag{1.54}$$

In these relations $\bar{d}_A(\bar{z})$ and $\bar{d}_L(\bar{z})$ represent the angular diameter and the luminosity distances between the events of emission and absorption in a perfectly smooth universe.

1.4.2 Matter power spectrum

Given the complex spatial structure of a perturbed cosmic fluid, the focus is not on predicting the time evolution of the density field $\delta(r, t)$ at each spatial location. Instead, we are interested in its large-scale statistical properties, particularly its clustering properties. The clustering of density fluctuations is typically described by means of the power spectrum $P(k)$, which is defined by

$$\langle\delta_{\boldsymbol{k}}\delta_{\boldsymbol{k}'}\rangle = (2\pi)^3\delta_D(\boldsymbol{k} + \boldsymbol{k}')P(k) \tag{1.55}$$

where δ_D is Dirac delta function, the $\langle.\rangle$ denotes the ensemble average, and $\delta_{\boldsymbol{k}}$ is a the Fourier transformation of the density contrast field,

$$\delta_{\boldsymbol{k}} = \int \delta(\boldsymbol{r})e^{-i\boldsymbol{k}\cdot\boldsymbol{r}}\mathrm{d}^3r, \tag{1.56}$$

It is a stochastic variable with zero mean $\langle \delta_{\boldsymbol{k}} \rangle = 0$, and $\delta_{-\boldsymbol{k}} = \delta^*_{\boldsymbol{k}}$ because $\delta(\boldsymbol{r})$ is real. As a consequence, the power spectrum is the Fourier transformation of the 2-point correlation function $\xi(r)$,

$$P(k) = \int \xi(r) e^{-i\boldsymbol{k}\cdot\boldsymbol{r}} \mathrm{d}^3 r = 4\pi \int \xi(r) \frac{\sin(kr)}{kr} r^2 \mathrm{d}r. \tag{1.57}$$

In practice, we cannot measure the point-like density contrast $\delta(\boldsymbol{x})$ at each position in space. Instead, we can measure the density smoothed over some volume. We thus replace the density field $\delta(\boldsymbol{x}, t)$ by a filtered version $\delta_R(\boldsymbol{x}, t)$,

$$\delta_R(\boldsymbol{x}, t) = \int_V \delta(\boldsymbol{x} + \boldsymbol{r}) W(\boldsymbol{r}) \mathrm{d}^3 r \tag{1.58}$$

where $W(\boldsymbol{r})$ is a smoothing function. The most typically adopted window function is the spherical Top-Hat of radius R, $W_R(r) = 3/(4\pi R^3)$ if $r < R$ and zero otherwise. The Fourier transformation of this window function is $W_R(k) = 3j_1(kR)/(kR)$, where j_1 is the spherical Bessel function of order 1. The power spectrum of the smoothed density contrast field is $P(k)|W(k)|^2$, and the variance of the mass distribution smoothed with a sphere of radius R is thus (using equations 1.55, 1.56 and 1.58),

$$\sigma^2(R) = \langle \delta_R^2 \rangle = \frac{1}{2\pi^2} \int P(k) |W(k)|^2 k^2 \mathrm{d}k. \tag{1.59}$$

The parameter σ_8 is the square root of the variance of the mass distribution smoothed on a $R = 8h^{-1}$ Mpc scale

$$\sigma_8^2 = \frac{1}{2\pi^2} \int P(k) \left(\frac{3j_1(kR)}{kR} \right)^2 k^2 \mathrm{d}k \tag{1.60}$$

and it is a crucial quantity for assessing how much the actual universe deviates from the ideal conditions of uniformity. Observational constraints on this parameter are discussed in section 1.6.

1.5 Observational evidences in favour of the ΛCDM model

1.5.1 Galaxy distance probes

A remarkably straightforward yet effective method for measuring standard cosmological parameters—such as the Hubble constant (H_0), the curvature of the Universe's spatial sections, or the energy densities of its constituent fluids—is geometrical. This approach involves measuring distances to cosmological objects independently of redshift and comparing them to theoretical predictions to constrain the unknown parameters in the models.

At low redshift theoretical predictions are sensitive only to the local expansion rate of the universe via the Hubble-Lemaître law $d = H_0^{-1} z$, while if the photon flight time is important, then its geodesic path is sensitive also to curvature effects in addition to the expansion rate at earlier epochs. Because of this, it is only with distances estimated at high redshift that one can hope to constrain a larger set of cosmological parameters.

However, it is also interesting to analyze the discrepancy between theoretical pre-

dictions and observed distances at a given redshift, z. This residual is proportional to peculiar velocities and provides valuable insight into the amplitude of the density inhomogeneities that cause matter to deviate from the Hubble flow—the isotropic expansion of the universe near the observer. Indeed, the small magnitude of peculiar velocities ($v/c \sim 10^{-3}$) means the distortions they induce are quickly overwhelmed by noise in the distance measurements. This is due to the fact that the relative distortions $\delta d/d$ caused by peculiar motions on the theoretically smooth distance is proportional to v/d and becomes negligible at larger distances.

Distances determined using redshift-independent techniques in the local universe are particularly important for this thesis. As I will discuss in the following chapters, studying the anisotropies in the distance-redshift relation offers a potential avenue for gaining insight into the metric that describes the local region of the universe in a fully model-independent manner—without relying on FLRW assumptions or perturbative approaches, such as peculiar velocities or related linearly perturbed quantities.

Here below I thus briefly discuss the main extragalactic phenomena that can be exploited to determine cosmic distances.

Cepheids variables

The Cepheids are giant variable stars that undergo periodic fluctuations in their observed brightness, with a distinct period and amplitude. In 1912, Henrietta Swan Leavitt discovered the linear relation between the logarithm of the period (later on correctly conjectured by Eddington to be induced by the star's radial pulsation) and the apparent magnitude of classical Cepheids by studying variable stars in the Small Magellanic Cloud [65]. Since the stars in this cloud are nearly equidistant from Earth, this linear relation also applies to their absolute magnitudes. By measuring the absolute magnitude of nearby Cepheids through stellar parallax, we can calibrate the zero point of the period-(absolute) luminosity relation. Given their brightness, Cepheids can be used to measure distances to galaxies up to about 20 Mpc with an accuracy of roughly 5%.

A similar type of periodic variable star, though different in nature, is the RR Lyrae. These stars are also used as extragalactic distance indicators, though they are much dimmer than Cepheids, making distant RR Lyrae more challenging to observe [66].

Tip of the red-giant branch

For low-mass stars ($\approx 1 - 2\ M_\odot$), after exhausting hydrogen in their cores and expanding into red giants, the core becomes primarily composed of helium, while hydrogen continues fusing in a surrounding shell. This process adds more helium to the core until the core temperature reaches a critical point, triggering a helium core flash—a brief, explosive ignition of helium fusion. At this stage, the red giant attains its maximum luminosity. Afterward, the star's luminosity decreases as it transitions from the tip of the red giant branch (TRGB) to the horizontal branch in the Hertzsprung–Russell diagram. The TRGB luminosity, which is slightly dependent on metallicity but mainly determined by the nearly constant helium core mass, serves as a reliable standard candle. This makes the TRGB an effective distance indicator [66, 67] for distances up to 20 Mpc, with an accuracy of $\sim 5\%$.

As seen, these primary distance indicators are effective for measuring distances to nearby objects, but they are not luminous enough to be observed at higher redshifts. To address this limitation, secondary distance indicators, which are calibrated using the

primary ones, become essential. In the following sections, I will discuss the key secondary indicators used for mapping greater regions of the cosmos.

The Tully–Fisher relation

In 1977, Tully and Fisher introduced an ingenious method for estimating the absolute luminosity of rotating disc galaxies [68]. They leveraged the observation that a galaxy's maximum rotational velocity—measured through the Doppler effect, and which is a redshift-independent observable, correlates with its mass. Since a galaxy's mass is directly related to its absolute luminosity, this relationship provides a powerful tool for determining the intrinsic luminosity of spiral galaxies and therefore its distance.

The rotation velocity can be extracted either studying the optical spectrum of a galaxy or the 21 cm neutral hydrogen line profile shape in the radio band. Since the method is theoretically applicable to all spiral galaxies (though in practice only to those whose discs are not too inclined relative to the observer's line of sight), it remains one of the best tools for mapping distances in the local universe. Typically, this method provides individual distance estimates with an accuracy of around 20%. Furthermore, since spiral galaxies often cluster in groups, the error on the average distance to these structures can be reduced by a factor of $1/\sqrt{N}$, where N is the number of galaxies in the group.

Fundamental plane

he Faber–Jackson relation describes the correlation between the velocity dispersion of stars in pressure-supported elliptical galaxies and their absolute luminosity [69]. It is conceptually similar to the Tully–Fisher relation for spiral galaxies, as both leverage the relationship between a galaxy's dynamical (and redshift-independent) property and its mass, and hence its intrinsic luminosity. The Fundamental Plane technique refines the Faber–Jackson relation by incorporating surface brightness as a third variable, which reduces the scatter seen in the Faber–Jackson relation, leading to more accurate distance estimates for elliptical galaxies [70]. Like the Tully–Fisher method, distance estimates using the Fundamental Plane method typically achieve an accuracy of around 20%.

Surface Brightness Fluctuations

This method was proposed by Tonry and Schneider in 1988 [71], it relies on the fluctuations in observed brightness across each pixel of a galaxy's CCD image. It is based on the principle that, if the number of stars in each pixel follows Poisson statistics, independent of the stars' individual luminosities, and the weighted average luminosity of the stars, $\bar{L}$, is known (and does not vary significantly between galaxies), the distance can be estimated using the relationship between the variance and mean of the observed flux per pixel. Specifically, the ratio variance/mean $= \bar{L}/(4\pi d^2)$ allows for the calculation of the distance. This method is most effective for early-type galaxies and can be calibrated using galaxies with distances determined by primary distance indicators to refine the value of $\bar{L}$. While this approach is limited to measuring distances up to around 100 Mpc—less than methods like Tully-Fisher or the Fundamental Plane—it offers greater accuracy, with typical uncertainties of about 5% [72].

Type Ia supernovae

Supernovae Type Ia (SNe Ia) occur when a white dwarf in a binary system accrete matter from its companion star, gradually increasing its mass until it approaches the Chandrasekhar limit ($\approx 1.4\ M_\odot$). At this point, the electron degeneracy pressure can no longer support the star against gravitational collapse, triggering reactions that result in a massive explosion. Since the explosion occurs at almost the same mass, SNe Ia are considered almost ideal standard candles in luminosity. Being extremely bright transient events, with an absolute magnitude (peak luminosity) of around -19.3, SNe Ia are visible at great distances, allowing to map the position of the hosting galaxies even on Gpc scales.

SNe type I are identified by the absence of hydrogen features in their spectra, while SNe Ia, in particular, exhibit silicon features. In contrast, Type II supernovae (SN II), which exhibit hydrogen features, are more abundant but less luminous. SN II can also be used to measure distances by taking into account the correlation between their luminosity and the expansion velocity of their ejecta [73, 74].

Consider an expanding universe consisting only of matter and radiation. Within the FLRW model, equation (1.7) indicates that the scale factor has a negative second derivative, meaning the expansion of the universe is slowing down. Measuring this deceleration rate was the primary goal of two independent teams: the Supernova Cosmology Project [75] and the High-Z Supernova Search Team [76]. Their technique involved analyzing the scaling of luminosity distance with redshift—commonly referred to as the "Hubble diagram"—for SNe Ia. The cosmological parameters can then be constrained by fitting FLRW theoretical models for the luminosity distance to the observed data (see Figure 1.2).

Surprisingly, analysis of the Hubble diagram revealed that the expansion of the universe was not decelerating but accelerating. These initial findings suggested that the universe is consistent with being flat and provided compelling evidence that nearly 75% of the energy density required for flattening the spatial surfaces of the Universe is contributed by the cosmological constant, or equivalently, by a fluid with a negative equation of state, $w = -1$ (consistent with vacuum energy). Since then, these findings have been consistently confirmed and strengthened by numerous independent analyses using increasingly larger samples of SNe Ia. For instance, the latest results from around 1500 SNe Ia (Pantheon+ sample) indicate that, assuming a flat universe, the best-fitting value for the local Hubble parameter is $H_0 = 73.5 \pm 1.1$. Additionally, the best fitting "dark energy" perfect fluid has a density of $\Omega_x = 0.666 \pm 0.180$ and a constant equation of state parameter $w_x = -0.90 \pm 0.14$. As there is no evidence for time evolution, these results remain consistent with the acceleration being driven by the Einstein cosmological constant [77].

1.5.2 CBM radiation probes

The Cosmic Microwave Background (CMB) is the earliest "snapshot" of our Universe. This radiation, a relic of the high-density early phases, carries crucial information about primordial fluctuations seeded by inflation. These fluctuations, amplified by cosmic gravity, eventually evolved into the large-scale structures we observe today. The initial energy density perturbations manifest as temperature fluctuations in the CMB, on the order of $\Delta T/T \sim 10^{-5}$. First detected by the COBE satellite [78], and later measured with greater precision on smaller angular scales by WMAP [79], these fluctuations are now mapped in remarkable detail by the Planck satellite [80]. These fluctuations are the result of the competition between gravitational pull which tend to collapse an overdensity fluctuation

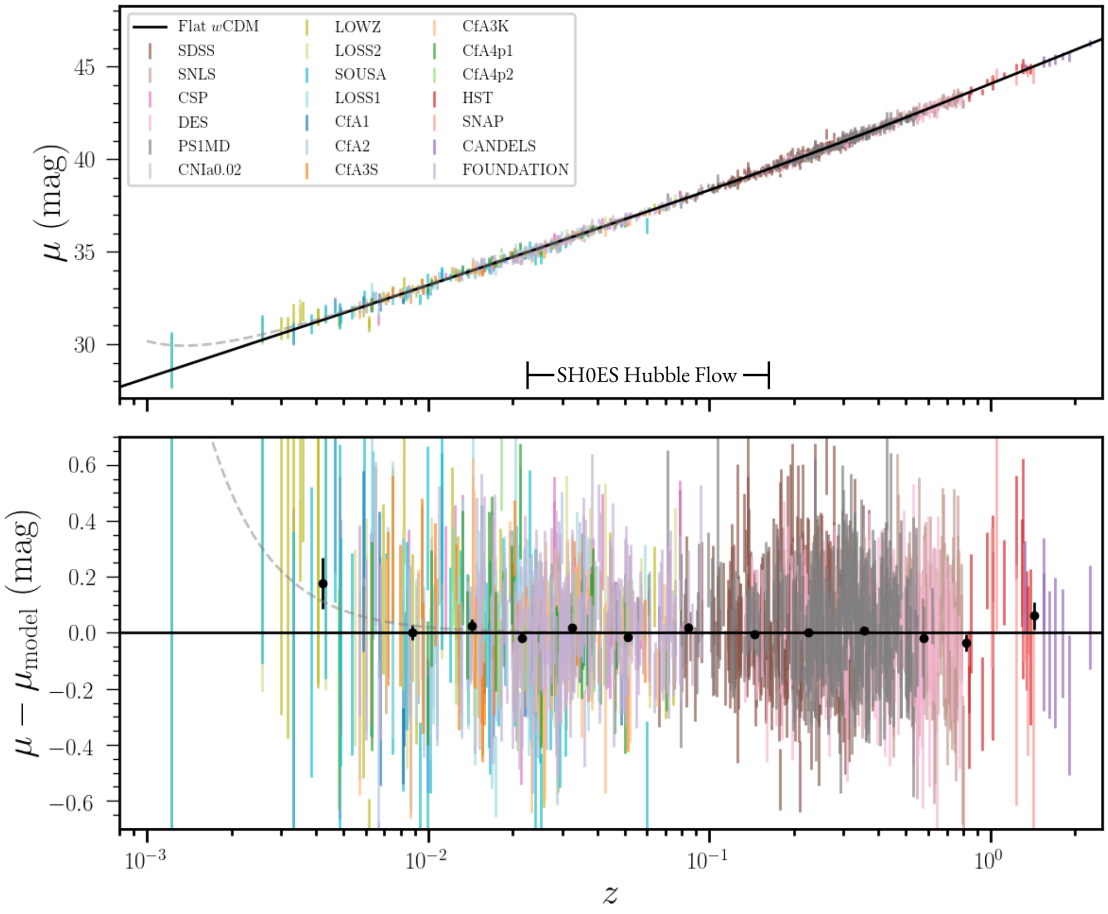


Figure 1.2: *Top*: the Pantheon+ "Hubble diagram" showing the distance modulus μ vs. redshift z. The 18 different surveys are each given different colors. *Bottom*: the distance modulus residuals relative to a best-fit cosmological model with binned data for reference (black points). Source: [77].

and the radiation pressure that opposes to it and make the fluctuation expand. The typical scale for this process is the so called "sound horizon scale" at the last scattering epoch $\lambda_{\rm sh}(t_{\rm ls}) \sim c_{\rm s} t_{\rm ls}$ (where $c_{\rm s}$ is the sound speed in the primordial fluid).

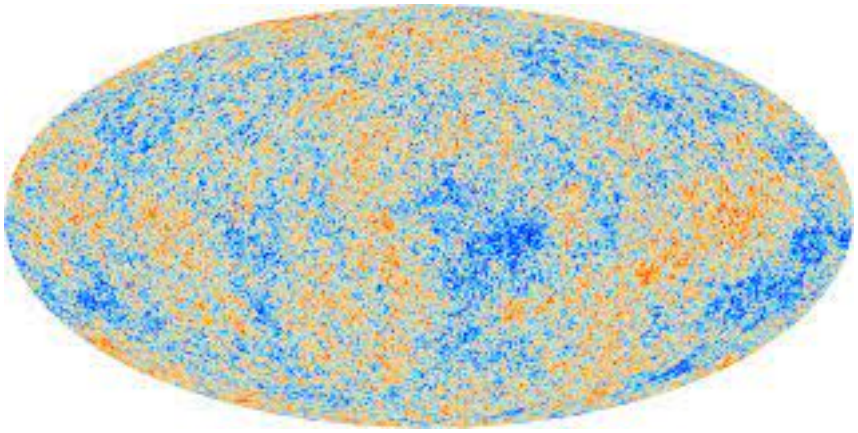
This represents the maximum distance that sound waves could travel to drive oscillations, making it the longest (fundamental) wavelength that acoustic waves could have at the epoch of recombination. These waves subtend an angle $\theta_{\rm ls}$ at the observer's position. To detect this fundamental frequency and its higher harmonics, it is useful to perform a spherical harmonic decomposition of the temperature fluctuation maps, extracting the power spectrum of the signal. The multipoles are characterized in Fourier space by the angular modes $\ell = \pi/\theta$. Consequently, the power spectrum is predicted to exhibit characteristic peaks, with the fundamental peak at

$$\ell_{\rm sh} = \frac{\pi}{\theta_{\rm sh}} = \frac{\pi}{\lambda_{\rm sh}(t_{\rm ls})} \frac{\lambda_{\rm sh}(t_{\rm ls})}{\theta_{\rm sh}(t_{\rm ls})} = \frac{\pi}{\lambda_{\rm sh}(t_{\rm ls})} d_A(t_{\rm ls}).$$

By observing the scale at which the first peak occurs in the CMB temperature power spectrum, we can thus constrain the angular diameter distance at last scattering ($d_A(t_{\rm ls})$) and thus the cosmological parameters that enters into its theoretical expression. An in-depth analysis, though theoretically straightforward due to the linear nature of small initial fluctuations, reveals that the positions and relative amplitudes of all harmonics of the fundamental tone contain a wealth of information about cosmological parameters. This makes the CMB the most powerful single probe for measuring the parameters of the FLRW model. An up-to-date table with Planck's determinations is shown in Figure 1.3.

1.5.3 Galaxy clustering probes

After recombination, the CMB photons almost ceased to interact with matter, so they streamed away from the matter density perturbations leaving baryons inhomogeneities "frozen" in the state they were at this epoch. The angular scale of the sound horizon (and its multipoles) at last scattering can thus still be seen today in the baryon fluid (the so called Baryon Acoustic Oscillations (BAO)). The fundamental tone of these oscillations can be extracted from the analysis of the galaxy clustering (at low redshift) and compared to those inferred at high redshift from the CMB. The BAO were detected at low redshift by the *Sloan Digital Sky Survey* (SDSS). The correlation function of galaxy clustering displayed a peak for a galaxy separation distance of ~ 150 Mpc, which corresponds to today's extrapolated value of the sound horizon at last scattering [82]. The existence of these coherent oscillations in both the early radiation field and the galaxy distribution at lower redshift guarantees the coherence of our understanding of the evolution of density perturbations in an expanding universe. The BAO provides also a complementary way to estimate cosmological parameters which has statistical degeneracies that are independent from those of the CMB and SNe Ia probes. The combinations of all these probes allows us to constrain in a more effective way the values of the cosmological parameters as displayed in Figure 1.4.



Parameter	Plik best fit	Plik [1]	CamSpec [2]	([2] − [1])/σ_1	Combined
$\Omega_b h^2$	0.022383	0.02237 ± 0.00015	0.02229 ± 0.00015	−0.5	0.02233 ± 0.00015
$\Omega_c h^2$	0.12011	0.1200 ± 0.0012	0.1197 ± 0.0012	−0.3	0.1198 ± 0.0012
$100\theta_{MC}$	1.040909	1.04092 ± 0.00031	1.04087 ± 0.00031	−0.2	1.04089 ± 0.00031
τ	0.0543	0.0544 ± 0.0073	$0.0536^{+0.0069}_{-0.0077}$	−0.1	0.0540 ± 0.0074
$\ln(10^{10} A_s)$	3.0448	3.044 ± 0.014	3.041 ± 0.015	−0.3	3.043 ± 0.014
n_s	0.96605	0.9649 ± 0.0042	0.9656 ± 0.0042	+0.2	0.9652 ± 0.0042
$\Omega_m h^2$	0.14314	0.1430 ± 0.0011	0.1426 ± 0.0011	−0.3	0.1428 ± 0.0011
H_0 [km s^{-1}Mpc^{-1}]	67.32	67.36 ± 0.54	67.39 ± 0.54	+0.1	67.37 ± 0.54
Ω_m	0.3158	0.3153 ± 0.0073	0.3142 ± 0.0074	−0.2	0.3147 ± 0.0074
Age [Gyr]	13.7971	13.797 ± 0.023	13.805 ± 0.023	+0.4	13.801 ± 0.024
σ_8	0.8120	0.8111 ± 0.0060	0.8091 ± 0.0060	−0.3	0.8101 ± 0.0061
$S_8 \equiv \sigma_8(\Omega_m/0.3)^{0.5}$	0.8331	0.832 ± 0.013	0.828 ± 0.013	−0.3	0.830 ± 0.013
z_{re}	7.68	7.67 ± 0.73	7.61 ± 0.75	−0.1	7.64 ± 0.74
$100\theta_*$	1.041085	1.04110 ± 0.00031	1.04106 ± 0.00031	−0.1	1.04108 ± 0.00031
r_{drag} [Mpc]	147.049	147.09 ± 0.26	147.26 ± 0.28	+0.6	147.18 ± 0.29

Figure 1.3: *Top*: CMB map of the sky observed by Planck, with the temperature anisotropies, credit ESA and the Planck Collaboration. *Bottom*: values of the cosmological parameters estimated by Planck [81].

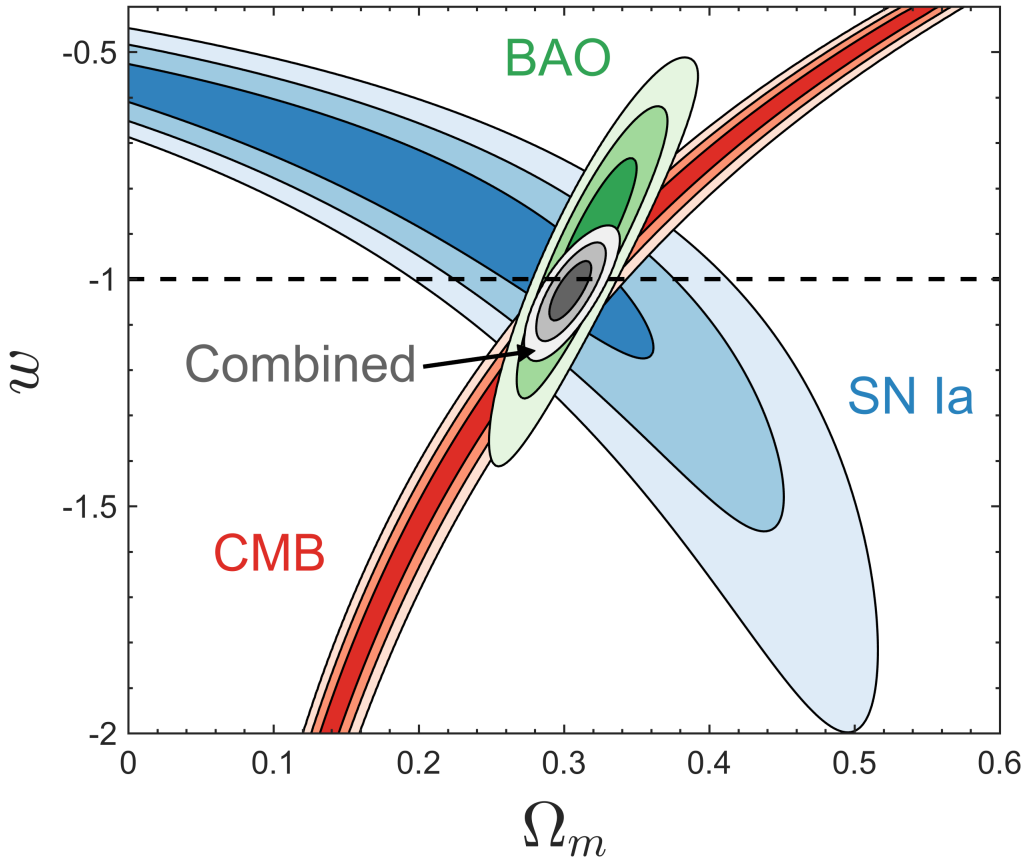


Figure 1.4: Constraints on $(w_\Lambda, \Omega_{\mathrm{m},0})$ using joint analysis between SN Ia, CMB and BAO. Source: [83].

1.6 Tensions in the standard model

The ΛCDM model has shown remarkable consistency with a wide range of cosmological and astrophysical observations across different scales. However, recent data have started to reveal tensions in some of the estimates of the model's parameters, including the Hubble parameter (Hubble tension), the root mean square of the matter density field fluctuations (S_8 tension) and the velocity of the observer with respect to the CMB (cosmic dipole tension).

Hubble tension

The Hubble tension refers to the $> 4\sigma$ discrepancy between the Hubble constant H_0 inferred in a model-dependent manner from high-redshift CMB studies by the Planck collaboration [80] (67.4 ± 0.5 km/s/Mpc) and the value directly measured using astrophysical techniques at low redshift by the Pantheon+SH0ES collaboration, which reports $H_0 = 73.5 \pm 1.1$ km/s/Mpc, based on SNe Ia samples calibrated by Cepheids [77]. To further illustrate this discrepancy, Figure 1.5 presents the constraints on H_0 derived from various methods and samples.

Whether this discrepancy is the result of systematic errors affecting at least one of the two estimation techniques is still hotly debated. Probably, on the observational front, a major step toward resolving this issue may come from the refinement of innovative

and independent probes, such as those based on gravitational waves. However, if both estimates are indeed accurate, as each team asserts, then the source of the discrepancy likely lies in new physics.

The literature offers numerous theoretical proposals to resolve the Hubble tension. Some focus on new physics in the early universe, such as early dark energy, while others explore modified gravity theories [84]. However, several indications suggest that resolving the Hubble tension may also require new physics in the late (local) universe [8].

In [85], the ages of ancient astrophysical objects (up to redshift ≈ 8) are used to place an upper limit on H_0 (since the age of the universe is proportional to H_0^{-1}). Their analysis finds an upper limit of $H_0 < 73.2$ km/s/Mpc at the 95% confidence level, revealing a 2.3σ discrepancy with locally observed H_0 values. Another indication is that the Hubble constant seems to show a decreasing trend with increasing redshift, as reported by [86] (and earlier by [87]). Using a dataset that includes megamasers, cosmic chronometers, type Ia SNe, and BAO up to redshift $\lesssim 0.7$, they found a statistically significant non-zero slope ($\Delta H_0/\Delta z \approx -22 \pm 9$) with a significance of 2.1σ. This trend was also observed in the Pantheon Sample of SNe Ia by [44]. Although the decrease in H_0 is smaller in this case, fitting the relation $H_0(1+z)^{-\alpha}$ showed that the significance level of α varies from 1.2σ to 2σ, depending on the number of bins used to estimate H_0.

Is this an indication that the new physics manifests as a severe failure of the CP in the low redshift universe, say $z < 0.3$? Tentative observations suggest that the local structure of the universe is highly irregular. In [88], using the CLASSIX galaxy cluster survey, the authors found that we are situated in an underdense region extending up to approximately 140 Mpc. Additionally, [89], analyzing the peculiar motions of galaxies from the Cosmicflows-4 sample [72] within a sphere of radius $\sim 200\ h^{-1}$ Mpc, found that the probability of observing a bulk flow—coherent galaxy motion within this volume—as large as the observed one in the ΛCDM model is around 2×10^{-6}. After reanalyzing the data, [90] reported a probability of 0.11%, which, while slightly higher, remains intriguingly low.

Linear perturbation theory predicts that measurements of the Hubble constant in a non-uniform universe should be systematically influenced by local gravitational effects from inhomogeneities. According to this theory, the cosmic variance of H_0 is estimated to be 1.5 km/s/Mpc in the redshift range $0.01 < z < 0.15$ [91]. Therefore, While accounting for cosmic variance can reduce the tension in H_0 measurements, it does not lower the discrepancy below the 3σ threshold. Note, moreover, that in [77], the authors correct for inhomogeneity effects by adjusting the redshift of objects for peculiar velocity, using galaxy density reconstructions from the 2M++ catalog [92, 93]. This correction helps minimize the impact of cosmic variance on the measurement, but ultimately, the tension remains largely unaffected.

The S_8 tension

From an observational standpoint, estimating σ_8 through galaxy clustering analysis reveals a strong degeneracy with the Ω_m parameter, which affects the amplitude of the power spectrum $P(k)$. To address this issue, it is practical to introduce a rescaled parameter that is less affected by this degeneracy: $S_8 \equiv \sigma_8 \sqrt{\Omega_\mathrm{m}/0.3}$, and thus optimally suited for statistical inferences.

The early universe data, specifically the analyses of the Planck TT,TE,EE+lowE power spectra [81] indicate that $S_8 = 0.834 \pm 0.016$. The analyses at low redshift, instead, seems to prefer lower values. For example [95], via a tomographic weak gravitational lensing analysis of Dark Energy Survey (DES) Year 3 data, found $S_8 = 0.759^{+0.025}_{-0.023}$ which

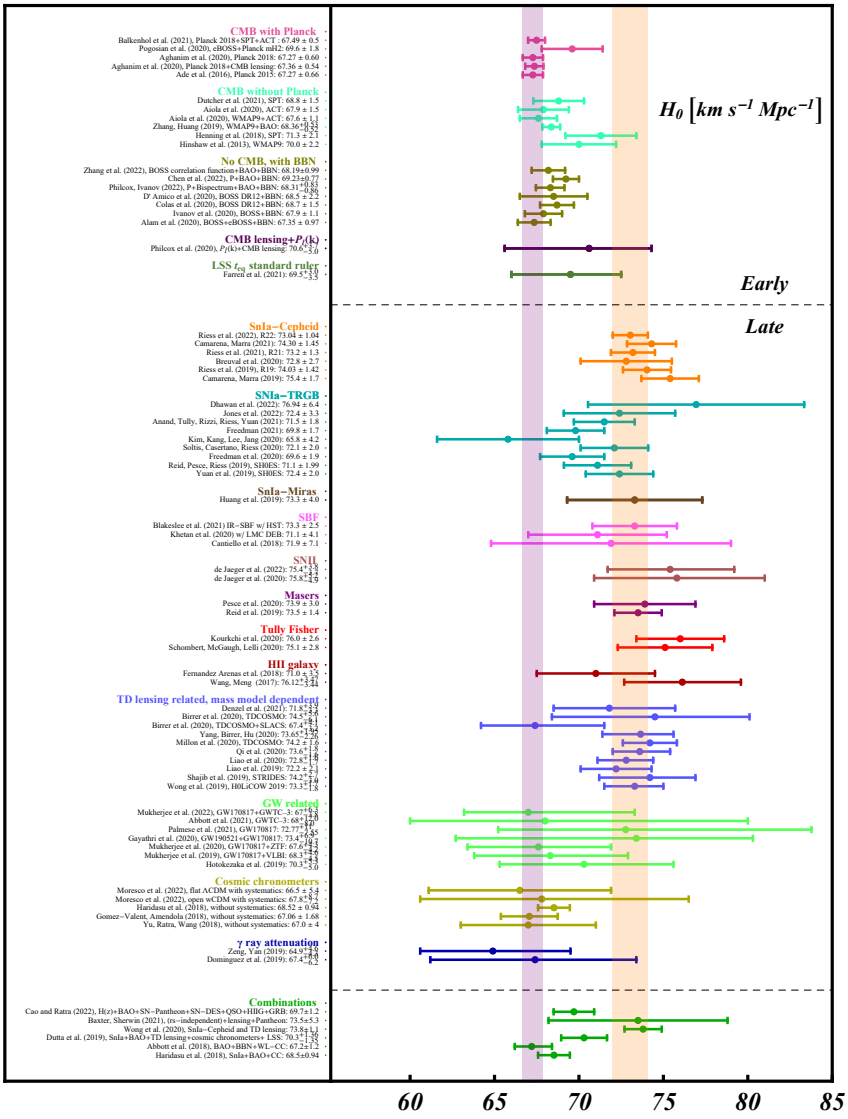


Figure 1.5: The Hubble constant H_0 values with the 68% CL constraints derived by a multitudes of methods and samples. Source: [94].

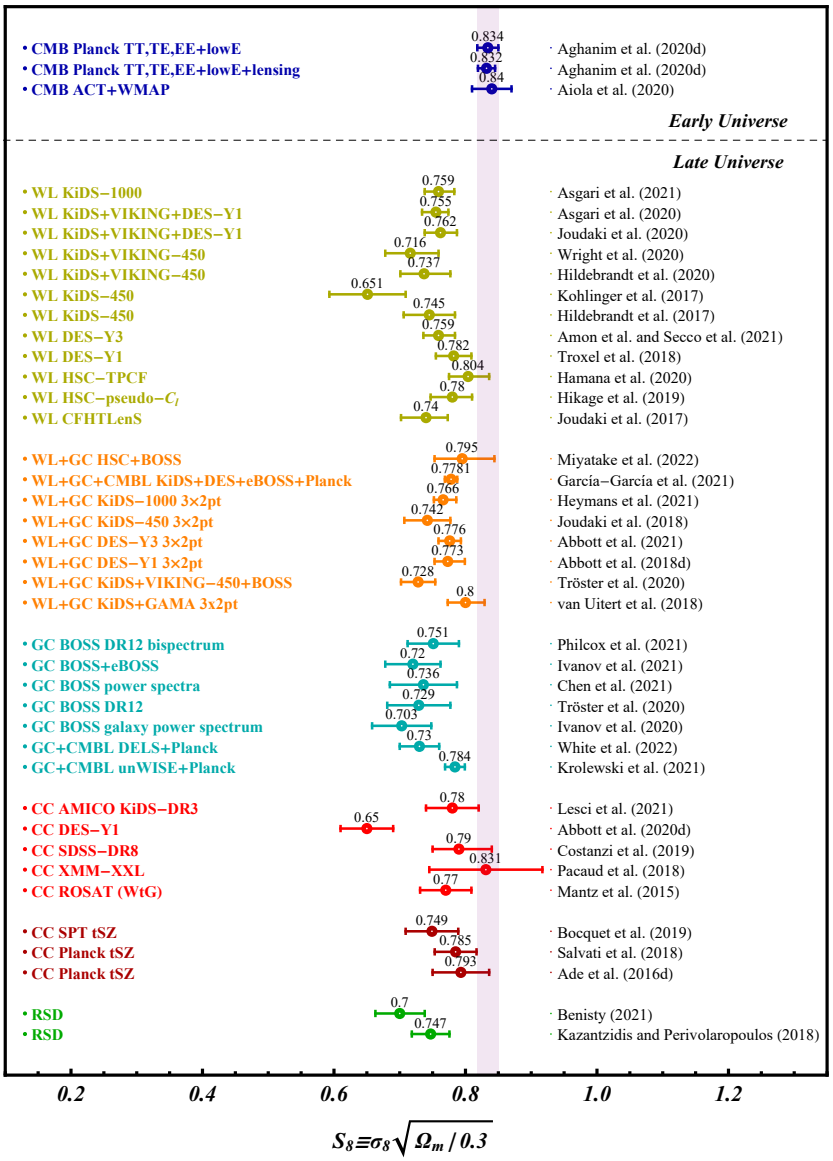


Figure 1.6: Constraints on S_8 from multiple samples and independent techniques. The corresponding 68% statistical error is also quoted. Source: [94].

is in $\sim 2.5\sigma$ tension with the Planck estimate. The independent analysis of 1000 deg^2 of imaging data from the Kilo Degree Survey (KiDS) consistently indicate $S_8 = 0.759^{+0.024}_{-0.021}$ [96].

Additionally, analyses of the low-redshift clustering properties of galaxies indicate that S_8 estimates are lower and show a marginal inconsistency with the Planck results, with a discrepancy of approximately 2σ. For example, [97], using the BOSS DR12 dataset, find $S_8 = 0.751 \pm 0.039$ (see [98] for a review of the latest measurements).

The dipole tension

In 1984, Ellis and Baldwin [99] predicted the existence of a dipolar pattern in the all-sky maps of distant radio galaxy number counts. This modulation is due to the observer's motion with respect to the matter frame defined by the radio sources. If this distant matter frame coincides (comoves) with the CMB frame, as required by the CP, then the velocity of the observer as inferred from the analysis of the radio galaxy dipole should

align in direction and coincide in amplitudes. with that independently estimated from the analysis of the CMB temperature dipole. This last is indeed traditionally attributed to a similar kinematical effect: the motion of the observer (the Solar System) relative to the CMB rest frame. The extremely well measured amplitude of the temperature dipole in the CMB (in the Solar System frame) ($\Delta T = 3.362 \pm 0.001$ mK) , corresponds to an observer velocity of 369.8 ± 0.1 km/s [80] in the direction $(l, b) = (264.021 \pm 0.011, 48.253 \pm 0.005)$ degrees in galactic coordinates.

Intriguingly, the latter measurement is not in agreement with that infereed from the analysis of the radio dipoles. For example [100], analyzing the radio sources in the NRAO VLA Sky Survey (NVSS) [101] (at $z \sim 1$) found that the direction was consistent with that measured using the CMB [80], but the amplitude was nearly 4 times larger ($\approx 1600 \pm 400$) ($\approx 3\sigma$ tension with the CMB amplitude). In [40], the dipole in the number counts was detected in the mid-infrared data collected by the Wide-field Infrared Survey Explorer (WISE) [102] ($z \sim 1.2$). These authors also found a dipole with a direction consistent with the CMB dipole, but with an amplitude approximately twice as large. Also this discrepancy is statistically significant, with a significance level of $\approx 4.9\sigma$.

Clearly, detecting a weak dipolar signal in distant source counts is technically challenging, especially given the significant statistical and systematic uncertainties. However, it is intriguing that the tension in distant and local measurements—mimicking an analogous tension in the early-late estimates of the Hubble constant—seem to suggest that the main issue could be an unexpected breakdown of the CP.

The curvature tension

For a universe that satisfies to the CP, the only possibility is that its hypersurfaces of constant time have constant curvature. This means that the spatial sections of the 4D cosmic spacetime must be either flat, negative constant curvature, or positive constant curvature.

Over the past two decades, a wide range of observational data has not ruled out the hypothesis that the universe is flat. However, rather than treating this as a null hypothesis, it may be more appropriate to call it a strong theoretical bias. In fact, the physical justification for a flat universe, without resorting to exceptional fine-tuning of initial conditions, was one of the primary motivations for the development of the inflationary mechanism for the evolution of the early universe.

In 2018, Planck measured a lensing amplitude anomalously high compared to that predicted by the standard cosmological model (which assumes a flat universe) [80]. As originally suggested by the Planck team and later reinforced by independent studies (e.g., [103]), this tension could be alleviated by relaxing the flatness constraint. When curvature is treated as a free parameter in the analysis, Planck data shows a strong preference for closed models ($\Omega_{K0} \in [-0.0095; -0.007]$) with a 3.4σ confidence level, as illustrated in Figure 1.7.

However, it quickly became evident that a closed universe was in conflict with evidence from other datasets. For instance, the BAO probe, which is particularly sensitive to curvature, strongly rejects the closed FLRW model that best fits the Planck data, with a significance of more than 3σ. This is shown in Figure 1.8.

[4]The galactic coordinates which are used throughout this thesis are specified by two angles: the longitude l, which measures the angular separation eastward along the galactic equator from the Galactic Center (in almost the direction of the radio source Sagittarius A* in the Sagittarius constellation), and the latitude b, which measures the angle northward of the galactic equator as viewed from Earth.

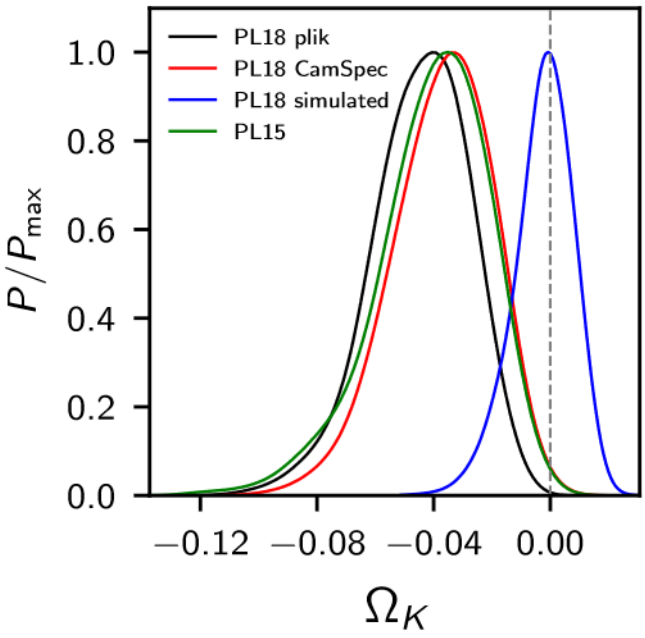


Figure 1.7: Posterior distribution on the value of Ω_{K0} from Planck. The blue curve is a simulation assuming a flat universe, the other ones are from real data without assuming flatness. Source: [103].

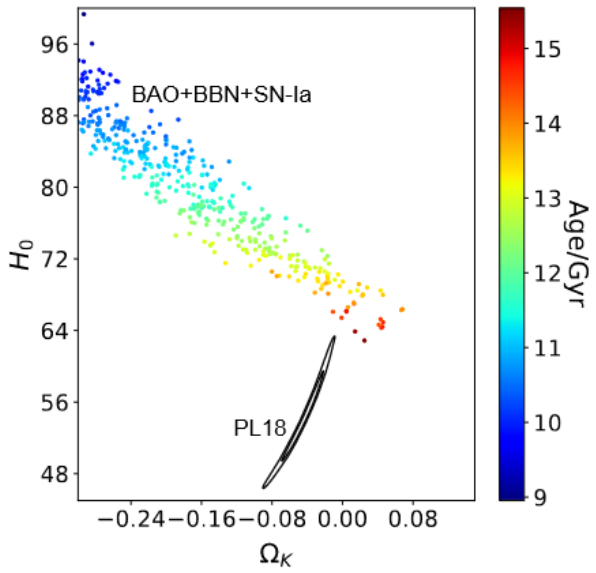


Figure 1.8: Tension between the Planck data (black ellipse), agreeing with a closed FLRW universe, and the combined data from BAO+BBN+SN Ia (colored points). Source: [103].

1.7 Conclusions

Until about ten years ago, the main limitation of the standard cosmological model was though to be largely conceptual, stemming from its lack of theoretical appeal. To explain the universe's behavior, Einstein's field equations for gravity had to be supplemented with poorly motivated, extra physics: the elusive dark matter, the speculative inflationary phase, and a late-time acceleration driven by either a cosmological constant or dark energy.

In the last decade, it has become increasingly clear that even this standard model, despite its reliance on exotic components, faces significant challenges in accounting for the growing body of observational data. This raises the question of whether we need to introduce yet another unknown physical ingredient, further refine our understanding of the 'dark components,' or critically reassess the very foundations of the model—namely, the Einstein field equations and the CP.

In this thesis, I focus on the possibility that the CP may be an inadequate approximation, at least for describing the local universe. So inadequate that even linear cosmological pertubation theory cannot account for it failures. I thus explore what the data reveal about the scale at which the CP holds by developing an analysis framework that does not impose any assumptions of symmetry on the cosmic metric at any stage. By allowing the data to speak for themselves, the aim is to minimize the risk of propagating theoretical biases in the cosmological conclusions and to contribute to pave the way for a better interpretation of their physical content.

Chapter 2

The expansion rate fluctuation field η

It has long been known that in the local outskirts of the Milky Way, at scales $r < 150$ h^{-1}Mpc, the CP does not apply (e.g. [104, 105]). This region represents about half of the volume used to determine the Hubble parameter H_0, a fundamental constant of the standard model and a consequence of the cosmological principle hypothesis. Traditionally, deviations from CP predictions are treated perturbatively by expanding the cosmological quantities into a smooth background component and a fluctuating part. Among the latter, a central role is occupied by peculiar velocities. These super-Hubble motions contain a lot of interesting cosmological information (e.g. [106]) and indeed their amplitude confirms that the deviations from the CP are in general agreement with the limits imposed by the perturbation theory of the standard cosmological model. However, it was soon realised that many subtle systematic errors, if not properly subtracted, can compromise their use as efficient cosmological probes; non-Gaussian issues, homogeneous and in-homogeneous Malmquist biases, incompleteness of mass catalogs used to predict the amplitude of peculiar velocities are among the pitfalls that most hamper the analysis [107].

In order to avoid the statistical and observational complications typically associated with investigating local inhomogeneities within the standard model, I have pursued an alternative approach that directly examines fluctuations in the expansion rate of the Universe. This method, referred to as the *expansion rate fluctuation field* η, shifts focus away from traditional perturbation theory. Notably, in standard cosmological perturbation theory, the expansion rate H is treated as an invariant background parameter, providing the reference frame against which perturbed quantities like overdensity contrasts and peculiar velocities are defined and measured.

The key advantage of this observable (η) lies in its scalar nature, allowing it to be easily Fourier transformed on the sphere. The resulting multipoles can then be used to explore and classify the nature of inhomogeneities in the expansion rate. A spherical harmonics analysis of the η signal provides an orthogonal perspective on the local redshift-distance relation, extending beyond the traditional dipole model typically used to describe anisotropies in the nearby Universe.

Furthermore, this method deepens and expands on previous studies—such as those by [108, 109, 110, 104, 111]—which attempt to constrain the tidal field component by analyzing the shear of the velocity field induced by local gravitational fluctuations. I will demonstrate that it is possible to robustly extract up to the octupole (and potentially even the hexadecapole) of the expansion rate field in Chapters 3 and 4.

In addition to offering insights into fluctuations in the local expansion rate, the η field is also easily comparable to theoretical predictions. I will demonstrate that it provides a model-independent framework for analyzing inhomogeneities, without requiring the cosmological principle as a foundational assumption. This flexibility allows the results to be directly interpreted within alternative spacetimes, potentially guiding the search for unconventional line elements that better capture the key characteristics of local inhomogeneities.

In the following, I introduce the expansion rate fluctuation field η, and discuss its physical and statistical properties. I will then describe how to estimate η from discrete galaxy distributions and the techniques used to decompose it into spherical harmonic components. Finally, I will establish a framework for understanding how η and its power spectrum relate to more familiar perturbative quantities within the specific context of the standard model of cosmology. The connection to a more elegant and general theoretical framework, the covariant cosmographic formalism, which allows for the interpretation of cosmic expansion without the restrictive assumptions of the standard model, will be fully detailed in Chapter 5 of this thesis.

2.1 Definition

The expansion rate fluctuation field [112] is constructed as the monopole-free decimal log of the ratio between the redshift z and the luminosity distance d_L

$$\eta(z,\boldsymbol{n}) \equiv \log\left(\frac{z}{d_L(z,\boldsymbol{n})}\right) - \mathcal{M}(z)$$

and

$$\mathcal{M}(z) \equiv \int_S \frac{\mathrm{d}\Omega}{4\pi} \log\left(\frac{z}{d_L(z,\boldsymbol{n})}\right), \tag{2.1}$$

where S is a 2D spherical surface of radius z centered on the observer and $\boldsymbol{n}$ is a unit vector specifying the observer's line of sight. Redshifts and distances (measured without redshift information) of objects on S are the only data needed to construct the η indicator.

In practice, however, due to the discrete and sparse nature of the data, η at redshift z is more conveniently estimated using a spherical shell of relatively small width δz. Note that I fix the radius of S using redshift and not distances. There are several reasons for this choice. Firstly, the distance depends on a dimensional normalization that varies from sample to sample and hampers direct comparisons between different data sets. Secondly, from an observational point of view, distances are affected by greater uncertainties (statistical and systematic) than redshifts (which, for the purposes of our analysis, are effectively treated as error-free).

By construction, the fluctuating field $\eta(z,\boldsymbol{n})$ averages to zero on S. Consequently, it is only sensitive to the angular structure of the fluctuating component and its possible evolution with redshift. It is only in the presence of angular anisotropies of the luminosity distance, at a given redshift, that η deviates from zero. For example, in an idealised FLRW cosmological model, $\eta = 0$ at every epoch.

An observable without a monopole ($\mathcal{M}$) has several advantages. First, η is completely independent of the normalization of the redshift-distance relationship, a fact that allows comparison of the signal extracted from different distance datasets, regardless of their

zero-point calibration. This does not mean that the η observable is blind to the Hubble constant. Information about H_0 is locked in the normalization term $\mathcal{M}$ appearing in 2.1. The additional advantage is that any potential systematic errors in measurements of the luminosity distances as a function of redshift do not affect the signal of η. The expansion rate fluctuation field is also independent of the chosen measuring units. Their only effect is to rescale the value of the monopole term $\mathcal{M}$. I fix this freedom by choosing to express d_L in Mpc units and the redshift in velocity units (km/s).

I express the observable as a ratio between the redshift and luminosity distance, in order to ensure that the function is well-behaved in the surroundings of the observer. If the standard model is assumed, in the limit $z \to 0$ the ratio converges to the Hubble constant. Furthermore, when exploring beyond the standard metric, the ratio converges to the so-called covariant Hubble function, which generalizes the Hubble constant (as will be discussed in Chapter 5) in the redshift-distance relation [50, 59, 113, 114, 115, 116, 117]. The logarithmic mapping was chosen for statistical reasons. The errors are Gaussian only in the distance modulus and not in the luminosity distance d_L. In this way, the estimator of η,

$$\hat{\eta} = \log(z) + 5 - \frac{\mu}{5} - \mathcal{M}\,, \tag{2.2}$$

is unbiased, and its uncertainty is $\sigma_\mu/5$, where σ_μ is the uncertainty of the distance modulus.

However, in order to interpret the η signal, I need to specify in which reference frame it is measured. At a given arbitrary point in spacetime, there is, among others, a characteristic observer of the large-scale structure of the Universe: the *matter-comoving* observer, who shares the motion of the surrounding dust flow. In the following, adopting the notation of [50], I use a tilde (i.e. $\tilde{d}(\tilde{z}), \tilde{z}....$) to explicitly emphasize when relevant quantities are measured in an arbitrary frame boosted with respect to the 'natural' frame defined by matter. Without loss of generality for our conclusions, I assume that the boosted frame represents an observer at rest in a reference frame in which the CMB dipole – whatever its nature (local or cosmological) – disappears. I will refer to this boosted frame as the CMB frame. Note that the CMB and the matter frames are indistinguishable in a uniform Universe described by the standard cosmological metric. On the other hand, these observers provide different estimates of the redshift and distance of the same source in a spacetime with arbitrary geometry. Therefore, although in the following chapters, I will show that η provides insight into the fluctuations of the space metric in a completely nonperturbative way, thus allowing investigation beyond the standard cosmological scenario in a model-independent way, the amplitude of these fluctuations is, fundamentally, observer-dependent. A full theoretical investigation of this crucial point will be provided in Chapter 5 of this thesis.

2.2 Spherical harmonic decomposition of $\boldsymbol{\eta}$

The finer structure of the expansion rate fluctuation field is best appreciated by expressing it by means of its spherical harmonic components.

On the practical side, by decomposing the signal into an orthonormal basis, I ensure that the contributions from different angular scales are statistically independent and that statistical likelihood analyses are minimally affected by correlations between different modes.

There is also a key theoretical motivation for decomposing the expansion rate fluctua-

tion field η into spherical harmonics. This decomposition provides a systematic approach to analyzing and classifying anisotropies in the distance-redshift relation, making it easier to identify underlying symmetries. Each multipole contains independent information about the cosmic metric, offering valuable insights into the structure of the spacetime line element in our local universe.

This argument will become clearer in Chapter 5, where I introduce the covariant cosmographic formalism—a fully model-independent framework that allows us to interpret the physical meaning of the η signal without relying on standard model perturbative quantities or assumptions. The formalism has a finite number of degrees of freedom, which are encoded in the multipoles of its fundamental functions. Therefore, the multipoles of η provide a straightforward and direct estimation of the multipoles within the covariant cosmographic framework.

On the technical side, any function $f(\theta, \phi)$ can be decomposed into the Spherical Harmonic (SH) components as follows

$$f(\theta,\phi) = \sum_{\ell=0}^{\infty} \sum_{m=-\ell}^{\ell} a_{\ell m} Y_{\ell m}(\theta,\phi) \tag{2.3}$$

where $Y_{\ell m}(\theta, \phi)$ is the real spherical harmonic function [118],

$$Y_{\ell m}(\theta,\phi) = \sqrt{\frac{(2\ell+1)(\ell-|m|)!}{4\pi(\ell+|m|)!}} P_\ell^{|m|}(\cos\theta) S_m(\phi), \tag{2.4}$$

and

$$S_m(\phi) = \begin{cases} 1 & m = 0 \\ \sqrt{2}\cos(m\phi) & m > 0 \\ \sqrt{2}\sin(m\phi) & m < 0 \end{cases} \tag{2.5}$$

These spherical harmonics are orthonormal, meaning

$$\int Y_{\ell m}(\theta,\phi) Y_{\ell' m'}(\theta,\phi) \sin\theta \, \mathrm{d}\theta \, \mathrm{d}\phi = \delta^K_{\ell\ell'} \delta^K_{mm'} \tag{2.6}$$

where $\delta^K_{ll'}$ is Kronecker delta (1 if $\ell = \ell'$, and 0 otherwise). So, the spherical harmonic coefficients $a_{\ell m}$ can be expressed as

$$a_{\ell m} \equiv \int_0^{2\pi} \int_0^{\pi} f(\theta,\phi)\, Y_{\ell m}(\theta,\phi) \sin\theta \, \mathrm{d}\theta \, \mathrm{d}\phi. \tag{2.7}$$

Moreover, in order to quatify the amplitude of each multipole, I use the estimator

$$\hat{C}_\ell = \frac{1}{2\ell+1} \sum_{m=-\ell}^{\ell} a_{\ell m}^2, \tag{2.8}$$

If there are no error in the SH coeffiecents, $\hat{C}_\ell$ is an unbiased estimation for the angular power spectrum

$$C_\ell = \langle a_{\ell m}^2 \rangle, \tag{2.9}$$

which, in the standard model of cosmology, actually depends on the multipole order ℓ

only, as will be shown in section 2.3.

Two important points should be noted. First, the expansion rate fluctuation field η is defined as a monopole-free field (see Eq. (2.1)). The monopole subtraction is performed as follows: I first define an intermediate quantity that includes the monopole,

$$\nu \equiv \log \frac{z}{d_L} = \log z + 5 - \frac{\mu}{5} \tag{2.10}$$

and then compute its multipoles. The multipoles for $\ell \geq 1$ coincide with those of η, while the monopole ($\ell = 0$) corresponds to $\mathcal{M}$. Therefore, the expansion rate fluctuations can be estimated as $\eta = \nu - \mathcal{M}$.

Second, when dealing with discrete measurements of an observable f, and thus not a sample continuous field on a 2-sphere, which moreover has associated uncertainties—as in our case with the η observable—estimating the multipoles becomes more involved.

In the following, I describe two methods I employed to estimate the expansion rate fluctuation field and its multipoles as well as the associated reconstruction errors.

2.2.1 Estimation of η and its multipoles using pixelization

The first method I employed to estimate the multipoles involves pixelization. For a given shell in redshift with thickness δz, I construct a 2D field out of a discrete point ν_i. I start first by partitioning the sky in $N_{\rm pix}$ identical pixels using HEALPix (Hierarchical Equal Area isoLatitude Pixelisation of a 2-sphere)[119]. I then define an average $\nu(p)$ for each pixel as

$$\nu(p) = \frac{\sum_i^N \sum_j^N \nu_i \Psi_{ij} \mathcal{W}(p, \delta z)}{\sum_i^N \sum_j^N \Psi_{ij} \mathcal{W}(p, \delta z)}, \tag{2.11}$$

where N is the total number of objects in the catalog, $\mathcal{W}(p, \delta z)$ is a window function which evaluates to unity if the object is inside the pixel p and the shell δz, and is null otherwise, and Ψ_{ij} is the precision matrix (the inverse of the covariance matrix) of the measurements inside the pixel. The presence of $\boldsymbol{\Psi}$ reduces the variance of the estimated mean. In the case of no correlation ($\boldsymbol{\Psi}$ is diagonal), only a single sum is needed in eq. (2.11), and the precision matrix can be replaced by the inverse of the variance of each measurement ($1/\sigma_i^2$).

It is clear that smoothing has the advantage of reducing noise at the cost of a lower angular resolution. The latter is essentially controlled by the aperture of the solid angle Ω (the size of the pixels). The choice of the size of the pixels depends, in principle, on the thickness of the shell δz on which the averaging is performed.

HEALPix is an algorithm which tessellates a spherical surface into curvilinear quadrilaterals, although these pixels are characterized by different shapes, each covering the same area as every other. Moreover, the resulting pixels are located on lines of constant latitude. This property is essential for speeding up computation but is less than optimal for pixelating the discrete field. In fact, the counts of objects can show large variations from pixel to pixel. In addition, some of the pixels may end up containing no data at all. To tackle this issue, I first rigidly rotate the galaxy field randomly, by looking for configurations in which all the HEALPix pixels are filled with objects *and* the least populated cell contains a maximum number of objects. If, as a result of different rotations, the maximum number of galaxies in the least populated cells stays the same, I pick up

the configuration for which the distribution of the number of the galaxies in the pixels has the minimum variance. This allows to minimize pixel-to-pixel fluctuations in the reconstructed field and increase the signal-to-noise ratio in the determination of the SH coefficients. Once the latter have been estimated, I apply an inverse rotation to the pixels and $\eta(p) = \nu(p) - \mathcal{M}$ maps, so that, for the sake of clarity, the results are presented in standard galactic (l, b) coordinates. The whole strategy is graphically illustrated in Figure 2.1. The resolution of the HEALPix grid is calculated as $N_{\rm pix} = 12N_{\rm side}^2$ where $N_{\rm side} = 2^t$, and $t \in \mathbb{N}$. The baseline grid, corresponding to $t = 0$, has 12 pixels.

Estimation of the SH coefficients

I estimate the Fourier coefficients of the spherical harmonic decomposition by slightly modifying the reconstruction scheme provided by the HEALPix algorithm [120]. HEALPix accomplishes that by means of an iteration scheme, the so-called *Jacobi iteration*. The zeroth order estimator of the coefficients of the expansion field is,

$$\hat{a}_{\ell m}^{(0)} = \frac{4\pi}{N_{pix}} \sum_{p=1}^{N_{pix}} \nu(p) Y_{\ell m}(\theta_p, \phi_p), \tag{2.12}$$

where (θ_p,ϕ_p) are the angular coordinates of the center of each pixel p and $\nu(p)$ is calculated by eq. (2.11). The Fourier coefficients $a_{\ell m}$ are then calculated up to the order $\ell_{\rm max}$. The maximum multipole can be estimated by a HEALPix tessellation is $3N_{\rm side} - 1$. The higher order estimators are

$$\hat{a}_{\ell m}^{(k+1)} = \hat{a}_{\ell m}^{(k)} + \frac{4\pi}{N_{pix}} \sum_{p=1}^{N_{pix}} \Big(\nu(p) - \nu^{(k)}(\theta_p, \phi_p) \Big) Y_{\ell m}(\theta_p, \phi_p), \tag{2.13}$$

where

$$\nu^{(k)}(\theta_p, \phi_p) = \sum_{\ell=0}^{\ell_{\rm max}} \sum_{m=-\ell}^{\ell} \hat{a}_{\ell m}^{(k)} Y_{\ell m}(\theta_p, \phi_p). \tag{2.14}$$

In matrix notation,

$$\boldsymbol{a}^{(0)} = \boldsymbol{A}\boldsymbol{\nu} \tag{2.15}$$

$$\boldsymbol{a}^{(k+1)} = \boldsymbol{a}^{(k)} + \boldsymbol{A}(\boldsymbol{\nu} - \boldsymbol{\nu}^{(k)}) \tag{2.16}$$

$$\boldsymbol{\nu}^{(k)} = \boldsymbol{S}\boldsymbol{a}^{(k)}, \tag{2.17}$$

where $\boldsymbol{a}$ is the vector of the spherical harmonic coefficients (containing $(\ell_{\rm max} + 1)^2$ elements), using a simple indexing scheme introduced by [118] (see also [121]) with one index $j(\ell, m)$, such that $j(\ell, m) = \ell^2 + \ell + m + 1$, and the inverse relations are $\ell = \text{integer}\left(\sqrt{j-1}\right)$ and $m = j - \ell^2 - \ell - 1$. $\boldsymbol{\nu}$ and $\boldsymbol{\nu}^{(k)}$ are vectors representing the measured and estimated values of $\nu(p)$ in each pixel (and thus contain $N_{\rm pix}$ elements) respectively. Moreover, the elements of $\boldsymbol{A}$ are $A_{jp} = \frac{4\pi}{N_{\rm pix}} Y_{\ell(j)m(j)}(\theta_p, \phi_p)$ and $\boldsymbol{S} = \frac{N_{\rm pix}}{4\pi}\boldsymbol{A}^T$. The calculation of $\boldsymbol{a}^{(k)}$ is repeated until convergence i.e. until the residual has zero SH coefficients up to $\ell_{\rm max}$.

Instead of going through the iteration scheme, I proceed in a different way. I estimate analytically the asymptotic limit $\boldsymbol{a}^{(\infty)}$ that should be ideally obtained in the limit of an infinite number of iterations. I first write equation (2.16) as

$$\boldsymbol{a}^{(k+1)} = \boldsymbol{a}^{(k)} + \boldsymbol{A}\boldsymbol{\eta} - \boldsymbol{A}\boldsymbol{S}\boldsymbol{a}^{(k)}, \tag{2.18}$$

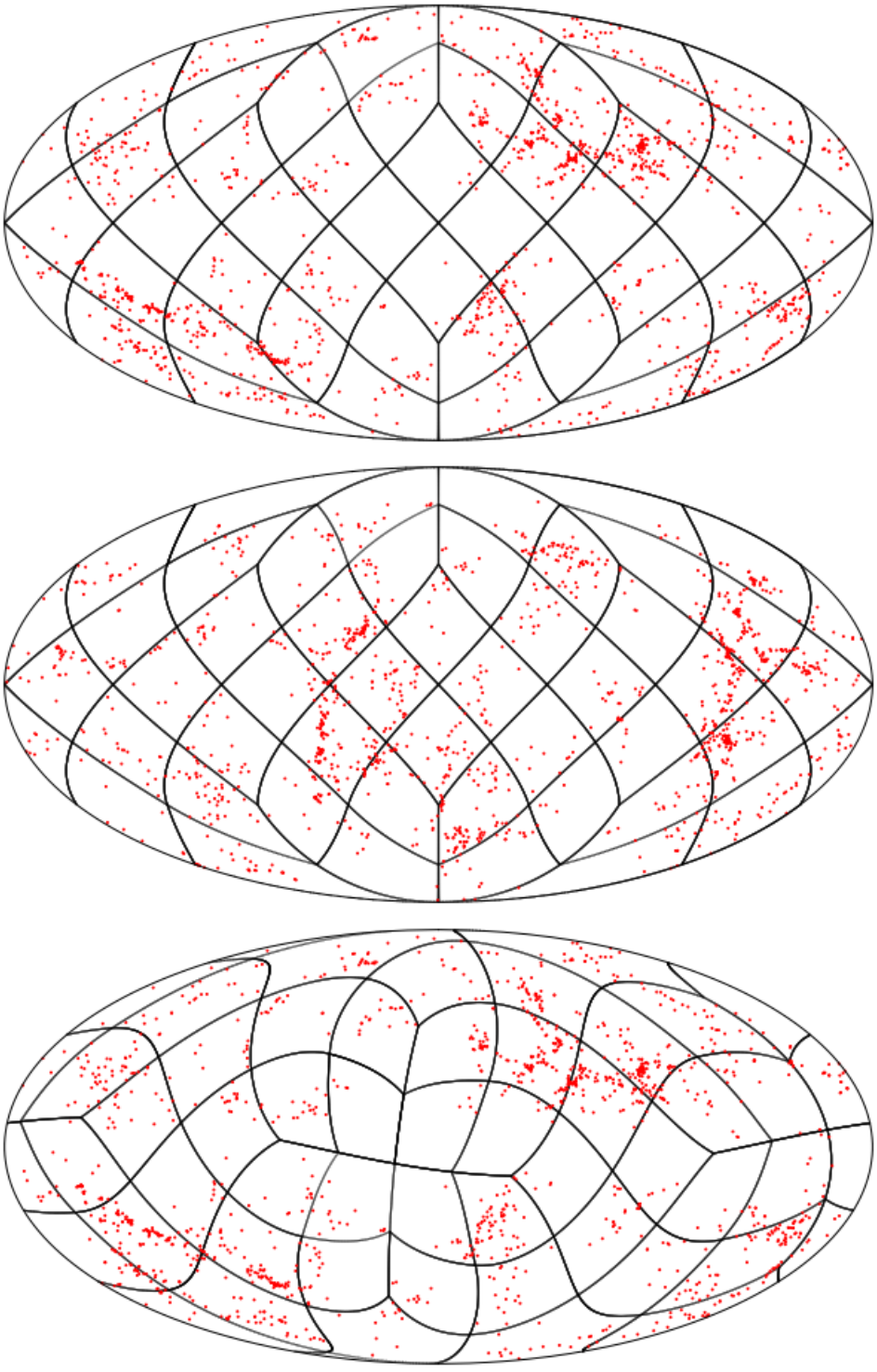


Figure 2.1: Illustration of the rotation strategy to improve the estimation of SH coefficients. *Left:* the standard HEALPix pixels ($N_{\rm side} = 2$ and $N_{\rm pix} = 48$) tessellating the distribution of galaxies in the galactic coordinates. Note the presence of an empty pixel. *Center :* rigid rotation applied to the sample so that in each pixel falls at least one galaxy (the minimum number is 5 in this example). *Right :* the inverse rotation is applied to both galaxies and pixels.

so

$$\boldsymbol{a}^{(k+1)} = \boldsymbol{A\eta} + (\boldsymbol{I} - \boldsymbol{AS})\boldsymbol{a}^{(k)}, \tag{2.19}$$

where $\boldsymbol{I}$ is the identity matrix with size $(\ell_{\max}+1)^2 \times (\ell_{\max}+1)^2$. By using $\boldsymbol{a}^{(0)} = \boldsymbol{A\eta}$ I obtain

$$\boldsymbol{a}^{(k+1)} = \boldsymbol{a}^{(0)} + (\boldsymbol{I} - \boldsymbol{AS})\boldsymbol{a}^{(k)}. \tag{2.20}$$

Under the assumption that this is convergent, for $k \to \infty$, $\boldsymbol{a}^{(k+1)} \to \boldsymbol{a}^{(k)}$ I get

$$\boldsymbol{a}^{(\infty)} = \boldsymbol{a}^{(0)} + (\boldsymbol{I} - \boldsymbol{AS})\boldsymbol{a}^{(\infty)}, \tag{2.21}$$

which results in

$$\boldsymbol{a}^{(\infty)} = \boldsymbol{M}\boldsymbol{a}^{(0)}, \tag{2.22}$$

where $\boldsymbol{M} = (\boldsymbol{AS})^{-1}$. Note that I cannot take the inverse of $\boldsymbol{A}$ or $\boldsymbol{S}$ individually because they are not square matrices. The elements of the vector $\boldsymbol{a}^{(\infty)}$ represents our best estimate $(\hat{a}_{\ell m})$ of the coefficients of the spherical harmonic decomposition $a_{\ell m}$. The first element in $\boldsymbol{a}^{(\infty)}$ which is $\hat{a}_{00}$ is related $\mathcal{M}$ by $\mathcal{M} = \hat{a}_{00}/2\sqrt{\pi}$, and for for $\ell > 0$, $\hat{a}_{\ell m} = \eta_{\ell m}$, where $\eta_{\ell m}$ are the SH coefficients of η.

This estimation for the spherical harmonic (SH) coefficients is more intuitive when understood as equivalent to minimizing $\mathcal{S}^2$,

$$\mathcal{S}^2(\boldsymbol{a}) = \boldsymbol{\Delta\nu}^T\, \boldsymbol{I}\, \boldsymbol{\Delta\nu} \tag{2.23}$$

where $\boldsymbol{\Delta\nu} = \boldsymbol{\nu} - \boldsymbol{\nu}^{(\mathrm{model})}$, and

$$\nu^{(\mathrm{model})}(\boldsymbol{a}) = \sum_{\ell=0}^{\ell_{\max}} \sum_{m=-\ell}^{\ell} a_{\ell m} Y_{\ell m}(\theta_p, \phi_p) \tag{2.24}$$

As shown in eq. (2.23), all the pixels have the same weight in the sum because they have the same area, and so this estimator is unbiased. The only possible source of bias is in $\nu(p)$ if the objects are not uniformly distributed inside each pixel.

Random and systematic errors

Here, I explain in detail the random and systematic errors affecting the power spectrum, their sources, and the methods I use to estimate them.
In the following, I consider the SH coefficients $a_{\ell m}$ as a deterministic variable whose estimate

$$\hat{a}_{\ell m} = a_{\ell m} + \epsilon_{\ell m}, \tag{2.25}$$

fluctuates due to measurement errors $\epsilon_{\ell m}$ induced by uncertainties in the distance modulus. The expectation over different observational measurements made on the same sample is thus $E[\hat{a}_{\ell m}] = a_{\ell m}$. i.e. I assume that the estimator provides an unbiased estimate of the coefficients of the spherical harmonic expansion.

The variance of the estimator is defined as

$$V[\hat{a}_{\ell m}] = V[\epsilon_{\ell m}] \equiv \sigma^2_{\ell m}, \tag{2.26}$$

and, in general, depends on both modes ℓ and m, and they can be estimated by Monte Carlo simulations as will be discussed at the end of this section. The estimation of the

angular power spectrum in (2.8), can be defined as

$$\hat{\hat{C}}_\ell^{(1)} = \frac{1}{2\ell+1}\sum_{m=-\ell}^{\ell}\hat{a}_{\ell m}^2. \tag{2.27}$$

This estimator is an biased estimation. If I assume that the correlation between the SH coefficients is zero, then the average of the estimator is

$$E\left[\hat{\hat{C}}_\ell^{(1)}\right] = \hat{C}_\ell + \frac{1}{2\ell+1}\sum_{m=-\ell}^{\ell}\sigma_{\ell m}^2\,. \tag{2.28}$$

Measurements errors on the distance modulus lead to a systematic overestimation of the angular power spectrum. Therefore, I define the unbiased estimator

$$\hat{\hat{C}}_\ell = \frac{1}{2\ell+1}\sum_{m=-\ell}^{\ell}\hat{a}_{\ell m}^2 - \frac{1}{2\ell+1}\sum_{m=-\ell}^{\ell}\sigma_{\ell m}^2, \tag{2.29}$$

The variance of this estimator is

$$V\left[\hat{\hat{C}}_\ell\right] = \left(\frac{1}{2\ell+1}\right)^2\sum_{m=-\ell}^{\ell}\left(4a_{\ell m}^2\sigma_{\ell m}^2 + 2\sigma_{\ell m}^4\right), \tag{2.30}$$

Expression (2.30) can be further simplified if I make assumptions about the nature of the errors. If the distribution of the galaxies is isotropic and all of them have the same error in η, then, the uncertainty of the SH coefficients will not depend on the considered harmonics ($\sigma_{\ell m}^2 = \sigma^2$), so,

$$V\left[\hat{\hat{C}}_\ell\right] = \frac{2}{2\ell+1}\left[(\sigma^2+\hat{C}_\ell)^2 - \hat{C}_\ell^2\right]. \tag{2.31}$$

The above formula neatly isolates the two quantities contributing to the observed variance: the error in the estimation of the distance modulus and the measured amplitude of the angular power spectrum $\hat{C}_\ell$.

Note, incidentally, that eq. (2.31) differs from the expression that would be obtained by averaging over a statistical ensemble. Indeed, in this latter case $\langle\hat{a}_{\ell m}\rangle_e = 0$ (so $\hat{C}_\ell$ will be replaced by zero) and also $V_e[\hat{a}_{\ell m}] = C_\ell+\sigma^2$. It thus follows that the theoretical expression factoring in the contributions of cosmic variance is $V_e[\hat{\hat{C}}_\ell] = 2/(2\ell+1)(\sigma^2+C_\ell)^2$, if, again, it is assumed that $\sigma_{\ell m}$ is isotropically distributed. The statistical bias term calculated in eq. (2.29) might not fully remove the systematic shift.

Indeed, expression (2.29) is strictly unbiased if the estimator $\hat{a}_{\ell m}$ (cf. eq. (2.25)) is, as I assumed, affected only by statistical errors. It is true, however, that incompleteness and anisotropies in the sky distribution with pixelization and resolution strategy adopted to transform the discrete η observable into a field, could bias the $\hat{a}_{\ell m}$ estimator. Although any constant systematic term added in (2.25) does not affect the variance of the coefficients $\hat{a}_{\ell m}$, it will result in an additional (and analytically nontrivial) term in eq. (2.29). The total systematic bias ΔC_ℓ affecting the estimator $\hat{\hat{C}}_\ell$ is thus more conveniently quantified using Monte Carlo simulations.

Monte Carlo simulations

I determine the errors, both random and systematic, that plague the SH reconstruction by means of Monte Carlo simulations. I consider as input model the Fourier coefficients (up to $\ell_{\max}$) measured from the data, and I use them to simulate a fiducial η field. I then randomly perturb the expansion rate fluctuation field, at the angular position of the objects, by means of a Gaussian noise with mean value η and with standard deviation $\delta = \sigma_\mu/5$. I construct in this way a suite of 1000 mock catalogs which are tessellated with HEALPix and Fourier transformed in exactly the same way as the data. This means I apply the same rotation scheme to fill all the pixels with objects, and the same numerical scheme to calculate the power spectrum up to $\ell_{\max}$. The difference between the average of the output and the input is the bias, which I use to correct the first measured values, and the variance of the distribution is the variance of the estimator.

2.2.2 Maximum Likelihood method for estimating η and its multipoles

For discrete points on a sphere, the η field and its spherical harmonic coefficients can be estimated by fitting all measurements up to a maximum multipole $\ell_{\max}$, without applying any smoothing. I will show that this estimation remains unbiased only if the higher multipoles $\ell > \ell_{\max}$ are either zero or negligible compared to the associated uncertainties.

For each spherical shell S at redshift z, with thickness δz and containing $N_{\rm g}$ objects, I first estimate ν for each galaxy in that shell using eq. (2.10). I then assume that this estimate is subject to Gaussian error, which is valid due to the definition of η, provided that the distance modulus μ is also Gaussian distributed. Finally I find the best fitting multipolar model by minimizing the χ^2 statistics

$$\chi^2 = \boldsymbol{\Delta\nu}^T \, \boldsymbol{\Psi} \, \boldsymbol{\Delta\nu} \tag{2.32}$$

where $\boldsymbol{\Psi}$ is the precision matrix (the inverse of the covariance matrix, which is the covariance matrix of the distance modulus μ multiplied by $1/25$ because of the relation between ν and μ), and $\boldsymbol{\Delta\nu} = \boldsymbol{\nu}^{(\rm obs)} - \boldsymbol{\nu}^{(\rm model)}$, where

$$\boldsymbol{\nu}^{(\rm model)} = \boldsymbol{Y}\boldsymbol{a} \tag{2.33}$$

where $\boldsymbol{a}$ is a vector with size $(\ell_{\max}+1)^2$ contains the SH coefficients $\hat{a}_{\ell m}$ which I want to estimate, using a simple indexing scheme introduced in section 2.2.1. $\boldsymbol{Y}$ is a matrix of size $N_{\rm g} \times (\ell_{\max}+1)^2$, and its elements are $\mathcal{Y}_{ij} = Y_{\ell(j)m(j)}(\theta_i, \phi_i)$, where (θ_i, ϕ_i) are the angular coordinate of the i-th object in the shell.

I search for the minimum of the χ^2 statistics by looking for the point (in the space of $\hat{a}_{\ell m}$) where its first derivative is zero, and the result in the matrix form is

$$\boldsymbol{a} = \boldsymbol{\psi}^{-1}\boldsymbol{s} \tag{2.34}$$

where

$$\boldsymbol{\psi} = \boldsymbol{Y}^T \, \boldsymbol{\Psi} \, \boldsymbol{Y} \tag{2.35}$$

and

$$\boldsymbol{s} = \boldsymbol{\Psi} \, \boldsymbol{\nu}^{(\rm obs)} \, \boldsymbol{Y} \tag{2.36}$$

By taking the second derivative of χ^2, one finds that the covariance matrix of $\hat{\boldsymbol{a}}$ is simply

$\boldsymbol{C} = \boldsymbol{\psi}^{-1}$. As mentioned in section 2.2.1, the first element in $\boldsymbol{a}$ which is $\hat{a}_{00}$ is related $\mathcal{M}$ by $\mathcal{M} = \hat{a}_{00}/2\sqrt{\pi}$, and for for $\ell > 0$, $\hat{a}_{\ell m} = \eta_{\ell m}$.

This estimation of the spherical harmonics presents potential risks. If I limit the fitting to a specific multipole $\ell_{\rm max}$, the result may be biased if the η signal contains contributions from multipoles higher than $\ell_{\rm max}$. This bias can be demonstrated by examining the average of the estimator $\boldsymbol{a}$,

$$E\left[\hat{a}_j\right] = a_j + b_j \tag{2.37}$$

where

$$b_j = \sum_{k=L_{\rm max}+1}^{\infty} \sum_{q=0}^{L_{\rm max}} a_k C_{qj} \sum_{n=1}^{N_{\rm g}} \sum_{r=1}^{N_{\rm g}} \Psi_{nr} \mathcal{Y}_{nq} \mathcal{Y}_{rk} \tag{2.38}$$

and $L_{\rm max} = (\ell_{\rm max} + 1)^2$. The systematic effect is proportional to the true a_k for the multipoles higher than the maximum multipole included in the fit. However, it can also be inferred from eq. (2.38) that the bias decreases as the number of measurements increases and as the distribution of the measurements and their errors becomes more isotropic on the sky. In this case, the sum will closely approximate the integral of the orthonormal basis, which is zero. Furthermore, for the same case, by examining eq. 2.35, I find that the covariance matrix $\boldsymbol{C}$ will tend to be diagonal meaning that the correlation between the SH coefficients goes to zero.

2.3 Standard model predictions for η

The measurements of $\tilde{\eta}$ and its power spectrum, $C_\ell(r)$, are model-independent, making them powerful tools for testing—and potentially falsifying—predictions from specific cosmological models. Here, I demonstrate how to predict the amplitude of these observables in the context of the standard ΛCDM model.

In FLRW models, the expansion rate fluctuation field in the CMB frame is related to the radial component of the peculiar velocity of galaxies. Using eq. (1.51) at $\tilde{z} \ll 1$, with $\boldsymbol{v}_0 = 0$ for the CMB comoving observer, on can find:

$$\tilde{\eta} = \log\left(\frac{\tilde{z}}{\tilde{d}_L}\right) - \tilde{\mathcal{M}} \approx \log H_0 - \tilde{\mathcal{M}} + \frac{\boldsymbol{v}\cdot\boldsymbol{n}}{\tilde{z}} \tag{2.39}$$

This relationship can also be used in reverse: once η is reconstructed using some tracers, it can be employed to predict the radial component of the peculiar velocity field expected in the standard model. Later in this work (see section 3.2.5), I will demonstrate how this approach enables the subtraction of peculiar velocity distortions from the Hubble diagram of SNIa. Interestingly, this method allows for the removal of these distortions without requiring the linear theory gravitational reconstruction of the peculiar velocity field using complete, all-sky catalogs of galaxy redshifts.

In eq.(2.39), the first term has only a monopole component. Therefore, the monopole of the radial component of the peculiar velocity $(\boldsymbol{v}\cdot\boldsymbol{n})$ is indistinguishable from H_0, but for $\ell > 0$,

$$\tilde{\eta}_{\ell m} = \frac{(\boldsymbol{v}\cdot\boldsymbol{n})_{\ell m}}{\tilde{z}\ln 10} \tag{2.40}$$

Calculating the amplitude of the power spectrum of the expansion rate fluctuation field is somewhat more laborious. First, the relation in Fourier space given by equation

(1.50) is expressed as

$$\boldsymbol{v_k} = -\frac{2i\boldsymbol{k}f}{3aH\Omega_{\rm m}}\Phi_{\boldsymbol{k}} \tag{2.41}$$

Next, using the Poisson equation (1.46) in Fourier space , which states $-k^2\Phi_{\boldsymbol{k}} = (3/2)\ a^2\ H^2\ \Omega_{\rm m}\delta_{\boldsymbol{k}}$, we can find the relation between the peculiar velocity and the density contrast in Fourier space:

$$\boldsymbol{v_k} = i\frac{\boldsymbol{k}}{k^2}afH\delta_{\boldsymbol{k}} \tag{2.42}$$

Therefore, the SH coefficients of the radial component of the velocity are given by:

$$(\boldsymbol{v}\cdot\boldsymbol{n})_{\ell m} = \frac{iaHf}{(2\pi)^3}\int \frac{\boldsymbol{k}\cdot\boldsymbol{n}}{k^2}\delta_{\boldsymbol{k}}e^{i\boldsymbol{r}\boldsymbol{k}\cdot\boldsymbol{n}}Y^*_{\ell m}(\theta,\phi)\,\mathrm{d}\Omega\,\mathrm{d}^3k \tag{2.43}$$

The expansion of the plane wave in spherical harmonics is

$$e^{i\boldsymbol{r}\boldsymbol{k}\cdot\boldsymbol{n}} = 4\pi\sum_{\ell=0}^{\infty}\sum_{m=-\ell}^{\ell} i^\ell j(kr)Y^*_{\ell m}(\theta_k,\phi_k)Y_{\ell m}(\theta,\phi), \tag{2.44}$$

and by taking the derivative with respect r, one obtains

$$\boldsymbol{k}\cdot\boldsymbol{n}\,e^{i\boldsymbol{r}\boldsymbol{k}\cdot\boldsymbol{n}} = 4\pi\sum_{\ell=0}^{\infty}\sum_{m=-\ell}^{\ell} i^{\ell-1}kj'(kr)Y^*_{\ell m}(\theta_k,\phi_k)Y_{\ell m}(\theta,\phi) \tag{2.45}$$

By substitute eq. (2.45) in eq. (2.43), and using the orthonormality of the spherical harmonics $Y_{\ell m}$, one finds

$$(\boldsymbol{v}\cdot\boldsymbol{n})_{\ell m} = \frac{i^\ell aHf}{2\pi^2}\int \frac{\delta_{\boldsymbol{k}}}{k}j'(kr)Y^*_{\ell m}(\theta_k,\phi_k)\,\mathrm{d}^3k \tag{2.46}$$

the unit vector $\boldsymbol{n}$ is in the direction of the line of sight ($\boldsymbol{r} = r\,\boldsymbol{n}$) in the direction (θ,ϕ), and (θ_k,ϕ_k) is the direction of the vector $\boldsymbol{k}$. Therefore, with using (1.55), the power spectrum of the multipoles of the radial component of the peculiar velocity is related with matter power spectrum by

$$\langle|(\boldsymbol{v}\cdot\boldsymbol{n})_{\ell m}|^2\rangle(r) = \frac{2a^2H^2f^2}{\pi}\int P(k)(j'_\ell(kr))^2\mathrm{d}k \tag{2.47}$$

and by (2.40), the power spectrum of $\tilde{\eta}$ in CMB frame is

$$C_\ell(r) \equiv \langle|\tilde{\eta}_{\ell m}|^2\rangle = \frac{\langle|(\boldsymbol{v}\cdot\boldsymbol{n})_{\ell m}|^2\rangle}{z^2(\ln 10)^2} = \frac{2a^2H^2f^2}{\pi H_0^2r^2(\ln 10)^2}\int P(k)(j'_\ell(kr))^2\mathrm{d}k \tag{2.48}$$

Figure 2.2 shows the power spectrum of each multipole of $\tilde{\eta}$ as a function of the distance from the observer up to $\ell = 5$. The matter power spectrum is generated by the CAMB code assuming the best-fitting Planck cosmological parameters [80]. This figure shows that at a given fixed distance the power in each multipole systematically decreases as ℓ increases. This is due to the fact that different multipoles probes matter fluctuations on different distance scales, with the higher ℓ being sensitive to smaller scale effects. We also see that for a fixed multipole order ℓ, the power decreases with increasing distance

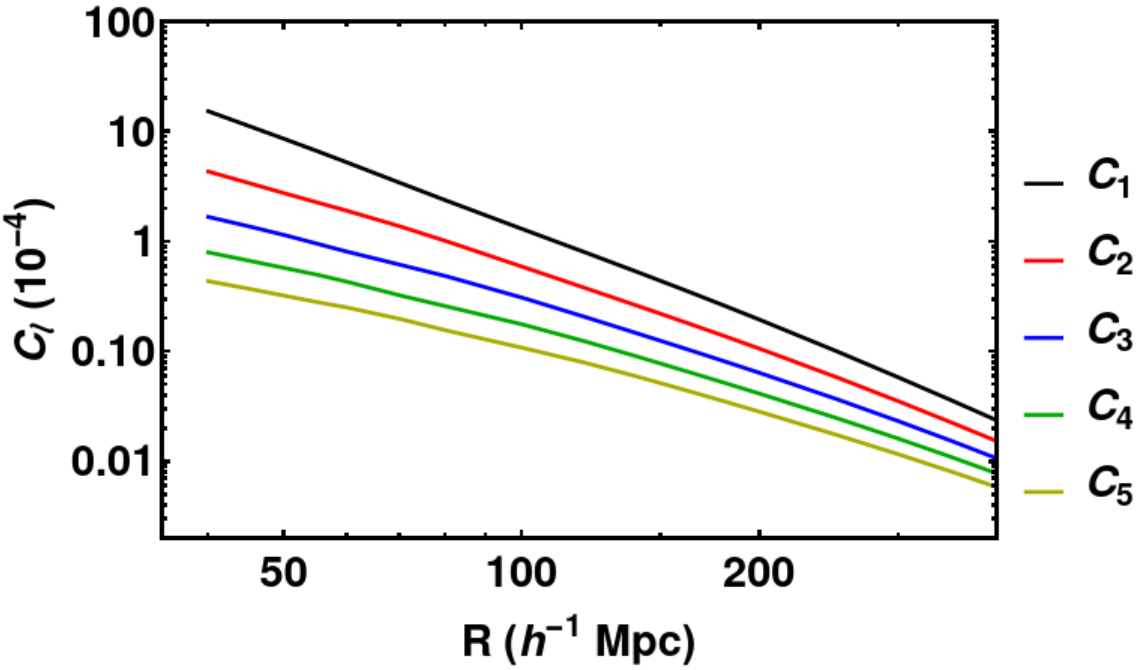


Figure 2.2: The power spectrum of each multipole of η as a function of the distance.

from the observer. It approaches zero at higher distances where the correlation between structures in different directions, according to the cosmological principle, is expected to vanish.

2.4 Conclusion

The failure to converge on a consensus value of the Hubble's constant triggered investigations into the reliability of geometric descriptions of the local spacetime that deviate from the standard cosmological metric. The question that arises is whether metrics with lower symmetries, while still simple, provide a reliable description of the data in the local patch of the universe where global uniformity is violated.

I've proposed to address this problem, from a new angle, trying to go beyond the standard perturbative approaches by which non-uniformities in the local expansion rate are accounted for in the standard model. To this end, I have designed an observable that captures, in a statistically unbiased way, the average angular fluctuations in the local expansion rate. The observable η is fully model independent not requiring any knowledge about the metric, the gravity model or the amount of matter in the Universe. It is thus instrumental to understand local violations of the cosmological principle, i.e. how far the spatial distribution of matter is from being homogeneous and how far the kinematics of the cosmic expansion is from being isotropic.

In this chapter, I have presented the η formalism and detailed several methods for estimating it from the data. I also discussed how its amplitude can be decomposed into spherical harmonic multipoles to facilitate signal interpretation.

In the first approach, outlined in the paper [112], I achieved this by smoothing the data using a HEALPix pixelization scheme. In subsequent analyses [122], I optimized a maximum likelihood statistical strategy that does not require data smoothing, allowing for improved resolution in extracting higher-order multipoles. Particular attention was paid to estimating both statistical and systematic uncertainties affecting the η reconstruction schemes, using both analytical methods and numerical simulations.

Finally, I conclude this section by demonstrating that, in the limit of small fluctuations, a perturbative expansion around the FLRW background allows to establish a "dictionary" between the amplitude of η and typical quantities from linear perturbation theory, such as density fluctuations relative to the cosmic mean and peculiar velocities. This formalism will ultimately serve as the basis for evaluating whether the expansion rate measurements presented in Chapters 3 and 4 of this manuscript are consistent with standard model predictions.

Chapter 3

The expansion rate fluctuation field in Cosmicflows-3 and Pantheon

The primary requirement for calculating the expansion rate fluctuation field is a galaxy sample that includes both redshift data and redshift-independent distance measurements.

From a conceptual standpoint measuring redshifts is relatively easier than estimating redshift-independent distances. Errors and especially systematics are largely subdominant so that I can overlook them (what I do for the purposes of this thesis). It is impressive how this measuring enterprise has fastly advanced in the last 30 years, from the Center for Astrophysics survey, with its 18,000 galaxies within a small specific sky volume [123], to the Sloan Digital Sky Survey (SDSS) which measured redshifts for over 3 million galaxies [124].

The compilation of galaxy distance catalogs has progressed more slowly than redshift measurements, achieving only an order of magnitude improvement over the same period. Extensive catalogs have been meticulously compiled over the years to map the sky, covering nearly the entire celestial sphere while excluding only regions obscured by the Milky Way (approximately 20% of the sky).

One of the earliest efforts to map galaxy distances was led by a team of seven astronomers known as the "Seven Samurai", headed by Sandy Faber. Their 1987 paper [125], *A Large-Scale Streaming Motion in the Local Universe* became highly influential in extragalactic astronomy and observational cosmology, particularly for studies of large-scale cosmic flows.

Another significant contribution was the *Nearby Galaxies Catalog*, published by Brent Tully in 1988 [126]. This catalog provided distances and other data for over 2,300 galaxies, serving as a foundational resource for studying the peculiar velocities of galaxies in the local universe and tracing the distribution of galaxies within approximately 40 Mpc. Notably, the entries in the catalog were reordered according to group assignments, which helped reduce noise in distance determinations and enhanced the resolution in the analysis of large-scale matter flows.

The *Mark III Catalog* of galaxy peculiar velocities, compiled by Willick and collaborators [127] marked another milestone in the field. This catalog contained distances for approximately 3,000 galaxies, achieved by improving the calibration of distance indicators—primarily Tully-Fisher and $D_n - \sigma$—and homogenizing various datasets to ensure compatible results when tracing the same large-scale structure using different distance indicators.

A significant increase in the number of estimated distances has come from the various

versions of the *Cosmicflows* catalog, starting with the first version in 2008 [128], which included around 2,000 distances, to the latest version (Cosmicflows-4) [72], which now maps distances for over 56,000 galaxies, making it the largest catalog of its kind.

Simultaneously, SNe Ia surveys like *Pantheon+* have provided direct, precise distance measurements for about 1,500 galaxies hosting these supernovae, spanning a wide redshift range and proving crucial for studying cosmological parameters such as dark energy.

In my thesis work, I initially reconstructed the expansion rate fluctuations field as traced by the Cosmicflows-3 [129] and Pantheon [130] samples. This analysis served as a proof of concept for the methodology while allowing me to draw initial conclusions about the structure of the expansion rate field in the local universe. I will present the results of this analysis in this chapter. The latest findings, based on the most up-to-date publicly available catalogs (Cosmicflows-4 and Pantheon+), will be presented in the next chapter.

The chapter is organized as follows: In section 3.1, I describe in some details the data analyzed. Results about the reconstruction of the expansion rate fluctuation field in the local universe are presented and interpreted in 3.2. I then demonstrate how these results can be applied within the framework of the standard cosmological model to correct the SN Ia Hubble diagram for the effects of peculiar motions, without relying on the dynamical reconstruction of velocities from gravitational theory or the need for all-sky catalogs of mass distribution. section 3.3 provides summary and conclusion.

3.1 Data

Here, I briefly describe the samples of redshift- independent distances used in this chapter.

3.1.1 The Pantheon sample

The Pantheon SN Ia compilation [130] is comprised of 1048 objects lying in the interval $0.01 < z < 2.26$. The catalog was assembled using data from the Supernova Legacy Survey (SNLS) [131], the Sloan Digital Sky Survey (SDSS) [132, 133], Pan-STARS1 (PS1) [130], [134, 135, 136, 137, 138] the Carnegie Supernova Project (CSP) [139] and various surveys made possible by the Hubble Space Telescope (HST), namely CANDLES/ CLASH [140, 141, 142], GOODS [143] and SCP [144].

Although many previous investigations of kinematical anisotropies rely on the analysis of the full Pantheon sample, in this study I follow a pretty conservative approach and consider only a SN Ia subsample with maximal spatial uniformity. To this end, I require the data to sample in a fairly isotropic manner the sky and also to display sufficient homogeneity in the radial coordinate. The goal is to minimize possible biases and systematic effects induced by incomplete spatial sampling without sensibly reducing the statistical constraining power of the data.

In Figure 3.1 (the first row) the angular distribution of the Pantheon data is shown together with the differential number counts profile $\mathrm{d}N(z)$ as a function of redshift. There are no objects in the very local patch of the universe, below $z = 0.01$, and the sample becomes quickly anisotropic as soon as the redshift is larger than $z = 0.05$. It also becomes in-homogeneous, i.e. the scaling of $\mathrm{d}N$ is not anymore proportional to z^2, for $z \gtrsim 0.04$. As a consequence, a trade-off threshold value $z = 0.05$ is chosen for selecting the SN Ia sample to be used in this study. This leaves us with a subsample containing 158 SNe Ia.

3.1.2 The Cosmicflows-3 data

For the purposes of our analysis, I complement the Pantheon supernovae sample with the Cosmicflows-3 catalog [129]. This is an all-sky galaxy catalog comprised of 17669 nearby galaxies $z \leq 0.116$ for which redshift-independent distances are inferred using mainly the Tully-Fisher relation or Fundamental Plane methods (see section 1.5.1).

This galaxy catalog offers two key advantages: a completely independent way of estimating galaxy distances and a richer collection of distance moduli μ (nearly a hundred times more than those contained in the supernovae catalog). It is this large statistical figure that helps beating down the large error with which the individual galaxy distances are estimated. These uncertainties are shown in Figure 3.2, where they are also compared to the typical inaccuracies that characterize the SNe Ia distances. The latter are at least a factor of 2 smaller than those based on the Tully-Fisher or the Fundamental Plane estimates (so each is four times or more valuable in a statistical weighting scheme).

The angular and radial distribution of the Cosmicflows-3 galaxies is shown in Figure 3.1 (the second and the third rows). They are fairly evenly distributed in both redshift and position in the sky except for redshifts greater than 0.05. So, I don't include the galaxies beyond this redshift since the sample becomes too sparse and covers the sky anisotropically. I also exclude from the sample, galaxies with redshift less than 0.01, in order to facilitate the comparison with the results obtained from the Pantheon data. We, therefore, focus our analysis on the Cosmicflows-3 subsample which is constrained in the range $0.01 < \tilde{z} < 0.05$ and includes 13661 galaxies. I add in this respect that the purpose of our analysis is to obtain a coarse-grained description of the expansion rate fluctuation. In the periphery of the Local Group, the geometry and dynamics of the metric are instead dominated by a few large nonlinear structures, and, as a consequence, the galaxies poorly track the large-scale gravitational field we are interested in.

Within this redshift range, the CF3 catalog contains 286 galaxies hosting a SN Ia (Figure 3.1 third row) for which the distance modulus is known using the standard candle method. Although systematically homogenized, this compilation of SN Ia-based distances remains fundamentally heterogeneous, with distance moduli derived from different light curve fitters. Although this dataset contains the Pantheon as a subsample, I use it as a control sample to check the robustness of the results I obtain using the Pantheon dataset alone. In what follows, I will refer to the CF3 subsample with SN Ia-based distances as CF3sn and indicate the complementary set with the acronym CF3g. Note that, in CF3sn, some measurements are done by using different methods in addition to SN Ia, in this case, I quote the average distance.

For both samples, Pantheon and CF3, I use the redshift in CMB frame, and as discussed in the previous chapter, over-tilde is used.

3.2 Results

In this section, I present and comment on the results obtained by applying the formalism (see section 2.2) to various datasets. The relevant parameters of the SH analysis of the expansion rate field are quoted in Table 3.1, using the pixelization method described in section 2.2.1. Note that for each entry in this table, I do not report the bare value returned by the spherical harmonic estimator, but that obtained after subtracting the systematic bias factors quoted in Table 3.2. The quoted biases and statistical uncertainties are those estimated numerically by means of 1000 Monte Carlo simulations, although, as I have

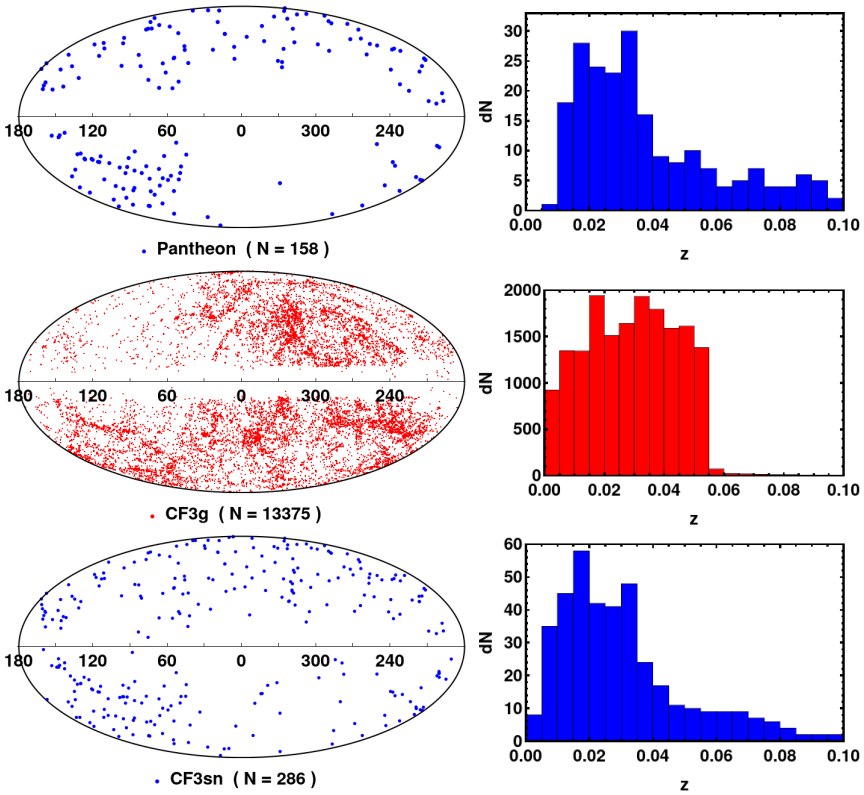


Figure 3.1: *Upper left :* Mollweide projection, in galactic coordinates, of the distribution of the Pantheon SNe Ia with redshift $0.01 < \tilde{z} < 0.05$. *Upper right :* histograms of the number of counts as a function of redshift. The second and the third rows are the same as the first, but for the CF3g and CF3sn samples respectively.

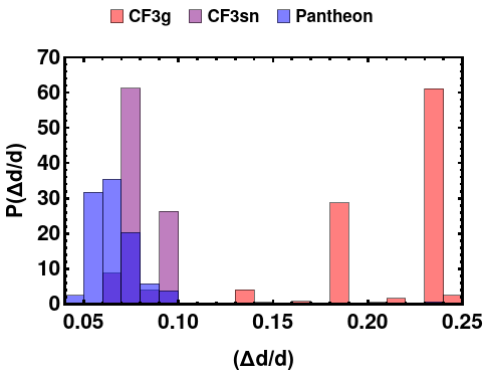


Figure 3.2: The probability distribution of the relative error in the distances ($\Delta d/d \approx \Delta\mu \ln 10/5$) measured in samples CF3g, CF3sn and Pantheon in the interval $0.01 < \tilde{z} < 0.05$.

Sample	N_{pix}	l_d	b_d	$\hat{C}_1$ (10^{-4})	$\frac{\tilde{\eta}_{\max}-\tilde{\eta}_{\min}}{2}$ (10^{-2})	p-value (%)	l_q	b_q	$\hat{C}_2$ (10^{-4})	$\frac{\tilde{\eta}_{\max}-\tilde{\eta}_{\min}}{2}$ (10^{-2})	p-value (%)	l_t	b_t	$\hat{C}_3$ (10^{-4})	$\frac{\tilde{\eta}_{\max}-\tilde{\eta}_{\min}}{2}$ (10^{-2})	p-value (%)
CF3 [0.01, 0.05]	192	291 ± 15	12 ± 7	3.0 ± 1.6	1.6	0.03	323 ± 16	9 ± 4	2.4 ± 0.9	1.9	0.12	289 ± 24	16 ± 15	0.1 ± 0.4	1.2	30.44
CF3 [0.01, 0.05]	48	283 ± 6	12 ± 5	5.3 ± 0.8	1.9	< 0.01	310 ± 11	4 ± 8	0.9 ± 0.3	1.1	< 0.01	284 ± 7	12 ± 5	0.5 ± 0.2	1.3	0.01
CF3g [0.01, 0.05]	48	286 ± 7	4 ± 6	7.0 ± 1.0	2.0	< 0.01	338 ± 8	22 ± 5	1.1 ± 0.4	1.3	< 0.01	255 ± 9	11 ± 5	0.7 ± 0.2	1.5	0.01
CF3 [0.01, 0.05]	12	285 ± 5	11 ± 4	5.1 ± 0.8	1.9	< 0.01	308 ± 7	1 ± 7	1 ± 0.3	1.1	< 0.01	-	-	-	-	-
CF3g [0.01, 0.05]	12	296 ± 6	18 ± 5	4.0 ± 0.6	1.7	< 0.01	323 ± 34	2 ± 17	1.3 ± 0.4	1.4	< 0.01	-	-	-	-	-
CF3sn [0.01, 0.05]	12	322 ± 23	-8 ± 18	3.7 ± 1.5	1.5	0.27	343 ± 15	-8 ± 10	1.7 ± 1.4	1.7	2.90	-	-	-	-	-
Pantheon [0.01, 0.05]	12	334 ± 42	6 ± 20	3.5 ± 2.7	1.6	4.37	337	-5	0.6 ± 1.9	1.6	33.33	-	-	-	-	-
CF3 [0.01, 0.03]	12	279 ± 5	12 ± 5	7.8 ± 1.0	2.3	< 0.01	310 ± 8	11 ± 6	2.9 ± 0.6	1.9	< 0.01	-	-	-	-	-
CF3 [0.03, 0.05]	12	301 ± 15	10 ± 14	1.1 ± 0.7	1.0	0.03	277 ± 28	-12 ± 11	0.9 ± 0.3	1.0	2.04	-	-	-	-	-

Table 3.1: Parameters of the spherical harmonic decomposition. Central values are not the bare value returned by the spherical harmonic estimator but are obtained after subtracting systematic effect determined by means of 1000 Monte Carlo simulations (the bias factors given in Table 3.2. Statistical errors are also determined using Monte Carlo simulations. I quote also the direction for the dipole, and direction of the peaks of the $\ell = 2$ and 3 multipoles which are close to the direction of the dipole. The p-value is computed by using 10000 Monte Carlo simulations. For Pantheon, the error in the direction of the quadrupole is not quoted because it is larger the 180 degrees.

highlighted in the previous chapter (see section 2.2.1).

Figure 3.3 shows the $\tilde{\eta}$ field for the CF3 sample tessellated according to different resolutions (192, 48 and 12 pixels). Smoothing mostly impact the errors with which the relevant SH parameters are estimated, with generally smaller error as the number of pixels decreases. The central values of the SH parameter, instead, are statistically stable: they fluctuate from one reconstruction to the next, but the discrepancies are within what is expected from a random sampling of a common underlying Gaussian distribution. The results are thus globally independent of the pixelization strategy adopted.

However, a valid pixelization scheme for one sample may not be suitable for reconstructing the signal in another catalog. A 48-pixel smoothing is for example less than optimal for sizing even the dipole of the sparse SNe Ia sample. Only when the analysis is thus performed by tessellating the sky at lower resolution (12 pixels), I can unpack the information contained in the lowest multipoles. The price to pay is that now the higher multipoles cannot be estimated.

The strongest contribution to the signal is provided by the dipole term, whose maximal intensity is about 1% of the signal locked in the normalizing term $\log H_0$, i.e. $\sim 4.5\%$ of H_0. The power locked in the dipole (as determined using the the CF3g sample) is $\hat{C}_1 = (4.0 \pm 0.6) \cdot 10^{-4}$, an estimation characterised by a high signal-to-noise ratio (SNR ~ 6.6). Consistently, this value is in excellent agreement (well within 1σ) with that estimated from both the CF3sn and the Pantheon sample ($(3.7 \pm 1.5) \cdot 10^{-4}$ and $(3.5 \pm 2.7) \cdot 10^{-4}$ respectively).

Due to the increased statistical power, the angular position of the dipolar anisotropy axis is better resolved when the whole CF3 sample is analyzed ($l_d = 285 \pm 5, b_d = 11 \pm 4$). The 95% C.L. uncertainty region falls within the 68% C.L. uncertainty region defined by any one of the SNe Ia samples. I remark that this direction is not far away from that of the Shapley Concentration [145]. I will further develop the physical implications of this preferential axis when I discuss bulk flows in section 3.2.2.

I then ask whether this long-range dipole correlation found in each data sample is

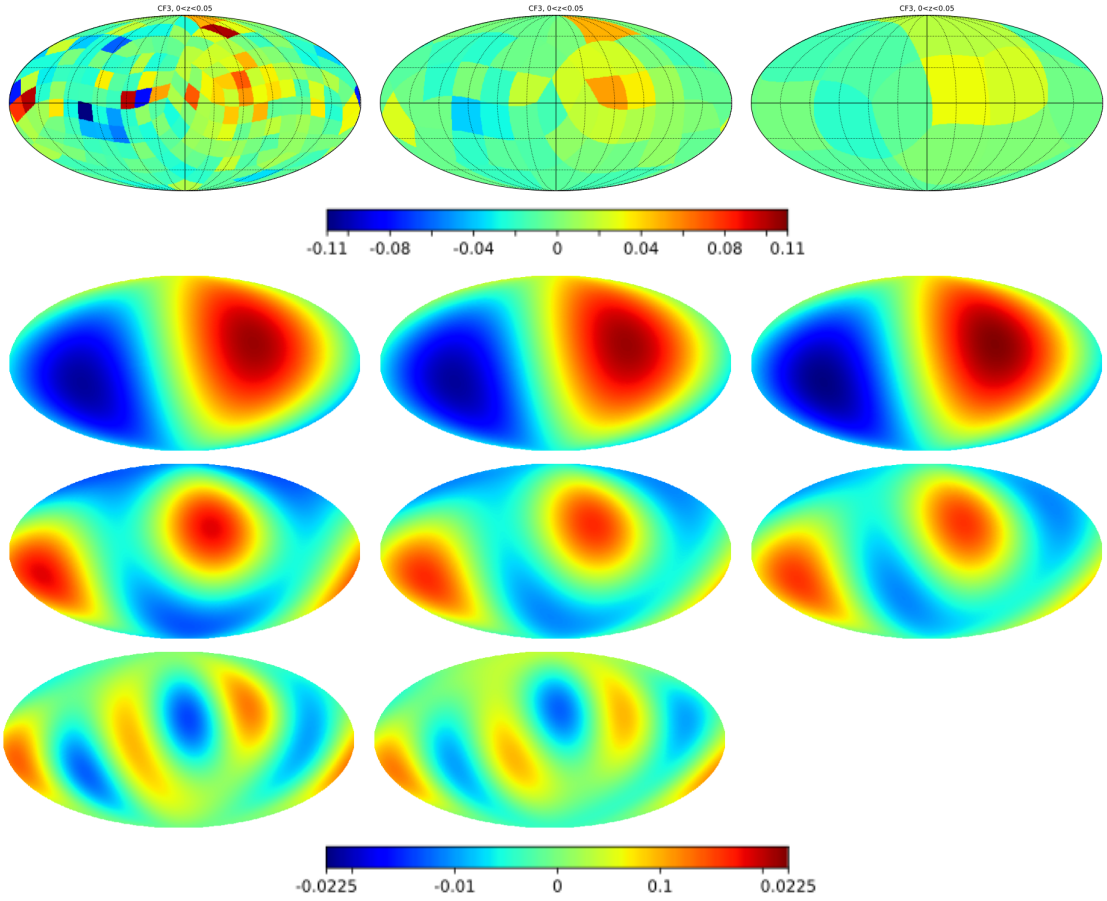


Figure 3.3: *Upper panel:* the angular $\tilde{\eta}$ field traced by the CF3. From left to right are shown different resolution maps corresponding to the tessellation of the sky with 192, 48 and 12 HEALPix cells. The dipole (second panel from the top), quadrupole (third panel from the top), and octupole (bottom panel) components are also shown.

Sample	N_{pix}	Δl_d	Δb_d	ΔC_1 (10^{-4})	Δl_q	Δb_q	ΔC_2 (10^{-4})	Δl_t	Δb_t	ΔC_3 (10^{-4})
CF3 [0.01, 0.05]	192	0	-2	-0.5	1	0	-0.1	5	-2	-0.4
CF3 [0.01, 0.05]	48	-5	-2	0.3	-1	-4	0	-2	-3	0
CF3g [0.01, 0.05]	48	0	-2	1.3	5	1	-0.1	-16	-2	0
CF3 [0.01, 0.05]	12	-1	-4	0	-5	3	0.1	-	-	-
CF3g [0.01, 0.05]	12	0	-4	0	12	7	0	-	-	-
CF3sn [0.01, 0.05]	12	17	-11	0.6	11	5	-0.5	-	-	-
Pantheon [0.01, 0.05]	12	13	-14	-1.1	-	-	-1.0	-	-	-
CF3 [0.01, 0.03]	12	0	-5	0.7	1	-3	0.5	-	-	-
CF3 [0.03, 0.05]	12	1	1	-0.3	2	7	0.1	-	-	-

Table 3.2: The systematic bias factor for different parameters of the SH reconstruction. The systematic error is computed using 1000 Monte Carlo simulations of the catalogs displayed in the first column.

statistically significant. To answer the question I compare our hypothesis (occurrence of a truly physical anisotropic dipole) against the probability of the occurrence of a dipole, as a statistical fluctuation, in a model where the fluctuations are uncorrelated. To this end, I perform Monte Carlo simulations to reconstruct the p-value statistics to invalidate our null-hypothesis against observed data. Specifically, I consider a model of the expansion rate fluctuation $\tilde{\eta}$ that contains only the monopole and no higher order terms and generate 10000 Monte Carlo mock catalogs simulating each data set. This is done by replacing the model distances with a fictitious one randomly drawn from a Gaussian distribution $G(\tilde{\eta}, \sigma_{\tilde{\eta}})$, where $\sigma_{\tilde{\eta}}$ is the observational error quoted for each object in the various data samples. For each simulation, I calculate the power in the resulting dipole ($\hat{C}_1^{\rm sim}$) and compare it with the observed one $\hat{C}_1^{\rm obs}$. I then estimate the frequency with which $\hat{C}_1^{\rm sim} > \hat{C}_1^{\rm obs}$. A standard rule of thumb consists in rejecting the null hypothesis, *i.e.* refute the statistical significance of the signal I observe, if $p > 5\%$. On the contrary, I find that p is virtually zero (i.e. $p < 10^{-4}$ for CF3g and also critically low $p = 0.3\%$ and 4.4% for CF3sn and the Pantheon sample respectively (see Table 3.1), thus confirming the non-accidental nature of the dipolar anisotropy.

Moreover, I find that the contribution of the quadrupole component to the anisotropies observed in the $\tilde{\eta}$ expansion field is significant both in terms of its amplitude, which is comparable to that of the dipole, and in terms of its statistical significance (measured by the signal-to-noise ratio ($SNR \sim 3.25$ for CF3g and $SNR \sim 1.2$ for CF3sn). Again, a p-value analysis of its significance performed simulating 10000 mock catalogs, still confirms that the chances of this signal being a statistical artifact are minimal (the probability of

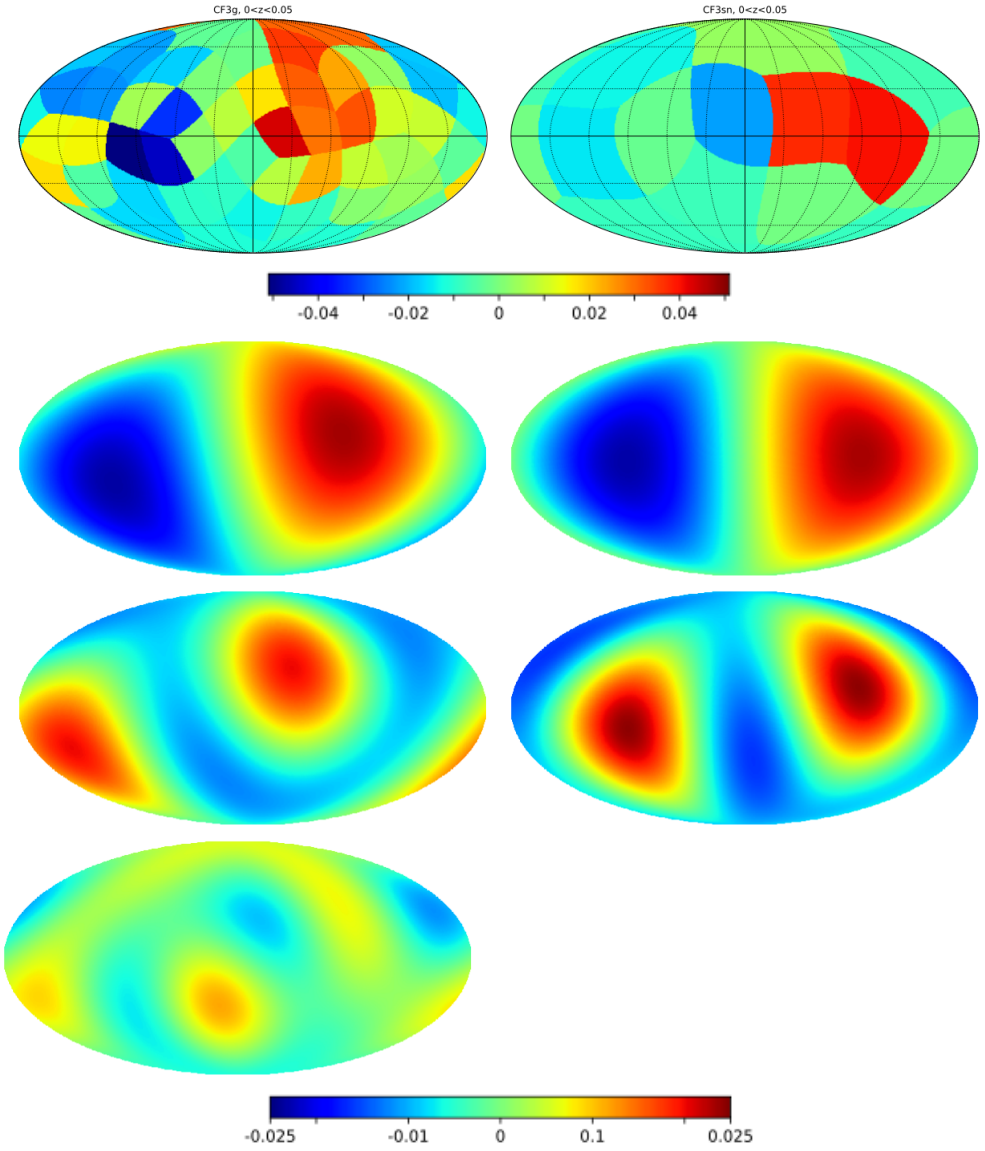


Figure 3.4: *Left panel:* the $\tilde{\eta}$ field tessellated into 48 pixels and traced by the CF3g sample. The dipole (second panel from the top), quadrupole (third panel from the top), and octupole (bottom panel) components are also shown. *Right panel:* same as above, but now the expansion rate fluctuation field is tessellated into 12 pixels and traced by the CF3sn sample.

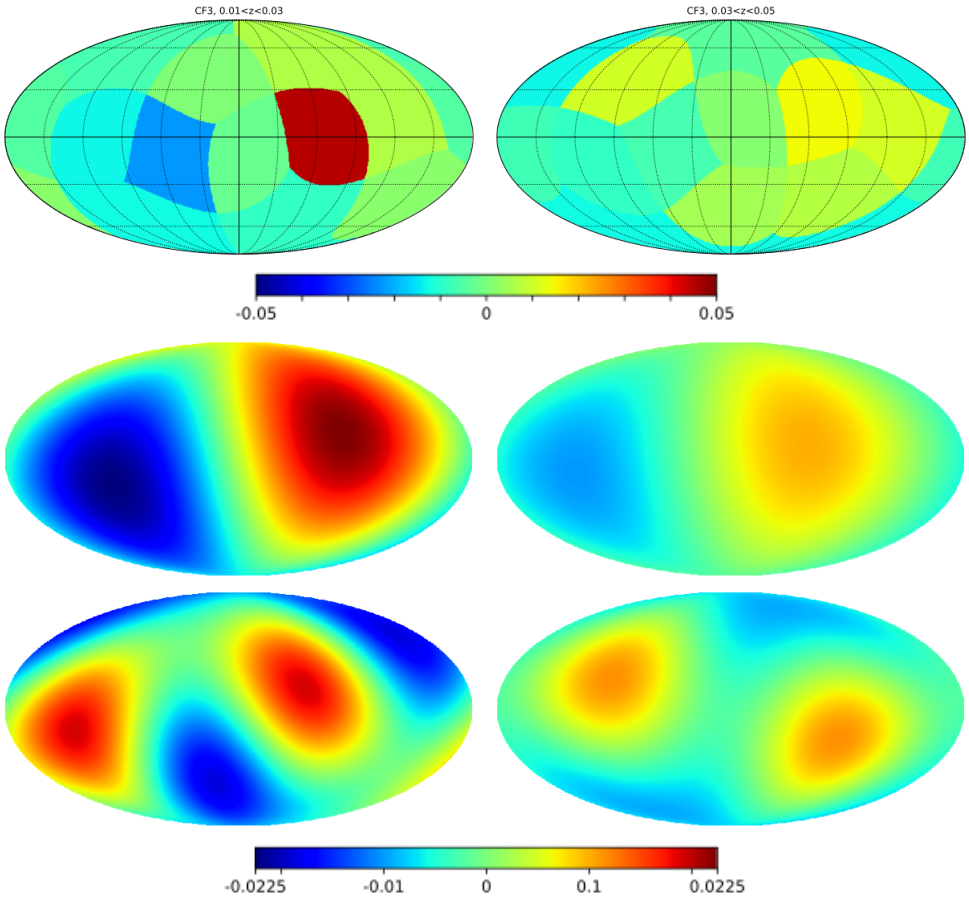


Figure 3.5: *Left panels:* The $\tilde{\eta}$ field (upper), its dipolar (center) and quadrupolar (lower) components traced by the CF3 sample in the redshift interval $0.01 \leq z \leq 0.03$. *Right panels* The same as before but for galaxies in the deeper redshift range $0.03 \leq z \leq 0.05$.

reconstructing a quadrupole larger than the observed one due to a random fluctuation is effectively zero for CF3g and smaller than 3% for CF3sn). The probability is reduced even more dramatically if the test is run to answer the question; what is the likelihood of finding a dipole and quadrupole of similar intensity to that observed in the case where the underlying expansion field is uniform? This result, both independently and in combination with what was found for the dipole term, confirms that the probability of the observed anisotropy being a statistical artifact is very small.

More intriguingly I find that the maximum of the quadrupole signal is aligned with the dipole direction (see Figure 3.3). This peculiar alignment is consistently and independently confirmed by both galaxy (CF3g) and SNe Ia (CF3sn) samples (see Table 3.1).

I highlight the fact that inferences made with the different samples are consistent, but there is one difference that deserves attention and further investigation: there is no evidence of a quadrupole component in the Pantheon data as judged from the amplitude of the $\hat{C}_2$ power, both in term of its SNR and of its p-value. This result confirms a similar null detection obtained by [111] although in a different redshift range and using an alternative method which is not based on the Fourier decomposition of the signal but on the maximum likelihood adjustment of quadrupolar coefficients. The possible reasons for this lack of signal will be analysed in section 3.2.1.

Interestingly, I find evidence ($SNR \sim 2.5$) that the contribution of the octupole is also not negligible, at least when the whole CF3 sample is analyzed with a 48 HEALPix pixel

Sample	l_d	b_d	$\hat{C}_1$ (10^{-4})	$\hat{C}_2$ (10^{-4})	$\frac{\chi^2_{\rm min}}{dof}$
CF3 [0.01, 0.05]	287 ± 5	10 ± 4	4.3 ± 0.8	1.2 ± 0.3	1.26
CF3g [0.01, 0.05]	290 ± 5	5 ± 4	5.3 ± 0.9	1.3 ± 0.3	1.25
CF3sn [0.01, 0.05]	293 ± 14	0 ± 10	5.5 ± 2.6	1.8 ± 1.1	1.60
Pantheon [0.01, 0.05]	311 ± 32	35 ± 36	3.4 ± 2.1	0.5 ± 0.9	0.98
CF3 [0.01, 0.029]	280 ± 5	11 ± 4	8.0 ± 1.4	2.4 ± 0.5	1.37
CF3 [0.03, 0.05]	324 ± 17	10 ± 12	1.4 ± 0.8	1.4 ± 0.5	1.16
CF3sn [0.01, 0.03]	274 ± 14	-5 ± 11	8.2 ± 4.3	3.1 ± 1.9	1.81
CF3sn [0.03, 0.05]	325 ± 23	6 ± 18	5.9 ± 5.0	0.9 ± 1.1	1.24

Table 3.3: Best fitting SH parameters obtained by minimizing the χ^2 difference between the expansion field $\tilde{\eta}$ and a model given by cutting the SH decomposition at $\ell = 2$.

smoothing. The power stocked in this component is roughly half that in the quadrupole although the intensity peaks at a value comparable to the maximum intensity of the quadrupole. Even more unexpected is the fact that the direction of the maximum of the octupole component ($l_t = 284 \pm 7, b_t = 12 \pm 5$) appears to be aligned with that of the dipole ($l_d = 283 \pm 6, b_d = 12 \pm 5$) and of the quadrupole ($l_q = 310 \pm 11, b_q = 4 \pm 8$) (see Table 3.1).

The fact that I cannot confirm the octupolar signal independently in the 192 and 48 pixels maps suggests the need to pursue another route to quantify its amplitude and direction, and also to ensure the general robustness of our results. I have thus determined the value of the SH parameters (direction of the dipole and power spectrum coefficients) by means of a maximum likelihood analysis as discussed in section 2.2.2. I run two independent analyses using $\ell_{\rm max} = 2$ and $\ell_{\rm max} = 3$. The resulting best fitting parameters together with the associated errors, are reported in tables 3.3 and 3.4 respectively.

Overall, the central values and errors deduced by means of this statistical procedure are in excellent agreement with pixelization method reported in TABLE (3.1) and provide independent confirmation of the soundness of our findings. Interestingly, the detection of the octupolar component is confirmed, at least for the whole CF3 sample. The best fitting amplitude $\hat{C}_3^{\rm fit} = 0.6 \pm 0.2$ is consistent with what is determined by pixelization ($\hat{C}_3 = 0.5 \pm 0.2$), and also the direction of the axis of maximum intensity is in the general direction of the dipole ($l \sim 287, b \sim 9$).

As discussed before, the advantage of a SH analysis of anisotropies over other approaches is that the fact that SH coefficients represent projections on an orthonormal basis implies that the multipoles have minimum correlation. It is however critical to assess whether their curious structure is the result of a fortuitous averaging coincidence, *i.e.* the accidental combination of different patterns at different depths, or it is a persistent feature independent from the radial depth of the survey.

Sample	l_d	b_d	$\hat{C}_1$ (10^{-4})	$\hat{C}_2$ (10^{-4})	$\hat{C}_3$ (10^{-4})	$\frac{\chi^2_{\rm min}}{dof}$
CF3 [0.01, 0.05]	282 ± 5	13 ± 4	5.0 ± 0.9	1.0 ± 0.2	0.6 ± 0.2	1.26
CF3g [0.01, 0.05]	285 ± 5	8 ± 4	6.0 ± 1.2	1.1 ± 0.3	0.7 ± 0.2	1.25
CF3sn [0.01, 0.05]	285 ± 16	2 ± 11	5.6 ± 3.1	2.4 ± 1.4	1.5 ± 1.1	1.60
Pantheon [0.01, 0.05]	247 ± 34	20 ± 23	7.3 ± 8.4	2.0 ± 3.2	2.4 ± 2.3	1.01
CF3 [0.01, 0.03]	279 ± 6	15 ± 5	7.3 ± 1.5	2.2 ± 0.4	1.1 ± 0.3	1.36
CF3 [0.03, 0.05]	323 ± 21	14 ± 14	1.5 ± 1.0	1.6 ± 0.7	0.2 ± 0.2	1.16

Table 3.4: Best fitting SH parameters obtained by minimizing the χ^2 difference between the expansion field $\tilde{\eta}$ and a model given by cutting the SH decomposition at $\ell = 3$.

To investigate this issue I repeat the analysis separately in two redshift intervals $0.01 \leq z \leq 0.03$ and $0.03 \leq z \leq 0.5$. These are the smallest subvolumes that still provide detections with acceptable *SNR* and low risk of misinterpretation (low p-value), if only for the CF3 sample. Results are shown in Figure 3.5.

The direction of the dipole and the quadrupole reconstructed in the two volumes consistently point in the same direction (to within about 1σ) and is also in excellent agreement with the results found for the whole samples. This confirms that the alignment phenomenon is not a random overlap but rather physical in nature. There is, instead a significant change in the power spectrum amplitude of the multipoles. The $\hat{C}_1$ component decreases by more than about 5.5σ as the redshift of the sample doubles. The same decrement with depth ($\sim 3\sigma$) is observed for the amplitude of the $\hat{C}_2$ coefficient.

As a further check, I investigated whether quadrupole or octupole components are spuriously generated by the anisotropic and inhomogeneous distribution of galaxies and supernovae. To this end, I simulate an expansion rate fluctuation field that has a dipole component of the same intensity as that detected by the data, but with zero quadrupole and octupole. I then perturb the model's redshift-independent distances by adding Gaussian noise that mimics observational errors. Finally, I apply the SH analysis pipeline and examine the detection rate of a quadrupole or octupole of the same intensity as those measured from the real data. The power in both channels ($\hat{C}_2$ and $\hat{C}_3$) is on average an order of magnitude lower than that inferred from the CF3 dataset. For example, 10000 Monte Carlo replicas of the CF3 sample, analyzed with a smoothing of 48 pixels, give, on average, $\hat{C}_2 = 0.1 \pm 0.1$ and $\hat{C}_3 = 0.09 \pm 0.06$. Moreover, the probability of simulated values even more extreme than those actually observed is effectively zero ($p < 10^{-4}$).

3.2.1 Axial symmetry of the multipoles

In Figure 3.6 I show the 3D structure of the quadrupole component of the expansion rate fluctuations reconstructed using either the galaxy or the supernovae sample. This figure offers a different perspective on the dipole-quadrupole alignment. It shows that both quadrupoles independently reconstructed using galaxy and supernova data present

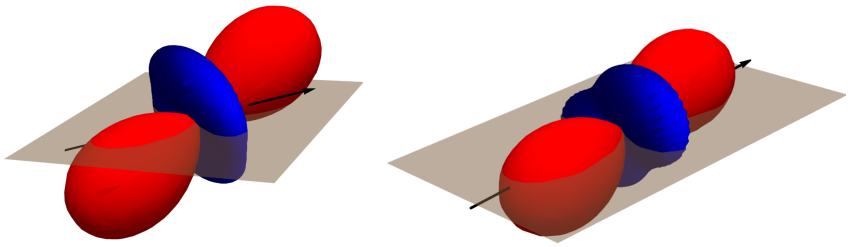


Figure 3.6: The 3D structure of the quadrupole component of the CF3g sample (left panel) and for the CF3sn sample (right panel). The radial coordinate represents the absolute value for $\tilde{\eta}$; the red and blue colors indicate positive and negative signs respectively. For reference, the gray surface represents the orientation of the galactic plane while the black arrow gives the direction of the dipole as reconstructed for each sample.

an axially symmetric configuration which polarizes in the direction defined by the dipole.

This additional symmetry, although physically unexpected since it seems to imply extreme fine-tuning in the local distribution of matter fluctuations, makes it possible to simplify, at least mathematically, the analysis of the anisotropies of the $\tilde{\eta}$ field. The fact that the direction (l_d, b_d) along which the multipoles align (Apex direction) defines not only a preferred axis, but indeed an axis of symmetry implies that the expansion rate fluctuation field $\tilde{\eta}$ effectively depends only on a single variable, the polar angle θ between the line-of-sight of an object and the direction (l_d, b_d). A simple expansion of the field in Legendre polynomials $P_\ell(\cos\theta)$, as opposed to the full spherical harmonics machinery, is thus enough for seizing the essential functional behavior of the field. In this case, Any for fluctuating field $f(z, \boldsymbol{n})$, including η, if the z-axis is aligned with direction of the axis of symmetry, the SH coefficients of the field $f_{\ell m}$ are zero for $m \neq 0$, and $f_{\ell 0} = [4\pi/(2\ell+1)]^{1/2} f_\ell$, where

$$f_\ell(z) = \frac{2\ell+1}{2} \int_{-1}^{1} f(z, \cos\theta) P_\ell(\cos\theta)\, \mathrm{d}(\cos\theta)\,, \tag{3.1}$$

are the Legendre coefficients. In this convention, $f_{2\ell+1} > 0$ means that there is a maximum at $\theta = 0$ and a minimum at $\theta = \pi$, and the opposite for $f_{2\ell+1} < 0$. For $f_{2\ell} > 0$, the field has a maximum at $\theta = 0$ and at $\theta = \pi$, while $f_{2\ell} < 0$ means that there is a minimum in both directions.

In this chapter, I estimated the Legendre coefficients using a method similar to HEALPix method. The average value $\tilde{\eta}(\theta)$ reconstructed in open circular sectors (like pixels) of identical width having the center on the axis of symmetry and angular separation θ from the apex direction is shown in Figures 3.7 and 3.8 for the galaxy and SN Ia samples.

After removing the monopole by taking the average of ν (see section 2.2.1), the Legendre coefficients can be estimated by

$$\tilde{\eta}_\ell = \frac{2\ell+1}{N_{\rm bins}} \sum_{i=1}^{N_{\rm bins}} \tilde{\eta}(\theta_i) P_\ell(\cos\theta_i), \tag{3.2}$$

and the results are quoted in Table 3.5 up to $\ell = 3$ with thir errors which can be calculating by using the fact that the variance of the sum of uncorrelated Gaussian random variables

Sample	$N_{\rm bins}$	$\tilde{\eta}_1$ (10^{-2})	$\tilde{\eta}_2$ (10^{-2})	$\tilde{\eta}_3$ (10^{-2})	χ^2_1/dof	χ^2_2/dof	χ^2_3/dof	v_b (km/s)
CF3 $0.01 < \tilde{z} < 0.05$	15	1.9 ± 0.1	1.1 ± 0.2	1.1 ± 0.2	7.22	4.35	1.97	318 ± 22
CF3g $0.01 < \tilde{z} < 0.05$	15	2.0 ± 0.1	1.0 ± 0.2	1.0 ± 0.2	6.55	4.07	2.23	334 ± 24
CF3sn $0.01 < \tilde{z} < 0.05$	15	1.7 ± 0.4	1.2 ± 0.6	1.4 ± 0.6	1.57	1.48	1.10	244 ± 64
CF3 $0.01 < \tilde{z} < 0.05$	10	1.7 ± 0.1	0.9 ± 0.2	0.6 ± 0.2	8.50	4.83	2.71	292 ± 21
CF3g $0.01 < \tilde{z} < 0.05$	10	1.8 ± 0.1	0.9 ± 0.2	0.5 ± 0.2	7.59	4.34	2.83	307 ± 23
CF3sn $0.01 < \tilde{z} < 0.05$	10	1.3 ± 0.4	0.5 ± 0.5	0.4 ± 0.5	1.53	1.40	1.18	195 ± 57
Pantheon $0.01 < \tilde{z} < 0.05$	10	1.6 ± 0.7	0.1 ± 0.7	-0.8 ± 0.5	0.46	0.46	0.54	243 ± 110

Table 3.5: The coefficients of Legendre expansion for 15 and 10 bins in $\cos\theta$ where θ is the angle between the and principal axis $(l, b) = (285, 11)$.

is equal to the sum of the variance of each term. Again, since the Legendre basis is orthogonal, the estimation of other moments almost does not modify the value already calculated moments. As a check of the stability of the estimation, I have also calculated the Legendre coefficients as $\tilde{\eta}_\ell = \sqrt{\frac{2\ell+1}{4\pi}}\tilde{\eta}_{\ell 0}$ where the coefficients $\tilde{\eta}_{\ell 0}$ is the SH component reconstructed after rotating the z axis into the position defined by the symmetry axis. I find that the results from the two methods are effectively indistinguishable.

The first thing I remark is that the coefficients computed for different samples are all compatible among themselves, within 1-σ uncertainty. For this reason, the data from various samples shown in Figures 3.7 and 3.8 are compared to the best-reconstructed template, the one with smaller errors, *i.e.* that resulting from the analysis of the whole CF3 sample. This helps in judging the consistency of different datasets in tracing the same underlying expansion rate fluctuation field. Concerning the contributions to the signal, I see that the dipole term alone, as expected, on the basis of the results of the previous section provides a poor description of the angular modulation of $\tilde{\eta}$. This is true for both the CF3g and CF3sn samples. An analysis of the goodness of the fit with a reduced χ^2 statistic (after binning) gives values of 6.55 and 1.57 respectively, i.e. a probability $p \sim 0$ and $p \sim 7\%$ respectively of having this χ^2 using only the dipolar model. Although the latter value is formally higher than the traditional rejection threshold of 5%, and thus the risk of rejecting a good model is not negligible, it is equally true that once the quadrupole and octupole terms calculated for the CF3 sample are added to the model, the description of the CF3sn data improves, as evidenced by the systematic decrease in the χ^2 statistic.

As already discussed in section 3.2 the Pantheon sample provides an exception, in that it does not show sign of a quadrupolar or higher order multipole components. A simple dipole optimally captures the angular modulation of the fluctuations of the expansion rate $\tilde{\eta}$ ($\chi^2/dof = 0.66$). Moreover, by including the quadrupole and octupole terms, the goodness of fit systematically degrades. The lack of signal is explained by the concomitance of two effects: the larger error bars with which the $\tilde{\eta}$ observable is reconstructed from the sparse Pantheon sample and also, importantly given the alignment between the dipole and quadrupole found in the CF3g and CF3sn samples, the lack of objects along such a critical direction in the Pantheon sample.

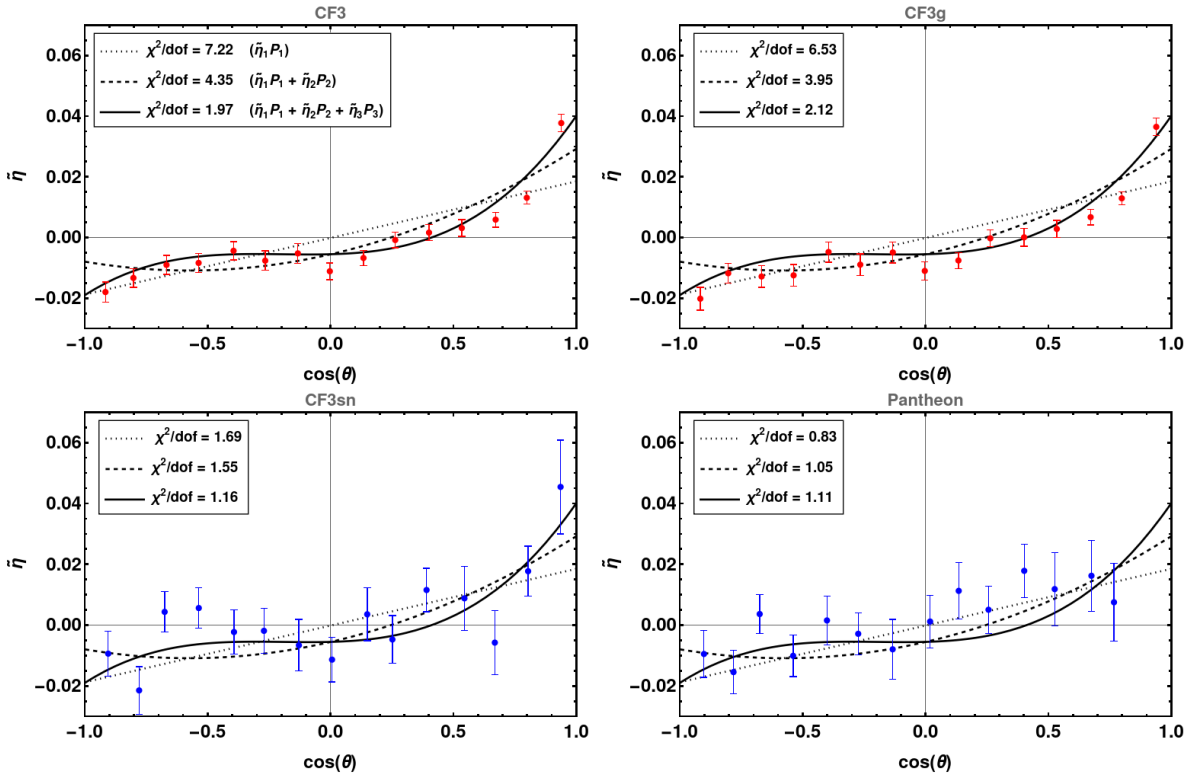


Figure 3.7: *Upper left:* average value of $\tilde{\eta}$, for the CF3 sample, in open spherical sectors of identical width $\Delta \cos\theta = 2/15$ and angular separation θ from the direction $l = 285, b = 11$. The dotted line corresponds to the dipolar model ($\tilde{\eta}_1 = 1.9{\cdot}10^{-2}$), the dashed line includes also the contribution of a quadrupole term ($\tilde{\eta}_2 = 1.1 \cdot 10^{-2}$). The effects of adding the octupole term ($\tilde{\eta}_3 = 1.1 \cdot 10^{-2}$) are shown by the solid line. These models are compared to CF3g data (*upper right*), the CF3sn data (*lower right*) and the Pantheon data (*lower right*). In this latter case, Note the absence of data in the rightmost bin, i.e., along the direction in which the low-order multipoles of the CF3 sample align.

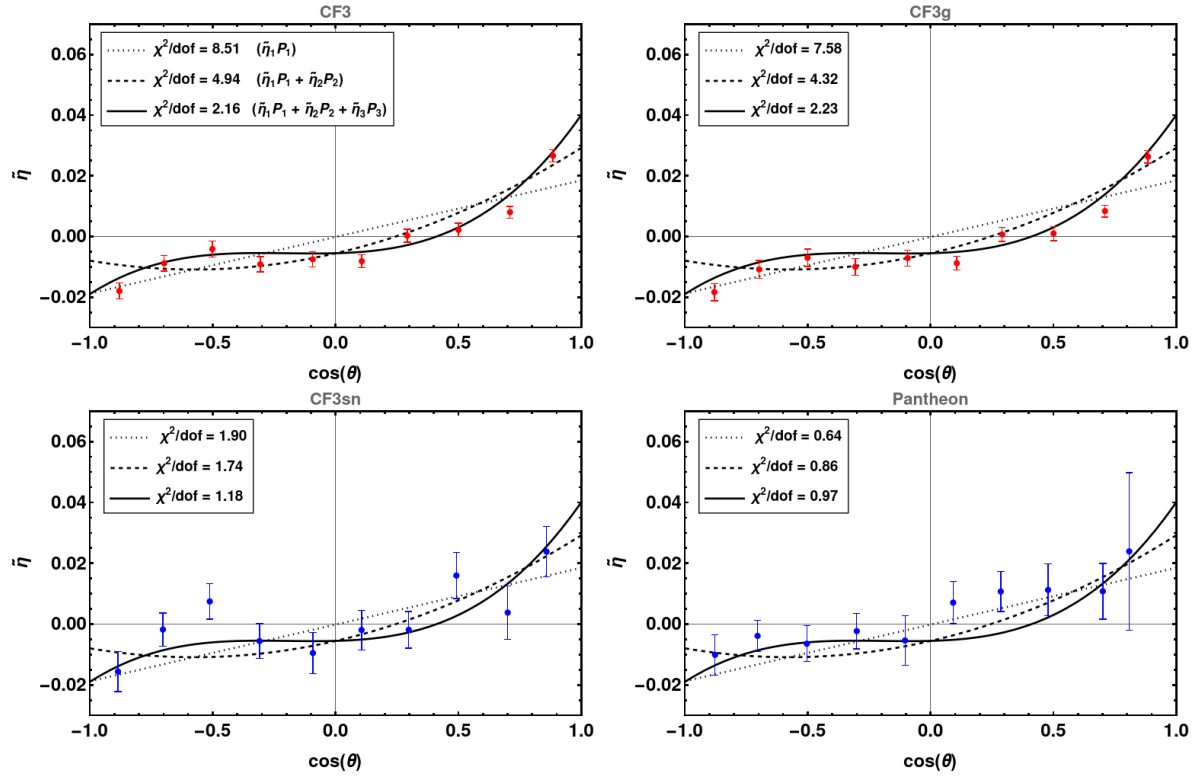


Figure 3.8: The same as figure 3.7, with the same curves, but the number of bins is 10 here.

3.2.2 Bulk motion model

As shown in 2.3, the perturbation theory of the standard cosmological model provides a framework for interpreting our results. Here I estimate the bulk velocity which is defined as the dipole of the radial component of the peculiar velocity field in a given volume. Therefore, the dipole of the expansion field in CMB frame is predicted to be[1]

$$\tilde{\eta}_1 = \frac{v_b}{\ln 10}\langle (1+z)/z \rangle \tag{3.3}$$

where that $\langle (1+z)/z \rangle$, is the average over the volume under study, and so the bulk velocity can be estimated by

$$v_b = \frac{\tilde{\eta}_1 \ln 10}{\langle (1+z)/z \rangle}. \tag{3.4}$$

Note that in this picture, the amplitude of the bulk is controlled by the amplitude of the dipolar parameter $\tilde{\eta}_1$ and also by the depth of the survey volume.

The direction of the bulk motion for the three samples is shown in Figure 3.9. It is interesting to note that the direction of the bulk flow of the CF3g sample agrees remarkably well ($\sim 4^\circ$ apart) with that of the bulk component of the Local Group velocity (~ 455 km/s in the direction $l \sim 299, b \sim 15$). This latter is obtained subtracting from the velocity of the LG with respect to the CMB (~ 631 km/s in the direction $l \sim 270, b \sim 27$ [146]) the local perturbations due to the infall of the LG onto the Virgo cluster (~ 185

[1]Here, in relation 3.3, I add the factor $(1+z)$, in contrast to relation 2.39, where this factor is neglected for $z \ll 1$.

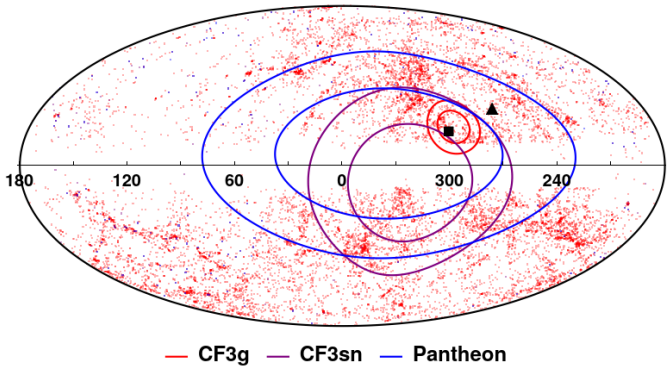


Figure 3.9: Likelihood contours (1σ and 2σ) for the direction of the dipole reconstructed using 12 pixels for the CF3g (red lines), CF3sn (purple lines) and Pantheon (blue lines) samples. For reference, the direction of the motion of the barycenter of the Local Group with respect to the CMB $(l, b) \approx (270, 27)$ [146] is marked (black triangle) together with the direction of its bulk component $(l, b) \approx (299, 15)$ (black square).

km/s in the direction $l \sim 284, b \sim 74$ (e.g. [147, 148])) as well as to the repulsion from the local void (259 km/s in the direction $l \sim 210, b \sim -2$) [147]). This alignment suggests that most of the LG motion is indeed generated by sources at a distance not less than the depth of the samples analyzed here, i.e. $z \sim 0.05$.

I also confirm that the bulk motion traced by the CF3g sample points in the general direction in which the most massive concentrations in this region of the sky are located, namely Hydra-Centaurus ($\sim 302, l = 21$) and the Shapley supercluster ($l = 311, b = 32$) (which are about 6 and 19 degrees away, respectively).

The amplitude of the bulk flow estimated from the CF3sn ($v_b = 195 \pm 57$ km/s) is comparable with that measured using the Pantheon sample (243 ± 110 km/s) and both values are statistically compatible with the result obtained using the CF3g sample (307 ± 23 km/s), although the large error on the latter sample makes agreement almost a foregone conclusion. These different samples also agree on the direction of the velocity field which is best determined using the total CF3 sample ($l = 285 \pm 5$, $b = 11 \pm 4$).

Comparing our results with those in the literature, I find 2σ overlap with those of [149], who, using a different compilation of redshift-independent distances covering approximately the same volume of the CF3 sample, found $v_b = 252 \pm 11$, $l = 293 \pm 5, b = 14 \pm 5$. They also compare favorably with those of [150] ($v_b = 292 \pm 28$ km/s, $l = 296 \pm 16, b = 19 \pm 6$), [151] ($v_b = 249 \pm 76$ km/s, $l = 319 \pm 18, b = 7 \pm 14$) and [152] ($257 \pm 44$ km/s $l = 279, b = 10$). Regarding the results of [153], although there is general agreement on the bulk amplitude, the directions are misaligned by about 40 degrees.

Finally, note that in addition to the bulk component, the velocity field has also quadrupole and octupole components.

3.2.3 The scale of anisotropies

How far does this anisotropic pattern extend? For galaxy samples, the determination of redshift-independent distances becomes problematic at high redshift. Only SN data give access to the deep regions of the universe. However, the SN sample is very incomplete in its coverage of the sky, a fact that prevents the extension of the study of angular anisotropies beyond the $z = 0.05$ limit.

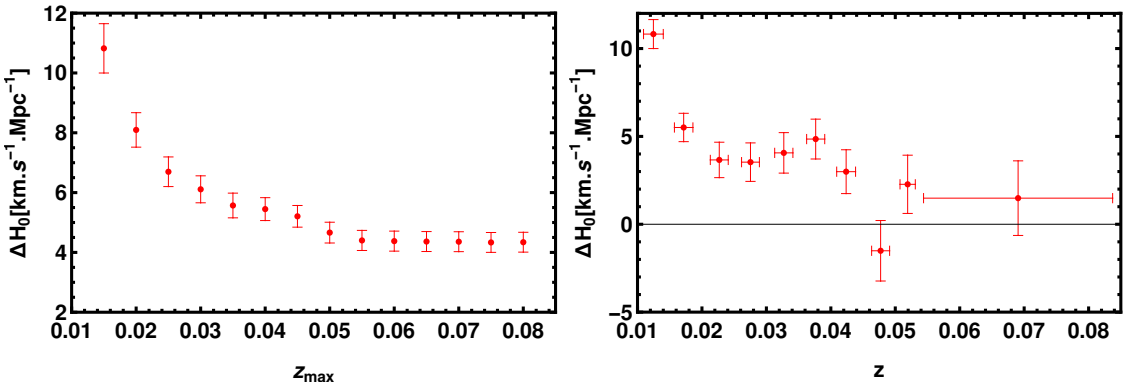


Figure 3.10: Difference between the best fitting antipodal values of H_0 for CF3 objects. The Hubble diagram is constructed using objects within 60° from the apex ($l = 285, b = 11$) and antiapex directions. Points represent estimates in the cumulative intervals $0.01 < z < z_{\max}$ (left panel) and in differential intervals (right panel).

Many studies seem to agree that the expansion rate is slightly higher in the direction of the generic CMB dipole (see [105] for a review) even at redshifts much higher than those I investigated. However, the reported magnitude of this anisotropy depends on the sample analyzed and, for the same sample, seems to depend on the technique used to measure it (e.g., [24]). The statistical significance of deviations from uniformity is also at stake. For example, with regard to studies of supernovae samples, some papers either indicate their significance, and thus the potential biasing effect on the inference of cosmological parameters ([43]), or refute them as pure statistical fluctuation ([154, 26]).

Figure 3.10 shows the difference between the best fitting H_0 in the apex and antiapex direction also including all objects in the CF3 sample (also those beyond the $z = 0.05$ cut imposed for our analysis, i.e. $N = 739$ objects in the apex direction and $N = 159$ in the antiapex direction) by fitting the relation $\mu = 5\log(z/H_0) + 25$ separately. It is fair to say that the problem of characterising the extent of the radial scale of the local anisotropy remains unanswered by current data.

3.2.4 p-value of the multipoles in ΛCDM

It is worth investigating whether the observed amplitude of the multipoles of η—the anisotropies in the expansion rate measured in the local universe within $0.01 < z < 0.05$—is consistent with predictions from the ΛCDM model. This essentially assumes that the deviations are perturbative in nature, generated by the gravitational influence of local mass fluctuations whose amplitude and spatial distribution, i.e., power spectrum, are in line with expectations from the standard cosmological model.

If I consider the multipoles of CF3 at $0.01 < \tilde{z} < 0.05$ with average redshift ~ 0.03, then the standard deviation of the $\tilde{\eta}_{\ell m}$ in ΛCDM is ($\approx 1.3 \times 10^{-2}$, $\approx 0.9 \times 10^{-2}$ and $\approx 0.6 \times 10^{-2}$) for $\ell = 1, 2, 3$ respectively. To check if the measured SH coefficients are consistent with the standard model, I first compute

$$\chi^2_\ell = \sum_{m=-\ell}^{\ell} \left(\frac{\tilde{\eta}^2_{\ell m}}{C_\ell + \sigma^2_{\ell m}} \right) \tag{3.5}$$

using the fact that the ensemble average of $\tilde{\eta}_{\ell m}$ is zero in the standard model according to the cosmological principle and C_ℓ can be calculated by eq. (2.48). After that, I estimate the probability (p-value) to obtain a χ^2_ℓ higher than the calculated one. I find $p \sim 4\%$, 27% and 20% respectively. Thus, all the observed multipoles are broadly consistent with theoretical expectations. In other terms, there is no indication of any statistically significant tension with the predictions of the standard model within the volume investigated.

3.2.5 Removing peculiar motions from the Hubble diagram by means of the η field

As a consequence of the alignment of the maximal intensities of its dipole, quadrupole and octupole components, the expansion field displays an 'apex' towards which the rate of expansion is significantly higher than average and an anti-apex where the expansions is coherently lower than the monopole component. This preferred axis characteristically shows up in the Hubble diagram.

Figure 3.11 shows the difference between the best estimates of H_0 deduced from the Hubble diagram analysis in two antipodal directions. In practice this is achieved by fitting the relation $\mu = 5\log(z/H_0) + 25$ separately to the distance modulus of the Pantheon objects falling in two cones of total width 120° (about 25% of the sky) centered on the observer and whose axes point in antipodal directions (apex and antiapex). Objects in sky regions where the expansion rate is larger (apex direction) do show systematically lower values of the distance modulus. The maximal deviation observed is $\Delta H_0 = 4.1 \pm 1.1$ km/s/Mpc in the direction $(l = 305, b = 30)$. For the sake of comparison, the difference is $\Delta H_0 = H_0^{\rm apex} - H_0^{\rm antiapex} = 5.1 \pm 0.4$ km/s/Mpc for the CF3g sample (in the direction $(l = 295, b = 5)$), $\Delta H_0 = 5.9 \pm 1.2$ km/s/Mpc for the CF3sn dataset (in the direction $(l = 280, b = -5)$) all values compatible with that obtained for Pantheon to better than 1σ.

In the standard cosmological model, anisotropies in the expansion rate are accounted for by peculiar motions. When estimating H_0 using the Hubble diagram, it is essential to correct the observed redshifts to remove their contributions (see section 1.4.1). This is done by using velocity maps derived from the linear perturbation analysis of large-scale mass fluctuations. This correction can be applied to the Pantheon catalog since, for each entry, the radial velocities (derived from the analysis of [155]) are given. Figure3.11 shows the maximal antipodal anisotropy ΔH_0 after such a correction is implemented.

As it can be seen, factoring out the non-cosmological contribution induced by peculiar motions reduces the amplitude of the dipolar anisotropy (now the maximal change between antipodal directions, $\Delta H_0 = 2.4 \pm 1.1$, is reduced in both amplitude and signal to noise) . Although this removal is in the direction of making the results more consistent with what the standard model predicts (see, for a similar conclusion, [156]), the remaining anisotropic signal still has a non-trivial structure that makes it incompatible with being a residual fluctuation of random nature. In fact, the largest residual deviations are also the most statistically significant, as can be seen by contrasting the map of the residual signal with the signal-to-noise ratio maps (see the upper central panel of Figure 3.11). The former clearly shows that for a given distance, redshifts are systematically higher than expected over a large and contiguous region of sky.

A second remarkable fact is that the direction of the dipolar anisotropy in the Pantheon sample is not affected by removing the peculiar velocity distortions. A spherical harmonic decomposition of the expansion rate fluctuation field $\tilde{\eta}$ (using a 12 pixel tessellation and

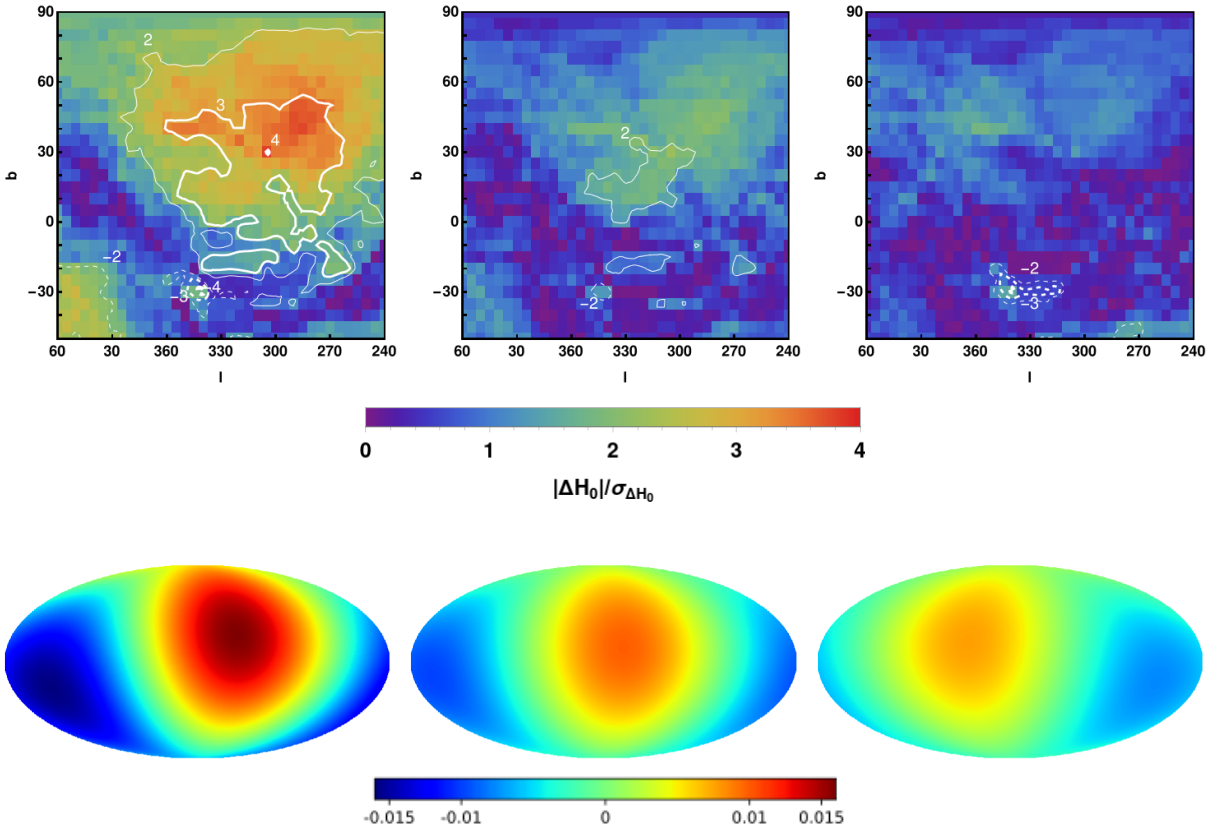


Figure 3.11: *Upper left panel:* Solid and dashed lines represent positive and negative isocontours of $\Delta H_0 = H^{\rm apex} - H_0^{\rm antiapex}$ calculated using Pantheon SNe with angular separation $\leq 60^\circ$ from an axis of coordinates (l, b). Different thicknesses correspond to different amplitudes, as indicated by the labels. Isocontours are superimposed to the smoothed signal-to-noise map. *Bottom left panel:* the dipole component (12 pixel map) of the expansion rate fluctuation calculated using the observed redshifts. *Central panels:* as above, but after subtracting from the redshift of each object the peculiar velocities listed in the Pantheon catalog. *Right panels:* as above, but after correcting the redshift using the $\eta(\alpha)$ model (3.7) with Fourier coefficients computed from the CF3g data (and quoted in the fifth row of TABLE 3.5). The maximum antipodal anisotropy detected are $(l, b, \Delta H_0) = (305, 30, 4.1 \pm 1.1), (305, 30, 2.4 \pm 1.1)$ and $(360, 40, 1.9 \pm 0.9)$ respectively.

cosmological redshifts) confirms that the angular structure of the fluctuation is preserved and only its amplitude is rescaled. Indeed, the lower central panel of Figure 3.11 shows that the dipole map reconstructed after correcting the redshifts for peculiar velocities still displays an anisotropy axis pointing in the direction ($l = 341, b = 11$). This latter is only 22 degrees away from the direction of the expansion rate reconstructed using the observed (uncorrected) redshifts ($l = 334, b = 6$), and still close to the direction of the bulk component of LG motion, which is in turn close to that of the CMB dipole. However, the power locked in this component is $\hat{C}_1 = 1.4 \cdot 10^{-4}$ nearly a factor 3 lower than what measured by neglecting peculiar velocity effects ($\hat{C}_1 = 3.9 \cdot 10^{-4}$).

I checked whether this residual systematicity was the result of incorrect redshift determinations in the Pantheon catalog. In this respect, I redid the analysis using the redshift catalog made available by [157] which should also provide updates on the angular position of the host galaxies. The systematic is still detected, but this time with an even greater significance. The maximal variation of the Hubble constant between antipodal directions before applying any peculiar velocity correction is $\Delta H_0 = (4.5 \pm 1.1)$ km/s/Mpc in the direction ($l = 305, b = 30$), After correction, both the systematic difference ($\Delta H_0 = 2.9 \pm 1.1$ km/s/Mpc in the direction ($l = 305, b = 30$)) and the residual dipolar power($\hat{C}_1 = 1.7 \times 10^{-4}$) are larger than in the original Pantheon catalogue.

This residual signal might indicate flaws in our understanding of gravity on a local scale and might even motivate the exploration of new physics beyond the standard model. However, I will show in the following that these results rather highlight the need for further efforts to calibrate SN data if they are to be used to constrain the value of H_0 even more accurately. Mapping the observed redshift of supernovae into the cosmological redshift by subtracting from each object the peculiar velocity reconstructed at that spatial position by linear perturbation theory is indeed a far from trivial task. In addition to the uncertainties and systematics inherent to the reconstruction scheme adopted and to the samples of galaxies used to trace the matter density fluctuations, such a reconstruction is model-dependent. It inevitably involves the choice of a gravitational theory and therefore the value of cosmological parameters such as, for example, the matter density parameter $\Omega_{\rm m}$.

From a conceptual standpoint, removing anisotropies through the reconstruction of the peculiar velocity field presents a circular reasoning problem. One uses the model they aim to validate to eliminate deviations from that model and then claims that the cleaned data confirms the model. At best, this method serves only as a consistency check that the model has not been disproven.

Furthermore, the perturbative methods employed to reconstruct peculiar velocity fields require prior knowledge of the Hubble constant H_0—the very value that one intends to determine from the Hubble diagram after correcting for peculiar motion distortions.

Interestingly the $\tilde{\eta}$ formalism allows to bypass these technical and conceptual difficulties. Indeed it provides a neat way to take into account systematic perturbations in the expansion rate in a completely model-independent manner. I have shown that, as expected, galaxies and supernovae trace, within observational errors, the same underlying anisotropies. When estimating H_0 via the analysis of the Hubble diagram of supernovae, it is thus sufficient to remove the $\tilde{\eta}$ fluctuations estimated from the independent galaxy catalog of redshift-independent distances. In other terms, galaxy tracers are used to refine the expansion field of SN Ia tracers. This approach ensures that uncertainties are independent, allowing for the safe application of standard error analysis.

The anisotropy corrected amplitude of the distance modulus is

$$\mu = 5 \log \left(\frac{\tilde{z}}{H_0} \right) + 25 - 5\tilde{\eta} \tag{3.6}$$

where $\tilde{\eta}$ is approximated using the Legendre expansion up to $\ell_{\max} = 3$,

$$\tilde{\eta}(\theta) = \sum_{\ell=1}^{3} \tilde{\eta}_\ell P_\ell(\cos\theta), \tag{3.7}$$

with Legendre coefficients computed from the CF3g data (and quoted in the fifth row of TABLE 3.5).

The difference between the best fitting H_0 recovered in various antipodal directions by means of eq. 3.6 is shown in the upper right panel of Figure 3.11. The distribution of ΔH_0 values has an amplitude that is now not only reduced but also more centered on zero. Also the spherical harmonic analysis of the residual expansion rate fluctuation field $\tilde{\eta}$(pantheon) $-$ $\tilde{\eta}$(CF3g) shows that the axial anisotropy is now effectively removed: the residual dipolar modulation points in the direction ($l \sim 40, b \sim 15$)) and the power locked in this component is $\hat{C}_1 = 0.8 \times 10^{-4}$, about twice as small than the residual signal obtained after correcting redshifts with the peculiar velocity field model.

The advantages of this debiasing scheme are not insignificant. First, I achieve better anisotropy subtraction with a three-parameter model (cf. eq. 3.7) than using corrected redshift using numerical grids of peculiar velocities. In addition, correcting for $\tilde{\eta}$ fluctuations has a significant impact on the estimate of H_0. The Hubble parameter that best fits the Pantheon sample (in the range $0.01 < z < 0.05$) is larger by 2σ than that determined on the basis of observed redshifts alone ($\delta H_0 = 0.7$ km/s/Mpc). Also the normalized χ^2 (for 157 degrees of freedom) improves in a statistically significant way (from 1.03 to 0.96), signaling that data are better described by a linear redshift-distance relation.

3.3 Conclusion

I have estimated the $\tilde{\eta}$ field in CMB frame using catalogs of redshift-independent distances such as the Cosmicflows-3 galaxy sample and the Pantheon sample of supernovae. I have then compressed the resulting signal into independent spherical harmonics components to better analyse the structure of the anisotropies in the linear redshift-distance relation. Particular care was paid to assess the reliability of the reconstructions, either analytically, computing the variance of relevant SH parameters, either numerically by means of Monte Carlo simulations. This last approach has the advantage of also correcting the systematic bias induced by the scarcity and incompleteness of the data used in our analysis as well as by the pixelization strategies applied to them.

All data samples analyzed consistently suggest the existence of a preferred axis in the local universe ($0.01 < z < 0.05$), in the direction $(l, b) = (285 \pm 5, 11 \pm 4)$, along which the local redshift-distance relation displays a dipolar pattern. Within the standard model of cosmology, notably its linear perturbative extension, this dipolar modulation of the angular expansion rate can be understood as the imprint of a large-scale bulk flow model. I find that galaxies inside the survey volume $r < 150h^{-1}$Mpc coherently moves with an average speed $v_b = (299 \pm 22)$ km/s. This direction agrees fairly well with the estimated direction of the bulk component of the Local Group velocity $(l, b) \approx (299, 15)$

[147] confirms that the LG participates in a bulk flow that extends out to distances of at least $z = 0.05$

Interestingly, the SH analysis suggests that a simple dipole provides a poor representation of the angular fluctuations in the local expansion rate. A more sophisticated description is necessary if we are to properly model the anisotropies in the redshift-distance relation. I find, that about 50% of the anisotropic signal is contributed by a quadrupole component. This is independently confirmed by the CF3g and CF3sn samples, which also consistently show that the axis of maximal expansion of the quadrupole is aligned with the direction of the dipole. This intriguing feature persists when the sample is split in two and the analysis is repeated in two separate spherical shells of different depths. This evidence allows us to exclude the possibility that the observed alignment is a casual coincidence, that is, a volume-dependent fluke. The analyses of both samples also agree on the shape of the quadrupole. It is a rather axisymmetrical configuration, with no indication of prominent secondary axes.

The findings about the alignment of quadrupole in the general direction of the dipole independently confirms results of [108] or, more recently, of [104] who, using smaller samples, showed that the eigenvector expansion of the shear tensor (a proxy for the quadrupole moment) is aligned in the direction of the Hydra-centaurus/Shapley superclusters. I extend the validity of these results over a volume four times larger through a separate analysis the galaxy and SN samples. Furthermore I find that the octupole is also involved in the alignment. Despite the large errors induced by the sparsity of the sample and the relatively large coarse graining of the multipole reconstruction scheme, there is indeed tentative evidence for the detection of an octupole signal, at least for the CF3 sample of galaxies. Its intensity is of similar amplitude to that of the quadrupole. Its configuration is also quite peculiar, with its axis of maximal intensity colinear with the axes of the dipole and the quadrupole.

I note, as a curiosity, that, the direction where the quadrupole of the expansion field has a maximum does not coincide with that where the quadrupole of the CMB temperature fluctuations reaches its maximum. Also their configuration is different: planar for the CMB and axisymmetric for the local expansion field.

There are several independent indications confirming the robustness of our findings about the geometry of the multipolar structure of the expansion rate fluctuation field: a) the anisotropies detected in different samples agree both in amplitude and direction, b) the probability that they are random fluctuations is ruled out by Monter Carlo analyses c) the random alignment of the independent dipole, quadrupole and, tentatively, octupole moments is statistically improbable. Given that the amplitude of the dipole, quadrupole and octupole components of the fluctuation field scale differently with distance from the gravitational sources, one would expect that their peculiar configuration is due either to an extraordinary fine-tuning in the alignment of the sources themselves or to the dominant role of a single structure dominating the gravitational dynamics in the local universe. I note that indeed [158] finds evidence that the LG lies approximately on the line joining the barycenter of three large cosmic structures, the Shapley concentration and the Great Attractor on one side, and a large galactic underdensity in the diametrically opposite direction.

According to the standard model, the departures from uniformity are the manifestation of deviations from co-mobility induced by local gravitational fields. After factoring out from the Pantheon sample the contribution of these peculiar velocities (reconstructed by applying prescriptions of the theory of linear perturbations to the observed fluctuations in

the spatial distribution of galaxies), I observe that the H_0 perturbations, although reduced in amplitude, do not distribute as random (Gaussian) residuals. Curiously, the structure of the expansion rate field still present an axial anisotropy in the same general direction as the CMB dipole. I find that the power in the residual dipole component, as quantified by the coefficient $\hat{C}_1$ is reduced only by about 50%, and that, as a consequence, the Hubble parameter still has a sinusoidal modulation of amplitude $\Delta H_0 = 1.6 \pm 1.1$km/s/Mpc between the apex and antiapex directions (as opposed to $\Delta H_0 = 2.6 \pm 1.0$ before any peculiar velocity corrections).

This residual systematicity does not indicate the failure of the standard model, but rather the need to improve methods of reconstructing peculiar velocities. In this regard I show how to exploit the expansion rate fluctuation field $\tilde{\eta}$ to subtract redshift anisotropies. In practice, I correct the redshift of the Pantheon sample with a neat three-parameter formula (see eq. (3.7)) calibrated using the independent sample CF3g. Despite its simplicity, the approach proves effective: not only is the dipole pattern suppressed by a factor of about five in power, but even its direction is now offset from the general direction of the CMB dipole. The low signal-to-noise ratio of the residuals is also consistent with the virtual absence of any systematicity. As a result, the best-fit Hubble parameter is 0.7 km/s/Mpc higher than if the distance modulus were calculated with the observed redshifts, and also the goodness of fit, as measured by the χ^2_ν, improves in a statistically significant way.

In addition to the similarities among results inferred from independent samples, there are also differences that require further study. Of these, the most intriguing is the fact that no quadrupole nor octupole component shows up in the Pantheon catalog. This is essentially due to the fact that this catalog contains virtually no objects in the direction where the $l = 1, 2, 3$ multipole aligns. This also explains why the axisymmetric $\tilde{\eta}$ model calibrated using the CF3g and CF3sn data sets, and which incorporates quadrupolar and octupolar contributions, also effectively explains the purely dipolar anisotropies characteristic of the Pantheon data sample. It would therefore be very useful to look for SN candidates in this critical region of the sky if one wants to advance towards a more solid understanding of the anisotropies in the local expansion rate.

To conclude, the key objective of this chapter has been to show, as a proof-of-concept, the potential power of a new observable, the expansion rate fluctuation field, both to study the structure of the anisotropies in the redshift-distance relation. In the next chapter I will present follow-up results, obtained using the updated and expanded data sets Cosmicflows-4 [72], and Pantheon+ [159].

Chapter 4

The expansion rate fluctuation field in Cosmicflows-4 and Pantheon+

In the previous chapter, I explored the anisotropy of the local universe by estimating the expansion rate fluctuation field and its multipoles using the CF3 and Pantheon samples. I compared various analyses methods introduced in Chapter 2 and assessed their consistency, laying a solid foundation for deeper investigation which is attempted in this chapter.

A major result of Chapter 3 is the existence of an axial symmetric anisotropy in all the multipoles ℓ investigated, which persists up to $150\,h^{-1}$ Mpc, highlighting the necessity to expand our analysis to richer and deeper samples. The newly released datasets, Cosmicflows-4 and Pantheon+, present a valuable opportunity to double the explored domain to approximately $300\,h^{-1}$ Mpc.

This upper boundary extends beyond the Shapley attractor, allowing the survey of an additional large-scale cosmic fluctuation: an underdensity referred to as the gravitational repeller by [104]. If no other significant mass fluctuations exist beyond these structures, the polarity of the multipoles in the expansion rate fluctuations should reverse. This would result in a globally vanishing average of the expansion rate fluctuations over the larger volume. Such an outcome is expected if the cosmological principle begins to hold at these scales. There is additional support for this conclusion within the standard model. If peculiar velocities maintain the same amplitude at large distances as they do in the local universe, the relative perturbation imprinted on the redshift becomes negligible with increasing distance. It is thus interesting to explore whether the different multipoles of the expansion rate field align with the expectations of the standard model.

A richer sample also provides the opportunity to split it into independent subsamples based on galaxy morphology. This enables us to estimate the expansion rate field using different tracers, specifically early-type and late-type galaxies. Since each subsample is likely affected by independent errors and systematics, this provides a valuable method to test the consistency and robustness of the estimated expansion rate fluctuation field, η, which should clearly remain the same regardless of the tracer used.

This chapter also introduces a technical innovation in the analysis pipeline. Specifically, it addresses how we assess whether the η field exhibits axial symmetry and the optimal method for estimating its multipolar coefficients through expansion on a Legendre polynomial basis.

In the first section 4.1 of this chapter, I will present the samples used for the analysis. In section 4.2, I will determine the multipoles of the expansion rate fluctuation field η,

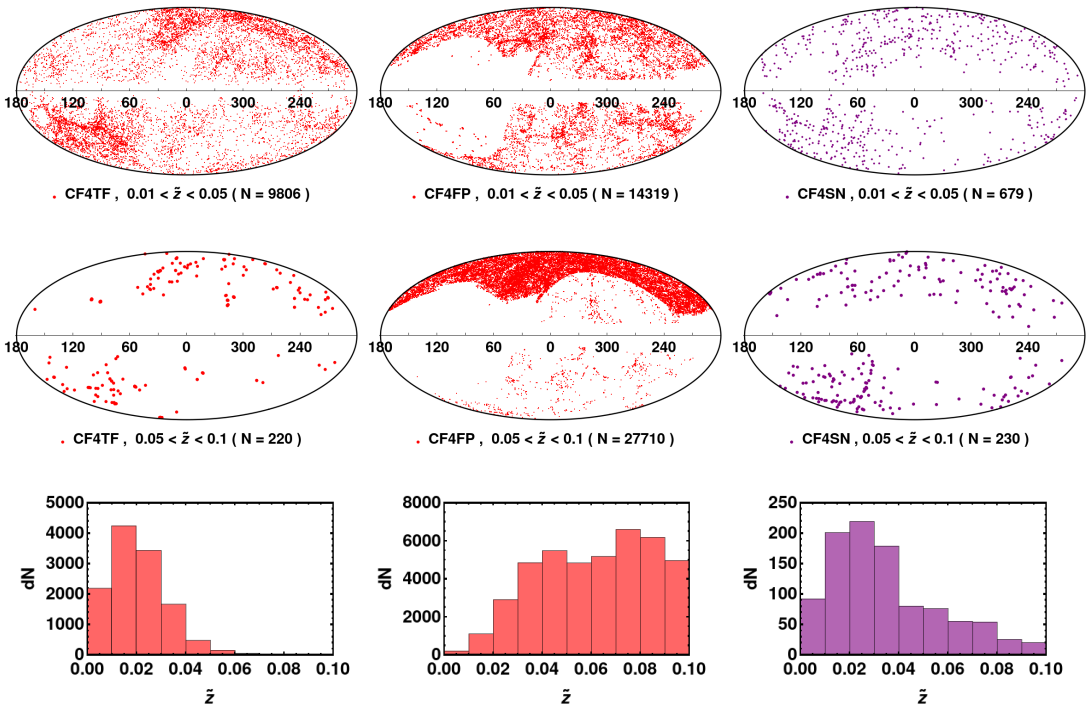


Figure 4.1: Mollweide projection, in galactic coordinates, of the distribution of CF4TF, CF4FP, and CF4SN, with histograms of the number counts as a function of redshift

investigate their robustness, and check their consistency with standard model predictions. Conclusions are drawn in section 4.3.

4.1 Data

4.1.1 Cosmicflows-4 sample

The Cosmicflows-4 (CF4) catalog [72] is comprised of 55874 nearby galaxies ($z \leq 0.1$) for which redshift-independent distances are inferred using complementary and independent methods. In particular, the catalog contains 1004 galaxies hosting a SN Ia (Fig. 4.1) for which the distance modulus is inferred using the standard candle method. There are 12221 galaxies whose distance is determined using the Tully-Fisher relation, and 42221 galaxies whose distance is determined using the Fundamental Plane method (see section 1.5.1). They will respectively be referred to as CF4SN, CF4TF and CF4FP. The corresponding errors in the distance modulus are ~ 0.15, ~ 0.4 and ~ 0.5 respectively (or relative error in the luminosity distance $\sim 7\%$, $\sim 18\%$ and $\sim 23\%$). As with CF3, distances in CF4 are also obtained through other methods, including SBF and TRGB (see section 1.5.1), though the number of galaxies measured by these methods is minor. When a distance is measured using multiple methods, the average of these measurements is calculated to determine the distance modulus, weighted by the uncertainties associated with each measurement.

In Figure 4.1, I present the sky coverage of each individual sample in galactic coordinates in two different redshift ranges, along with the measured redshift distributions of the source number counts. This figure shows that CF4TF and CF4SN are mainly found at redshift $\tilde{z} < 0.05$. In the deeper redshift shell, $0.05 < \tilde{z} < 0.1$, the sample is dominated

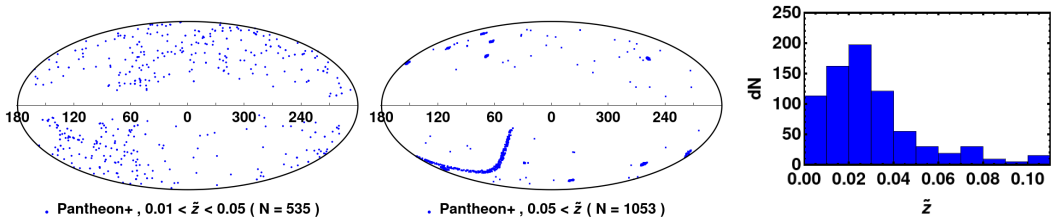


Figure 4.2: Mollweide projection, in galactic coordinates, of the distribution of Pantheon+, with a histogram of the number counts as a function of redshift up to $\tilde{z} = 0.1$.

by early type objects, most of which are distributed in the northern hemisphere.

Additionally, to assess the robustness of the results, I utilize the CF4-CF3 dataset.This dataset consists of CF4 objects after removing those that are common with CF3 (based on the PGC identifier[1]). This sample includes approximately 12400 objects in the redshift range $0.01 < \tilde{z} < 0.05$ with 58% belonging to CF4FP, 39% to CF4TF, and 3% to CF4SN. I note that around 2000 objects in CF3 are not included in CF4 according to the PGC.

Given its density, I can split the CF4 sample according to redshift. I impose a lower redshift cut at $\tilde{z} = 0.01$ because, as will be clarified in Chapter 7 when we interpret the results from this chapter using the cosmographic covariant approach, the fluid approximation for describing discrete datasets as a continuous field breaks down below this threshold. In the next sections, I will use the following designations to avoid repetition: CF4 to indicate objects in the redshift range $0.01 < \tilde{z} < 0.1$, CF4a for $0.01 < \tilde{z} < 0.03$, CF4b for $0.03 < \tilde{z} < 0.05$, and CF4c for $0.05 < \tilde{z} < 0.1$.

For this analysis, I use the Chauvenet's criterion to exclude 8 outliers from the analysis (the PGC numbers of these objects are 5037, 10302, 12384, 31586, 32512, 43423, 53805, and 59808). Their distance moduli deviate by more than 5σ from predictions based on the standard model of cosmology or the more general covariant cosmographic model (see Chapter 7). A large number of high-σ deviating objects is not statistically expected if the distance modulus follows Gaussian statistics, as we assume here.

4.1.2 Pantheon+ sample

The Pantheon+ SN Ia compilation [159] contains 1701 objects in the range $0.001 < z < 2.26$. As CF4, I excluded objects with $z < 0.01$ and limited the sample to $z < 0.1$ so to allow proper comparison with CF4. This results in a dataset containing 695 objects. Figure 4.2 shows their sky and redshift distributions. Compared to the older Pantheon catalog, this compilation features an increased number of objects, with around 80% of the new measurements at low redshift ($z \lesssim 0.1$), where I focus in this study.

Since the η field is sensitive only to the fluctuating component of the Hubble diagram rather than its monopole, its amplitude does not depend on the overall calibration of distances. This allows me to exclude Cepheids from the analysis, simplifying the statistical treatment. Indeed, I do not need to estimate the absolute magnitude of the SNe Ia. Instead, I can use either the SNe Ia magnitudes directly or the calibrated distance moduli from the Pantheon+ sample, both of which will yield the same results presented in the next section.

[1]The PGC identifier refers to the unique name assigned to each galaxy in the Principal Galaxies Catalogue [160].

In accordance with the notation adopted in Chapter 3, the redshift and the expansion rate fluctuation field expressed in the CMB frame are denoted with an overtilde.

4.2 Results

In Chapter 3, I explored two methods for performing the multipolar expansion of $\tilde{\eta}$: one based on the HEALPix algorithm and the other on a maximum likelihood approach (see sections 2.2.1 and 2.2.2, respectively). Since both methods yielded consistent results, I will reconstruct the η multipoles for CF4 and Pantheon+ using only the fitting technique. This approach minimizes bias from pixelization, simplifies the analysis, and provides results with the least error. Furthermore, this method has been shown to be unbiased in Chapter 2, even when the distribution of sources is not isotropic on the sky, as long as the signal does not extend beyond a certain $\ell_{\rm max}$ (see discussion in section 2.2.2).

First, for illustrative purposes, the upper part of Figure 4.3 shows the field $\tilde{\eta}$ pixelized over the sky, along with the corresponding signal-to-noise ratio for each pixel (as described in 2.2.1) for each sample: CF4, CF4a, CF4b, and CF4c, respectively. The number of pixels is 48, except for CF4c, where I use 12 pixels due to the highly anisotropic distribution of measurements across the sky. This results in larger empty regions than the pixel size when using 48 pixels.

The maps of $\tilde{\eta}$ show a maximum around the same direction $(l, b) \sim (300, 0)$. While the signal-to-noise ratio in that direction is very high in the first shell (CF4a), it weakens at higher shells. Despite this, the behavior of the field $\tilde{\eta}$ shows a systematically similar trend across these shells, which confirms that the fluctuations in the field are not random.

In the lower part of Figure 4.3, I represent the multipolar components of the η field estimated using the CF4, CF4a, CF4b and CF4c samples, each row from top to bottom corresponds respectively to dipole, quadrupole octupole and hexadecapole. One can see that a strong dipolar fluctuation is detected in each redshift shell. Its amplitude, approximately 2.5×10^{-2}, and direction $(l, b) \sim (290, 0)$ are compatible in the two lowest redshift intervals (CF4a and CF4b). In the last redshift bin (CF4c), the amplitude and its SNR decrease, while the direction remains roughly the same. Using Monte Carlo simulations, I conclude that it is risky to reject the hypothesis of a non-zero dipole. The p-value (see section 3.2) is fairly low, even in the deepest redshift shell ($p = 1\%$).

The amplitude of the quadrupole is approximately 2×10^{-2} for CF4a. It decreases in the intermediate redshift shell and then increases again in the last shell (see Figure 4.3). The direction of the quadrupole's maximum is moving around the direction of the dipole across the redshift. It points in the direction $(l, b) \approx (330, 27)$ for CF4a, $(304, 2)$ for CF4b and $(287, 10)$ for CF4c. Using Monte Carlo simulations, I conclude that, similarly to the dipole, also the existence of the quadrupole cannot be rejected for all the samples (CF4, CF4a, and CF4c). The probability of a fake signal 1% for CF4c, and even lower for CF4 and CF4a. For CF4b, the p-value is around 33%, indicating that the signal is consistent with being random, as expected since its amplitude is dominated by the noise.

Regarding the octupole, its signal remains relatively consistent across the probed redshift range, with a local maximum observed in the direction of the dipole. The signal associated with the octupole is statistically significant for CF4 and CF4a, resulting in a very low probability of it being a false positive (the p-value is less than 0.1%). However, for the other samples, the measurements are inconclusive, with p-values around 13% for CF4b and 40% for CF4c, respectively. Similarly, the hexadecapole signal is statistically significant only for CF4 and CF4a (with a p-value of less than 0.1%), while it is dominated

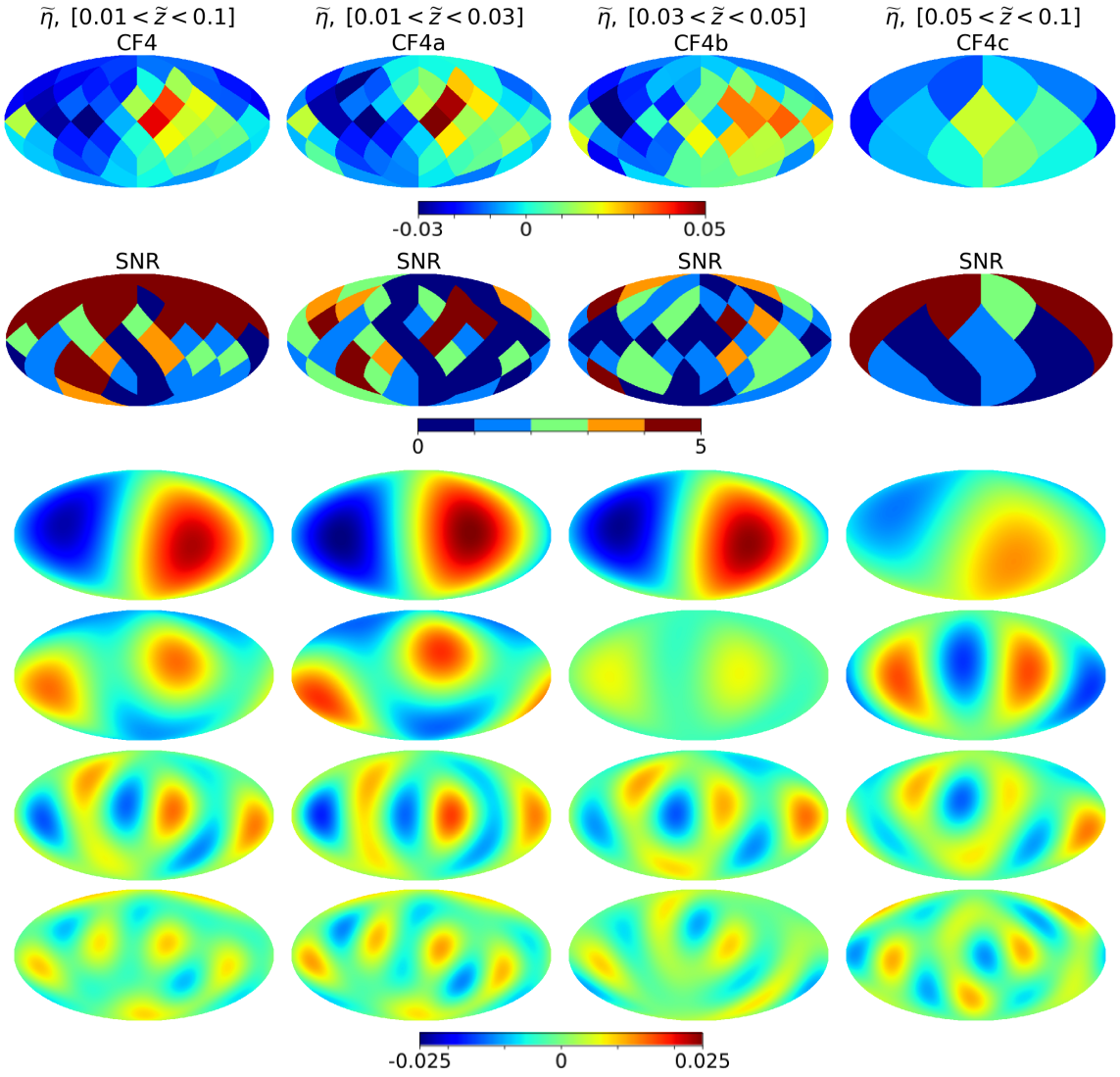


Figure 4.3: From left to right, each column corresponds to CF4 ($0.01 < \tilde{z} < 0.1$), CF4a ($0.01 < \tilde{z} < 0.03$), CF4b ($0.03 < \tilde{z} < 0.05$) and CF4c ($0.05 < \tilde{z} < 0.1$). *Top:* Pixelized maps of the fluctuation field $\tilde{\eta}$. *Middle:* SNR of the fluctuation field. *Bottom:* Representation of the multipolar decomposition of $\tilde{\eta}$ each row corresponds from top to bottom to the dipole, quadrupole, octupole and hexadecapole.

by noise in the other samples.

To compare with the results from CF3, I combine CF4a and CF4b, which corresponds to a single sample covering the redshift range $0.01 < \tilde{z} < 0.05$. The power spectrum yields $\hat{C}_1 = 8.3 \pm 0.9$, $\hat{C}_2 = 0.9 \pm 0.2$, $\hat{C}_3 = 0.3 \pm 0.1$, and $\hat{C}_4 = 0.3 \pm 0.1$ for each multipole, respectively, with strong signals indicated by the low p-values (less than 0.1% for each multipole ℓ). These values can be compared with the results from CF3 presented in Table 3.4, where I used the same Maximum Likelihood method to estimate the multipoles. The quadrupoles are highly consistent, while the octupole is fairly consistent (up to approximately 1.4σ).

Regarding the dipole in CF4, it is higher by about 2.5σ. Specifically, the dipole in the first redshift shell ($0.01 < \tilde{z} < 0.03$) is consistent between CF3 and CF4. However, for the intermediate shell ($0.03 < \tilde{z} < 0.05$), CF4 exhibits a stronger dipole of (8.0 ± 1.8) compared to CF3.

Another way to ensure the robustness of the estimates for the higher-order multipoles in the fluctuation field $\tilde{\eta}$ is to assess any effects induced by the chosen redshift binning strategy. If we assume that there are no fluctuations in the expansion rate, but the CMB observer is boosted with respect to local matter frame, then the field $\tilde{\eta}$ will only have a dipole signal approximately proportional to $1/\tilde{z}$ as will be shown in the next chapter (see eq. (5.55)). As a result, because of the inhomogeneity of the distribution and the thickness of the redshift shells, we might be measuring fake higher order multipoles.

Therefore, I simulate a model with only a dipole in $\tilde{\eta}$, oriented in the direction of the dipole of each shell and proportional to $1/\tilde{z}$ with an amplitude corresponding to the observer's relative velocity of 400 km/s, and then use 1000 Monte Carlo realizations to find the p-value for $\ell > 1$. The multipoles for the entire sample (CF4) and the first shell (CF4a) remain significant. For the second shell, however, all higher multipoles beyond the dipole appear weak. For the third shell, the quadrupole remains strong. In conclusion, this test does not exclude any additional multipoles. It is worth noticing that when considering the $\ell = 5$ multipole, its p-value within the constant velocity model is relatively high, even for the strongest shell ($0.01 < \tilde{z} < 0.1$), reaching 10%. This indicates that it is susceptible to being faked. Therefore, this justifies truncating the analysis at $\ell_{\rm max} = 4$.

Finally one can wonder whether the signal that I measured in each redshift shell is compatible with the ΛCDM prediction. Indeed as shown in section 2.3, it is possible to predict the expected variance of the multipolar decomposition of $\tilde{\eta}$ within the standard ΛCDM model. This quantity depends on the matter power spectrum which is sourcing the velocity field felt by galaxies. When using the power spectrum at the average redshift of the objects in each shell, the p-value of the measured multipoles in the standard model calculated as described in section 3.2.4 is approximately 18%, 48%, 90%, 74% for $\ell = 1$ to 4 respectively for CF4a. This indicates that the measured multipoles are consistent with the standard model. Instead, when considering the intermediate redshift shell (CF4b), the probability is approximately 0.01%, 89%, 66%, 52%, revealing a significant tension between the expected dipole and the observed one. In the deepest redshift shell (CF4c), the probabilities are approximately (2%, 3.3%, 36%, 22%), indicating that the dipole tension persists. Additionally, now also the quadrupole amplitude shows some disagreement with the predictions of the standard model.

In [89], the authors measured the bulk velocity up to a distance of $200\,h^{-1}$ Mpc using CF4 and found $v_b = 419 \pm 36$ km/s in the direction $(l, b) = (298 \pm 5, -8 \pm 4)$. This direction is consistent with the orientation of the dipole found in this work. Additionally, confirming the tension in the dipole presented here, they noted that this result is in

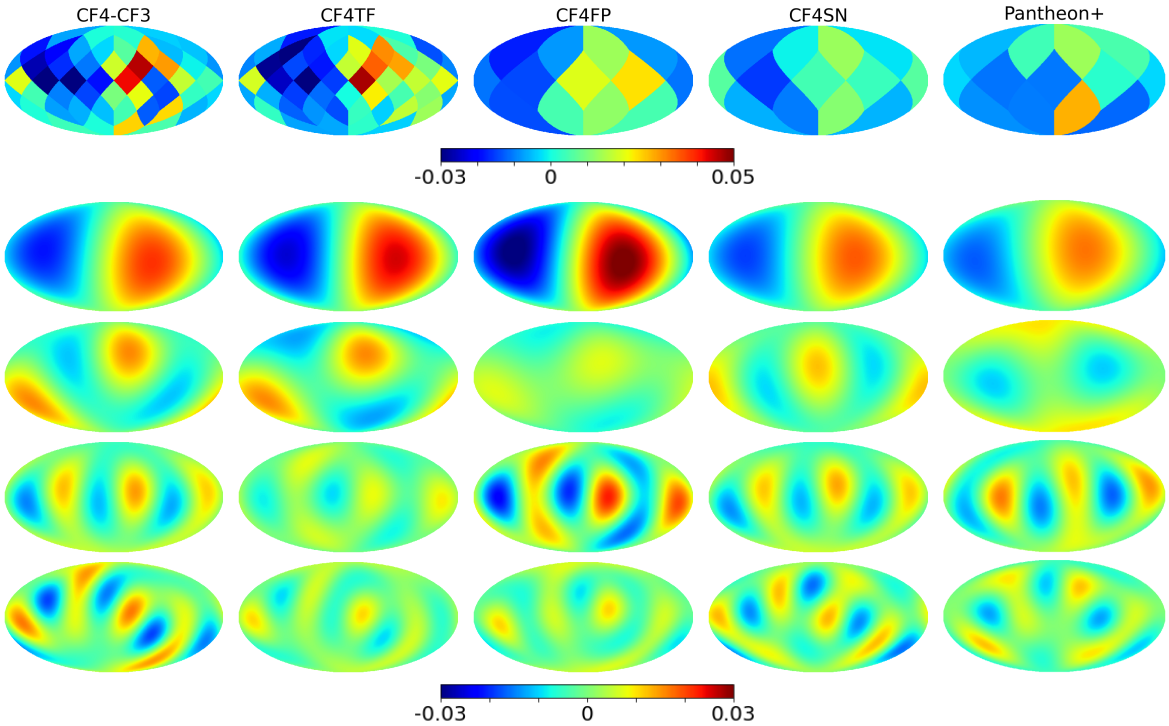


Figure 4.4: The maps of $\tilde{\eta}$ for different samples, in the range $0.01 < \tilde{z} < 0.05$. The multipoles that have p-value $< 5\%$ are $(\ell = 1, 2, 4)$ $(\ell = 1, 2)$ $(\ell = 1, 3)$ $(\ell = 1)$ $(\ell = 1)$

tension with the predicted value in the standard model, reporting a p-value of 2×10^{-6}. However, after reanalyzing the data, [90] reported a probability of 0.11%, which, while higher, remains notably low.

As discussed in section 4.1, most of the measurements for CF4c are obtained using the Fundamental Plane distance indicator (see Figure 4.1), so it is difficult to compare the results from different tracers at that redshift ($\tilde{z} > 0.05$). Notwithstanding I find that the quadrupole signal estimated in this shell using individual distance indicators alone is weak and statistically not significant, only their combination yields a significant signal.

Therefore, it is interesting to compare the $\tilde{\eta}$ signals inferred by using different distance indicators in the range $0.01 < \tilde{z} < 0.05$. The corresponding pixelized $\tilde{\eta}$ maps and multipolar decompositions are shown in Figure 4.4. This comparison will help assess the consistency of the results from these indicators at a redshift where they are more effective ($\tilde{z} < 0.05$), which provides confidence in their reliability at higher redshifts ($\tilde{z} > 0.05$), where each sample alone performs less effectively.

All samples exhibit strong dipoles with low p-values (below 5%), all oriented in the same direction. The dipole in CF4FP is the strongest, with an amplitude of approximately 3×10^{-2}, while in CF4SN and Pantheon+, it is the weakest, with an amplitude of around 1.7×10^{-2}.

The quadrupole is notably strong with low p-values only for CF4-CF3 and CF4TF. Although the quadrupole for CF4FP and CF4SN are weak and statistically non-significant, each has a maximum that is similar in direction to the maximum of the quadrupole found in CF4TF. The octupole is only significant in CF4FP, with an amplitude of $\sim 2 \times 10^{-2}$, and its maximum is aligned with the dipole direction. The octupole in CF4TF is weak but shares a similar structure with CF4FP. For the hexadecapole, it is significant only for

CF4-CF3, with an amplitude of $\sim 2 \times 10^{-2}$.

The consistency between the results of the different samples at $\tilde{z} < 0.05$ is visually quite clear in Figure 4.4. This similarity suggests that all samples provide complementary insights into the underlying structure of the quadrupole and octupole. Such agreement enhances our confidence in the robustness of the results at higher redshifts ($\tilde{z} > 0.05$).

4.2.1 Axial symmetry

Since at least the first three multipoles have a maximum in almost the same direction one might wonder whether the signal is indeed axially symmetric as suggested by the results of CF4 in Chapter 3. In such case the spherical harmonic decomposition of the fluctuation field $\tilde{\eta}$ would have the following particular structure

$$\tilde{\eta}_{\ell m} = \frac{4\pi}{2\ell + 1} \tilde{\eta}_\ell Y_{\ell m}(\boldsymbol{n}_a) \tag{4.1}$$

where $\boldsymbol{n}_a$ is a unit vector in the direction of the axis of symmetry and $\tilde{\eta}_\ell$ is the unique number specifying the multipolar decomposition (the Legendre coefficient) at a given order ℓ. As mentioned in section 3.2.1, if the polar axis of the spherical coordinate system is aligned with the axis of symmetry $\boldsymbol{n}_a$ then all the $\tilde{\eta}_{\ell m}$ vanish except for $m = 0$ and $\tilde{\eta}_{\ell 0} = [4\pi/(2\ell + 1)]^{1/2} \tilde{\eta}_\ell$.

The lower panel of Figure 4.5 shows the coefficients $\tilde{\eta}_{\ell m}$ for CF4a, CF4b and CF4c. For each multipole, I found the best axis of symmetry by fitting the relation (4.1) and fix that axis to be the z-axis. These directions are shown in the upper panel of Figure 4.5. For the quadrupole of the deepest redshift shell and the octupole of the last two shells, the probability distribution of the direction $\boldsymbol{n}_a$ has many local maxima. There is however always one maximum near the direction of the dipole, and this is what I chose.

As shown in Figure 4.5, the dipole is by definition, axially symmetric. However, it is noteworthy that its direction remains very stable across redshifts. The quadrupole and octupole also exhibit compatibility with axial symmetry, maintaining stable directions in redshift. The coefficients $\tilde{\eta}_{20}$ and $\tilde{\eta}_{30}$ are consistently different from zero (and positive, indicating that the axis of symmetry aligns with the maximum of each multipole) for all shells, while the other coefficients (with $m \neq 0$) do not show this behavior. Furthermore, Figure 4.5 shows that, most of the coefficients with $m \neq 0$ and significant amplitudes fluctuate between positive and negative values at different redshifts. This indicates that any deviations from axial symmetry average to zero over the entire volume under study.

These results support the idea of assuming an overall axial symmetry as a good model description of the local universe data. The "global axis of symmetry" – for all of the multipoles – is assumed unchanged for all of the redshift shells and its orientation, $(l, b) = (299, 5)$, is chosen as the the direction that gives the minimum χ^2 when fitting the covariant cosmographic model as will be discussed in the chapter 7.

To further test the assumption of axial symmetry, Figure 4.6 shows the minimum χ^2 statistic obtained by fitting the η signal reconstructed from the CF4 sample in the redshift range $0.01 < \tilde{z} < 0.1$ either with the full spherical harmonic model or with the axially symmetric multipoles as models. As illustrated, the axially symmetric model performs well despite having significantly fewer degrees of freedom. For $\ell_{\max} = 4$, the degrees of freedom decrease from $(\ell_{\max} + 1)^2 = 25$ to $\ell_{\max} + 1 = 5$.

The direction $(l, b) = (299, 5)$ that I chose as the axis of symmetry is consistent with the direction of the bulk velocity for Pantheon+SH0ES as reported by [161] and [162] (using

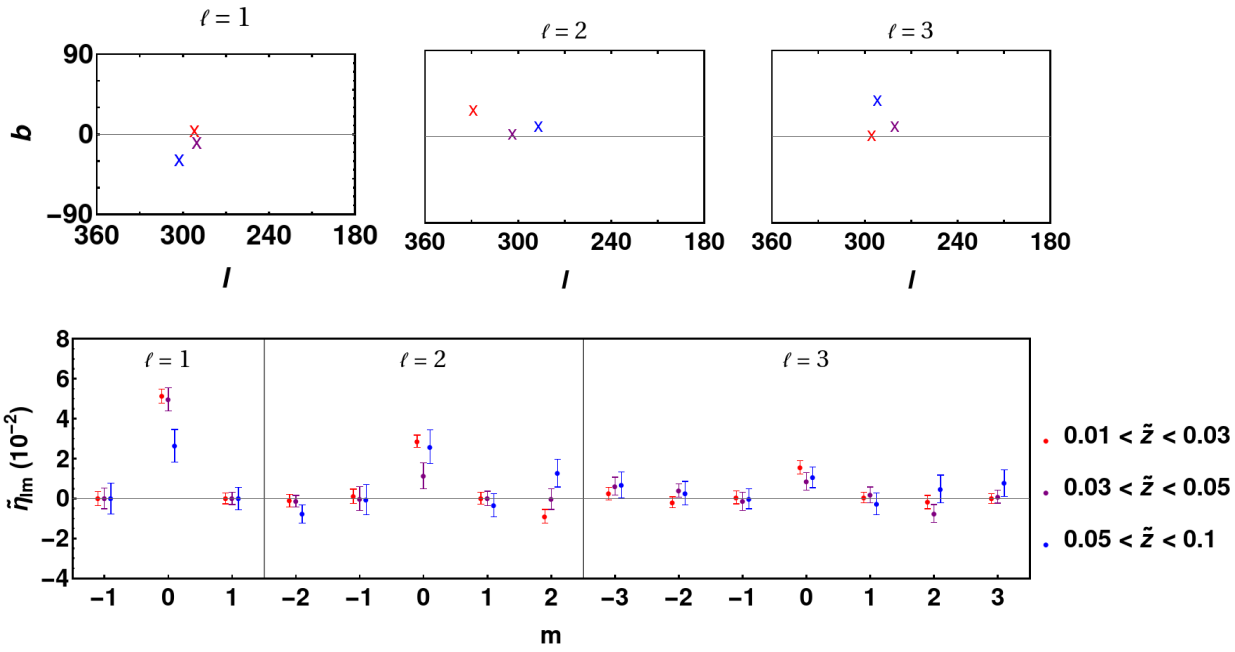


Figure 4.5: The coefficients $\tilde{\eta}_{\ell m}$ for CF4 at different shells in redshift ($0.01 < \tilde{z} < 0.03$, $0.03 < \tilde{z} < 0.05$ and $0.05 < \tilde{z} < 0.1$). For each multipole, I found the best axis of symmetry by fitting the relation (4.1) and fix that axis to be the z-axis. These directions are shown in the upper panel.

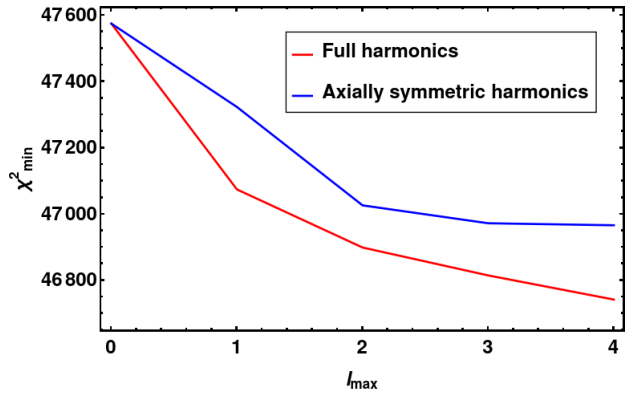


Figure 4.6: Minimum χ^2 obtained by fitting the η signal reconstructed from the CF4 sample in the redshift range $0.01 < \tilde{z} < 0.1$ either with the full spherical harmonic model (red curve) or with the axially symmetric multipoles (blue curve) as models. The direction of the axis of symmetry is $(l, b) = (299, 5)$.

different ranges in redshift). It also aligns with the direction of the bulk velocity from [163] using Cosmicflows-2, which extends to $z = 0.1$ but has a depth around $z = 0.01$ [164]. Additionally, it corresponds with the direction of the bulk velocity measured in [165], which employed the Revised Flat Galaxy Catalogue (RFGC).

Moreover, the direction I suggest for the axis of symmetry is around 2.5σ far from the direction of the maximum of the quadrupole of the peculiar velocity field for the total Pantheon+ sample by [166]. Those authors found that the maximum of the quadrupole is aligned ($\approx 1\sigma$) with the bulk velocity (dipole). My chosen direction is also consistent with the direction of the bulk velocity of [167] and the direction of the maximum of the quadrupole using a compilation "COMPOSITE" (with a characteristic depth around 50 Mpc) which is in general included in CF4.

In [104], the authors studied the structure of the local universe ($z \lesssim 0.05$) using Cosmicflows-2 sample. They found the maximum of the quadrupole is dominated by Shapley supercluster $(312, 31)$ at around $z \approx 0.048$, and the dipole (or the bulk velocity) is dominated by the repeller (the repeller at $(93, -18)$ around $z \approx 0.053$, and the opposite direction is $(273, 18)$. The chosen direction of the axis of symmetry here is in the region between Shapley supercluster and the opposite of the repeller.

If the Shapley supercluster is the dominant structure in the region, the multipoles in the deepest redshift shell ($0.05 < \tilde{z} < 0.1$) should reverse direction and their amplitude should decay as will be shown, using a theoretical model, in Chapter 6 [122]. Moreover, Figures 4.3 and 4.5 show that the structure of the dipole, quadrupole, and octupole components (both in amplitude and orientation) remains consistent in the deepest redshift shell, which surveys the region beyond the Shapley Supercluster. This provides strong evidence for the existence of a coherent, large-scale structure beyond $z \approx 0.05$, within which the local volume is embedded.

Fitting axially symmetric multipoles

In this chapter, instead of estimating the Legendre coefficient by means of eq. (3.2), I use a maximum likelihood technique which is similar to that adopted for estimating the full spherical harmonic coefficients in section 2.2.2. However, in this specific case, the size of the vector $\boldsymbol{a}$ which contains the Legendre coefficients is $(\ell_{\rm max} + 1)$. Moreover, I need to replace the matrix $\boldsymbol{Y}$ by the matrix $\boldsymbol{P}$ with a size $N_{\rm g} \times (\ell_{\rm max} + 1)$, and whose elements are $\mathcal{P}_{ij} = P_{j-1}(\cos\theta_i)$, where θ_i is the angular separation of the i-th object from the axis of symmetry. Now, the Legendre coefficients $\boldsymbol{a}$ for the field ν can be estimated by eq. (2.34). The monopole is the first element in $\boldsymbol{a}$ ($\mathcal{M} = \hat{a}_0$), and $\hat{a}_\ell = \eta_\ell$ for $\ell > 0$. Finally, the covariance matrix for the resultant multipoles is $\boldsymbol{C} = \boldsymbol{\psi}^{-1}$, where $\boldsymbol{\psi} = \boldsymbol{P}^{\rm T}\boldsymbol{\Psi}\boldsymbol{P}$. As in section, 2.2.2, the matrix $\boldsymbol{\Psi}$ is the precision matrix of the measurements ν.

Similar to what was done with CF3 in Figures 3.7 and 3.8, Figure 4.7 shows the estimated $\tilde{\eta}$ for CF4 as a function of $\cos\theta$ alongside the corresponding modeling with increasing orders of multipoles. It is clear that the fluctuations of $\tilde{\eta}$ are significant, and similar to the results obtained from the analysis of the CF3 dataset (see section 3.2.1). The dipole alone provides a poor fit for the expansion rate fluctuations. Higher multipoles, especially the quadrupole, are necessary. Furthermore, the results obtained from the analysis of the additional redshift slice made accessible by the CF4 dataset ($0.05 < \tilde{z} < 0.1$) are also presented in Figure 4.7 (see the third panel), and similar to the previous redshift shells, the last shell reinforces the need for both the dipole and quadrupole.

Table 4.1 presents the Legendre coefficients of $\tilde{\eta}$ for different redshift shells. Similar to the full harmonic analysis, in the axial symmetry analysis, the dipole remains nearly

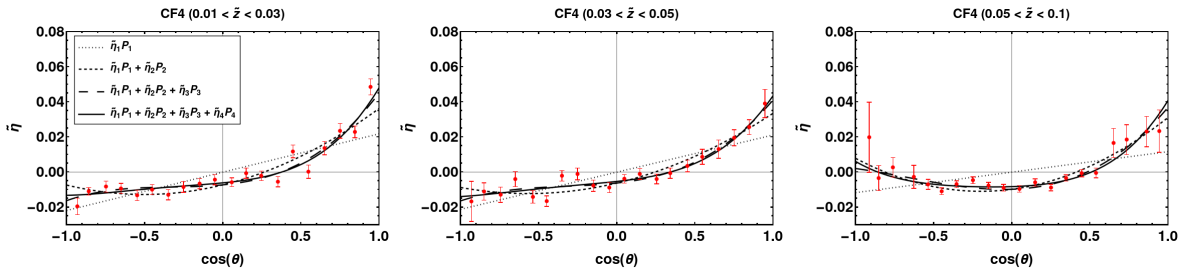


Figure 4.7: η for the CF4 sample, in open spherical sectors of identical width $\Delta \cos\theta = 2/20$ and angular separation θ from the direction $l = 299, b = 5$.

Redshift range	$\tilde{\eta}_1$	$\tilde{\eta}_2$	$\tilde{\eta}_3$	$\tilde{\eta}_4$
$[0.01, 0.03]$	2.2 ± 0.1	1.4 ± 0.2	0.9 ± 0.2	0.3 ± 0.3
$[0.03, 0.05]$	2.1 ± 0.2	1.2 ± 0.3	0.8 ± 0.3	0.2 ± 0.3
$[0.05, 0.1]$	1.2 ± 0.3	2 ± 0.4	0.6 ± 0.3	0.4 ± 0.3

Table 4.1: The Legendre coefficients of the expansion rate fluctuation field $\tilde{\eta}_\ell$ for CF4 at different redshifts.

constant up to $\tilde{z} = 0.05$, but its amplitude is roughly halved in the final redshift shell. In contrast, the quadrupole is larger in the deepest shell analyzed. The octupole shows a decreasing trend, though not significantly, given the error bars. Finally, the axially symmetric hexadecapole is consistent with zero across all three redshift bins.

4.3 Conclusion

In Chapter 3, I have reconstructed the expansion rate fluctuation field and its multipolar expansion using the CF3 and Pantheon samples within distances of $150\,h^{-1}$ Mpc. In this chapter, I provide similar insights using the updated CF4 and Pantheon+ samples, extending the analysis to nearly double the distance, $300\,h^{-1}$ Mpc. These richer datasets has allowed me to estimate the amplitudes of the multipoles up to $\ell_{\rm max} = 4$.

The analysis of the new data over volumes similar to those covered by the older samples allows me to confirm the results presented in Chapter 3. The expansion rate fluctuation field traced by CF4 shows a somewhat stronger dipole, while the quadrupole and octupole for each sample remain consistent.

Overall the observed multipoles display axial symmetry around the same axis found by analysing the CF3 sample, approximately $(l = 299, b = 5)$. Notably I show that an axisymmetric model for the expansion rate fluctuation field effectively reduces the χ^2 with a significantly smaller number of parameters compared to the full harmonic expansion, while also greatly simplifying the numerical analysis and physical interpretation. This axially symmetric configuration is not anymore a tentative evidence, but it is a feature of the local universe now established on a firmer and more robust basis.

Interestingly, a stable alignment of the maxima of the measured multipoles for $\ell \leq 4$ continues to be observed in the new volume accessed by CF4 data, specifically in the redshift range $150h^{-1}$ Mpc $< r < 300h^{-1}$ Mpc. However, only the power in the dipole and quadrupole signals is statistically significant in these regions (the octupole has a signal-to-noise ratio of just 2). Remarkably, the multipoles remain aligned in the same direction

and exhibit structures consistent with those observed in shells at shallower redshifts. When I compare the results to ΛCDM expectations, I find that both the dipole and the quadrupole signals are stronger than predicted by more than 2σ.

These findings confirm the results of other studies using CF4, which also report tensions with the standard model (e.g., [90, 89, 168]). Those model-dependent studies focused on the bulk velocity, showing that even when peculiar velocities are averaged over large spherical volumes centered on the observer the bulk is larger than expected. In our model-independent framework, these results relates to an unexpectedly large dipole in the expansion rate fluctuation field η in the deepest redshift shell investigated. Our analysis extends these findings by demonstrating that the amplitude of the quadrupole, along with its alignment with the dipole, is unaffected by the presence of the Shapley concentration. This suggests the existence of a large-scale, low-probability, perturbation mode comparable in size to the volume being studied, with no indication of its node. In other words, a spherical volume with a diameter of 800 Mpc is not yet representative of the overall universe. At the same time, the expansion rate fluctuation field η reconstructed in each tomographic slice within that volume consistently exhibits the same anisotropic pattern.

Looking ahead, it will be of great interest to apply this analysis strategy to samples with more data, improved distance precision and greater depth, such as those from the Zwicky Transient Facility (ZTF) survey. This could significantly enhance our understanding of the scale at which the "end of greatness" occurs [169], referring to the transition scale to a uniform universe.

Chapter 5

Covariant Cosmography

In 1966, Kristian and Sachs published their seminal paper "Observations in Cosmology" [59], where they critically examined the foundational assumptions of modern cosmology, particularly homogeneity and isotropy. They noted that while these assumptions form the backbone of the standard cosmological model, they are not directly observable in every cosmological context, raising suspicions about their universal applicability. To address this, they introduced a more general formalism that could be applied to arbitrary spacetimes. A key contribution of their work was the expansion of the luminosity distance as a function of redshift in a general spacetime, which allowed for the introduction of covariant cosmographic parameters. These parameters, which depend on the line-of-sight, characterize the local metric structure in the observer's vicinity without assuming homogeneity or isotropy. For example, they show that at first order, the expansion field around the observer is

$$u^i = H^{ij} r^j$$

where u^i is the Cartesian component of the Hubble flow (dr^i/dt), with the observer at the origin (repeated indices are summed). The "generalized" Hubble parameter is expressed as

$$H^{ij} = \theta \delta^{ij} + \sigma^{ij}$$

where θ is the isotropic expansion term, σ^{ij} is a symmetric tensor with zero trace and it represents shearing effects.

Importantly, Kristian and Sachs employed observational data, notably the galaxy catalog of Humason et al. [170], to empirically constrain the first-order coefficients of their expansion. They showed that the shear contribution cannot be larger than about 20% of the expansion term θ. Trendowski [171], by analyzing the same catalog, found that the ratios of the components of σ_{ij} to the monopole, expressed in a coordinate system rotated to make σ_{ij} diagonal were

$$(0.1, 0.03, -0.13)$$

that is reducing the observational limit on deviation from isotropy to about 10%. This early attempt to use actual astronomical observations to test theoretical predictions marked a significant advance in cosmological methods, and their results provided one of the first empirical limits on the deviations from homogeneity.

The ideas presented by Kristian and Sachs were further refined and generalized by Ellis and collaborators [114, 113, 172, 173], who extended the covariant cosmological framework. Ellis, in particular, emphasized the importance of applying general relativity consistently to cosmological observations, thereby incorporating perturbations and

anisotropies in a more rigorous way. Peebles [174] highlighted the significance of this formalism, pointing out that it offers a powerful tool for constraining cosmological perturbations and the effects of shear on the Hubble-Lemaître law, especially in models that allow for deviations from perfect isotropy.

Despite the conceptual breakthroughs of Kristian, Sachs, and Ellis, progress in fully analyzing the covariant structure of the expansion field has been slow. Several factors have contributed to this, including the inherent technical challenges in modeling inhomogeneous spacetimes and the lack of extensive datasets with high-precision measurements of large-scale structure and redshift distributions. While modern cosmology benefits from a wealth of new data the application of these datasets to covariant cosmography remains complex.

However, significant contributions have continued to emerge over the decades, building on the foundations laid by Kristian, Sachs, and Ellis. For example, works such as those by Hasse [175] and Clarkson with Maartens [115, 116] have advanced the theoretical framework by exploring higher-order effects in the luminosity distance-redshift relation, while others, like Umeh in his Ph.D thesis [176], have applied these ideas in the context of relativistic perturbation theory. More recently, efforts by Heinesen [117] and Maartens [50], as well as by Adamek and collaborators [177], have revitalized interest in using general relativistic frameworks to study the effects of inhomogeneities and anisotropies in cosmology.

Additionally, recent observational efforts, such as the analysis of large datasets by Dhawan et al. [178] and Cowell et al. [179], have started to push the boundaries of how cosmological perturbations and anisotropies are constrained empirically. These works demonstrate that while significant technical and observational challenges remain, the tools and datasets required to rigorously analyze the covariant structure of the expansion field are gradually coming into place.

In this chapter, I review the approach of Kristian and Sachs, aiming to formulate a general framework for observational cosmology, and extend it so that it can be applied to a wider range of cosmological models and increasingly precise datasets. Specifically, I discuss the formalism that introduces *covariant cosmographic parameters in the matter frame*, a set of line-of-sight dependent functions that encapsulate key metric information, including the generalized Hubble parameter, deceleration, curvature, jerk, and snap. Then I show how these parameters relate to the metric coefficients $g_{\mu\nu}$, regardless of the chosen line element used to describe cosmic spacetime.

The primary original result I present is an expansion of the (model-independent) expression for the luminosity distance to fourth order in redshift. This leads to an analytical formula that expresses the "snap" in terms of the expansion scalar, the shear, and the Ricci tensors within a general metric $g_{\mu\nu}$. This refinement of the existing formalism enhances the resolution of the model-independent description of the luminosity distance, allowing for improved accuracy in reproducing observational data.

Particular emphasis is placed on quantifying the degrees of freedom associated with each cosmographic parameter. This information is encoded in the spherical harmonic multipoles of each parameter. A thorough analysis is performed, revealing inconsistencies in the literature, which are identified and corrected.

Another original contribution of this section is the clarification and analytical quantification of the observer's motion on the amplitude of the cosmographic parameters. This analysis also helps to explain certain anomalies and inconsistencies previously reported in the literature.

Finally, I establish the relationship between the observable η multipoles and the mul-

tipoles of the covariant cosmographic parameters in the case of axial symmetry. This forms the basis for the data analysis and statistical inference to be conducted in the next chapters of this thesis.

5.1 Cosmography in a general spacetime

The cosmographic parameters in an FLRW spacetime were introduced in section 1.3. These parameters represent a special limiting case of a more general set of functions, known as covariant cosmographic parameters. These functions depend on the observer's line of sight and allow the luminosity distance to be expressed in a model-independent way, without assuming a specific underlying metric for the universe.

In this section, I introduce these covariant cosmographic parameters and derive their relationships with the metric and the 4-velocity of the cosmological matter fluid in general spacetimes.

5.1.1 Null geodesic congruence

Consider the time-like congruence defined by the 4-velocity field u^μ of the cosmic matter distribution. This is what I define as the *matter frame*. Following [50, 122], I assume that the matter distribution is described by a pressureless 'dust' fluid, so that $u^\nu \nabla_\nu u^\mu = 0$. I further assume that it is irrotational, i.e. $\omega_{\mu\nu} = h_{\alpha[\mu} h_{\nu]\beta} \nabla^\alpha u^\beta = 0$, where $h_{\mu\nu} = g_{\mu\nu} + u_\mu u_\nu$ projects into the rest-space of u^μ. A matter observer O, comoving with u^μ, receives information via light rays, which are described by a null geodesic congruence, defined by the affinely parametrized tangent vector p^μ, which is irrotational since it generates the past lightcones [53]. We can decompose it as

$$p^\mu = E(u^\mu - n^\mu) \quad \text{where} \quad E = -p^\mu u_\mu \,, \quad n^\mu n_\mu = 1 \,, \quad n^\mu u_\mu = 0 \,. \tag{5.1}$$

Here E is the photon energy, as measured by O, and n^μ is the unit direction of the incoming light ray. The screen-space projection tensor [180, 53],

$$S^{\mu\nu} = h^{\mu\nu} - n^\mu n^\nu \quad \text{where} \quad S^{\mu\nu} u_\mu = 0 = S^{\mu\nu} n_\mu \,, \tag{5.2}$$

projects into the observer's 2-plane (screen) that is orthogonal to the lightray direction.

Using (5.2), the expansion tensor for the null congruence can be decomposed as

$$\hat{\Theta}_{\mu\nu} \equiv S^\alpha_\nu S^\beta_\mu \, \nabla_\alpha p_\beta = \frac{1}{2} \hat{\Theta} \, S_{\mu\nu} + \hat{\sigma}_{\mu\nu} \,, \tag{5.3}$$

where

$$\hat{\Theta} \equiv S^{\mu\nu} \, \nabla_\mu p_\nu = \nabla_\mu p^\mu \qquad \text{and} \qquad \hat{\sigma}_{\mu\nu} \equiv \hat{\Theta}_{\mu\nu} - \frac{1}{2} \hat{\Theta} \, S_{\mu\nu} \,, \tag{5.4}$$

are the area expansion rate (the trace) and the shear rate (symmetric traceless part) of $\hat{\Theta}_{\mu\nu}$, respectively. For our purpose, we only need the evolution of $\hat{\Theta}$ along the lightrays, which can be derived using the trace of the geodesic deviation equation [180, 181] (see also [182, 183, 184, 53, 185, 186]):

$$p^\mu \nabla_\mu \hat{\Theta} + \frac{1}{2} \hat{\Theta}^2 + \hat{\sigma}_{\mu\nu} \hat{\sigma}^{\mu\nu} = -R_{\mu\nu} p^\mu p^\nu, \tag{5.5}$$

where $R_{\mu\nu}$ is the Ricci tensor.

5.1.2 Angular diameter distance expansion

Consider the angular diameter distance d_A. Assuming that it is differentiable and not multi-valued, one can expand it in terms of the affine parameter λ, where $\mathrm{d}/\mathrm{d}\lambda = p^\mu \nabla_\mu$, around the event of observation o:

$$d_A = d_A|_o + \left.\frac{\mathrm{d}d_A}{\mathrm{d}\lambda}\right|_o \lambda + \frac{1}{2}\left.\frac{\mathrm{d}^2 d_A}{\mathrm{d}\lambda^2}\right|_o \lambda^2 + \frac{1}{6}\left.\frac{\mathrm{d}^3 d_A}{\mathrm{d}\lambda^3}\right|_o \lambda^3 + \frac{1}{24}\left.\frac{\mathrm{d}^4 d_A}{\mathrm{d}\lambda^4}\right|_o \lambda^4 + \mathcal{O}(\lambda^5)\,. \tag{5.6}$$

Clearly $d_A|_o = 0$ and since the spacetime is close to Minkowski near o, one has [50, 117]

$$\left.\frac{\mathrm{d}d_A}{\mathrm{d}\lambda}\right|_o = -E_o\,, \qquad \hat{\sigma}_{\mu\nu}|_o = 0\,. \tag{5.7}$$

Since $\hat{\Theta}$ is the rate of change of the area of the ray bundle, we have $\hat{\Theta} = [\mathrm{d}(\delta A)/\mathrm{d}\lambda]/\delta A$. Then $\mathrm{d}\delta\Omega/\mathrm{d}\lambda = 0$ implies, using the definition (1.25), that

$$\frac{\mathrm{d}d_A}{\mathrm{d}\lambda} = \frac{1}{2} d_A \hat{\Theta}\,. \tag{5.8}$$

Differentiating and using equation (5.5), one finds the focusing equation

$$\frac{\mathrm{d}^2 d_A}{\mathrm{d}\lambda^2} = -\frac{1}{2} d_A \left(\hat{\sigma}_{\mu\nu}\hat{\sigma}^{\mu\nu} + R_{\mu\nu}p^\mu p^\nu\right). \tag{5.9}$$

Therefore $\mathrm{d}^2 d_A/\mathrm{d}\lambda^2 \mathrel{\mathring{=}} 0$, where $\mathrel{\mathring{=}}$ indicates that all the quantities are evaluated at the event of observation o. By differentiating (5.9) and using (5.8), one has

$$\frac{\mathrm{d}^3 d_A}{\mathrm{d}\lambda^3} \mathrel{\mathring{=}} \frac{1}{2} E_o (R_{\mu\nu}p^\mu p^\nu)_o\,. \tag{5.10}$$

A further differentiation leads to

$$\frac{\mathrm{d}^4 d_A}{\mathrm{d}\lambda^4} \mathrel{\mathring{=}} -\frac{\mathrm{d}d_A}{\mathrm{d}\lambda}\, p^\alpha \nabla_\alpha \left(\hat{\sigma}_{\mu\nu}\hat{\sigma}^{\mu\nu} + R_{\mu\nu}p^\mu p^\nu\right) \mathrel{\mathring{=}} E_o p^\mu p^\nu p^\alpha \nabla_\alpha R_{\mu\nu}\,, \tag{5.11}$$

where I used $p^\alpha \nabla_\alpha p^\mu = 0$ and $\hat{\sigma}^{\mu\nu} p^\alpha \nabla_\alpha \hat{\sigma}_{\mu\nu} \mathrel{\mathring{=}} 0$ [by (5.7)]. Substituting these results in (5.6), we have

$$d_A = -E_o\lambda + \frac{1}{12} E_o \left(R_{\mu\nu}p^\mu p^\nu\right)_o \lambda^3 + \frac{1}{24} E_o \left(p^\mu p^\nu p^\alpha \nabla_\alpha R_{\mu\nu}\right)_o \lambda^4 + \mathcal{O}(\hat{\lambda}^5). \tag{5.12}$$

This is consistent with [181] [their eq. (26)].

Following [50, 122], it is useful to use the reverse (past-pointing) and normalised 4-vector

$$K^\mu = \frac{p^\mu}{p^\nu u_\nu}, \tag{5.13}$$

which also removes the E_o factor. This means that the new affine parameter is $\hat{\lambda} = -E_o\lambda$

and $p^\mu \mathrel{\mathring{=}} -E_o K^\mu$. Then (5.12) becomes

$$d_A = \hat{\lambda} - \frac{1}{12}\left(R_{\mu\nu}K^\mu K^\nu\right)_o \hat{\lambda}^3 - \frac{1}{24}\left(K^\mu K^\nu K^\alpha \nabla_\alpha R_{\mu\nu}\right)_o \hat{\lambda}^4 + \mathcal{O}(\hat{\lambda}^5). \tag{5.14}$$

From now on, I drop the hat on the affine parameter for convenience, i.e. $\hat{\lambda} \to \lambda$.

One can Taylor expand the redshift in terms of the null affine parameter by making use of the relation $1 + z = p^\mu u_\mu/(p^\nu u_\nu)_o = K^\mu u_\mu$. Defining the expansion tensor of the matter $\Theta_{\mu\nu} = \nabla_\nu u_\mu$, we have:

$$z = \mathbb{X}^{(1)}_o \lambda + \frac{1}{2}\mathbb{X}^{(2)}_o \lambda^2 + \frac{1}{6}\mathbb{X}^{(3)}_o \lambda^3 + \frac{1}{24}\mathbb{X}^{(4)}_o \lambda^4 + \mathcal{O}(\lambda^5) \tag{5.15}$$

where

$$\mathbb{X}^{(1)} \mathrel{\mathring{=}} K^\mu K^\nu \Theta_{\mu\nu}, \tag{5.16}$$
$$\mathbb{X}^{(2)} \mathrel{\mathring{=}} K^\mu K^\nu K^\alpha \nabla_\mu \Theta_{\nu\alpha}, \tag{5.17}$$
$$\mathbb{X}^{(3)} \mathrel{\mathring{=}} K^\mu K^\nu K^\alpha K^\beta \nabla_\mu \nabla_\nu \Theta_{\alpha\beta} \tag{5.18}$$
$$\mathbb{X}^{(4)} \mathrel{\mathring{=}} K^\mu K^\nu K^\alpha K^\beta K^\rho \nabla_\mu \nabla_\nu \nabla_\alpha \Theta_{\beta\rho}\,. \tag{5.19}$$

I also define

$$\mathbb{Y}^{(1)} = K^\mu K^\nu R_{\mu\nu}\,, \qquad \mathbb{Y}^{(2)} = K^\mu K^\nu K^\alpha \nabla_\mu R_{\nu\alpha}\,. \tag{5.20}$$

Here the expansion tensor of the matter,

$$\Theta_{\mu\nu} = \frac{1}{3}\Theta h_{\mu\nu} + \sigma_{\mu\nu}, \tag{5.21}$$

describes the matter flow-lines in terms of the volume expansion rate Θ and the shear rate $\sigma_{\mu\nu}$. For the interested reader, a deeper explanation of the formalism presented here can be found in [50], which also gives the multipole expansions of $\mathbb{X}^{(1,2)}$ in terms of the matter kinematic parameters. The multipole expansions of $\mathbb{X}^{(3,4)}$ and $\mathbb{Y}^{(2)}$ are presented in Appendix A.

Proceeding with the distance-redshift relation derivation, relation (5.15) can be inverted by using the Lagrange inversion theorem, which gives

$$\begin{aligned}\lambda = \frac{1}{\mathbb{X}^{(1)}_o} z - \frac{\mathbb{X}^{(2)}_o}{2\left(\mathbb{X}^{(1)}_o\right)^3} z^2 + \frac{3\left(\mathbb{X}^{(2)}_o\right)^2 - \mathbb{X}^{(1)}_o \mathbb{X}^{(3)}_o}{6\left(\mathbb{X}^{(1)}_o\right)^5} z^3 \\ - \frac{15\left(\mathbb{X}^{(2)}_o\right)^3 - 10\mathbb{X}^{(1)}_o \mathbb{X}^{(2)}_o \mathbb{X}^{(3)}_o + \left(\mathbb{X}^{(1)}_o\right)^2 \mathbb{X}^{(4)}_o}{24\left(\mathbb{X}^{(1)}_o\right)^7} z^4 + \mathcal{O}(z^5)\end{aligned} \tag{5.22}$$

By combining eq. (5.22) with eq. (5.12), I can find the relation between the angular

diameter distance and the redshift,

$$d_A = \frac{1}{\mathbb{X}_o^{(1)}} z - \frac{\mathbb{X}_o^{(2)}}{2\left(\mathbb{X}_o^{(1)}\right)^3} z^2 + \frac{6\left(\mathbb{X}_o^{(2)}\right)^2 - 2\mathbb{X}_o^{(1)}\mathbb{X}_o^{(3)} - \mathbb{Y}_o^{(1)}}{12\left(\mathbb{X}_o^{(1)}\right)^5} z^3 \tag{5.23}$$
$$- \frac{15\left(\mathbb{X}_o^{(2)}\right)^3 - 10\mathbb{X}_o^{(1)}\mathbb{X}_o^{(2)}\mathbb{X}_o^{(3)} + \left(\mathbb{X}_o^{(1)}\right)^2\mathbb{X}_o^{(4)} - 3\mathbb{Y}_o^{(1)}\left(\mathbb{X}_o^{(1)}\right)^2\mathbb{X}_o^{(2)} + 2\left(\mathbb{X}_o^{(1)}\right)^3\mathbb{Y}_o^{(2)}}{24\left(\mathbb{X}_o^{(1)}\right)^7} z^4$$
$$+ \mathcal{O}(z^5)$$

and the inverse

$$z = \mathbb{X}_o^{(1)} d_A + \frac{1}{2}\mathbb{X}_o^{(2)} d_A^2 + \frac{1}{12}\left(2\mathbb{X}_o^{(3)} + \mathbb{Y}_o^{(1)}\mathbb{X}_o^{(1)}\right) d_A^3 + \frac{1}{24}\left(2\mathbb{Y}_o^{(1)}\mathbb{X}_o^{(2)} - \mathbb{Y}_o^{(2)}\mathbb{X}_o^{(1)} + \mathbb{X}_o^{(4)}\right) d_A^4 \,. \tag{5.24}$$

In the form of eq. (1.38), we have:

$$d_A(z,\mathbf{n}) = \frac{z}{\mathbb{H}_o}\Bigg[1 - \frac{1}{2}\left(3 + \mathbb{Q}_o\right) z + \frac{1}{6}\left(11 + 7\mathbb{Q}_o + 3\mathbb{Q}_o^2 + \mathbb{R} - \mathbb{J}_o\right) z^2$$
$$+ \frac{1}{24}\left(-50 - 10\mathbb{R} - \mathbb{Q}_o(46 + 6\mathbb{R} + 39\mathbb{Q}_o + 15\mathbb{Q}_o^2) + \mathbb{J}_o(13 + 10\mathbb{Q}_o) + \mathbb{S}_o\right) z^3\Bigg] \tag{5.25}$$

and

$$d_L(z,\mathbf{n}) = \frac{z}{\mathbb{H}_o}\Bigg[1 + \frac{1}{2}\left(1 - \mathbb{Q}_o\right) z + \frac{1}{6}\left(3\mathbb{Q}_o^2 + \mathbb{Q}_o - 1 + \mathbb{R}_o - \mathbb{J}_o\right) z^2$$
$$+ \frac{1}{24}\left(2 - \mathbb{Q}_o(2 + 15\mathbb{Q}_o + 15\mathbb{Q}_o^2) + 5\mathbb{J}_o(1 + 2\mathbb{Q}_o) - 2\mathbb{R}_o(1 + 3\mathbb{Q}_o) + \mathbb{S}_o\right) z^3\Bigg] + \mathcal{O}(z^5) \,. \tag{5.26}$$

where

$$\mathbb{H} \doteq K^\mu K^\nu \Theta_{\mu\nu} \,, \tag{5.27}$$

$$\mathbb{Q} \doteq -3 + \frac{K^\mu K^\nu K^\alpha \nabla_\alpha \Theta_{\mu\nu}}{\mathbb{H}^2} \,, \tag{5.28}$$

$$\mathbb{R} \doteq 1 + \mathbb{Q} - \frac{K^\mu K^\nu R_{\mu\nu}}{2\mathbb{H}^2} \,, \tag{5.29}$$

$$\mathbb{J} \doteq -10\mathbb{Q} - 15 + \frac{K^\mu K^\nu K^\alpha K^\beta \nabla_\alpha \nabla_\beta \Theta_{\mu\nu}}{\mathbb{H}^3} \,. \tag{5.30}$$

See also [180, 115, 117]. As a byproduct of this analysis, I introduce a new covariant *snap*

parameter defined as [187]

$$\mathbb{S} \triangleq 113 + 17\mathbb{J} + 115\mathbb{Q} + 10\mathbb{Q}^2 - 8\mathbb{R} - \frac{K^\mu K^\nu K^\alpha \nabla_\alpha R_{\mu\nu}}{\mathbb{H}^2} - \frac{K^\alpha K^\beta K^\rho K^\mu K^\nu \nabla_\alpha \nabla_\beta \nabla_\rho \Theta_{\mu\nu}}{\mathbb{H}^4}$$
$$= 129 - \frac{1}{\mathbb{H}^2}\left[123\,\mathbb{X}^{(2)} + \mathbb{Y}^{(2)}\right] + 17\,\frac{\mathbb{X}^{(3)}}{\mathbb{H}^3} + \frac{1}{\mathbb{H}^4}\left[10\,(\mathbb{X}^{(2)})^2 - \mathbb{X}^{(4)}\right]\,. \tag{5.31}$$

The multipoles of the first four covariant cosmographic parameters given in equations (5.27)–(5.30) are known (see [181, 115, 117, 188, 50]). The snap has independent multipoles from $\ell = 0$ to $\ell = 5$. Furthermore, the multipoles of $\mathbb{X}^{(3)}$ and $\mathbb{X}^{(4)}$ are given in Appendix A in terms of the matter kinematic parameters Θ and $\sigma_{\mu\nu}$. The multipoles of $\mathbb{Y}^{(1,2)}$ are also given in Appendix A.

5.2 Degrees of freedom

Expanding the distance-redshift relation to fourth order introduces additional degrees of freedom (d.o.f.). Each independent multipole contributes a total of $2\ell+1$ d.o.f. Table 5.1 summarizes the d.o.f. for each relevant cosmographic parameter under various assumptions. In the general case, without assuming any symmetry, 86 fitting parameters are required to fully reconstruct the functional forms of $\mathbb{H}$, $\mathbb{Q}$, $\mathbb{J}-\mathbb{R}$ and $\mathbb{S}$ for the case of a non-geodesic fluid. Note that the jerk adds 25 d.o.f. and not 36 as given in [117].

Motivated by the results of Chapter 3 and 4 [112], which found observational evidence for the fluctuations of the local universe displaying an axially symmetric configuration, I now determine how this condition reduces the d.o.f. of the covariant cosmographic parameters.

In this case, each multipole contributes one degree of freedom only. If one adds the constraint that the motion of the cosmic fluid elements is geodesic (no 4-acceleration), the total number of degrees of freedom decreases to 17 (see the second column in Table 5.1).

Although the parameters $\mathbb{X}^{(1,2,3,4)}$ have a limited number of multipoles, as shown in appendix A, the covariant cosmographic parameters display more multipoles because of the power of $\mathbb{H}$ appearing in the denominator of the defining equations. These higher multipoles are not new d.o.f. since they can be related to the lower multipoles and they are subdominant – because they are suppressed by a factor proportional to the ratio of the quadrupole to the monopole of $\mathbb{H}$ [122], which is much smaller than 1 as will be shown in Chapter 7 using recent datasets. Here, I present their forms in the case of axial symmetry, after linearizing with respect to $\mathbb{H}_2/\mathbb{H}_0$. [1] For $\mathbb{Q}$:

$$\mathbb{Q}_4 = -\frac{36\,\mathbb{H}_2}{35\,\mathbb{H}_0}\,\mathbb{Q}_2\,, \tag{5.32}$$

$$\mathbb{Q}_5 = -\frac{20\,\mathbb{H}_2}{21\,\mathbb{H}_0}\,\mathbb{Q}_3\,, \tag{5.33}$$

[1] Note that I omit the subscript o from the cosmographic parameters for simplicity. The subscript here denotes the multipole order ℓ as I define in eq. (3.1).

and for $\ell > 5$ the multipoles are second order in $\mathbb{H}_2/\mathbb{H}_0$. For the curvature, I find

$$\mathbb{R}_3 = \mathbb{Q}_3 + \frac{6\,\mathbb{H}_2}{5\,\mathbb{H}_0}(\mathbb{Q}_1 - \mathbb{R}_1)\,, \tag{5.34}$$

$$\mathbb{R}_4 = -\frac{36\,\mathbb{H}_2}{35\,\mathbb{H}_0}\,\mathbb{R}_2\,, \tag{5.35}$$

$$\mathbb{R}_5 = -\frac{20\,\mathbb{H}_2}{21\,\mathbb{H}_0}\,\mathbb{Q}_3\,. \tag{5.36}$$

For $\ell > 5$ the multipoles are second order in $\mathbb{H}_2/\mathbb{H}_0$. For the jerk,

$$\mathbb{J}_5 = -\frac{10\,\mathbb{H}_2}{21\,\mathbb{H}_0}(3\mathbb{J}_3 + 10\mathbb{Q}_3)\,, \tag{5.37}$$

$$\mathbb{J}_6 = -\frac{15\,\mathbb{H}_2}{11\,\mathbb{H}_0}\,\mathbb{J}_4\,. \tag{5.38}$$

For $\ell > 6$ the multipoles are second order in $\mathbb{H}_2/\mathbb{H}_0$. For the snap, the maximum independent multipole is $\ell = 5$, and the higher multipoles can be expressed as

$$\mathbb{S}_6 = \frac{1000\,\mathbb{Q}_3^2}{231} + \frac{5\mathbb{H}_2}{7623\,\mathbb{H}_0}\left(11781\mathbb{J}_4 + 15840\mathbb{Q}_1\mathbb{Q}_3 + 320\mathbb{Q}_3^2 - 2772\mathbb{S}_4\right)\,, \tag{5.39}$$

$$\mathbb{S}_7 = -\frac{252\,\mathbb{H}_2}{143\,\mathbb{H}_0}\,\mathbb{S}_5\,, \tag{5.40}$$

$$\mathbb{S}_8 = -\frac{3200\,\mathbb{H}_2}{429\,\mathbb{H}_0}\,\mathbb{Q}_3^2\,. \tag{5.41}$$

For $\ell > 8$ the multipoles are second order in $\mathbb{H}_2/\mathbb{H}_0$.

According to [189], the degrees of freedom can be further reduced since only a subset of the multipoles of the covariant cosmographic parameters significantly contribute to the signal. For each covariant cosmographic parameter these *dominant* multipoles are the monopole and the $\ell \geq 1$ multipoles containing the maximum number of spatial derivatives in each expansion term. Indeed these gradients boost the amplitude proportionally to $\xi_H^{-1} \equiv R_H/R_s \gg 1$, the ratio between the Hubble horizon scale and the size of the fluctuations in the Hubble diagram [122]. The dominant multipoles are shown in the fourth column of Table 5.1.

Covariant cosmographic parameters	General case (including 4-acceleration) d.o.f	With axial symmetry (and geodesic motion) d.o.f.	Dominant multipoles (approximation) d.o.f
$\mathbb{H}$	9	2	2 ($\ell = 0,\, 2$)
$\mathbb{Q}$	16	4	3 ($\ell = 0,\, 1,\, 3$)
$\mathbb{J} - \mathbb{R}$	25	5	3 ($\ell = 0,\, 2,\, 4$)
$\mathbb{S}$	36	6	4 ($\ell = 0,\, 1,\, 3,\, 5$)
Total	86	17	12

Table 5.1: Degrees of freedom associated with specific covariant cosmographic parameters. The maximum independent multipole is $\ell = 2,\, 3,\, 4,\, 5$ for $\mathbb{H}$, $\mathbb{Q}$, $\mathbb{J} - \mathbb{R}$ and $\mathbb{S}$ respectively.

5.2.1 Boosted observer

As mentioned before, the relation between the distance and the redshift (5.26) holds only for the matter-comoving observer with 4-velocity u^μ (the velocity of the cosmological fluid). Although theoretically clear and computationally advantageous, the this frame is operationally difficult to define. In other words, it is not easy to prescribe an observational procedure for identifying the observer that comoves with the surrounding matter fluid. For boosted observer $\tilde{O}$ with physical velocity $\tilde{\boldsymbol{v}}_o$ with respect to the matter-comoving observer, the redshift and the distance will be different. This is derived in detail in [50]. The redshift of an object in a boosted frame is related to that measured in the matter frame as

$$\tilde{z} = z - \tilde{\boldsymbol{v}}_o \cdot \boldsymbol{n}\,(1+z)\,, \tag{5.42}$$

where I assume that the boosted frame has a physical velocity $\tilde{v}_o \equiv |\tilde{\boldsymbol{v}}|_o \ll 1$ with respect to the matter observer at the event of observation o. Note that at linear order in velocity, $\tilde{\boldsymbol{v}}_o \cdot \boldsymbol{n} \approx \tilde{\boldsymbol{v}}_o \cdot \tilde{\boldsymbol{n}}$ where $\tilde{\boldsymbol{n}}$ defines the line of sight of the boosted observer. The luminosity distance, instead, transforms between different frames as [50, 190, 64]

$$\tilde{d}_L(\tilde{z}, \boldsymbol{n}) = (1 - \tilde{\boldsymbol{v}}_o \cdot \boldsymbol{n})\, d_L(z(\tilde{z}), \boldsymbol{n})\,. \tag{5.43}$$

If we write the luminosity distance in the matter frame as

$$d_L = d_L^{(1)} z + d_L^{(2)} z^2 + d_L^{(3)} z^3 + d_L^{(4)} z^4 + \mathcal{O}(z^5)\,. \tag{5.44}$$

then for the boosted frame,

$$\tilde{d}_L = \tilde{d}_L^{(0)} + \tilde{d}_L^{(1)} \tilde{z} + \tilde{d}_L^{(2)} \tilde{z}^2 + \tilde{d}_L^{(3)} \tilde{z}^3 + \tilde{d}_L^{(4)} \tilde{z}^4 + \mathcal{O}(\tilde{z}^5), \tag{5.45}$$

where

$$\tilde{d}_L^{(0)} = d_L^{(1)} \tilde{\boldsymbol{v}}_o \cdot \boldsymbol{n}\,, \quad \tilde{d}_L^{(1)} = d_L^{(1)} + 2 d_L^{(2)} \tilde{\boldsymbol{v}}_o \cdot \boldsymbol{n}\,, \quad \tilde{d}_L^{(2)} = d_L^{(2)} + \left(d_L^{(2)} + 3 d_L^{(3)}\right) \tilde{\boldsymbol{v}}_o \cdot \boldsymbol{n}\,,$$
$$\tilde{d}_L^{(3)} = d_L^{(3)} + 2(d_L^{(3)} + 2 d_L^{(4)}) \tilde{\boldsymbol{v}}_o \cdot \boldsymbol{n}\,, \quad \tilde{d}_L^{(4)} = d_L^{(4)} + \left(3 d_L^{(4)} + 5 d_L^{(5)}\right) \tilde{\boldsymbol{v}}_o \cdot \boldsymbol{n}\,.$$

In the last equation, $d_L^{(5)}$ appears multiplied by the velocity, but it can be ignored since it will be multiplied by $\tilde{z}^4$, and $\tilde{z}^4 \tilde{v}_o$ is at least in order $\tilde{z}^5$ which is ignored in this expansion.

I emphasize that neither the heliocentric frame nor the frame at rest relative to the Local Group of galaxies represents the rest frame of the matter observer, although the latter provides a closer, albeit misleading, approximation. A full characterization, requiring the establishment of the covariant cosmography framework, will be addressed in section 5.3.1.

5.3 Relation between η an the covariant cosmographic parameters

By the definition of η (2.1), one can write its relation with the covariant cosmographic parameters in matter frame as

$$\eta(z,\boldsymbol{n}) = -\mathcal{M}(z) + \log\mathbb{H}(\boldsymbol{n}) - \frac{1-\mathbb{Q}(\boldsymbol{n})}{2\ln 10}\,z + \frac{7-\mathbb{Q}(\boldsymbol{n})[10+9\mathbb{Q}(\boldsymbol{n})]+4[\mathbb{J}(\boldsymbol{n})-\mathbb{R}(\boldsymbol{n})]}{24\ln 10}\,z^2 \tag{5.46}$$
$$+\frac{1}{24\ln 10}\Big\{-5\mathbb{J}(\boldsymbol{n})[2\mathbb{Q}(\boldsymbol{n})+1]+2[\mathbb{J}(\boldsymbol{n})-\mathbb{R}(\boldsymbol{n})][\mathbb{Q}(\boldsymbol{n})-1]$$
$$+\mathbb{Q}(\boldsymbol{n})\Big[9+2\mathbb{Q}(\boldsymbol{n})[5\mathbb{Q}(\boldsymbol{n})+8]+6\mathbb{R}(\boldsymbol{n})\Big]+2\mathbb{R}(\boldsymbol{n})-5-\mathbb{S}(\boldsymbol{n})\Big\}\,z^3+\mathcal{O}(z^4)\,.$$

There is also a theoretical motivation for decomposing the expansion rate fluctuation field into spherical harmonics. This approach parallels a similar decomposition of the covariant cosmographic parameters, which is of physical significance. Unlike standard functional parameterizations that involve infinite degrees of freedom, the degrees of freedom for each covariant cosmographic parameter are finite and are represented by their multipoles [175, 115, 116, 176, 117, 50]. By fitting a finite set of these multipoles to data, we can fully reconstruct the functional form of the Hubble, Deceleration, Jerk, Curvature, and snap parameters.

Moreover, the multipoles of the covariant cosmographic parameters offer a systematic method to inspect and classify anisotropies in the distance-redshift relationship, helping to identify potential symmetries. Each multipole carries independent information about the geometry of the geodesic congruence, providing powerful guidelines for determining the form of the line element that describes spacetime in our surroundings. The task now is to establish the link between the multipoles of the expansion rate fluctuations η and the multipoles of the covariant cosmographic parameters in an axisymmetric field configuration.

For simplicity, here, I present the relations between the multipoles of η and the dominant multipoles of the cosmographic parameters (see Table 5.1). For the monopole,

$$\mathcal{M}(z) \approx \log\mathbb{H}_0 - \frac{1-\mathbb{Q}_0}{2\ln 10}\,z + \frac{(28\mathbb{J}_0-7\mathbb{Q}_0(9\mathbb{Q}_0+10)-21\mathbb{Q}_1^2-9\mathbb{Q}_3^2-28\mathbb{R}_0+49)}{168\ln 10}\,z^2 \tag{5.47}$$
$$+\frac{1}{504\ln 10}\Big[-21\mathbb{J}_0(8\mathbb{Q}_0+7)+3\mathbb{Q}_0\left(14\mathbb{Q}_0(5\mathbb{Q}_0+8)+70\mathbb{Q}_1^2+30\mathbb{Q}_3^2+28\mathbb{R}_0+63\right)$$
$$+112\mathbb{Q}_1^2+60\mathbb{Q}_3^2+84\mathbb{R}_0-21\mathbb{S}_0-105\Big]\,z^3\,.$$

One would naively expect that only the monopoles of the covariant cosmographic parameters contribute to the amplitude of the normalization term $\mathcal{M}$. This is not the case because the monopole of $\mathbb{Q}^2$ (see eq. (5.46)) is not simply the square of the monopole. Furthermore, the third-order term includes contributions from the product of multiple parameters.

The first multipole of η that in principle does not vanish, unless it is calculated at $z=0$, is the dipole

$$\eta_1(z) \approx \frac{\mathbb{Q}_1}{2\ln 10}\, z - \frac{(9\mathbb{Q}_0+5)\mathbb{Q}_1 z^2}{12\ln 10} - \frac{1}{27720\ln 10}\Big\{ -33\mathbb{Q}_1\Big[280\mathbb{J}_0 + 112\mathbb{J}_2 - 5\left(14\mathbb{Q}_0(15\mathbb{Q}_0+16) + 46\mathbb{Q}_3^2 + 28\mathbb{R}_0 + 63\right)\Big] + 8\mathbb{Q}_3\left(-297\mathbb{J}_2 - 220\mathbb{J}_4 + 135\mathbb{Q}_3^2\right) + 6930\mathbb{Q}_1^3 + 5940\mathbb{Q}_1^2\mathbb{Q}_3 - 1155\mathbb{S}_1\Big\} z^3\,, \tag{5.48}$$

A multipole of η which might be different from zero, even when estimated in the limit $z \to 0$, is the quadrupole. Its dependence on the multipoles of the cosmographic parameters is

$$\eta_2(z) \approx \frac{\mathbb{H}_2}{\mathbb{H}_0\ln 10} + \frac{14\mathbb{J}_2 - 3(\mathbb{Q}_1+\mathbb{Q}_3)(7\mathbb{Q}_1+2\mathbb{Q}_3)}{84\ln 10} z^2 + \frac{1}{504\ln 10}\Big[-21\mathbb{J}_2(8\mathbb{Q}_0+7) + 60\mathbb{Q}_0(\mathbb{Q}_1+\mathbb{Q}_3)(7\mathbb{Q}_1+2\mathbb{Q}_3) + 224\mathbb{Q}_1^2 + 4\mathbb{Q}_3(81\mathbb{Q}_1+20\mathbb{Q}_3)\Big] z^3\,, \tag{5.49}$$

At the observer's position, the quadrupole of η is mainly sourced by the ratio of the first two nonzero multipoles of the covariant Hubble parameter. As the redshift increases, the quadrupole of higher-order cosmographic parameters also contributes to the signal. The relation between the octupole of the expansion rate fluctuation field measured in the matter rest frame and the covariant cosmographic parameters is similar to that displayed by the dipole,

$$\eta_3(z) \approx \frac{\mathbb{Q}_3}{2\ln 10} z - \frac{(9\mathbb{Q}_0+7)\mathbb{Q}_3 z^2}{12\ln 10} + \frac{1}{154440\ln 10}\Big[-6435(\mathbb{Q}_3(8\mathbb{J}_0 - 6\mathbb{Q}_0(5\mathbb{Q}_0+6) - 13) + \mathbb{S}_3) - 3432\mathbb{J}_2(9\mathbb{Q}_1+4\mathbb{Q}_3) - 1040\mathbb{J}_4(22\mathbb{Q}_1+9\mathbb{Q}_3) + 30\left(858\mathbb{Q}_1^3 + 3289\mathbb{Q}_1^2\mathbb{Q}_3 + 1404\mathbb{Q}_1\mathbb{Q}_3^2 + 723\mathbb{Q}_3^3 + 858\mathbb{Q}_3\mathbb{R}_0\right)\Big] z^3\,, \tag{5.50}$$

The hexadecapole

$$\eta_4(z) \approx \frac{154\mathbb{J}_4 - 9\mathbb{Q}_3(44\mathbb{Q}_1+9\mathbb{Q}_3)}{924\ln 10} z^2 + \frac{\Big[12\mathbb{Q}_3(44(5\mathbb{Q}_0+3)\mathbb{Q}_1 + 15(3\mathbb{Q}_0+2)\mathbb{Q}_3) - 77\mathbb{J}_4(8\mathbb{Q}_0+7)\Big]}{1848\ln 10} z^3\,, \tag{5.51}$$

is dominated by the hexadecapole of the Jerk. Finally, the 32-pole multipole ($\ell = 5$)

$$\eta_5(z) \approx \frac{\left\{60\mathbb{Q}_3\left[5\left(26\mathbb{Q}_1^2 + 27\mathbb{Q}_1\mathbb{Q}_3 + 6\mathbb{Q}_3^2\right) - 52\mathbb{J}_2\right] - 40\mathbb{J}_4(91\mathbb{Q}_1 + 36\mathbb{Q}_3) - 819\mathbb{S}_5\right\}}{19656\ln 10} z^3\,, \tag{5.52}$$

is dominated by $\mathbb{S}_5$.

The farther away from the observer the η multipoles are estimated, the larger the contribution to the signal of the higher-order terms in the redshift-distance relation.

5.3.1 The η field for a boosted observer

For any boosted observer, by using equations (5.46), (5.42) and (5.43), the field $\tilde{\eta}$ can be expressed as

$$\begin{aligned}
\tilde{\eta}(\tilde{z}, \boldsymbol{n}) \;\approx\; & \eta(\tilde{z}, \boldsymbol{n}) - \log\left[1 + \frac{\tilde{\boldsymbol{v}}_o \cdot \boldsymbol{n}}{\tilde{z}}(1+\tilde{z})\right] + \mathcal{M}(\tilde{z}) - \tilde{\mathcal{M}}(\tilde{z}) \\
& + \tilde{\boldsymbol{v}}_o \cdot \boldsymbol{n}\left\{\frac{1}{\ln 10} - \frac{1 - \mathbb{Q}(\boldsymbol{n})}{2\ln 10} + \frac{1 - \mathbb{Q}(\boldsymbol{n})[4 + 9\mathbb{Q}(\boldsymbol{n})] + 4[\mathbb{J}(\boldsymbol{n}) - \mathbb{R}(\boldsymbol{n})]}{12\ln 10}\,\tilde{z}\right. \\
& \frac{\tilde{z}^2}{24\ln 10}\Big(\mathbb{Q}(\boldsymbol{n})(-30\mathbb{J}(\boldsymbol{n}) + 6(\mathbb{J}(\boldsymbol{n}) - \mathbb{R}(\boldsymbol{n}))) + 18\mathbb{R}(\boldsymbol{n}) + 7) \\
& -15\mathbb{J}(\boldsymbol{n}) + 2(\mathbb{J}(\boldsymbol{n}) - \mathbb{R}(\boldsymbol{n})) + 30\mathbb{Q}(\boldsymbol{n})^3 + 30\mathbb{Q}(\boldsymbol{n})^2 + 6\mathbb{R}(\boldsymbol{n}) \\
& \left.-3\mathbb{S}(\boldsymbol{n}) - 1\Big)\right\}.
\end{aligned} \tag{5.53}$$

In order to obtain a real output, the logarithm of the second term on the right-hand side must be applied only to positive numbers. This gives the condition $1 + \tilde{\boldsymbol{v}}_o \cdot \boldsymbol{n}(1+\tilde{z})/\tilde{z} > 0$, which implies $\tilde{z} > \tilde{\boldsymbol{v}}_o \cdot \boldsymbol{n}$. It also implies that terms of order $\tilde{z}^2 \times \tilde{v}_o$ can be safely neglected. The above relationship gives the expansion rate fluctuations measured in an boosted frame as a function of the covariant cosmographic parameters. Note, however, that the values of the latter are expressed in the matter frame, which is the most natural choice for cosmological interpretations if no specific symmetry is attributed a priori to the cosmic line element.

If the matter comoving observer observes axial symmetry in the universe, then by symmetry, the dipole of the CMB will be aligned with that axis. Consequently, the CMB observer will also observe this symmetry, as any artificial multipole generated by the relative velocity is axially symmetric around the same axis. This is why I choose the CMB observer rather than the heliocentric observer in this work.

The advantage of estimating the expansion rate fluctuations η in the CMB frame is that, in addition to cosmographic parameters, we can obtain also critical information about the velocity $\boldsymbol{v}_o$ of the matter comoving observer relative to the CMB frame ($\boldsymbol{v}_o = -\tilde{\boldsymbol{v}}_o$). This fact is all the more important if one considers that the estimation of the observer's velocity can be obtained in a completely model-independent manner, without making any assumptions about the metric (FLRW), nor requiring information about the peculiar velocity field of galaxies, the background cosmology or the power spectrum of matter perturbations (for model-dependent approaches, and a discussion of the systematics induced by an improper definition of the background matter rest frame in that type of analysis, see for example [191, 161]).

Note that the velocity $\boldsymbol{v}_o$ of the matter frame relative to the CMB frame should not be confused with the concept of bulk velocity in standard model studies. This bulk velocity characterizes the average of peculiar velocities over volumes in the FLRW background metric. In contrast, the nonperturbative and model-independent approach has no notion of peculiar motions of galaxies [50]. Nevertheless, we can make a comparison with the standard perturbative approach: in section 3.2.2, I show how the standard bulk velocity relates to the multipoles of the expansion rate fluctuation field in the CMB frame.

In order to constrain $\boldsymbol{v}_o$ I proceed as follows. In the limit $v_o \ll z \ll 1$, which well encompasses the range of available data, the relation between the expansion rate fluctuations measured in the matter frame (η) and in the CMB frame ($\tilde{\eta}$) is (cf. eq. (5.53))

$$\tilde{\eta} - \eta \approx -\log\left(1 - V_o \cos\theta\right) + \mathcal{M} - \tilde{\mathcal{M}} \quad \text{where} \quad V_o = \frac{(1+\tilde{z})}{\tilde{z}}\, v_o \,. \tag{5.54}$$

As a consequence, the mapping between the lowest multipoles ($\ell \leq 4$) measured in both frames is fairly well approximated by

$$\begin{aligned} \tilde{\mathcal{M}}(\tilde{z}) &\approx \mathcal{M}(\tilde{z}) + \frac{V_o^2}{6\ln 10}\,, \\ \tilde{\eta}_\ell(\tilde{z}) &\approx \eta_\ell(\tilde{z}) + \frac{V_o}{\ln 10}\left[\delta^K_{1\ell} + \frac{V_o}{3}\delta^K_{2\ell} + \frac{V_o^2}{15}\left(3\delta^K_{1\ell} + 2\delta^K_{3\ell}\right)\right], \end{aligned} \tag{5.55}$$

where $\delta^K_{\ell\ell'}$ is the Kronecker delta. The difference between the full $\tilde{\eta}_\ell$ and the approximated one is less than 10% of the typical error of $\tilde{\eta}_\ell$. Although each multipole of $\tilde{\eta}$ shows a specific dependence on v_o, in practice, i.e. in the redshift range where data are available for analysis ($z > 0.01$) [112], the motion of the observer has a measurable effect only on the dipole $\tilde{\eta}_1$. As eq. (5.55) shows, $\mathcal{M}$, $\tilde{\eta}_2$ and $\tilde{\eta}_3$ becomes sensitive to v_o only at very low redshifts ($z < 0.01$), in a regime where data have no constraining power. As the equation 5.48 makes clear, the dipole of the deceleration parameter, which is naturally defined in the matter frame, will be systematically different if it is estimated in different reference frames, without explicitly factoring out the observer's motion. The discrepant estimates obtained by various authors [192, 193, 194, 179] are not induced by the different statistical inference schemes implemented in the analyses nor by systematic errors in the different measurements. It is a real, physically expected bias induced by the motion of the observer relative to the matter frame, but that can simply be eliminated by proper signal analysis.

Our method indeed offers the first model-independent estimate of the relative velocity between the CMB observer and the matter frame at the observer's position. It requires no assumptions about the nature of the CMB or the origin of its dipole, nor does it rely on references to the cosmological principle or Einstein Field Equations. Furthermore, our formalism allows for a clear separation between anisotropies induced by the kinematics of the observer (with respect to the matter frame) and pure metric fluctuations, i.e. intrinsic anisotropies of the congruence of (fluid) matter geodesics.

Applying the method to real data holds the promise of potentially solving the dipole tension or at least clarifying the nature of any anisotropic signals measured at high redshift. This will be addressed in a future analysis. In the following, I show that although the observer's motion is degenerate with cosmographic parameters, a combined analysis of the low-order multipoles of $\tilde{\eta}$ allows us to disentangle metric and kinematic effects and, in particular, to constrain $\boldsymbol{v}_o$.

Figure 5.1 shows the maps of η with the dipole and the quadrupole components for

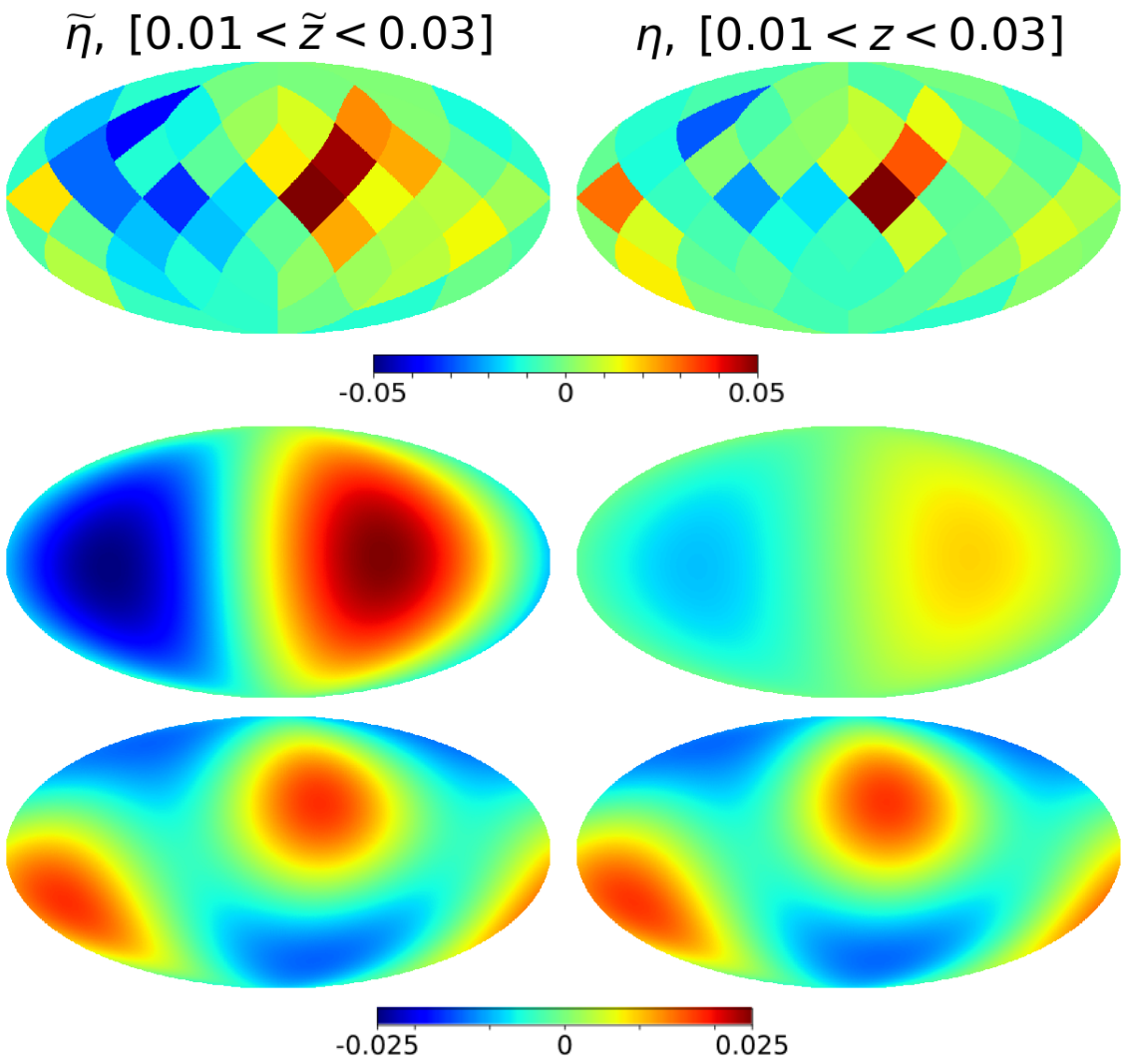


Figure 5.1: The maps of η for the CF4 sample in the redshift range $0.01 < z < 0.03$ in the CMB frame (left) and the matter frame (right), using the best-fit resultant velocity v_o of the matter observer with respect to the CMB observer from Chapter 7. The second and third rows show the dipole and the quadrupole components respectively for each frame.

the CF4 sample in the redshift range $0.01 < z < 0.03$ in both the CMB frame and the matter frame, using the best-fit resultant velocity v_o from Chapter 7. It is evident that the η map in the matter frame has a weaker dipole and approaches a quadrupolar configuration, which primarily arises from the quadrupole of the Hubble parameter. The residual dipole is mainly sourced by the higher-order expansion coefficients, mainly the deceleration parameter.

5.4 Conclusion

In this chapter, I've reviewed the covariant cosmographic approach to cosmology. This fully model-independent and non-perturbative framework allows for the interpretation of expansion rate data without assuming any specific spacetime metric $g_{\mu\nu}$. Its characteristic parameters, the covariant cosmographic parameters, are the coefficients of the redshift expansion of the luminosity distance in a generic spacetime. They depend on the geometric properties of spacetime and the 4-velocity of the cosmological matter fluid. The exact functional form of this dependence was previously known only up to the third order. Motivated by evidence suggesting that this range may be insufficient to fully capture the expansion rate kinematics in a highly inhomogeneous local universe (as will be shown in Chapter 6), I've extended these results to the fourth order in redshift, incorporating the snap parameter $\mathbb{S}(\boldsymbol{n})$. I also demonstrate that the covariant Hubble parameter has multipoles up to the quadrupole ($\ell = 2$), while the independent multipoles of the deceleration parameter extend to the octupole ($\ell = 3$). The third-order expansion term, which includes the jerk and curvature parameters, has independent multipoles up to $\ell = 4$, and the snap parameter features independent multipoles up to $\ell = 5$.

The total number of degrees of freedom is 86 (with each multipole having $2\ell+1$ degrees of freedom), which is too large for meaningful data interpretation. However, I show that assuming axial symmetry and considering that matter particles move along geodesics reduces the number of degrees of freedom to 17. In addition, some multipoles involve spatial derivatives, which means that they are amplified by a factor equal to the ratio between the scale of the Hubble horizon and the scale of the perturbation that generates them. If we consider only these "boosted" multipoles, in addition to the monopoles, we end up with just 12 degrees of freedom, a fairly reduced number of degrees of freedom for statistical inference.

The datasets used in cosmological studies often provide measurements of redshift and distance relative to specific reference frames, typically the heliocentric frame or the Cosmic Microwave Background (CMB) frame, where the observer does not observe the CMB dipole. However, in theoretical calculations of cosmographic parameters, it is assumed that the observer is comoving with the cosmological matter fluid (the so called matter frame, which does not coincide with the heliocentric frame). While the matter and the CMB frames are indistinguishable in a perfectly uniform universe as described by the standard cosmological metric, they differ in arbitrary geometries. To address this issue, often overlooked in the literature, I introduce a new degree of freedom, the local relative velocity v_o between the theoretical matter frame and the observational frame in which measurements are analyzed. I show how, by incorporating this relative velocity into the analysis, we gain additional insight into the relative motion between the matter and CMB frames.

Chapter 6

An analytical model for testing the cosmographic reconstruction scheme

In this chapter, I test the covariant cosmography formalism introduced earlier using axis-symmetric analytical models that simulate large-scale linear fluctuations in the redshift-distance relation of the local Universe.

To this purpose, I perturb an Einstein-de Sitter background with a spherically symmetric overdensity, considering two different sizes for the overdensity and assuming the observer is off-center with respect to the perturbation. This model is selected so that the observed multipoles of η and the bulk velocity are compatible with the values I inferred from data in Chapters 3 and 4 of this thesis. I then discretely sample the model by trying to reproduce both the redshift distribution and the errors in distances expected from the Zwicky Transient Facility (ZTF) survey, a future and large survey of redshift independent distances.

This realistic model allows me to evaluate how the luminosity distance compares to the distance reconstructed using covariant cosmographic parameters, thereby assessing the strengths and limitations of the covariant cosmographic approach in the local universe. These analyses help determine the redshift range over which the expansion of the distance is valid and enable me to forecast the precision with which the covariant cosmographic parameters can be estimated.

6.1 The attractor model

The effectiveness of the cosmographic approach for model-independent reconstruction of the metric structure of the local Universe ($z < 0.1$) is examined by simulating linear (scalar) perturbations in an otherwise smooth FLRW background. This latter is chosen to be the Einstein de Sitter (EdS) Universe, a flat matter-dominated model ($\Omega_{\rm m} = 1$) that has simple analytical properties and thus perfectly suits illustrative purposes. The scale factor of the metric evolves as $a(t) = (t/t_0)^{2/3}$ (see eq. (1.13)) and the background Hubble expansion rate is simply $H(t) = 2/(3t)$.

By neglecting anisotropic stresses (I assume that Einstein's field equations hold) and adopting the Newtonian gauge, the perturbed metric can be written as

$$\mathrm{d}s^2 = -\left(1+2\Phi\right)\mathrm{d}t^2 + a^2(t)(1-2\Phi)\left[\mathrm{d}r^2 + r^2(\mathrm{d}\vartheta^2 + \sin^2\vartheta\,\mathrm{d}\phi^2)\right]. \tag{6.1}$$

I assume that the background/perturbation split is carried out, at linear order, in a

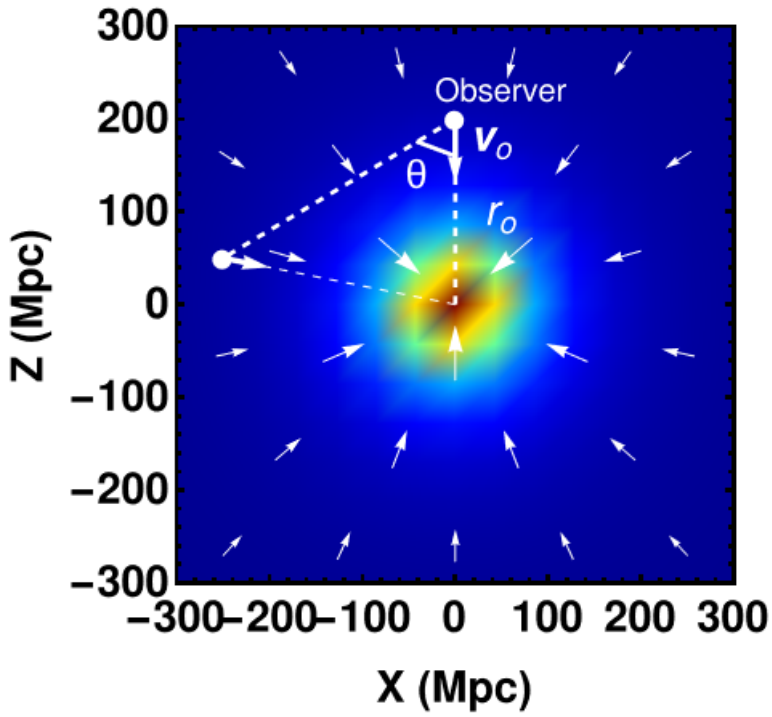


Figure 6.1: Analytical model's spherical density contrast projected onto a plane. I show the observer's position relative to the attractor and the peculiar velocity perturbation caused by the attractor. Model parameters (θ, r_o, $\boldsymbol{v}_o$) are also indicated.

smooth coordinate system where the CMB is at rest. This is not in general, and not in our specific perturbation model, the coordinate system in which matter is also at rest.

I then assume that the metric perturbation is sourced by a single "attractor", a massive spherically symmetric overdensity (see Figure 6.1) that sources the time-independent gravitational field. I model it as

$$\Phi(r) = \Phi_c \frac{R_s}{r} \sinh^{-1}\left(\frac{r}{R_s}\right) , \tag{6.2}$$

where R_s is the typical radial extension of the perturbation. This means that the relevant cosmological quantities measured by an off-center observer display an axially symmetric modulation. The potential Φ exactly solves, in Newtonian approximation and assuming that only the growing mode is of interest, the Poisson equation (1.46) for an overdensity contrast of the form

$$\delta(r, t_0) = \delta_c \left[1 + \left(\frac{r}{R_s}\right)^2\right]^{-3/2} . \tag{6.3}$$

This profile fairly characterizes large matter overdensities such as, for example, the Shapley Supercluster [195]. Here δ_c represents the central density contrast, which is related to the normalization of the potential as $\Phi_c = -3H_0^2 R_s^2 \delta_c/2$.

The peculiar velocity generated by the local gravitational field of the attractor can be found by eq. (1.50), and it has only a radial component:

$$v(r,t) = -\frac{2}{3aH}\frac{\partial \Phi}{\partial r} = \frac{2R_s\Phi_c}{3H_0 r^2}\left(\frac{t}{t_0}\right)^{1/3}\left[\sinh^{-1}\left(\frac{r}{R_s}\right) - \frac{r}{\sqrt{R_s^2 + r^2}}\right] . \tag{6.4}$$

This physical velocity is measured by observers located at the positions of the matter particles and with fixed coordinates in the Newtonian gauge coordinate system, i.e. at rest in the CMB frame (cf. [50]). Indeed they do not see any CMB dipole since fluctuations are induced only by Φ, and are thus negligible, being of second-order amplitude in velocity. These observers have 4-velocity $\tilde{u}^\mu$ and the matter particles have 4-velocity u^μ, where

$$\tilde{u}^\mu = (1-\Phi, \mathbf{0}), \quad u^\mu = \left(1-\Phi, \frac{v}{a}, 0, 0\right) , \tag{6.5}$$

in the given coordinates.

Despite its simplicity, this analytical model is flexible enough to closely match the observed multipoles of the expansion rate fluctuations field, as estimated using real data in Chapters 3 and 4, as I will show in section 6.4. Moreover it addresses two critical issues. First, it provides the ideal testbed for two different methods of reconstructing luminosity distances: the cosmographic method and the linear perturbation method. It is therefore instrumental in comparing the effectiveness of the model-independent approach in recovering fluctuations in the local expansion rate.

By randomly sampling the continuous analytical model, moreover, I can also simulate catalogs of distances measured without using redshift. Analysis of these catalogs allows us to forecast the precision with which future datasets will be able to constrain the multipoles of covariant cosmographic parameters, as well as the velocity of the matter frame at the observer's position.

In the following section, I truncate the expansion of the distance to third order in redshift (excluding the snap). After presenting the motivation for including the snap, I incorporate it into the analysis in section 6.8.

6.2 Luminosity distance of analytical model: cosmographic approach

The amplitude of the covariant cosmographic parameters $\mathbb{H}, \mathbb{Q}, \mathbb{J}$ and $\mathbb{R}$ can be calculated in an arbitrary spacetime, and thus in our specific analytical model, using the eqs. (5.27), (5.28), (5.29) and (5.30). The metric and the normalized photon 4-momentum K^μ at the observation event are all that are needed.

If the observer is not exactly at the center of the symmetry of the model (the overdensity peak), the expansion rate field manifests an axial symmetry around the line connecting the observer with the density peak. Because of this, we can assume, without loss of generality, that $k^3 = 0$ (where k^μ is the reverse (past-pointing) 4-momentum of the photon, $k^0 < 0$) and choose this axis of symmetry as the z-axis. Since $k^\mu k_\mu = 0$, two degrees of freedom are sufficient to fix k^μ. I choose to make the affine parameter coincide with the physical distance measured by the observer $\tilde{u}^\mu$, so $k^\mu \tilde{u}_\mu \mathrel{\mathring{=}} 1$ [186], which gives $k^0 \mathrel{\mathring{=}} -1+\Phi$ (using $a_0 = 1$). I also introduce the angle θ which measures the separation between the direction of reception of the light ray and the direction of the center of symmetry as measured by the observer $\tilde{u}^\mu$, which is chosen so that when $\theta = 0$ the observer line of sight is toward the center of the mass overdensity (see Figure 6.1). I thus obtain

$$k^\mu \mathrel{\mathring{=}} \left(-1+\Phi, -(1+\Phi)\cos\theta, \frac{1}{r}(1+\Phi)\sin\theta, 0\right) , \tag{6.6}$$

and by using eq. (5.13),

$$K^\mu \mathrel{\mathring{=}} \left(-1+\Phi-v_o\cos\theta, -(1+\Phi+v_o\cos\theta)\cos\theta, \frac{1}{r}(1+\Phi+v_o\cos\theta)\sin\theta, 0\right) . \quad (6.7)$$

As a check, note that $K^\mu u_\mu \mathrel{\mathring{=}} 1$ to leading order. By linearizing eq. (5.27) around the observer's position (using that the matter 4-acceleration is zero), I find

$$\mathbb{H} \mathrel{\mathring{=}} H\left(1-\frac{\dot{\Phi}}{H}-\Phi\right)+n^i n^j \partial_i v_j \,, \quad (6.8)$$

where all derivatives are computed at the event of observation. An observer comoving with matter measures no dipolar component for the generalized Hubble parameter, only a monopole and a quadrupole [50]. The latter, for our specific analytical model, are

$$\mathbb{H}_0 = H_0\left[1-\frac{1}{3}\delta_c\,\xi_o\left(\frac{\xi_o^2}{(1+\xi_o^2)^{3/2}}-\frac{9}{2}\xi_H^2\,\mathrm{csch}^{-1}(\xi_o)\right)\right], \quad (6.9)$$

$$\mathbb{H}_2 = \frac{2\delta_c H_0 \xi_o^3}{3(1+\xi_o)^{3/2}}\left[-4-3\xi_o^2+3(1+\xi_o^2)^{3/2}\,\mathrm{csch}^{-1}(\xi_o)\right], \quad (6.10)$$

and for the other parameters,

$$\mathbb{Q}_0 = q_0 + \frac{5\delta_c\xi_o^3}{6\,(1+\xi_o^2)^{3/2}}, \quad (6.11)$$

$$\mathbb{Q}_1 = -\frac{9\delta_c\xi_o^4}{5\xi_H(1+\xi_o^2)^{5/2}}, \quad (6.12)$$

$$\mathbb{Q}_2 = -\frac{5}{2}\frac{\mathbb{H}_2}{H_0}\,, \quad (6.13)$$

$$\mathbb{Q}_3 = \frac{2\delta_c\xi_o^4}{5\xi_H(1+\xi_o^2)^{5/2}}\left[15(1+\xi_o^2)^{5/2}\,\mathrm{csch}^{-1}(\xi_o)-23-35\xi_o^2-15\xi_o^4\right], \quad (6.14)$$

$$\mathbb{R}_0 = 1-2\mathbb{Q}_0\,, \quad (6.15)$$

$$\mathbb{R}_1 = \mathbb{Q}_1\,, \quad (6.16)$$

$$\mathbb{R}_2 = -\frac{\mathbb{Q}_2}{5}, \quad (6.17)$$

$$\mathbb{R}_3 = \mathbb{Q}_3\,, \quad (6.18)$$

$$\mathbb{J}_0 = j_0 - \frac{\delta_c\xi_o^3}{15\xi_H^2(1+\xi_o^2)^{7/2}}\left[9\xi_o^2(2-3\xi_o^2)-25\xi_H^2(1+\xi_o^2)^2\right], \quad (6.19)$$

$$\mathbb{J}_1 = -\mathbb{Q}_1\,, \quad (6.20)$$

$$\mathbb{J}_2 = -\frac{10\delta_c\xi_o^3}{21\xi_H^2(1+\xi_o^2)^{7/2}}\left[18\xi_o^2-7(1+\xi_o^2)^2(4+3\xi_o^2)\xi_H^2+21\xi_H^2(1+\xi_o^2)^{7/2}\,\mathrm{csch}^{-1}(\xi_o)\right], \quad (6.21)$$

$$\mathbb{J}_3 = -\mathbb{Q}_3\,, \quad (6.22)$$

$$\mathbb{J}_4 = \frac{8\delta_c\xi_o^5}{35\xi_H^2(1+\xi_o^2)^{7/2}}\left[105(1+\xi_o^2)^{7/2}\,\mathrm{csch}^{-1}(\xi_o)-7\xi_o^2(58+50\xi_o^2+15\xi_o^4)-176\right]. \quad (6.23)$$

where $\xi_o \equiv R_s/r_o$, $\xi_H \equiv R_s/R_H = R_s H_0$, and r_o is the radial coordinate of the

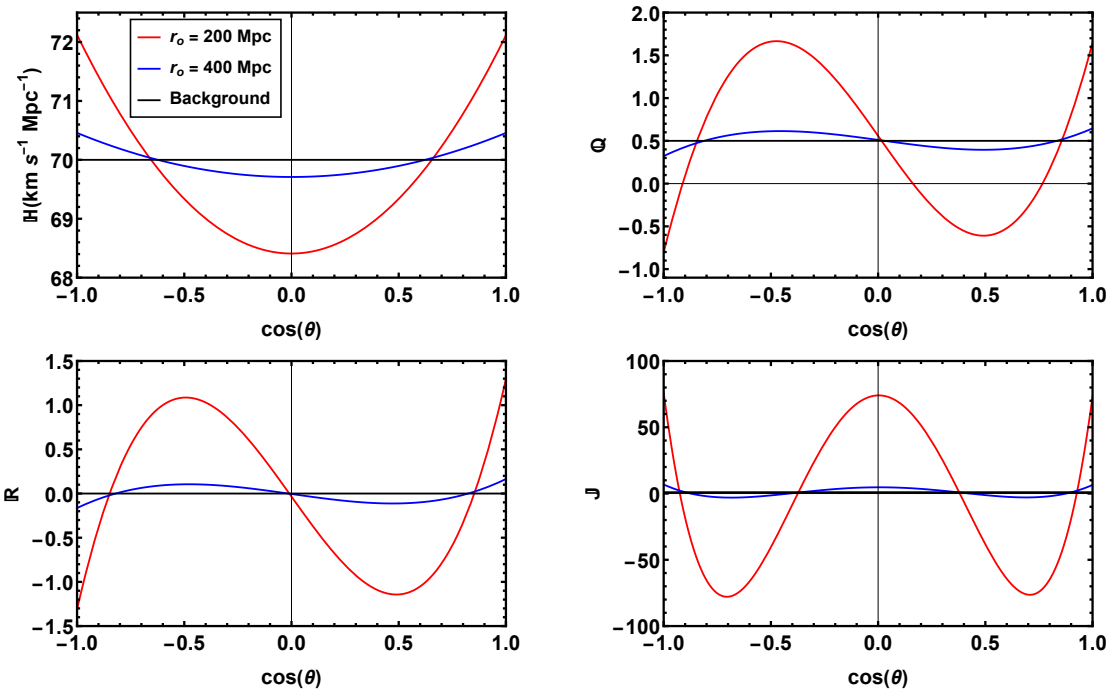


Figure 6.2: The lowest order covariant cosmographic parameters $\mathbb{H}$, $\mathbb{Q}$, $\mathbb{R}$ and $\mathbb{J}$ at the event of observation are shown as a function of $\cos\theta$, the angular separation from the symmetry axis. The red curves represent local measurements for an observer 200 Mpc away from the overdensity, and the blue for an observer at a distance of 400 Mpc. The same model is assumed, with parameters $H_0 = 70\,\mathrm{km/(s\ Mpc)}$, $\delta_c = 2.5$ and $R_s = 37.4\,\mathrm{Mpc}$.

observer. I remark that, at linear order in the perturbation parameter δ_c, the multipoles $\ell \geq 5$ vanish.

In Figure 6.2, I show the angular dependence of the covariant cosmographic parameters $\mathbb{H}, \mathbb{Q}, \mathbb{J}$ and $\mathbb{R}$, as functions of $\cos\theta$ for two observers at different distances, $r_o = 200$ and 400 Mpc, from the high density peak. I also show, for comparison, the input values of the Hubble, deceleration, jerk and curvature for the smooth background of the analytical model (the EdS model), whose value is, by construction, independent of direction. The amplitude of the anisotropies in each parameter becomes weaker as the distance of the observer from the density peak increases. As the observer moves away from the center, the covariant cosmographic parameters asymptotically converge to the background values.

6.3 Luminosity distance of analytical model: linear perturbation theory

We can determine the luminosity distance of objects in the single-attractor analytical model also through the linear cosmological perturbations. This independent determination, although based on knowledge of the line element (6.1), and thus model-dependent, provides a useful comparative tool for assessing the validity of the third-order cosmographic expansion in the local perturbed Universe.

In a linearly perturbed EdS background where the gravitational potential is independent on time, the redshift measured by a matter-comoving observer can be found by eq.

(1.51).

$$1 + z = (1 + \bar{z})[1 + \boldsymbol{n} \cdot (\boldsymbol{v} - \boldsymbol{v}_o) - (\Phi - \Phi_o)] \,, \tag{6.24}$$

For an observer in the matter frame, the luminosity distance to a galaxy with peculiar velocity $\boldsymbol{v}$ is (using eq. (1.54)),

$$d_L(z) = \bar{d}_L(\bar{z}(z)) \, (1 + 2\boldsymbol{n} \cdot \boldsymbol{v} - \boldsymbol{n} \cdot \boldsymbol{v}_o) \,. \tag{6.25}$$

Here $\boldsymbol{v}_o$ is the velocity of the matter-comoving observer and $\bar{d}_L(\bar{z})$ again is the luminosity distance between the events of emission and absorption, assuming that the Universe is perfectly smooth. In the EdS model, this takes the form

$$\bar{d}_L(\bar{z}) = \frac{2}{H_0} \left(1 + \bar{z} - \sqrt{1 + \bar{z}} \right) \,. \tag{6.26}$$

Note that the perturbation of the luminosity distance which is induced by the gravitational potential Φ is not taken into account. Although these provide a first-order correction to the redshift expression (cf. eq. (1.51)), at small redshift ($z \ll 1$), their relative contribution to the distance expression is negligible. Both the redshift and the luminosity distance measured in the CMB frame can be obtained by simply setting $\boldsymbol{v}_o = 0$.

All the quantities in the preceding expressions ($\bar{z}$, $\boldsymbol{v}$, Φ, $\boldsymbol{n}$) depend on the coordinates (t, r, ϑ), at which the photon reaching the observer at the event (t_0, r_o, ϑ_o) was emitted. I compute them by solving the geodesic equation of the photon in the EdS background for an off-center observer ($r_o \neq 0$) as detailed in Appendix B. This, in turn, allows us to calculate, numerically, the expression for the luminosity distance of the sources as a function of the redshift and the line-of-sight direction and, therefore, the value of $\eta(z, \theta)$.

As a consistency test, I have checked that the cosmographic and the linear perturbation formalisms consistently provide the same expression of the Hubble parameter as measured in the matter frame. The Hubble parameter in a generic spacetime is defined as

$$\mathbb{H} \doteq \frac{\mathrm{d}\, z}{\mathrm{d}\, d} \,. \tag{6.27}$$

In [50], we demonstrated that when calculated in the matter frame, this relation holds whatever is the operational definition of the distance d. Therefore, with $d = d_L$ and using eqs. (6.24) and (6.25), I obtain with ignoring $\dot{\Phi}$,

$$\begin{aligned} \mathbb{H} &\doteq H \left(1 - \boldsymbol{n} \cdot \boldsymbol{v} + \boldsymbol{n} \cdot \frac{\mathrm{d}\boldsymbol{v}}{\mathrm{d}\bar{z}} - \frac{\mathrm{d}\Phi}{\mathrm{d}\bar{z}} \right) \\ &\doteq H \left[1 - n^i v_i + \frac{n^j(- \dot{v}_j + n^i \partial_i v_j) - n^i \partial_i \Phi}{H_0} \right] \,. \end{aligned} \tag{6.28}$$

Since a dust fluid element moves along time-like geodesics, then at (t_0, r_o), when the scale factor is $a = 1$, its velocity must satisfy the equation of motion (1.45). Once inserted in eq. (6.28), this allows us to consistently retrieve the formula for the local Hubble parameter given in eq. (6.8) if we ignore the terms in order Φ. However, the terms containing the gravitational potential could also be found if the contribution of Φ was also taken into account in the expression of d_L (according to the formula C21 in [190]). We also note, incidentally, that if the 4-acceleration of the fluid element does not vanish, then the terms which have one n^i in eq. (6.28) will not cancel. As a consequence, the generalized Hubble

parameter measured by a matter-comoving observer will display also a dipolar component.

6.4 Expansion rate fluctuations field of the analytical model

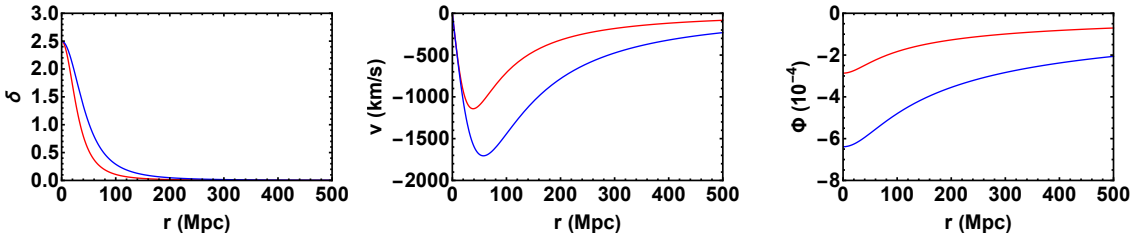


Figure 6.3: The density contrast, the radial component of the peculiar velocity, and the gravitational potential (Φ/c^2), all evaluated at present time, as a function of the radial coordinate r for the $M1$ (red) and $M2$ (blue) models.

As well as serving as a test bed for the limits of the cosmographic approach in the local Universe, the analytical model is designed to roughly reproduce the expansion rate fluctuations measured with real data by [112], thus enabling a better understanding of their physical origin. It also allows us to compare and contrast the structure and characteristics of the expansion rate fluctuation field, measured in two different reference systems, the matter-comoving and the CMB frames.

I set the parameters of the analytical model so as to describe two competing and antagonistic scenarios often invoked to explain the kinematics of the local Universe within the standard model of cosmology. One model (hereafter $M1$) has a peculiar velocity field which is sourced by a relatively local mass overdensity and thus results in a bulk motion which vanishes on small averaging scales. In the opposite scenario, dubbed $M2$, the attractor mass is larger and further away from the observer, thus a coherent bulk motion signal is still present in a large volume with typical size $R \sim 500$ Mpc.

The small-scale bulk model $M1$ is given by using

$$M1: \quad r_o = 200\,\mathrm{Mpc}\,, \quad \delta_c = 2.5\,, \quad R_s = 37.4\,\mathrm{Mpc}\,, \tag{6.29}$$

in eq. (6.3). This choice implies $\Phi_c = -2.9 \times 10^{-4}$. These values are suggested by studies of the peculiar velocity field in the local Universe [195] and fairly characterize the scenario in which such a field is generated by a single attractor like the Shapley supercluster. The values I choose for the parameters δ_c and R_s are consistent with [195], but they are fixed so that the observer (here assumed to be 200 Mpc far from Shapley) moves relative to the CMB with a velocity of 320 km/s. This value is the component of our Local Group which is generated by a matter distribution at distance > 38 Mpc, as measured by [196]. The large-scale bulk model $M2$ is given by

$$M2: \quad r_o = 400\,\mathrm{Mpc}\,, \quad \delta_c = 2.5\,, \quad R_s = 56\,\mathrm{Mpc}\,, \tag{6.30}$$

which generates the same observer's velocity (320 km/s).

The background EdS geometry is common to the two models, with $H_0 = 70$ km s^{-1}Mpc^{-1}, $q_0 = 0.5$, $\Omega_{k0} = 0$, and $j_0 = 1$. In Figure 6.3, the density contrast, the radial component

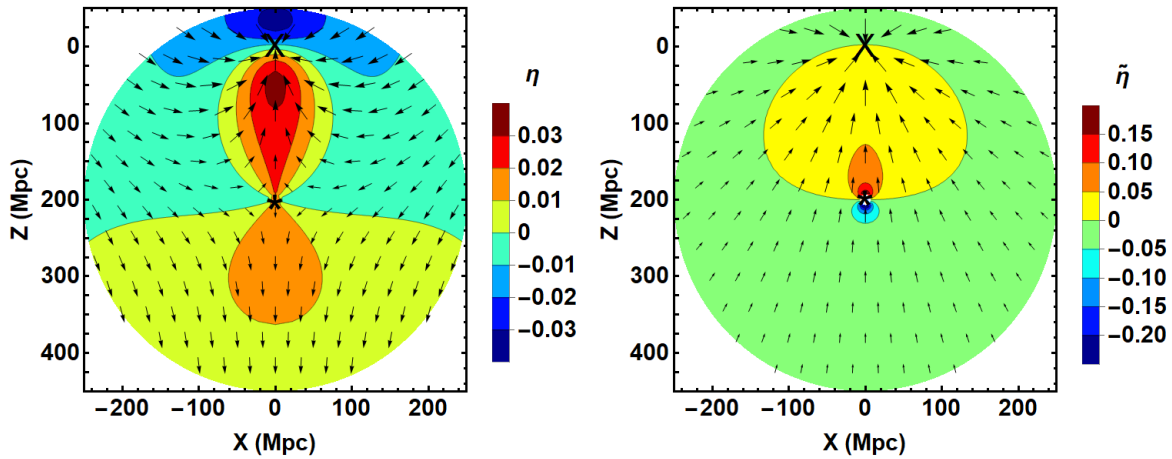


Figure 6.4: The expansion rate fluctuation field in the matter frame (left) and in the CMB frame (right) for the model $M1$ is portrayed in the (X, Z)-plane containing the axis between the center of the mass overdensity, at $(X, Z) = (0, 0)$, and the observer, at (0,200). Arrows display the peculiar velocity (vector) field, while color maps and isocontours display the amplitude of the expansion rate fluctuation (scalar) field.

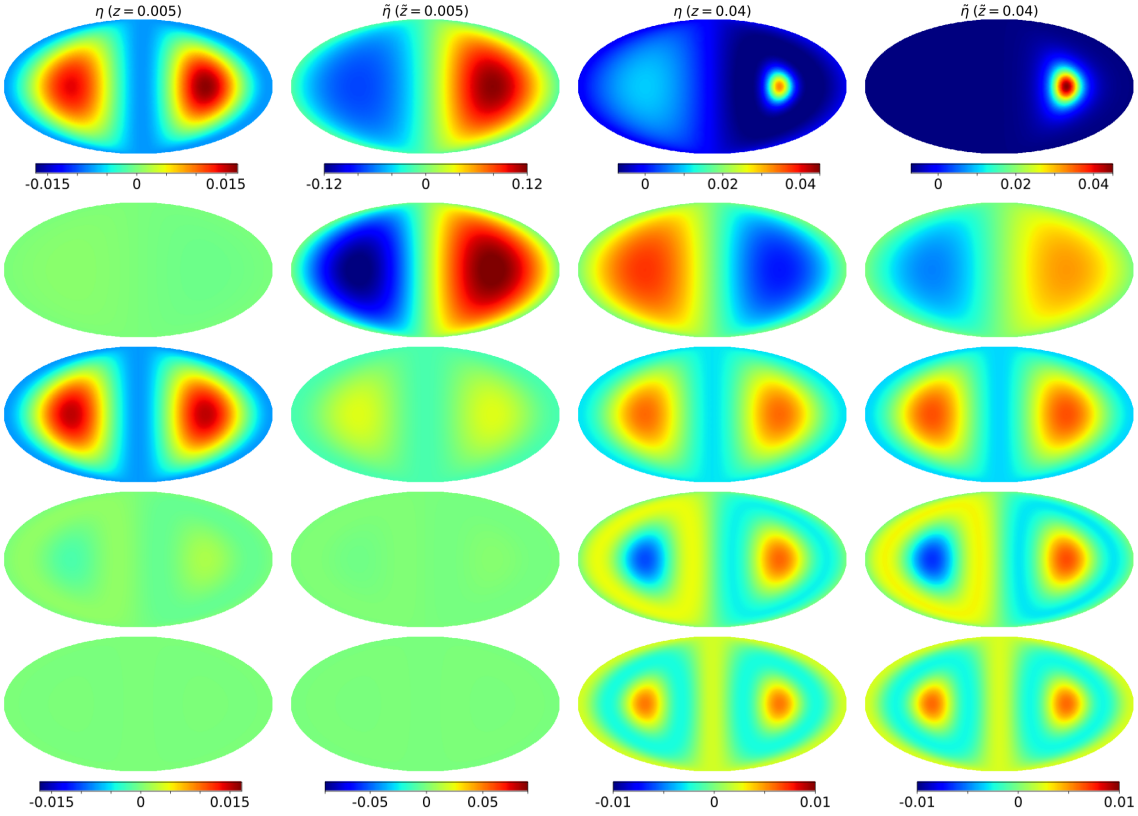


Figure 6.5: All-sky maps of the expansion rate fluctuations field generated by the $M1$ model in matter and CMB frames, at two redshifts (first row, 4 columns). The rows show the multipolar components: dipole (row 2), quadrupole (row 3), octupole (row 4), and hexadecapole (row 5). The first and second columns show η (matter frame) and $\tilde{\eta}$ (CMB frame) at $z = 0.005$. Columns 3 and 4 show the same fields at a deeper redshift ($z = 0.04$). The position of the overdense region is chosen to lie on the equator of the Mollweide projection, 90° away from the center.

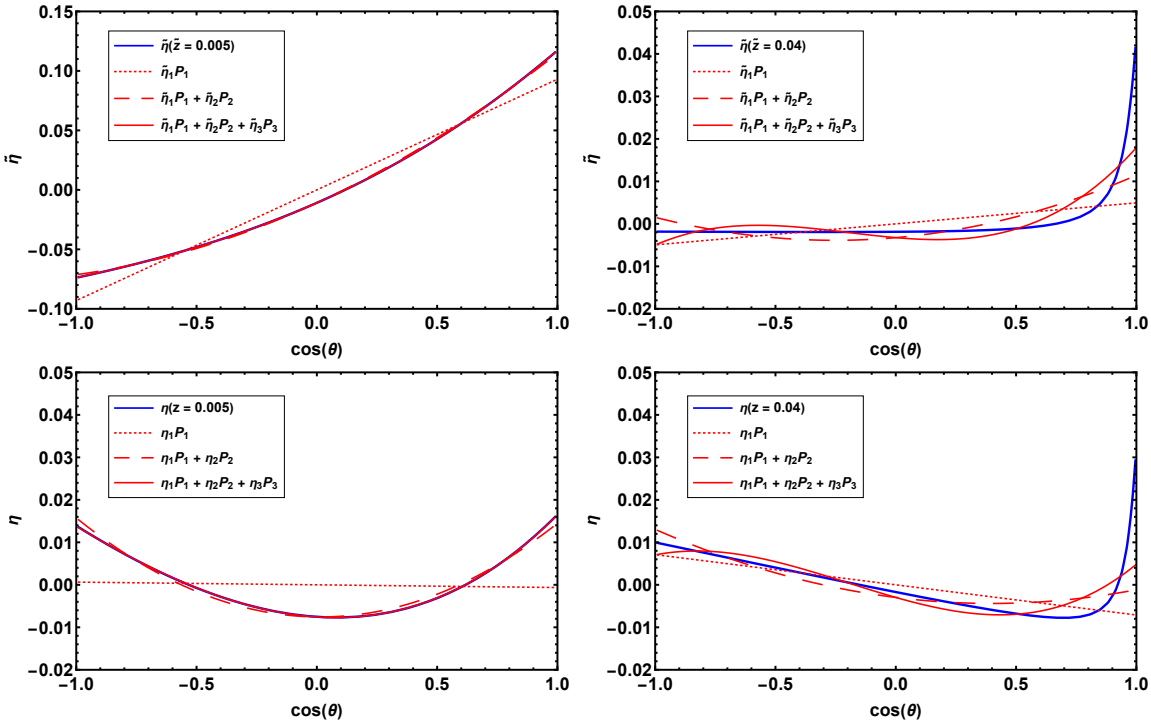


Figure 6.6: The expansion rate fluctuation field of the $M1$ model in the CMB frame (upper panels) and matter frame (lower panels), shown as a function of $\cos\theta$ at redshift $z = 0.005$ (left panels) and $z = 0.04$ (right panels). I also show how the signal is reconstructed by different order Legendre expansions, up to $\ell = 3$.

of the velocity profile today, and the gravitational potential for these two scenarios are shown as a function of the radial coordinate r.

In Figure 6.4, I display a planar section of the $M1$ analytical model of the Universe. This plane contains the center of the Shapley overdensity contrast and the observer, at a distance of 200 Mpc. I also show, superimposed, the peculiar velocity (vector) field generated by the mass overdensity as well as the isocontours of the expansion rate fluctuation (scalar) field. Both fields show different configurations, depending on whether they are measured in the matter or CMB frames respectively.

Regardless of the observer, a common feature that emerges from visual inspection is the characteristic anisotropic structure of the expansion rate fluctuations field induced by metric perturbations. In addition, when looking along a fixed direction of the observer's line of sight, one can also visually appreciate the nonlinearities in the distance-redshift relationships, which are most evident in the direction of the supercluster.

The scalar nature of the η observable allows the multipolar structure of the signal to be captured even if only visually. At low redshift (close to the observer), the amplitude of η measured in the matter frame is dominated by a quadrupolar component, while that inferred in the CMB frame shows a typical dipolar pattern. The fact that, by definition, the velocity field vanishes around the matter-comoving observer (see left panel of Figure 6.4), means that the fluctuations of the expansion velocity field are dominated by a shear component. In other words, the expansion rate is similarly perturbed in antipodal directions around the observer. When the distance increases, the peculiar velocity field reveals more complex characteristics. As a consequence, the expansion rate fluctuation field also acquires non-trivial distortions. In the CMB frame (right panel of Figure 6.4),

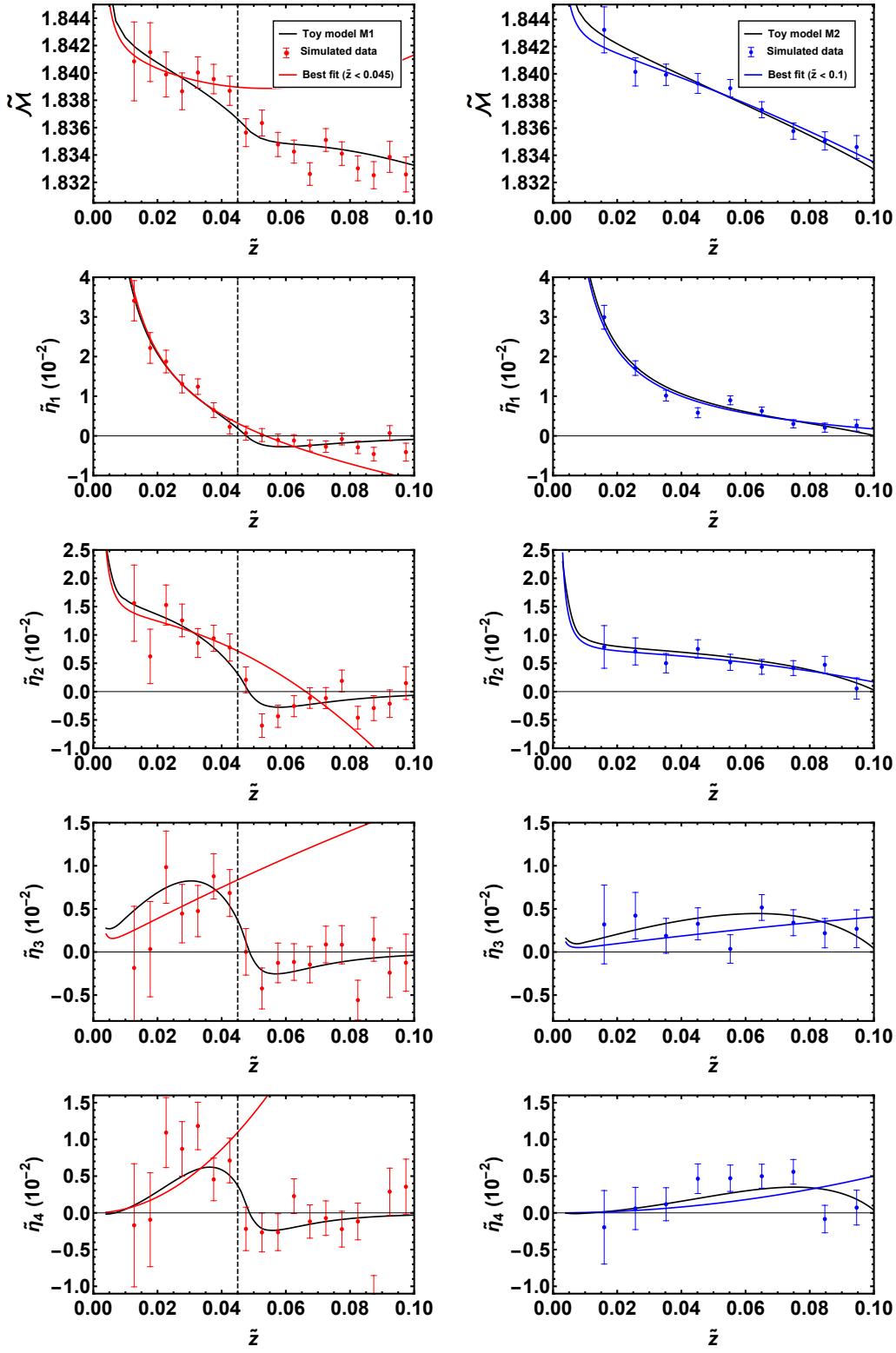


Figure 6.7: Left panels: The normalization $\mathcal{M}$, dipole, quadrupole and octupole of the expansion rate fluctuation field in the CMB frame ($\tilde{\eta}_\ell$), reconstructed using $M1$ simulated galaxy data in different redshift shells (red points). These are compared to the input continuous value (black solid line) and to the best-fitting theoretical predictions (red curves). The latter are obtained by expanding $\tilde{\eta}$ using the cosmographic approach, truncated up to $\mathcal{O}(z^3)$, and by fitting only the points with $\tilde{z} < 0.045$. Right panels: as on the left, but for the $M2$ simulated data (blue points). The best theoretical models (blue curves) are obtained by fitting all the available measurements up to $z = 0.1$.

the expansion rate field is locally dominated by a dipolar component, induced by the motion of the observer relative to the chosen reference frame. Its amplitude increases closer to the observer.

A quantitative estimation of the multipolar components of η for $M1$ is presented in Figure 6.5, where I show the multipoles of the expansion rate fluctuation measured by the matter-comoving and CMB-comoving observers. The multipole decomposition is shown at two characteristic redshifts, $z = 0.005$ – assumed to represent very local measurements, and $z = 0.04$ – representing regions where the peak density of the analytical model severely distorts the distance-redshift relationship. The nonzero value of a multipole provides information on the structure of the anisotropy in the expansion rate, while its evolution with redshift reflects the level of nonlinearity in the distance-redshift relation. The qualitative similarity with the signal extracted in Chapters 3 and 4 (in the CMB frame): the axes of the multipoles are aligned, the geometry is axisymmetrical, and the amplitude and redshift scaling of each multipole roughly reproduce what was observed (compare with Figures 3.3 and 4.3).

The expansion rate fluctuations in the CMB frame are enhanced relative to the signal measured by the matter-frame observer. This increase is essentially contributed by the dipolar component, which, as expected on the basis of eq. (5.55), is the multipole that is most sensitive to observer velocity effects. Furthermore, as eq. (5.53) makes clear, the smaller the volume surrounding the observer in which the dipole signal is estimated, the greater the increase in the signal. On the contrary, in the same limit $z \to 0$, the dipole of η in the matter frame is expected to vanish (cf. eq. (5.48)), as shown in Figure 6.5 (first column, second row). The distortions induced by the motion of the observer in the dipole are of order $v_o/\tilde{z}$. As one pushes the analysis to higher $\tilde{z}$, the amplitude of $\tilde{\eta}_1$ is suppressed inversely proportional to redshift. Consequently, the signal becomes more sensitive to metric contributions, particularly to the dipole of the deceleration parameter, $\mathbb{Q}_1$. The increasingly important effects induced by $\mathbb{Q}_1$ can be seen by comparing the low- and high-redshift dipolar components measured in the matter frame.

Visual inspection of Figure 6.5 shows that the relative motion of the CMB and matter observers only affects the dipole of $\tilde{\eta}$, while minimally affecting its quadrupole and octupole. In fact, already at very low redshift, the contribution of velocity-induced distortions to the signal is $\mathcal{O}(v_o^2/z^2)$ and $\mathcal{O}(v_o^3/z^3)$ respectively as shown in eq. (5.55). Note that, contrary to the case of other multipoles, η_2 does not vanish for $z \to 0$, but in this limit becomes proportional to the amplitude of the quadrupole $\mathbb{H}_2$.

Similarly to the case of the dipole, as redshift increases, the differences between the reconstructed multipoles of η in the matter and CMB frames, are reduced and the signal acquires specific dependencies on the higher-order multipoles of the covariant cosmographic parameters. Figure 6.5 shows that the quadrupole signal η_2 in the $M1$ model weakens with redshift, because the quadrupole contributions of $\mathbb{Q}$ and $\mathbb{J} - \mathbb{R}$ – which are negative in this model (see Table 6.1) – gradually become more important. The same applies to the octupole and the hexadecapole signals η_3 and η_4, whose low-z amplitude becomes progressively more sensitive to a mixture of multipoles of higher-order cosmographic parameters. Although these are only $\mathcal{O}(z^2)$ corrections, large values of the covariant cosmographic parameters, as indeed is the case if the metric has large fluctuations (see Table 6.1), compensate for the suppression induced by the powers of small z.

In Figure 6.6, I show how well the expansion rate fluctuations in the CMB and matter frames are reconstructed by the lower multipoles, at redshifts $z = 0.005$ and $z = 0.04$. As

Model	Small-Scale Bulk ($M1$) ($\delta_c = 2.5, R_s = 37.4$ Mpc, $r_o = 200$ Mpc)					Large-Scale Bulk ($M2$) ($\delta_c = 2.5, R_s = 56$ Mpc, $r_o = 400$ Mpc)				
X	X_0	X_1	X_2	X_3	X_4	X_0	X_1	X_2	X_3	X_4
$\mathbb{H}$ (km/s/Mpc)	69.65	-	2.47	-	-	69.86	-	1.29	-	-
$\mathbb{Q}$	0.51	-0.58	-0.09	1.88	0	0.505	-0.125	-0.05	0.51	0
$\mathbb{J}-\mathbb{R}$	-6.53	1.16	-57.3	-3.76	138.5	0.17	0.25	-6.37	-1.02	19.3
v_o (km/s)	320					320				
Best fitting values										
X	X_0	X_1	X_2	X_3	X_4	X_0	X_1	X_2	X_3	X_4
$\mathbb{H}$ (km/s/Mpc)	69.5 ± 1.0	-	2.1 ± 0.5	-	-	69.63 ± 0.30	-	1.1 ± 0.2	-	-
$\mathbb{Q}$	0.4 ± 2.0	-0.9 ± 0.3	0	0.9 ± 0.2	0	0.7 ± 0.3	-0.18 ± 0.05	0	0.23 ± 0.05	0
$\mathbb{J}-\mathbb{R}$	16 ± 87	0	-42 ± 32	0	73 ± 16	-2.3 ± 5.9	0	-7.4 ± 3.1	0	6.8 ± 1.9
v_o (km/s)	336 ± 32					303 ± 20				

Table 6.1: The upper table shows the Legendre multipoles X_ℓ ($\ell \leq 4$) of the covariant cosmographic parameters and the relative velocity v_o between the matter and the CMB frames for the $M1$ (left) and $M2$ (right) models. These quantities are calculated using the equations (6.9–6.23). The lower table shows the best-fit values (and the 68% confidence interval) deduced from the likelihood analysis performed using 15,000 discrete objects sampling the analytical models and roughly reproducing the ZTF survey characteristics. A cell containing a dash indicates that the multipole vanishes by definition. A cell containing a zero means that the multipole is intrinsically small and its value is therefore set to zero by default. Note that for $\ell > 0$, $\mathbb{J}_\ell - \mathbb{R}_\ell \approx \mathbb{J}_\ell$.

expected, a multipolar expansion up to $\ell = 2$ is enough to achieve percentage estimation precision at low redshift. However, the higher the redshift, the more inaccurate the estimation is. Note that, given the different functional shapes of the expansion rate fluctuations in different observer frames, at an equal order of expansion, the Legendre approximation in the matter frame has a somewhat higher level of precision than in the CMB frame, with the accuracy increasing by roughly 5%.

6.5 Forecasting precision on cosmographic parameter estimation

By means of the analytical models, I can also assess the accuracy with which the (idealized) continuous η field is reconstructed using a (real) discrete point process, and forecast the precision with which future data sets will constrain multipoles of the covariant cosmographic parameters in the local Universe ($z \lesssim 0.1$).

To this end, I simulate distances and redshifts for 15×10^3 galaxies, distributed in the redshift interval $0.01 < \tilde{z} < 0.1$, by sampling the continuous analytical models $M1$ and $M2$ according to the redshift distribution expected from the ZTF survey [197]. In order to make these two simulated catalogs of distances (measured without using redshift information) as realistic as possible, I assume that the distance modulus of each object has a Gaussian distribution with standard deviation $\sigma_\mu = 0.15$ [198], and no correlation between the measurements.

I measure the expansion rate fluctuations (in the CMB frame) in spherical shells S of thickness $\delta\tilde{z} = 0.005$ for the $M1$ model and $\delta\tilde{z} = 0.01$ for $M2$ model. In Figure 6.7, the amplitude of the multipoles $\tilde{\eta}_\ell$, inferred using the discrete catalogs $M1$ and $M2$, is compared to the input theoretical value characterizing the continuous matter density fields. The estimation is unbiased and its accuracy, for both the small- and large-scale bulk scenarios, is remarkable. However, extracting the value of covariant cosmographic parameters from these measurements is challenging.

Assuming axial symmetry and considering only the dominant multipoles up to the

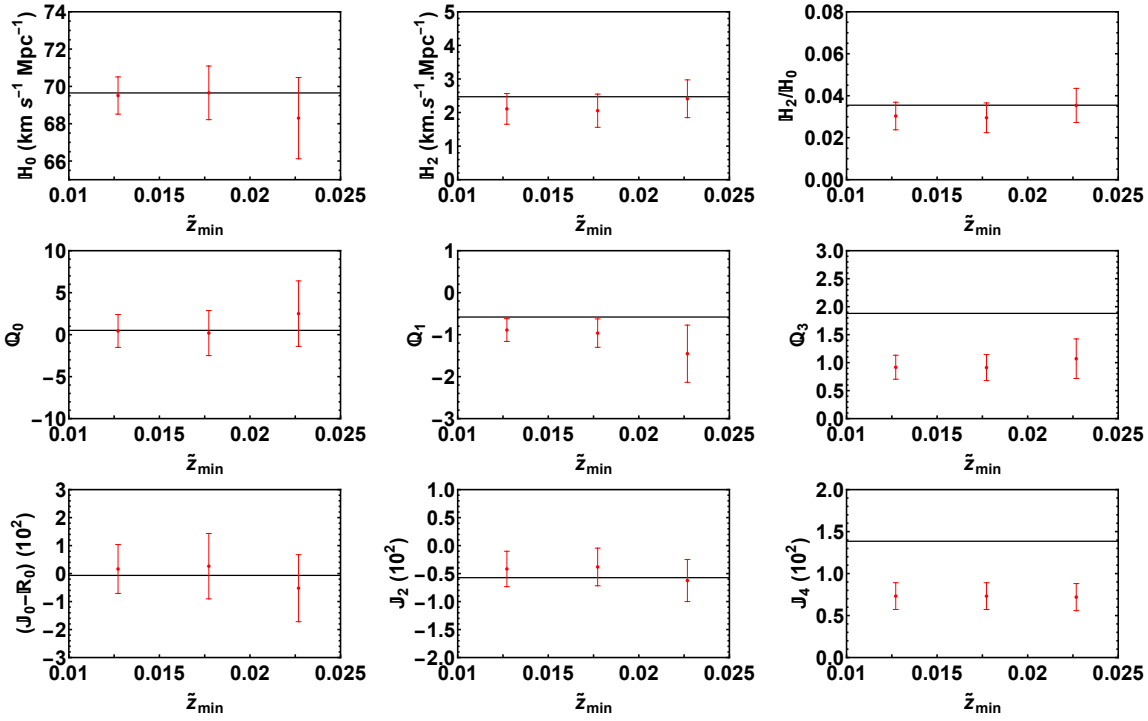


Figure 6.8: The best-fitting values (and the associated 1σ error bars) for the covariant cosmographic parameters extracted from the analysis of the $M1$ simulation in the shell $\tilde{z}_{\rm min} < \tilde{z} < 0.045$, are shown as a function of $\tilde{z}_{\rm min}$. The black lines show, for comparison, the true simulated input values (see Table 6.1).

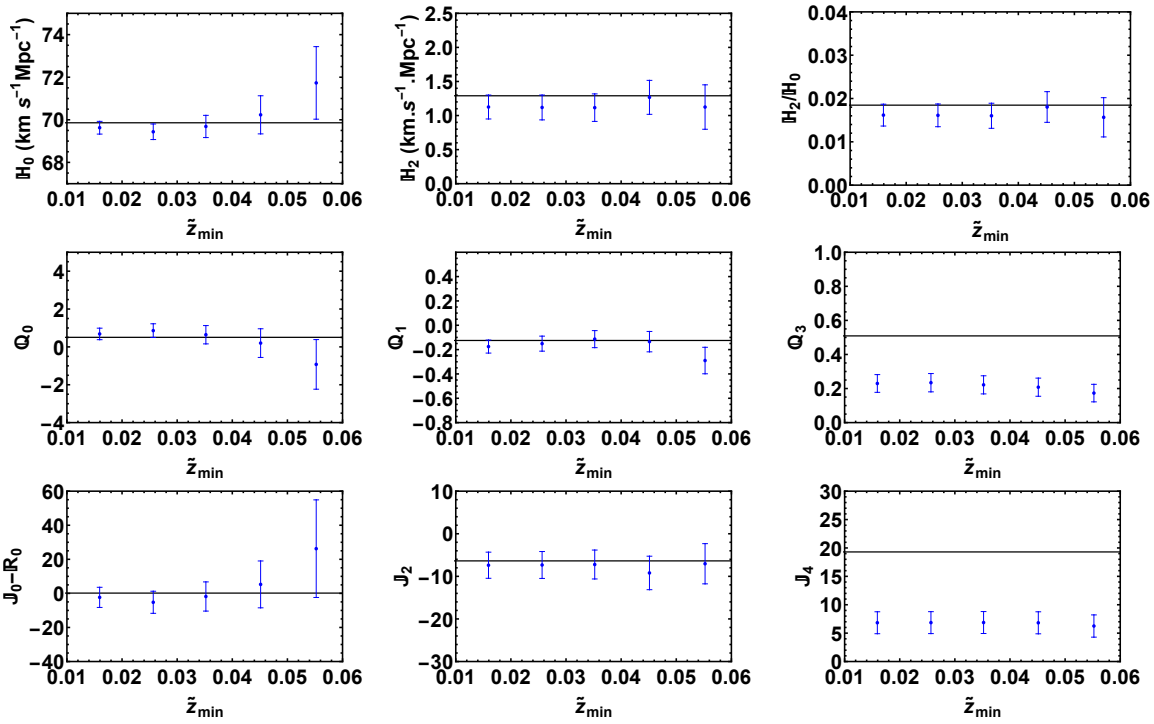


Figure 6.9: As in Figure 6.8, but for the $M2$ simulation. The best-fitting parameters recovered in the shell $\tilde{z}_{\rm min} < \tilde{z} < 0.1$ are shown as a function of $\tilde{z}_{\rm min}$.

third-order expansion of the distance (see section 5.2), the optimal analysis scheme therefore consists in decomposing $\tilde{\eta}$ measured in the CMB frame into spherical harmonics, then comparing each multipole with theoretical predictions via a likelihood analysis in order to constrain the free parameters of the model, $\boldsymbol{X} = (v_o, \mathbb{H}_0, \mathbb{H}_2, \mathbb{Q}_0, \mathbb{Q}_1, \mathbb{Q}_3, \mathbb{J}_0 - \mathbb{R}_0, \mathbb{J}_2, \mathbb{J}_4)$. This is achieved in practice by minimizing the χ^2 statistic

$$\chi^2(\boldsymbol{X}) = \sum_{i=1}^{N_{\rm sh}} \left[\frac{\tilde{\mathcal{M}}(\boldsymbol{X}, \tilde{z}_i) - \tilde{\mathcal{M}}_i}{\sigma_{\tilde{\mathcal{M}}_i}} \right]^2 + \sum_{\ell=1}^{\ell_{\rm max}} \sum_{i=1}^{N_{\rm sh}} \left[\frac{\tilde{\eta}_\ell(\boldsymbol{X}, \tilde{z}_i) - (\tilde{\eta}_\ell)_i}{\sigma_{(\tilde{\eta}_\ell)_i}} \right]^2, \tag{6.31}$$

where $N_{\rm sh}$ is the number of redshift shells, indexed by i, while ℓ labels each multipole ($\ell_{\rm max} = 4$). The theoretical models for $\tilde{\mathcal{M}}$ and $\tilde{\eta}_\ell$ are obtained by combining the equations truncated to second order in redshift for the multipoles (5.47), (5.48), (5.49), (5.50) and (5.51) with equations (5.55). The method for estimating the multipoles $\tilde{\mathcal{M}}_i$ and $(\tilde{\eta}_\ell)_i$, and their uncertainties in each shell i, is shown at end of section 4.2.1.

The accuracy of this inference scheme is tested using the catalogs $M1$ and $M2$. In Figure 6.7 (left panels), I show the result of fitting the redshift evolution of the lowest multipoles of $\tilde{\eta}$, together with the normalizing factor $\tilde{\mathcal{M}}$, by means of the $M1$ dataset. Figure 6.7 (right panels) presents similar results obtained from the analysis of the $M2$ catalog. In Table 6.1, I quote the best-fitting values of the covariant cosmographic parameters and compare them to the true input values, for both models $M1$ and $M2$.

Figure 6.7 shows how well the discrete objects simulating the ZTF survey trace the underlying continuous (exact) field and how well the multipoles of η are reconstructed using the expansion in covariant cosmographic parameters – *i.e.,* by neglecting $\mathcal{O}(z^3)$ terms in eqs. (5.47), (5.48), (5.49), (5.50) and (5.51). For the analytical model $M1$, we see that the goodness of the fit is satisfactory at low redshift, but breaks down at $z \approx 0.045$. This value is not an insignificant one: it is approximately the distance of the large density peak simulated in the model $M1$, the scale at which strong nonlinearities in the distance-redshift relationship emerge. The causes of these nonlinear effects and their effect on cosmographic reconstruction are discussed in detail in the next section. I observe that the existence and value of this break-down scale can be easily recognized from the data, without any prior knowledge of the magnitude and size of matter fluctuations in the local Universe.

In the case of the large-scale bulk model $M2$, where the attractor lies on the edge of the region covered by the simulated data ($0.01 < \tilde{z} < 0.1$), the cosmographic expansion is even more effective, describing the evolution of the signal over the entire redshift interval analyzed. As a consequence, the value of the χ^2 statistic becomes highly significant. I find $\chi^2 = 49.2$ for $9 \times 5 - 9 = 36$ degrees of freedom, implying that the probability of finding a higher χ^2 value is around 7%.

In Figures 6.8 and 6.9, I display the best-fitting values for the lowest multipoles of the covariant cosmographic parameters $\mathbb{H}$ (monopole and quadrupole), $\mathbb{Q}$ (monopole, dipole, and octupole), and $\mathbb{J} - \mathbb{R}$ (monopole, quadrupole, and hexadecapole). I also show how well these estimates approximate the simulated input values. Note that the cosmographic parameters characterize the structure of spacetime at the position of the observer. However, it is not feasible to constrain their amplitude using measurements of η at $z = 0$. Their value is extrapolated from η measurements made in spherical shells centered on the observer and with variable width. The upper boundary is fixed at the maximum redshift (at which the fit is not rejected by the χ^2 test), while the lower boundary of the shell, $\tilde{z}_{\rm min}$, is left free to vary. The smaller $\tilde{z}_{\rm min}$ becomes, the more

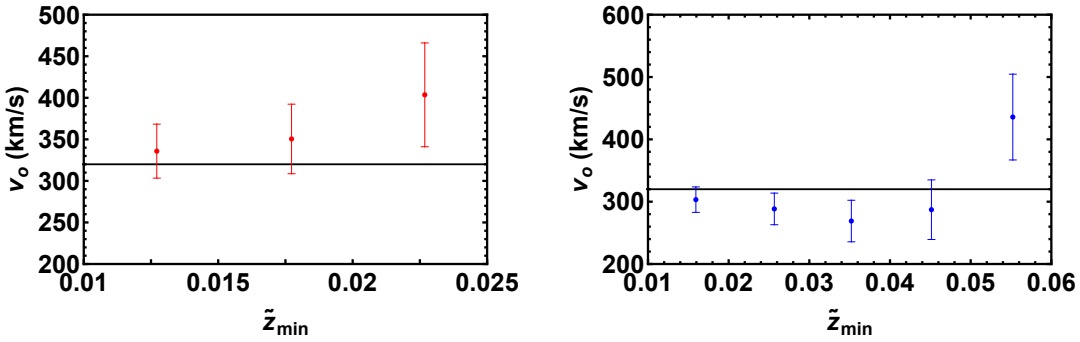


Figure 6.10: The best-fitting velocity (and the associated 1σ errorbar) of the matter frame relative to the CMB frame at the event of observation. *Left:* results from the analysis of the $M1$ simulation in shells $\tilde{z}_{\rm min} < \tilde{z} < 0.045$. *Right:* results from the analysis of the $M2$ simulation in shells $\tilde{z}_{\rm min} < \tilde{z} < 0.1$.

data are used in the likelihood analysis, and the closer the best-fitting parameter is to the actual value simulated at $z = 0$. As a matter of fact, virtually all the estimates of the cosmographic parameters converge to the simulated values as $\tilde{z}_{\rm min} \to 0$. The statistical uncertainties of the reconstructed parameters decrease as the volume in which the expansion rate fluctuation is calculated grows larger. Note however that estimates for different values of $\tilde{z}_{\rm min}$ are correlated, given the cumulative nature of the binning strategy.

It is important that the likelihood analysis is performed also by fitting the normalization factor $\mathcal{M}$. This quantity could be biased in principle because it contains information on the zero-point calibration of brightness distances. It is also sensitive to possible systematic, distance-dependent errors in the estimation of the distance modulus. If, for conservative reasons, I exclude the $\mathcal{M}$ function from the likelihood analysis, I cannot any more provide an independent estimate of the amplitudes of the monopole and quadrupole of the generalized Hubble parameter $\mathbb{H}$. Only the ratio $\mathbb{H}_2/\mathbb{H}_0$ (shown in the upper right plots in Figure 6.8 and 6.9) can be constrained in this case. By contrast, the accuracy in estimating the multipoles (with $\ell > 0$) of $\mathbb{Q}$ and $\mathbb{J}$ is not affected by the analysis strategy. As a consequence, any systematic miscalibration of the normalization of galaxy distances will not have any impact in the reconstruction of the multipoles of $\mathbb{Q}$ and $\mathbb{J}$.

As shown in Table 6.1 and also in Figures 6.8 and 6.9, the only parameters that are mis-recovered (for $M1$ or $M2$) are $\mathbb{Q}_3$ and $\mathbb{J}_4$. As a consequence of the subdominance of certain multipoles, the only term that contributes to the amplitude of η_3 (cf. eq. (5.50)) is the linear one (i.e. $\mathbb{Q}_3$), while the amplitude of η_4 is effectively determined only by $\mathbb{J}_4$ (cf. eq. (5.51)). Therefore, the theoretical form of the octupole and hexadecapole of the expansion rate fluctuation field is controlled by only one monomial of the redshift, which is a severe limitation in the ability to reproduce the observed redshift evolution of the data. The optimal way to tackle this issue is to include in the analysis the fourth and fifth derivatives of distance (snap and crackle) in the expansion (5.26), as will be shown in the section 6.8.

The velocity $v_o = 320$ km/s of the matter relative to the CMB is reconstructed quite well from the analysis of both simulated catalogs $M1$ and $M2$.

Figure 6.10 shows that the relative error of the best-fitting velocity is about 10% and 7% for the $M1$ and $M2$ scenarios respectively. The same caveat as before applies. If v_o is inferred from the analysis of $\tilde{\eta}$ reconstructed in shells at large distance from the observer, the estimation is affected by large uncertainties. However, as soon as the lower

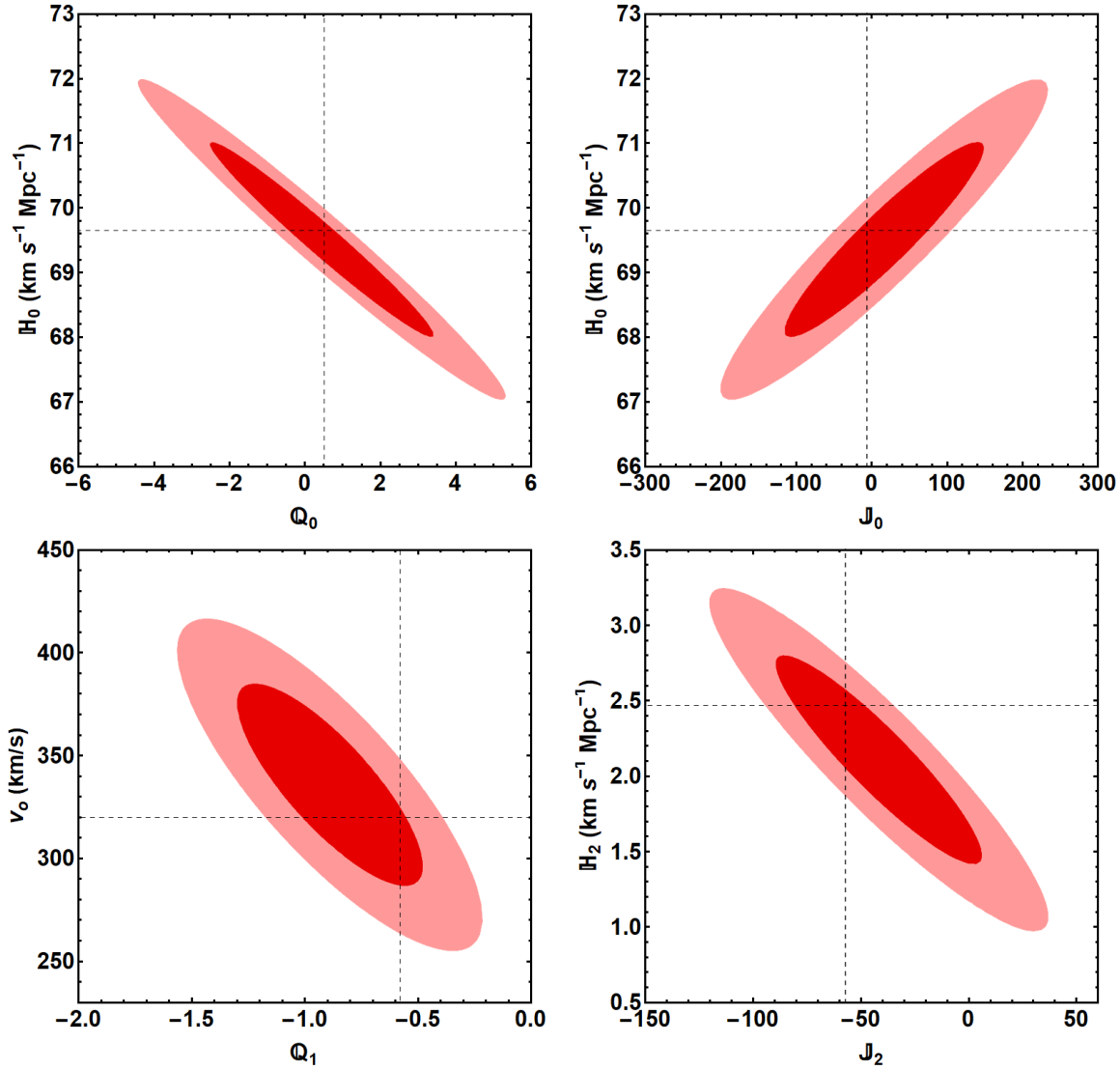


Figure 6.11: The 68% and 95% confidence level contours in various 2D parameter spaces obtained from the likelihood analysis of the $M1$ simulated data ($\tilde{z} < 0.045$). The intersection of the two dashed lines indicates the input value.

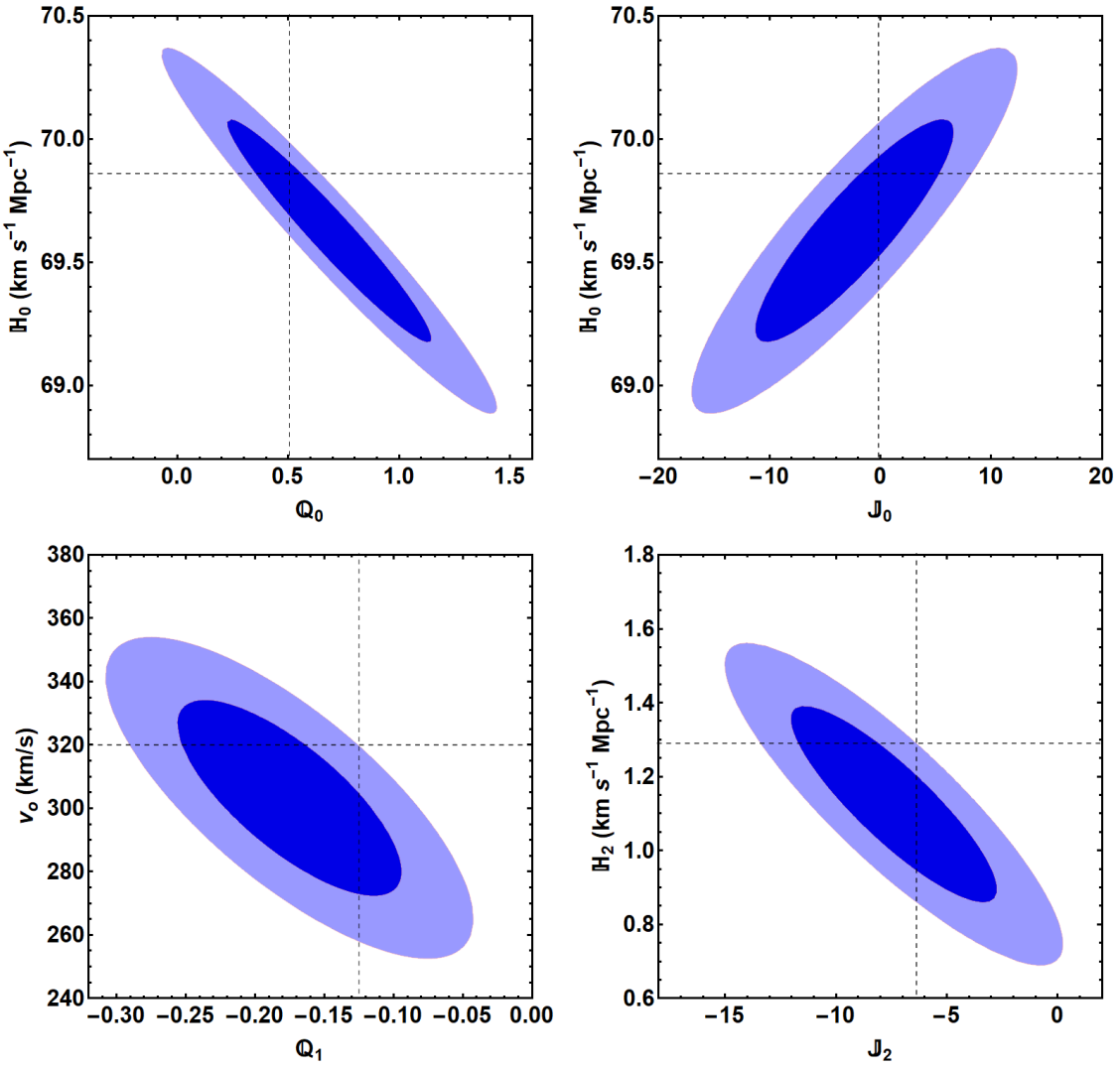


Figure 6.12: The 68% and 95% confidence level contours in various 2D parameter spaces obtained from the likelihood analysis of the $M2$ simulated data ($\tilde{z} < 0.1$). The intersection of the two dashed lines indicates the input value.

boundary $\tilde{z}_{\rm min}$ of the shell in which $\tilde{\eta}$ is reconstructed approaches zero, the estimates of the local covariant cosmographic parameters stabilize and in the limit converge to the input simulated values.

Parameter estimation is clearly affected by statistical degeneracies. These are visible in Figures 6.11 and 6.12 which show the 2-dimensional 68% and 95% likelihood contours of relevant cosmographic parameters. The analysis of $M1$ and $M2$ suggests that the accuracy of statistical inference depends critically on the structure of the expansion rate fluctuations, rather than on the quality and precision of the distance measurements. The higher the redshift at which the cosmographic expansion breaks down, i.e., the wider the redshift interval in which the amplitude of η can be approximated in a model-independent way by an expansion in powers of z, the smaller the uncertainties in the recovered cosmographic parameters. The smoother and more spread over a large volume are the perturbations in the local expansion rate (model $M2$), the better the precision of the recovered parameters will be – compared to the case where large perturbations are close to the observer's position (model $M1$).

Nevertheless, even in the latter 'pessimistic scenario', data from a future survey like the ZTF are sufficient to constrain the relevant covariant cosmographic parameters with a fair degree of precision. The parameters that one expects to better reconstruct are the local value of the monopole of the covariant Hubble parameter $\mathbb{H}_0$ (with an optimistic/ pessimistic resolution of 0.3/1.0 km s^{-1} Mpc^{-1}), the quadrupole of $\mathbb{H}$ ($\sim 4\sigma$ detection in the pessimistic scenario, i.e., a relative uncertainty of 24%), and the dipole in $\mathbb{Q}$, which is recovered with nearly a 33% precision under the most conservative assumptions.

The degree of reliability of the predictions depends strictly on the degree of realism of the analytical model. The constraints on the multipoles of the covariant cosmographic parameters could deviate from expectations even if the specific parameters of future surveys were significantly different from those simplistically assumed in this study. Nevertheless, the results obtained are encouraging and suggest the possibility of obtaining fairly precise estimates of the covariant cosmographic parameters at scales ($z \lesssim 0.1$) where the CP ceases to be applicable, and of characterising the expansion rate of the local universe in a more meaningful and complete way than is possible using the H_0 parameter of the Standard Model alone.

6.6 Limits of the cosmographic expansion

The tensorial expansion of redshift as a function of distance, which lies at the heart of covariant cosmography, demands smoothness and single-valuedness. Therefore, the applicability of these assumptions in the local, non-linearly perturbed universe must be critically analyzed.

The luminosity distance d_L to a source at redshift z depends on the direction of the line of sight, whether calculated in a model-independent cosmographic approach or in a linearly perturbed FLRW model. In Figure 6.13, I display its redshift scaling in the direction of the center of the mass overdensity ($\theta = 0$), and the opposite direction ($\theta = \pi$), for the matter- and CMB-comoving observers, at a distance of $r_o = 200\,$Mpc from the density peak of the $M1$ model.

The luminosity distance shows a characteristic elongated S-shaped trend along the observer's line of sight, bending approximately at the position of the density peak. This feature is induced by the radial component of the peculiar velocity of the emitters – which increases/ decreases relative to the background cosmological value for the observed

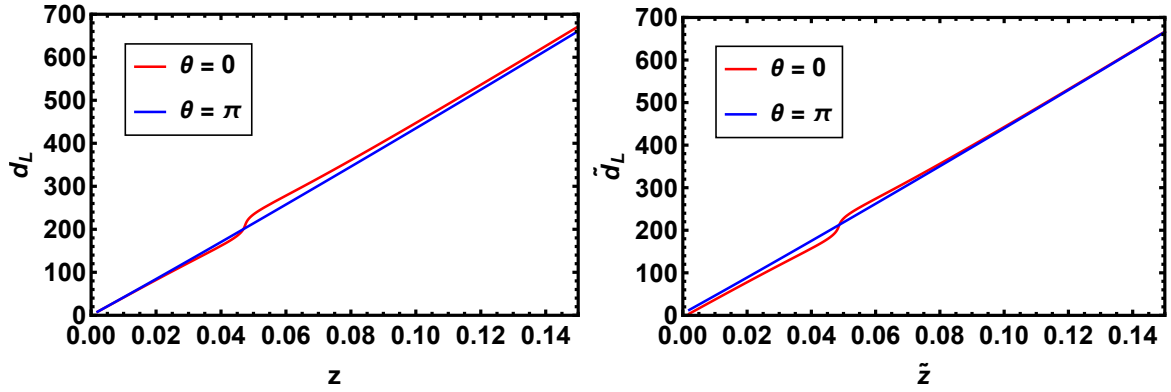


Figure 6.13: Luminosity distance in the $M1$ model, calculated using linear perturbation theory for a matter-comoving observer (left) and a CMB-comoving observer (right). The scaling with redshift along two different line-of-sight directions is shown: towards the center of the density peak ($\theta = 0$, solid red line) and in the antipodal direction ($\theta = \pi$, solid blue line).

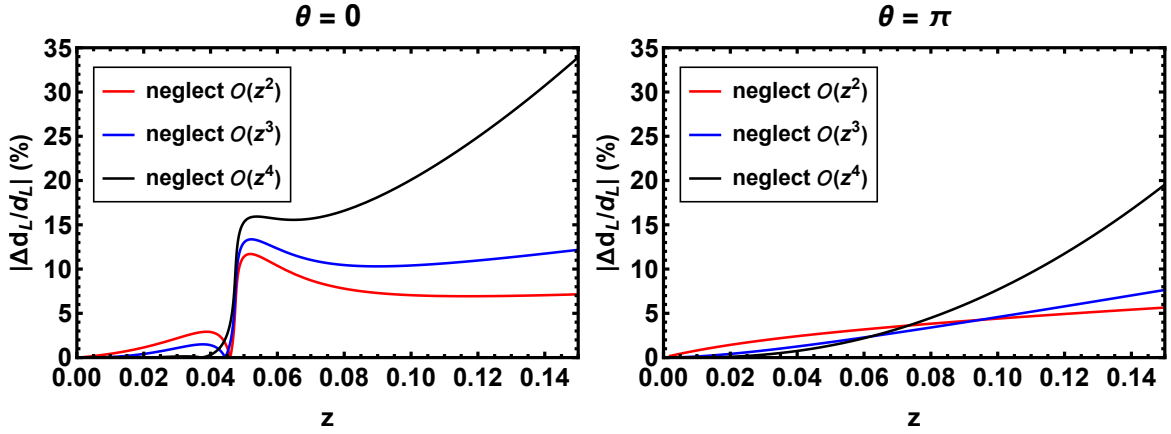


Figure 6.14: The relative discrepancy between different orders of expansion of the luminosity distance (measured by a matter comoving observer) and the true input value (model $M1$), in the direction of the center of the density peak (left) and in the opposite direction (right).

redshift of a source placed before/ after the density peak. If the density peak is sufficiently large (not far from our δ_c), the luminosity distance becomes a multivariate function of z, and the validity of the cosmographic expansion breaks down. Even before reaching this pathological configuration, the more nonlinear the density field, the poorer becomes the reconstruction of the distance using only lower-order expansion terms.

Figure 6.14 compares the luminosity distance reconstructed using the cosmographic approach against that reconstructed using linear perturbation theory. The relative discrepancy is shown along two line-of-sight directions ($\theta = 0$ and $\theta = \pi$) and for different expansion orders in redshift.

The cosmographic expansion of d_L, eq. (5.26), works extremely well locally, around the observer, and along any line of sight. It improves the higher the order of expansion is. However, already at relatively low redshifts, $z \approx 0.05$ in the case of the $M1$ model, its accuracy is severely limited if the field is dominated by a nearby large density peak. In this configuration, the luminosity distance deviates considerably from linearity and the

cosmographic parameters acquire a large amplitude to allow an accurate description of these distortions in regimes where $z \ll 1$.

In fact, a truncated polynomial expansion at a low order is ineffective in capturing these nonlinear features. It is therefore essential to know at what scales the covariant cosmographic expansion fails if it is to be successfully applied in the highly irregular regions of the local Universe. As expected, if the gravitational source is located far from the observer, as in the case of the $M2$ model, the redshift range in which cosmography can be safely applied increases accordingly. The combined analysis of the independent multipoles of η, as explained in the previous section, makes it easy to identify the scale at which the covariant cosmographic approach breaks down.

6.7 Multipoles of the radial peculiar velocity field

After showing how to recover model-independent information about the spacetime surrounding the observer, I move on to interpret $\tilde{\eta}$ anisotropies in a more conventional framework, as small deviations from the FLRW metric. In this scenario, fluctuations in $\tilde{\eta}$, instead of providing information on the covariant cosmographic parameters, and thus on the geometric structure of the geodesic congruence representing the cosmic fluid, simply give an insight into the amplitude and distribution of the radial peculiar velocity field, $v_n \equiv \boldsymbol{v} \cdot \boldsymbol{n}$, of galaxies relative to an idealized matter frame – which coincides with the CMB frame in perturbed FLRW. If we ignore the gravitational potential in the perturbed FLRW model, we have $\tilde{z} = \bar{z} + v_n(1+\bar{z})$ and $\tilde{d}_L = d_L^{\rm c}(1+2v_n)$. As a consequence, we can express $\tilde{\eta}$ as

$$\tilde{\eta} = \log\left[\frac{\bar{z} + v_n(1+\bar{z})}{\bar{d}_L(1+2v_n)}\right] - \tilde{\mathcal{M}} = \log\left(\frac{\bar{z}}{\bar{d}_L}\right) - \tilde{\mathcal{M}} + \log\left[1 + \frac{v_n}{\bar{z}}(1-\bar{z})\right]. \tag{6.32}$$

If $v_n \ll \tilde{z}$, the multipoles of the radial component of the peculiar velocity field are related to the multipoles of the expansion rate fluctuations field $\tilde{\eta}$ (for $\ell > 0$) as

$$v_{n\ell}(\tilde{z}) = \tilde{\eta}_\ell(\tilde{z})\, \tilde{z}\, \ln 10\,. \tag{6.33}$$

The average of the multipoles of v_n over a spherical volume of radius R is

$$\langle v_{n\ell}\rangle_R = \frac{\ln 10}{V(R)} \int_0^{\tilde{z}(R)} \tilde{\eta}_\ell\, \tilde{z}\, \mathrm{d}V\,, \tag{6.34}$$

where $\tilde{z}(R) \approx H_0 R$, and V is the volume. Note that $\langle v_{n1}\rangle_R \equiv v_{\rm b}$ (see section 3.2.2) corresponds to what is traditionally called in the literature the bulk velocity (cf. eq. (2) in [199]) that is a measure of the common radial streaming velocity shared by all the fluid elements inside the given region. To avoid possible confusion, it is worth stressing that v_o, the observer velocity with respect to CMB (see section 5.3.1), is not conceptually, and does not coincide numerically, with the bulk velocity of a spatial volume. Nevertheless, when the volume inside which the bulk velocity is reconstructed is decreased, i.e., when $R \to 0$, the bulk velocity of matter in that volume well approximates the motion of the matter observer relative to the CMB frame.

Figure 6.15 shows how the reconstructed bulk velocity and the average higher multipoles of the radial velocity field, estimated using eq. (6.34), compare with the simulated

values. The evolution, for both small-scale and large-scale velocity models, is shown as a function of the radius R of the spherical volume over which data are averaged. Note that in model $M1$ the bulk velocity decreases sharply once the averaging volume becomes large enough to contain the density fluctuation generating the peculiar motions. The bulk velocity becomes negative when the radius of the volume in which it is reconstructed becomes larger than the distance (from the observer) of the dominant inhomogeneity generating the peculiar velocity field. A similar fast asymptotic transition also characterizes the volume average of the quadrupole and octupole of the radial velocity fields. These latter quantities vanish if the volume becomes sufficiently large to contain the dominant inhomogeneity.

By contrast, in model $M2$ the slow decrease of the bulk velocity with the depth of the survey is accompanied by a systematic increase of the higher velocity moments. This is because the latter systematically peak at about the position of the large mass concentration that generates the streaming motions. Higher-order moments in the expansion rate fluctuations field η are therefore instrumental in investigating the structure and extent of density inhomogeneities, making it possible to complement or corroborate evidence about the convergence (or not) of matter flows in large regions of the Universe.

Figure 6.15 (upper panel) also shows the bulk velocity defined as the volume average of the three-dimensional peculiar velocity vectors (see eq. (1) in [199]) as opposed to that reconstructed from the radial component alone. Interestingly, the two estimates converge up to the common scales where both the quadrupole and octupole of the radial velocity field stop growing in a monotonic manner and reverse. In volumes with radii larger than this scale, the estimate obtained from the radial component of the peculiar velocities systematically underestimates the bulk velocity reconstructed from 3D information. I need further analysis whether this is a generic conclusion or depends on the specific asymmetric configuration of the model considered.

6.8 Incorporating the snap

As shown in section 6.5, the estimation of the dipole and octupole are biased if the luminosity distance expansion is truncated at third order in redshift. A major result was that including the often-overlooked local motion of the observer relative to matter as a free parameter helps to debias the dipole estimate, but does not correct the systematic shift of the octupole. Indeed, in this expansion approximation, the octupoles of the third-order covariant cosmographic parameters, the jerk $\mathbb{J}$ and the curvature $\mathbb{R}$, which are systematically multiplied by z^3, provide small contributions and do not improve the likelihood analysis. In this section, I tackle this issue by including the fourth-order covariant cosmographic parameter, the snap $\mathbb{S}$.

First, complementing equations (6.9–6.23), the multipoles of the snap $\mathbb{S}_\ell$ at linear order for the analytical model introduced in section 6.1 using the equation (5.31) are

$$\mathbb{S}_0 = -\frac{7}{2} - \frac{\delta_c \left[200\xi_H^2 \left(\xi_o^2+1\right)^2 \xi_o^3 - 81\xi_o^7 + 54\xi_o^5\right]}{30\xi_H^2 \left(\xi_o^2+1\right)^{7/2}}, \tag{6.35}$$

$$\mathbb{S}_1 = -\frac{9\delta_c \xi_o^4}{35\xi_H^3 \left(\xi_o^2+1\right)^{9/2}} \left[63\xi_H^2 \left(\xi_o^2+1\right)^2 + 25\left(5\xi_o^2-2\right)\xi_o^2\right], \tag{6.36}$$

$$\mathbb{S}_2 = \frac{10}{21}\delta_c \xi_o^3 \left[\frac{-27\xi_o^2/\xi_H^2 - 28\left(\xi_o^2+1\right)^2\left(3\xi_o^2+4\right)}{\left(\xi_o^2+1\right)^{7/2}} + 84\,\mathrm{csch}^{-1}\left(\xi_o\right)\right], \tag{6.37}$$

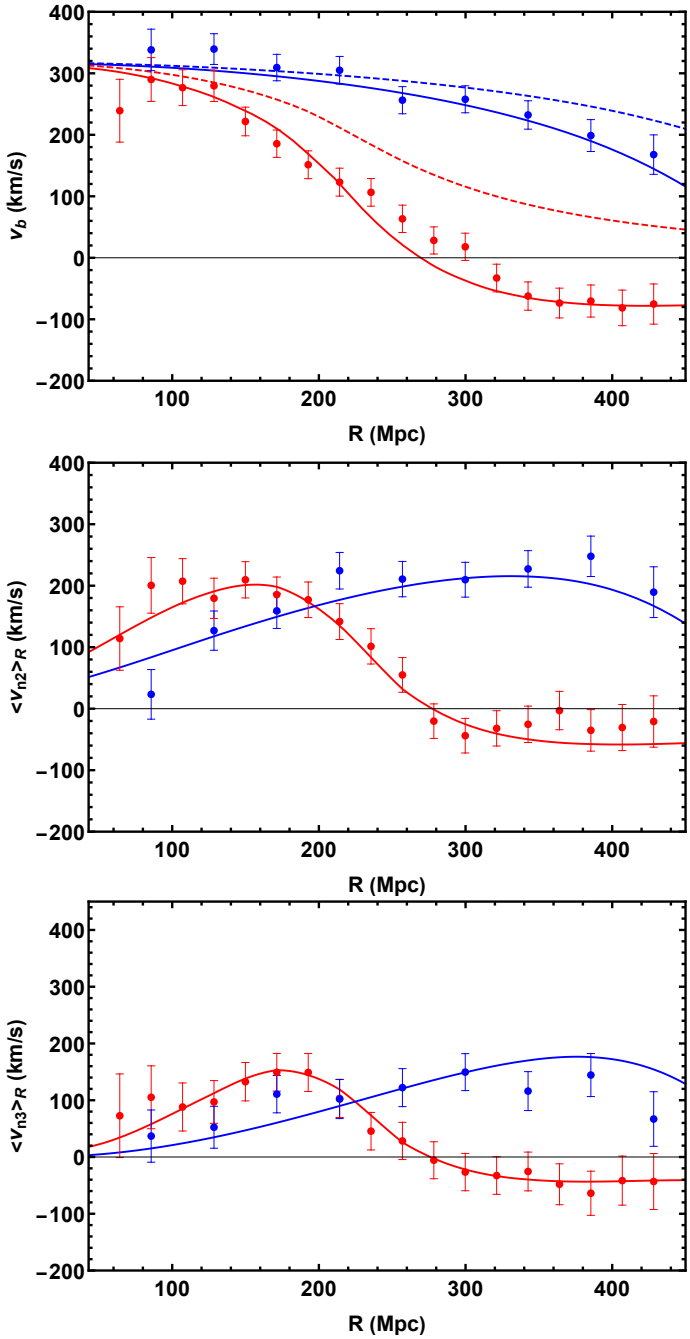


Figure 6.15: The bulk velocity $v_{\rm b} = \langle v_{n1} \rangle_R$ *(left)*, together with the mean value of the quadrupole *(centre)* and octupole *(right)* of the peculiar radial velocity field, estimated using eq. (6.34), are shown as a function of the radius R of the averaging volume. Dots represent the value inferred from discrete sampling (15,000 objects), while the continuous lines represent the underlying continuous field value. The red/ blue colors indicate results from the $M1/M2$ simulations. The dashed curves in the left panel present the estimates of the bulk velocity reconstructed by averaging the $3D$ peculiar velocity field, $v_{\rm b} = \langle v \rangle_R$.

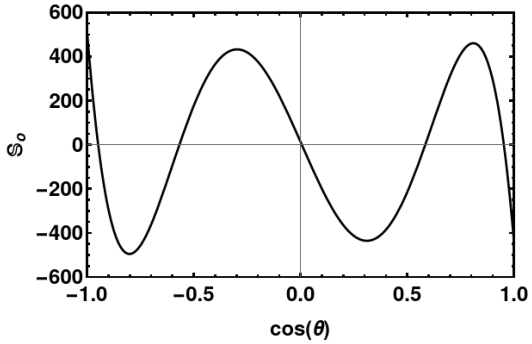


Figure 6.16: The snap parameter for the analytical model $M2$, as a function of $\cos\theta$.

$$\mathbb{S}_3 = \frac{4\delta_c\xi_o^4}{15\xi_H^3}\left[\frac{175\xi_o^2 - 6\xi_H^2\left(\xi_o^2+1\right)^2\left(15\xi_o^4+35\xi_o^2+23\right)}{\left(\xi_o^2+1\right)^{9/2}} + 90\,\xi_H^2\,\mathrm{csch}^{-1}\left(\xi_o\right)\right], \tag{6.38}$$

$$\mathbb{S}_4 = \frac{12\delta_c\xi_o^5}{35\xi_H^2}\left[\frac{-7\left(15\xi_o^4+50\xi_o^2+58\right)\xi_o^2 - 176}{\left(\xi_o^2+1\right)^{7/2}} + 105\,\mathrm{csch}^{-1}\left(\xi_o\right)\right], \tag{6.39}$$

$$\mathbb{S}_5 = \frac{8\delta_c\xi_o^6}{21\xi_H^3}\left[\frac{3\left(105\xi_o^6+455\xi_o^4+756\xi_o^2+582\right)\xi_o^2+563}{\left(\xi_o^2+1\right)^{9/2}} - 315\,\mathrm{csch}^{-1}\left(\xi_o\right)\right]. \tag{6.40}$$

In this section, I calculate the amplitude of the snap parameter and its multipoles only for the $M2$ model 6.30. Figure 6.16 shows the snap parameter for the model as a function of $\cos\theta$, computed by using the equation (5.31). The true values for the multipoles of the snap are $(-4.8,\ 93,\ -9,\ 363,\ 29,\ -936)$ for $\ell = 0$ to $\ell = 5$. The multipoles $\ell = 1$, 3 and 5 are dominant relative to the others since they have higher-order spatial derivatives as discussed in section 5.2. This clearly appears in eqs. (6.35)–(6.40), where the dominant multipoles have ξ_H^3 in the denominator but not the others.

Moreover, I assess how well these theoretical predictions describe simulated data using a χ^2 statistical analysis, following the procedure detailed in section 6.5. To this end, I randomly sample the analytical $M2$ model to construct a mock catalog of $N = 30,000$ redshift and distance measurements for objects isotropically distributed across the sky. The distribution in redshift and the error in the distance modulus are similar to those presented in section 6.5. However, for the purpose of this section, I simulate the observation with respect to a matter comoving observer for simplicity. Figure 6.17 shows the likelihood of the reconstructed monopole and dominant multipoles of the snap for model $M2$. By adding the snap correction, the estimation of the dominant multipoles up to $\ell = 3$ is unbiased, although this comes at the cost of larger error contours in the recovered parameters. As a rule of thumb, should one consider a survey with a different number N, the errors must be re-scaled by a factor of $\sim \sqrt{30,000/N}$.

Here, as after adding the snap, $\mathbb{Q}_3$ is no longer biased, $\mathbb{J}_4$ remains unaffected because $\mathbb{S}_4$ is not dominant and can be neglected. Therefore, to avoid the bias in $\mathbb{J}_4$, one needs to add the crackle, i.e., the fifth-order covariant cosmographic parameter. However, Figure 6.17 also shows that the recovered amplitude of the multipole $\mathbb{S}_5 = -170 \pm 68$ is significantly different from the input value (-936). In the same spirit advocated in this paper, to correct for this residual discrepancy, a higher-order expansion, to $\mathcal{O}(z^6)$, of the distance as a function of redshift is needed. The inclusion of the pop (sixth-order covariant cosmographic parameter) would help unbias the snap multipole $\ell = 5$.

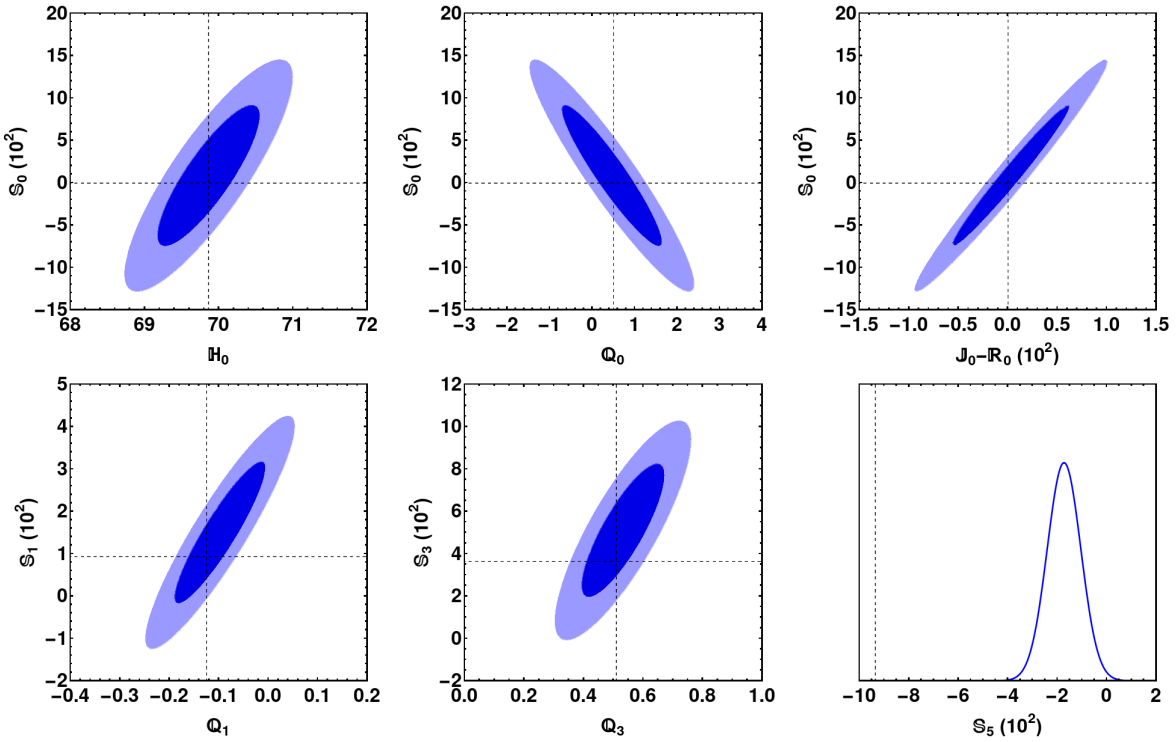


Figure 6.17: Likelihood of the multipoles of the snap as reconstructed for the analytical model $M2$. The intersection of the dashed lines presents the true input value. The subscript on the cosmographic parameters indicates the multipole ℓ.

6.9 Conclusion

The formalism is developed in such a way that it is straightforward to adapt it to observations carried out in a reference frame which is comoving with matter or in an arbitrary frame boosted with respect to it. It is crucial to carefully characterize the frame in which data is observationally measured and the frame in which quantities are theoretically characterized. I show that it is practical to estimate the η signal in the CMB frame, the frame of an observer who measures no CMB dipole, whatever the physical origin of that dipole is. At the same time, it is theoretically more convenient and natural to interpret the physical content of the signal in the matter frame, that of an observer at rest with respect to the surrounding matter fluid.

By exploiting a simple analytical model of metric perturbations, I highlight the virtues and also the limitations of a power series expansion of η as a function of redshift. Surprisingly, I find that the cosmographic expansion works well even in the local Universe, where large deviations in the distance-redshift relation, induced by density fluctuations, are expected. In particular, I show how to use the redshift evolution of η multipoles to identify the redshift intervals where the cosmographic expansion breaks down and those where a meaningful theoretical inference can be made.

By randomly sampling the continuous analytical model, I simulate all-sky catalogs of distances. I use them to assess the precision and accuracy with which future datasets, such as that under collection by the ZTF survey, will constrain the velocity of the observer (relative to the surrounding matter frame) and the multipoles of the covariant cosmographic parameters.

I found the multipoles of the estimation of the cosmographic parameters when the

expansion of the distance is truncated up to the third order in redshift is not biased except for the octupole of the deceleration parameter $\mathbb{Q}$ and hexadecapole of the jerk $\mathbb{J}$. That motivates us to go to the higher order to incorporate the snap. I have verified this prediction, showing that the inclusion of the snap term does indeed improve the likelihood of both the dipole $\mathbb{Q}_1$ and octupole $\mathbb{Q}_3$ of the deceleration parameter (see Figure 6.17) but not $\mathbb{J}_4$. The reason for this is now clearer. As discussed in section 5.2 and shown in Table 5.1, the dominant multipoles of the snap $\mathbb{S}$ are precisely $\ell = 0$, 1, 3 and 5, in accordance with $\ell = 0$, 1 and 3 for the case of the deceleration $\mathbb{Q}$. On the other hand, the dominant multipoles for the jerk $\mathbb{J}$ are $\ell = 0$, 2 and 4 – explaining why the inclusion of these terms had only a minor effect on reducing the bias in $\mathbb{Q}_{1,3}$. Following this same logic, one may expect that, in order to improve the bias found in the multipole $\mathbb{J}_4$, requires fifth-order term (the crackle). Given the finite amount of data, this will be a task for the future.

I also explore the cosmological potential of a more conventional analysis, in which the η signal is interpreted in the context of the standard cosmological model. I show that in this case, the multipoles of η provide insights into the amplitude of the multipoles of the radial peculiar velocity field of galaxies. Notably, the dipole of η extracted in a given volume V is proportional to the amplitude of the bulk motion on that characteristic scale.

Chapter 7

Estimation of the cosmographic parameters of the local universe

In Chapter 5, I introduced the theoretical ground leading to the cosmographic approach. Then, in Chapter 6, I designed a strategy to show that the expansion rate fluctuation field allows to estimate the cosmographic parameters. In the current Chapter, I will apply this inference scheme to the Cosmicflows-4 and Pantheon+ (see section 4.1) datasets.
Since cosmographic parameters are defined within general spacetime, their multipoles can be linked to any proposed model of the local universe. As a result, the constraints derived from these parameters serve as a powerful and efficient tool for investigating such models.

A few studies have presented preliminary results on a limited set of cosmographic parameters based on recent datasets, such as [111], which used the Pantheon and JLA samples, and [179], which utilized Pantheon+. However, to properly compare these analyses with the one I present in this chapter and to grasp the fundamental differences, it is important to highlight the significance of the chosen reference frame. While any frame can, in principle, be used, it is crucial to account for the observer's velocity relative to the matter rest frame as a new degree of freedom to be determined. As discussed in Chapters 5 and 6, this consideration is essential for estimating the covariant cosmographic parameters in an unbiased manner.

In the first section 7.1, I introduce the method for estimating the cosmographic parameters. In section 7.2, I analyze the evolution of the axially symmetric multipoles with redshift, using smaller redshift shells compared to Chapter 4, which provides a higher-resolution view of this evolution. Next, I present the best-fit values of the cosmographic parameters for different samples, along with the velocity of the matter comoving observer relative to the CMB frame. I then discuss the physical relevance of these results and examine the structure of the local universe that may explain them. Conclusions are provided in section 7.3.

7.1 Estimating the cosmographic parameters

I start estimating the Legendre coefficients of the expansion rate fluctuation field $\tilde{\eta}_\ell$ by means of the maximum likelihood method described at the end of section 4.2.1. The highest multipole included in the Legendre expansion is the hexadecapole ($\ell = 4$). Indeed, as discussed in Chapter 4, the 32-pole multipole ($\ell = 5$) is weak and its amplitude is statistically insignificant.

In contrast to the previous chapter, while I estimate the monopole $\tilde{\mathcal{M}}$, I do not

include it in the fitting process, making the results independent of the absolute calibration of distances. This approach helps to avoid biases arising from zero-point calibration systematics across different samples. The inclusion of the monopole will be explored in future studies. This conservative choice leads to degeneracies between certain multipoles of the cosmographic parameters. In particular, the monopole of $\mathbb{H}$ cannot be constrained, and the quadrupole of $\mathbb{H}$ cannot be directly measured. Instead, I can only determine the ratio between the quadrupole and the monopole of $\mathbb{H}$. Furthermore, at third order in the expansion of $\tilde{\eta}_\ell$, instead of directly measuring the dipole and octupole of the snap, I can only estimate the combinations $\mathbb{S}_1 + 4\mathbb{Q}_1(2\mathbb{J}_0 - \mathbb{R}_0)$ and $\mathbb{S}_3 + 4\mathbb{Q}_3(2\mathbb{J}_0 - \mathbb{R}_0)$ (see equations 5.48–5.51).

Therefore, the number of parameters that need to be fitted is 9 including the velocity of the matter observer with respect to CMB frame v_o (see eq. (5.55)):

$$\boldsymbol{X} = \{\mathbb{H}_2/\mathbb{H}_0, \mathbb{Q}_0,\ \mathbb{Q}_1,\ \mathbb{Q}_3,\ \mathbb{J}_2,\ \mathbb{J}_4,\ \mathbb{S}_1 + 4\mathbb{Q}_1(2\mathbb{J}_0 - \mathbb{R}_0),\ \mathbb{S}_3 + 4\mathbb{Q}_3(2\mathbb{J}_0 - \mathbb{R}_0),\ v_o\}\,. \quad (7.1)$$

I first estimate the Legendre coefficients $\tilde{\eta}_\ell$ in each redshift bin, as described in section 4.2.1, and then use these to infer the cosmographic parameters by minimizing the χ^2

$$\chi^2(\boldsymbol{X}) = \sum_{i=1}^{N_{\rm shells}} \boldsymbol{\Delta\tilde{\eta}}^T(i)\, \boldsymbol{\psi}(i)\, \boldsymbol{\Delta\tilde{\eta}}(i) \quad (7.2)$$

where $\boldsymbol{\Delta\tilde{\eta}}(i)$ is a vector with an index ℓ, with elements $\Delta\tilde{\eta}_\ell(i) = \tilde{\eta}_\ell(i) - \tilde{\eta}_\ell^{(\rm model)}(\tilde{z}_i, \boldsymbol{X})$, where $\tilde{\eta}_\ell(i)$ is the measured multipole of $\tilde{\eta}$ for the i-th shell, and $\tilde{\eta}_\ell^{(\rm model)}(\tilde{z}_i, \boldsymbol{X})$ is the theoretical model (equations 5.48–5.51 with 5.55). The matrix $\boldsymbol{\psi}(i)$ is the inverse of the covariance matrix between the multipoles in the i-th shell, and it is calculated as shown in section 4.2.1. The number of shells I use is 18 for CF4, 9 for CF4SN, CF4TF, and CF4FP, and 5 for Pantheon+ (see section 4.1). These choices optimize the number of objects within each shell for each sample.

Note that in Chapter 6 (eq. 6.31) I assumed that the precision matrix was diagonal which is well supported by the fact that the distribution of sources on the sky is close to be isotopic. Instead, in the present Chapter, the skycoverage in some redshift bins is not isotropic which introduces a non-negligible amount of correlation between the estimated multipoles. Thus, the precision matrix is not expected to be diagonal, so I will keep all its contributions to the χ^2 as shown in eq. (7.2).

The choice of the direction for the axis of symmetry is needed for estimating the Legendre coefficients of $\tilde{\eta}$ and subsequently determining the cosmographic parameters. Including the direction as a free parameter in the χ^2 in (7.2) is computationally expensive, since the observable $\tilde{\eta}(i)$ depends on this direction through a complex relationship, making the χ^2 function difficult to minimize.

Therefore, it is easier to start with a fixed direction before minimizing the χ^2. I do this by considering all possible directions and, each time, I calculate

$$\chi^2_{\rm total} = \sum_{i=1}^{N} \left(\frac{\tilde{\eta}_i - \sum_{\ell=1}^{\ell_{\rm max}=4} \tilde{\eta}_\ell^{\rm model}(\tilde{z}_i, \boldsymbol{X})}{\sigma_\eta} \right)^2 ,$$

and finally select the direction that yields the minimum $\chi^2_{\rm total}$ which I find to be $(l, b) = (299, 5)$. For this $\chi^2_{\rm total}$, I do not use binning and instead use the complete CF4 sample, which is the largest sample and includes the others, and so I assume the same direction

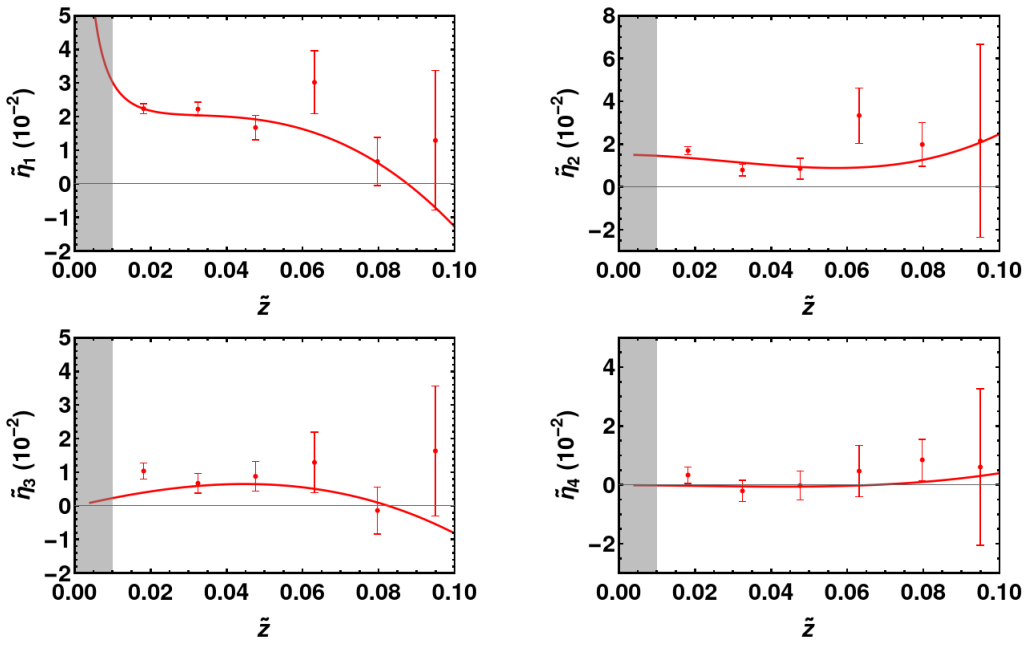


Figure 7.1: The Legendre coefficients of the expansion rate fluctuation field in CMB frame $\tilde{\eta}_\ell$ up to $\ell = 4$ for CF4 in redshift range $0.01 < \tilde{z} < 0.1$, with the best-fit curves using the relations 5.48–5.51 with the relation 5.55. The best-fit cosmographic parameters are shown in Table 7.1. For presentation purposes, I show here binning that yields 6 shells in redshift, which differs from the binning used to estimate the cosmographic parameters for CF4, where I use 18 shells.

for all the samples.

7.2 Results

I begin by focusing on the CF4 sample, which I can subdivide into a large number of redshift bins. In Figure 7.1, I present the estimated multipoles for CF4 along with the best-fit model using relations 5.48–5.51 and 5.55. The corresponding estimated cosmographic parameters are listed in the second column of Table 7.1 for CF4.

I do not present the results for the monopole $\mathbb{Q}_0$, even though I included it in the fitting process since it appears in the η_1 expression in equation (5.48); however, it remains unconstrained without utilizing $\mathcal{M}$. Additionally, while I use 18 redshift shells to estimate the cosmographic parameters for CF4, I display a different binning in Figure 7.1 for presentation purposes (only 6 redshift shells).

The dipole $\tilde{\eta}_1$ appears to be constant up to $\tilde{z} \sim 0.06$ (see Figure 7.1), indicating that this dipole cannot be eliminated simply by boosting the observer. Indeed, the dipole that is spuriously induced in an isotropic universe by the observer's motion has an amplitude that scales inversely with redshift (see eq. 5.55). This suggests the presence of an intrinsic dipole induced by the kinematics of expansion, with its structure described by the covariant deceleration parameter. Indeed, In addition to the reference frame effects, incorporated in the signal $v_o \approx 171 \pm 24$, I also find that the dipole of $\tilde{\eta}$ is sourced by $\mathbb{Q}_1 \approx 2.5 \pm 0.5$.

The dipole in $\tilde{\eta}$ seems to decrease after a redshift of 0.06, although the large error bars

Sample	CF4	CF4SN	CF4TF	CF4FP	Pantheon+
$\mathbb{H}_2/\mathbb{H}_0$ (10^{-2})	3.5 ± 0.5	0.3 ± 1.0	2.4 ± 0.8	4.9 ± 1.4	0.2 ± 1.0
$\mathbb{Q}_1$	2.5 ± 0.5	3.0 ± 1.1	2.0 ± 1.7	3.3 ± 1.1	-0.3 ± 2.0
$\mathbb{Q}_3$	1.2 ± 0.4	1.8 ± 0.9	1.3 ± 1.0	1.5 ± 0.8	-0.3 ± 1.4
$\mathbb{J}_2$	-60 ± 60	83 ± 131	-26 ± 114	-255 ± 113	-132 ± 124
$\mathbb{J}_4$	-2 ± 30	-60 ± 120	-97 ± 177	-51 ± 47	-185 ± 151
$\mathbb{S}_1 + 4\mathbb{Q}_1(2\mathbb{J}_0 - \mathbb{R}_0)$	4328 ± 1382	5206 ± 2507	863 ± 5791	6478 ± 4332	-1750 ± 6580
$\mathbb{S}_3 + 4\mathbb{Q}_3(2\mathbb{J}_0 - \mathbb{R}_0)$	2883 ± 1622	3685 ± 2750	2103 ± 6829	6364 ± 5541	-3493 ± 6650
v_o (km/s)	171 ± 24	100 ± 62	179 ± 51	232 ± 77	327 ± 118

Table 7.1: The covariant cosmographic parameters and v_o for different samples using the range $0.01 < \tilde{z} < 0.1$.

make it challenging to assess this conclusion with a high level of confidence. Furthermore, the best-fit curve shown in Figure 7.1 (upper left panel) is decreasing near $\tilde{z} = 0.1$, suggesting that the third term in the expansion of $\tilde{\eta}_1$ (see eq. 5.48) is negative, which implies that the dipole of the snap is positive.

The quadrupole $\tilde{\eta}_2$ also appears to be constant up to $\tilde{z} \sim 0.06$, indicating that the quadrupole of $\mathbb{H}$ ($\mathbb{H}_2/\mathbb{H}_0 = 3.5 \pm 0.5$) is the dominant contribution compared to the quadrupole of the jerk ($\tilde{\eta}_2 \approx \mathbb{H}_2/(\mathbb{H}_0 \ln 10)$), as shown in Table 7.1. At higher redshift, despite larger error bars, the best-fit curve suggests that the quadrupole is increasing, contrary to the dipole.

The best-fit model to the octupole $\tilde{\eta}_3$ is increasing (see the lower left panel of Figure 7.1), reaching a maximum around $\tilde{z} \sim 0.05$, and then decreases. The increase is related to the positive sign of the octupole of $\mathbb{Q}$ ($\mathbb{Q}_3 \approx 1.2 \pm 0.4$), while the decrease is associated with the positive sign of the octupole of the snap. Regarding the hexadecapole, it is consistent with zero for all the redshift shells, indicating no signal in the hexadecapole of the jerk, as presented in Table 7.1.

The observation that the dipole and octupole change their behavior around $\tilde{z} = 0.1$ may indicate the presence of a structure, a phenomenon typically associated with a spherical overdensity at around $\tilde{z} = 0.1$ (see section 6.4). However, the quadrupole does not exhibit a similar abrupt change in behavior, making it challenging to draw definitive conclusions. More precise measurements at redshifts greater than 0.06 would be necessary to strengthen this assessment.

Table 7.1 summarizes the results obtained from fitting the cosmographic parameters to the other datasets: CF4SN, CF4TF, CF4FP, and Pantheon+. It indicates that the quadrupole-to-monopole ratio of $\mathbb{H}$ is compatible at the 3σ level across the datasets. However, the two Supernova samples appear to suggest a lower amplitude, despite being characterized by a large uncertainty.

Additionally, it is evident that for what concerns the other cosmographic parameters, only CF4 shows a significant detection (greater than 3σ) of $\mathbb{Q}_1$ and of the combination $\mathbb{S}_1 + 4\mathbb{Q}_1(2\mathbb{J}_0 - \mathbb{R}_0)$.

Figure 7.2 shows the marginalised posterior distribution of the covariant cosmographic parameters. The contours represent the 68% and 95% confidence level regions, revealing degeneracies between the parameters. The combination $\mathbb{S}_1 + 4\mathbb{Q}_1(2\mathbb{J}_0 - \mathbb{R}_0)$ is highly correlated with the dipole $\mathbb{Q}_1$. Additionally, the relative velocity v_o exhibits significant degeneracy with $\mathbb{Q}_1$, with the axis of degeneracy showing some dependence on the sample being analyzed. The clear overlap of the contours demonstrates substantial agreement

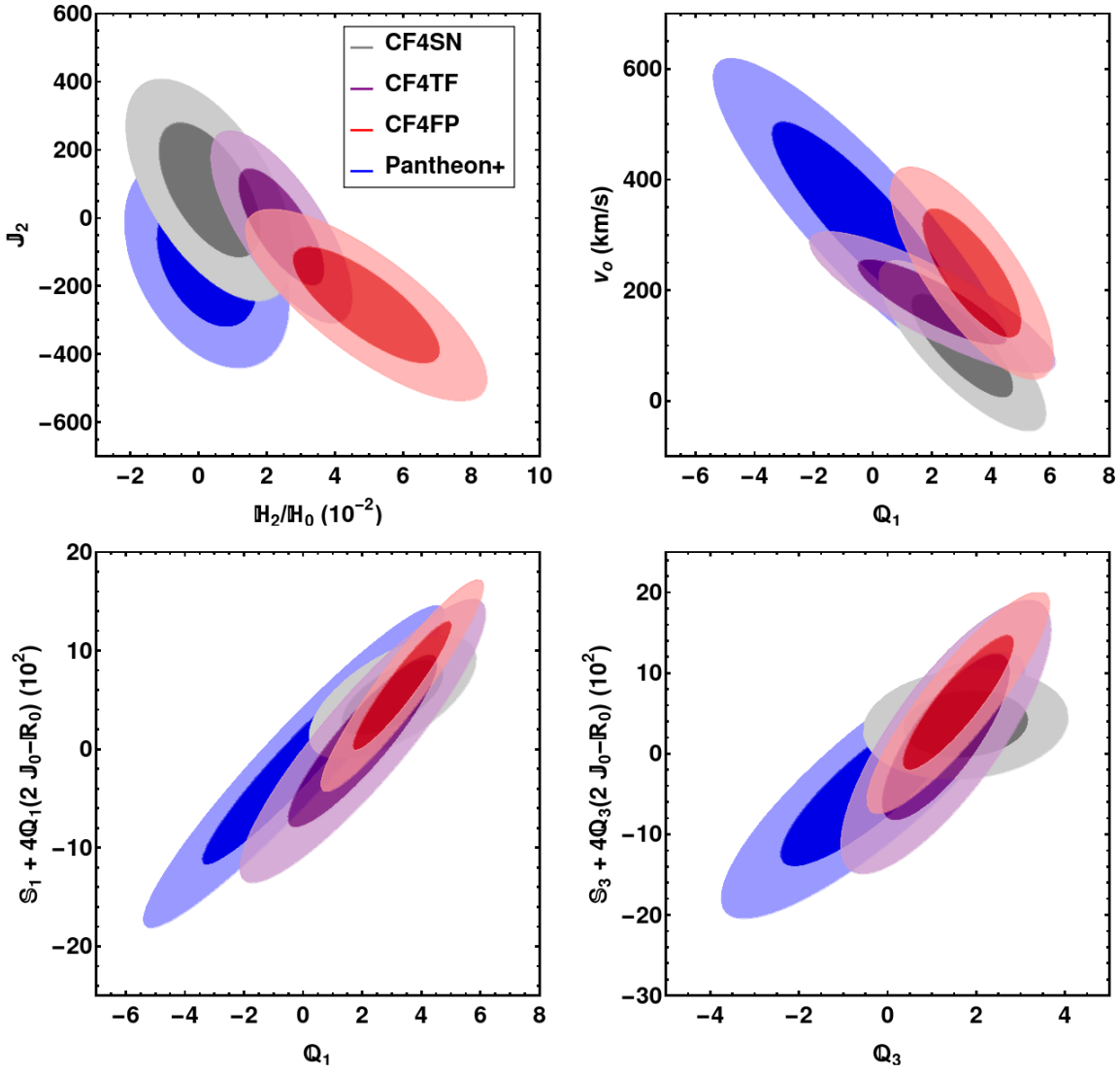


Figure 7.2: Marginalised posterior distribution of the cosmographic parameters, dark and light regions represent respectively the 68% and 95% confidence levels.

between the determinations from different datasets.

Regarding the CF4 samples, I find that CF4SN shows no signal for the quadrupole, consistent with the findings in Chapter 4. The only significant signal in this sample is the dipole, which the fit indicates originates from both v_o and the dipole of $\mathbb{Q}$. Both CF4TF and CF4FP exhibit signals for the axially symmetric multipoles up to $\ell = 3$. In both cases, the quadrupole is dominated by the quadrupole of the Hubble parameter ($\mathbb{H}_2$). The quadrupole $\mathbb{H}_2$ is approximately 1.6σ higher for CF4FP, with this sample also showing a negative value of $\mathbb{J}_2$ (with a signal-to-noise ratio of nearly 2). Similar to CF4SN, the dipole for both CF4TF and CF4FP is sourced by the observer's velocity v_o and the intrinsic metric anisotropy captured by $\mathbb{Q}_1$, with results for the two samples consistent within $< 1\sigma$. The octupole signal is primarily driven by the octupole of $\mathbb{Q}$, and its amplitude is consistently recovered in both samples.

As for Pantheon+, this sample shows a signal only for the dipole, similar to CF4SN, as discussed in Chapter 4. However, the dipole in Pantheon+ arises solely from the velocity

v_o, yielding a value approximately 1.3σ higher than that of the other samples, particularly when compared to the results from CF4.

Figure 7.3 displays the best-fit covariant cosmographic parameters and the velocity v_o of the matter observer as a function of $\tilde{z}_{\rm min}$, the lower redshift cutoff used in the fit (similar to Figure 6.8). While the parameters remain generally stable for any choice of redshift greater than $\tilde{z}_{\rm min} = 0.01$, their values systematically deviate when smaller redshift cuts are applied. This suggests that the fluid model underlying covariant cosmography consistently captures the cosmic expansion phenomenology, failing only when trying to explain the kinematics of the deepest region investigated ($z \sim 0.1$) including data below $\tilde{z} = 0.01$. Specifically, this occurs when trying to represent the matter comoving observer by averaging data within a spherical volume smaller than $30h^{-1}$Mpc, which corresponds to using redshift data (nearly 3000 objects) below $\tilde{z} = 0.01$.

This issue can be viewed from a different perspective. In Figure 7.4, I present the minimum χ^2 values corresponding to each best-fitting covariant cosmographic model from the analysis of the CF4 dataset. It is evident that while the goodness of fit remains stable for larger values of $\tilde{z}_{\rm min}$, it progressively worsens as the lower redshift cut is applied for $\tilde{z} < 0.01$. Given the assumption that the observed matter field follows a smooth 4-velocity (i.e., that matter particles are well-described by a fluid model), the sudden increase in $\chi^2_{\rm min}$ suggests a breakdown of this continuum approximation. Below $\tilde{z} = 0.01$, the observations become dominated by the 'thermal' motions of galaxies, reflecting local fluctuations in the matter density field that deviate from the large-scale behavior.

In Figure 7.3 (lower right panel), it is noteworthy that the velocity of the matter observer, v_o, relative to the CMB increases as progressively smaller redshift cuts are applied, approaching the large value inferred from the velocity of the barycenter of the Local Group of galaxies with respect to the CMB (631 ± 20 km/s [200, 128]). However, the axis of symmetry does not align with the direction of the Local Group's velocity vector $(270 \pm 3, 27 \pm 3)$ and therefore, the exact same value is not expected to be recovered.

As discussed in section 6.7, when interpreted within the framework of the standard model, v_o represents the bulk velocity of a volume surrounding the observer, assuming that local structures can be effectively abstracted away and only the large-scale gravitational field remains. This interpretation is derived from inspecting Figure 7.5, where I present the redshift evolution of the bulk velocity v_b, reconstructed in shells of $\Delta R = 45\,h^{-1}$ Mpc for the CF4 dataset. The bulk velocity is estimated by converting the information contained in the dipole ($\ell = 1$) of $\tilde{\eta}$ using the relation in equation (6.33). Notably, the amplitude decreases with decreasing redshift, and it is approximately 300 km/s, in the first redshift shell ($0.01 < z < 0.025$), where v_b can be directly estimated, suggesting that on smaller shells, it should asymptotically converge to $v_o = 171 \pm 24$ km/s

Using the same estimator, I also compute the bulk velocity characterizing galaxies within a spherical volume of radius $R = 200h^{-1}$ Mpc around the observer. I find that in the direction of the axis of symmetry $(299, 5)$, the amplitude is 534 ± 27 km/s. This finding is comparable, albeit slightly higher, than what was reported by [89], who found the bulk velocity to be 419 ± 36 km/s in the direction $(l, b) = (298 \pm 5, -8 \pm 4)$. The discrepancy in results primarily arises from my inclusion of higher multipoles in the fit, which mitigates any potential bias from them (see section 2.2.2).

The positive value for the quadrupole of $\mathbb{H}$ indicates that the cosmic fluid is being stretched along the axis of symmetry, and I showed in Chapter 6 that a single spherical "attractor" (over-density) can reproduce this feature. Additionally, I demonstrated that the same attractor provides opposite signs for the dipole and the octupole of $\mathbb{Q}$, which

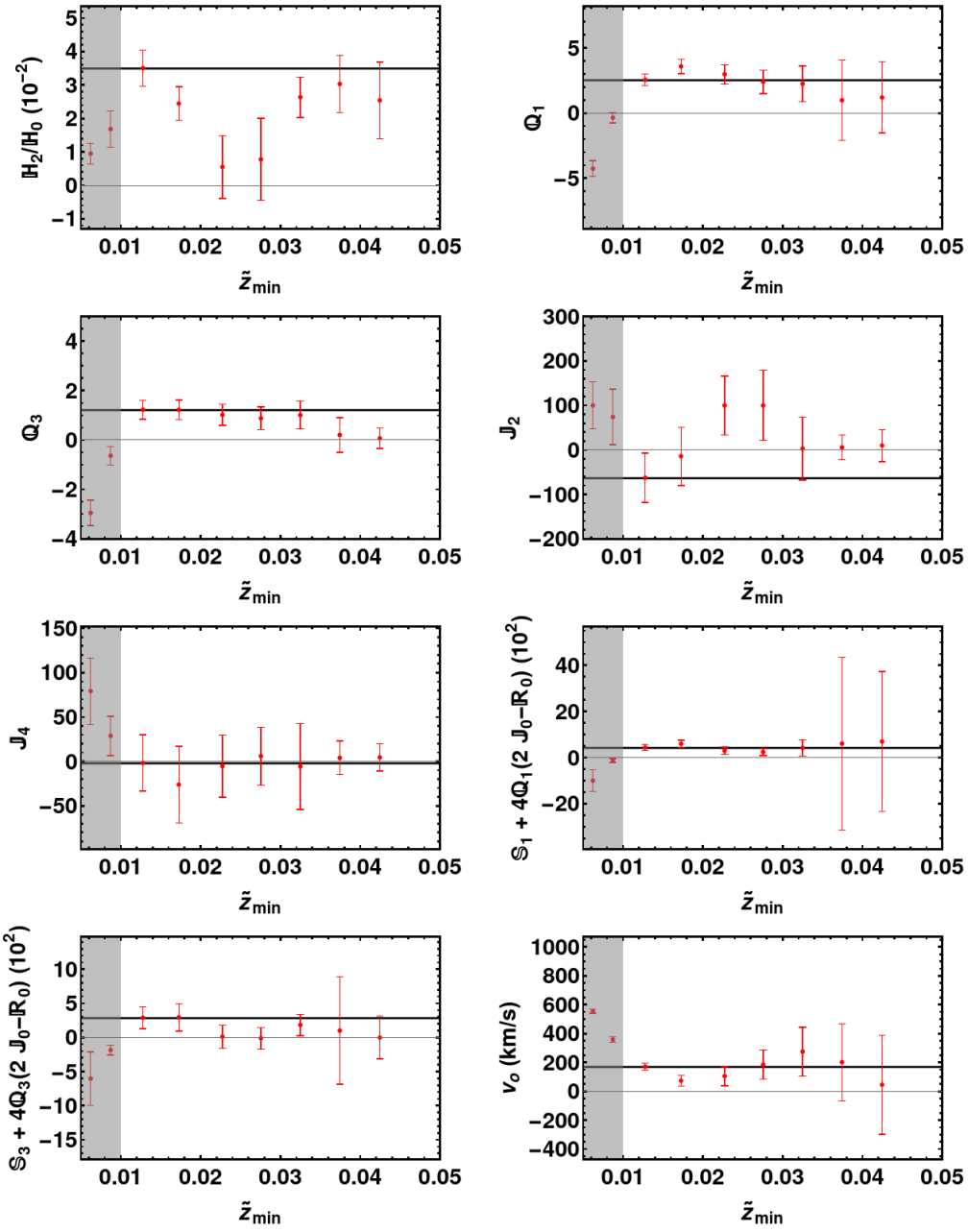


Figure 7.3: The best-fit covariant cosmographic parameters and the observer's velocity v_o as a function of the lower redshift cut ($\tilde{z}_{\rm min}$) for the CF4 sample. The black lines presents the best-values chosen for Table 7.1 and correspond to those estimated using $\tilde{z}_{\rm min} = 0.01$). The shaded area indicates the range excluded to estimate the parameters quoted in Table 7.1.

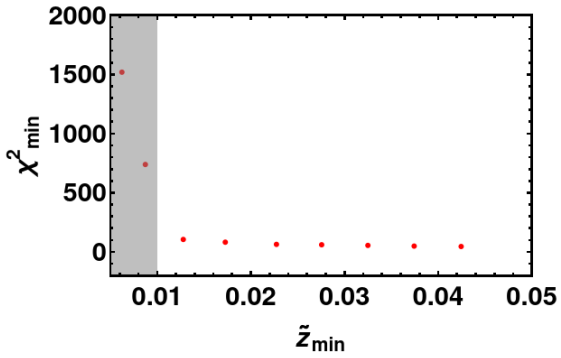


Figure 7.4: The minimum χ^2 shown in eq. (7.2) as a function of $\tilde{z}_{\rm min}$ for CF4.

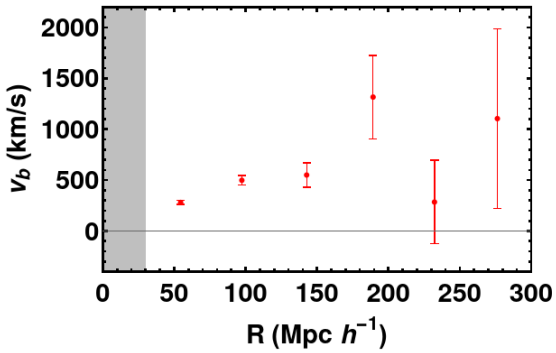


Figure 7.5: The bulk velocity v_b, reconstructed in shells of $\Delta R = 45\,h^{-1}$ Mpc for the CF4 dataset as a function of distance.

contradicts what is observed in my analysis. This implies that a single attractor cannot be a dominant structure in the local universe. As discussed in Chapter 4, because it is located at a distance of around 200 Mpc, and the multipoles —especially the dipole and quadrupole— do not change significantly beyond that distance, the Shapley attractor cannot explain, alone, the observed velocity flow.

Interestingly, the possible existence of a cosmic "repeller" (large under-density region) with a radius $\sim 140 - 250\,h^{-1}$ Mpc influencing the local expansion rate, has been suggested by various studies: [168] based on the CF4 sample and [88] based on the CLASSIX galaxy cluster survey.

I find that, similar to the attractor, a single spherical repeller cannot produce the same polarity for $\mathbb{Q}_1$ and $\mathbb{Q}_3$. Additionally, it cannot explain the positive sign of the quadrupole of $\mathbb{H}$, since, in the case of a repeller, the minimum of the quadrupole of $\mathbb{H}$ would align with the axis of symmetry.

If we consider a combination between an attractor and a repeller, this picture can only be viable if the attractor, the observer, and the repeller are well-aligned along a single axis to maintain axial symmetry in the overall configuration of the expansion rate fluctuation field. This combination can explain the polarity of the observed multipoles.

Since the cosmographic parameters are defined in a general spacetime, I can estimate the size and amplitude of the density contrast required to generate the observed multipoles using the analytical model introduced in Chapter 6. I assume that the two structures are spherical and rely on the fact that, at linear order, the resulting multipoles are simply

the sum of the multipoles of each structure. While the second assumption is rigorous, the first is rather crude. Additionally, I assume the background is an EdS (Einstein-de Sitter) spacetime, estimating that this simple cosmological model provides sufficiently accurate zero-order predictions.

I fix the position of Shapley, allowing its amplitude and size to vary, while also varying the position, amplitude, and size of the Repeller, which is constrained to be aligned with both the observer and the Shapley concentration. I then calculate the expected covariant cosmographic parameters for this mass configuration and compare them to the observed values using a χ^2 analysis. In a preliminary analysis, I find that even when exploring a large parameter space, there is no acceptable model that simultaneously explains both the amplitude of the multipoles of the cosmographic parameters and the velocity of the observer. Given the simplicity of this model, more elaborate frameworks should be developed if the repeller-attractor model is to adequately fit the expansion rate field data. I will explore various alternatives in future work.

7.3 Conclusion

I have estimated the cosmographic parameters in the expansion of the luminosity distance up to fourth order using CF4 and Pantheon+ samples. Additionally, I have inferred the velocity of the matter comoving observer in the CMB frame, and by analyzing various subsamples with different distance indicators, I showed that results from these different datasets are consistent.

In light of the results from Chapter 4, I conclude that the local universe should have coherent structures of the order of the sample size, in order to adequately explain the observed anisotropy at high distances. However, with such large structures, it is expected that the matter comoving observer at our position would have a much higher velocity than the measured one, unless we are sitting at finely tuned position.

In conclusion, the model-independent, fully unperturbative approach developed in this thesis contributes to shed light on the complex structure of the local expansion rate field of the universe. This complexity shows no clear tendency to fade with distance, and the expansion rate to evolve towards an isotropic state. These results motivate more analysis and observational programs aimed at collecting redshift-independent distances beyond $z = 0.1$ to gain physical insights into the nature and origin of the observed anisotropies.

Summary and Outlook

Cosmology faces anomalies—discrepancies between predictions and observations—that resist current investigative efforts. This impasse motivates the work undertaken in this thesis, which seeks to describe the data by relaxing theoretical constraints. The goal is to develop methods that allow the data to uncover cosmological information with minimal reliance on theoretical priors. In fact, these tensions not only highlight the limitations of our current understanding but also suggest the need to reassess some of the foundational assumptions in cosmology, particularly those concerning the structure of cosmic spacetime. For instance, the well-known discrepancy between local measurements of the Hubble constant (H_0) and estimates from the Cosmic Microwave Background may indicate a breakdown of the Cosmological Principle, pointing to a more complex and less symmetric nature of the cosmic line element.

By definition, the CP does not apply on small scales ($r \lesssim 150\ h^{-1}$ Mpc), which can affect determinations of the Hubble parameter. Traditionally, deviations from spatial uniformity on these scales are addressed using perturbative techniques. However, this approach has certain drawbacks: it is fundamentally model-dependent, as it requires the a priori assumption of the FLRW metric, implying the existence of well-defined smooth background variables that depend only on time. Additionally, it assumes that density fluctuations are small, which limits its applicability to more complex cosmic structures with strongly non-linear dynamics.

I have explored whether it is possible to use measurements to represent the cosmic spacetime nonperturbatively, without relying on peculiar velocities, and in a model-independent way, without any prior reference to principles or symmetry assumptions. Our ultimate goal is to characterize the expansion rate on local cosmic scales ($z \lesssim 0.1$ or $r \lesssim 300\ h^{-1}$ Mpc) more meaningfully and comprehensively than using the H_0 parameter of the Standard Model alone. This program involves two critical steps. First, we need to identify and classify deviations from isotropy in the observed redshift-distance relation in an unbiased and model-independent way. Then, we need to relate these angular distortions to geometric quantities, defined covariantly in arbitrary spacetimes, to gain insight into the effective structure of the cosmic line element in the observer's surroundings.

The first challenge was tackled by introducing the *expansion rate fluctuation field* η. This observable is defined as

$$\eta = \log\left(\frac{z}{d_L}\right) - \mathcal{M} \tag{7.3}$$

where z is the redshift, d_L is the luminosity distance and $\mathcal{M}$ is the normalizing factor to make the monopole of η equal to zero. Consequently, it is only sensitive to the angular structure of the fluctuating component and its possible evolution with redshift. It is only in the presence of angular anisotropies of the luminosity distance, at a given redshift, that η deviates from zero. For example, in an idealised FLRW cosmological model, $\eta = 0$ at every epoch.

As a scalar, Gaussian indicator, moreover η presents several statistical advantages and it lends itself quite readily to a decomposition on a spherical harmonic basis, facilitating straightforward signal interpretation. First, η, being defined without a monopole ($\mathcal{M}$), is completely independent of the normalization of the redshift-distance relationship, a fact that allows comparison of the signal extracted from different distance datasets, regardless of their zero-point calibration. This does not mean that the η observable is blind to the Hubble constant. Information about H_0 is locked in the normalization term $\mathcal{M}$ appearing in 7.3. The additional advantage is that any potential systematic errors in measurements of the luminosity distances as a function of redshift do not affect the signal of η.

The second challenge is to generalize the concept of the *cosmic expansion rate*. This requires addressing what the term 'expansion' means for an arbitrary observer within a generic space-time. This idea dates back to the seminal work by Kristian and Sachs, 'Observations in Cosmology' in 1966, where they represented non-standard (i.e. anisotropic) expansion rate histories through the tensorial expansion of the luminosity distance with respect to redshift. This approach yields covariant cosmographic parameters, $\mathbb{H}(\boldsymbol{n})$ (Hubble), $\mathbb{Q}(\boldsymbol{n})$ (deceleration), $\mathbb{J}(\boldsymbol{n})$ (jerk) and $\mathbb{R}(\boldsymbol{n})$ (curvature). These parameters are functions dependent on the line-of-sight direction $\boldsymbol{n}$ and characterize the metric structure around the observer, and at the same time, they are related to the expansion terms of the luminosity distance as a function of redshift which makes them observable. Although they are initially unknown (no particular gravitational theory is assumed in this approach), they have a finite number of spherical harmonic components. Consequently, the covariant cosmographic parameters can be fully reconstructed by fitting a limited subset of their multipoles to the data.

In this thesis, I've presented the results I obtained through exploring along these two routes.

In the first chapter, I review the standard model of cosmology, beginning with its fundamental physics, including the Einstein field equations and the Friedmann equations. Key cosmological concepts such as redshift, distance measures, and cosmography within the standard model are introduced. I also present the main observational techniques used to estimate the luminosity distance. Additionally, I synthetically present the linear perturbation theory and discuss the statistical properties of the perturbed matter density field, including the power spectrum and correlation function, which are needed throughout the thesis. Finally, I briefly review the tensions within the Standard Model of cosmology that motivate further research, with particular emphasis on the Hubble tension. Indeed, in the long term, I propose to address this issue using the approach developed in this thesis.

In the second chapter, I define the *expansion rate fluctuation field* η and describe how this new observable can be estimated from discrete data. I then show how to develop this field in spherical harmonics and present the methods used to estimate the multipolar expansion of η, starting with HEALPix (Hierarchical Equal Area isoLatitude Pixelization of a 2-sphere). This method involves smoothing the η field by averaging the measured values at each pixel and estimating the multipoles based on these pixelized data points. The second method involves directly minimizing the χ^2 for all measurements without applying any smoothing. I also discuss the statistical properties, biases, and uncertainties associated with each method.

Finally, since η is a model-independent quantity, I demonstrate how it relates to the radial component of the peculiar velocity field within the framework of the Standard Model.

This relationship allows me to show also how the power spectrum of the multipoles of η (or the cosmic variance of its spherical harmonic coefficients) is related to the matter power spectrum predicted by the ΛCDM model. This power spectrum is crucial for evaluating whether the observed multipoles align with or deviate from theoretical predictions.

In the third chapter, I present the all-sky map of η and of its multipolar expansion derived from local data ($z < 0.05$): the Cosmicflows-3 (CF3) and Pantheon catalogs. For the Pantheon catalog, the signal is confined to the dipole ($\sim 2\times10^{-2}$), while the CF3 data reveal signals in the quadrupole ($\sim 1\times10^{-2}$) and the octupole ($\sim 1\times10^{-2}$). I calculate the probability of observing these multipoles within the standard model at the given redshift and find that they are consistent with the model. Additionally, I've divided the CF3 sample into two subsamples: CF4sn, which contains distance measurements using Type Ia supernovae (SNIa), and CF4g, which includes the remaining data. The results from both subsamples were found to be compatible.

I find intriguing evidence that the direction of the dipole ($(l, b) \approx (290°, 8°)$) aligns with the maximum of the quadrupole, with the octupole also exhibiting a maximum in this direction. I further examine the multipolar expansion under the simplifying assumption of axial symmetry along this preferred axis and find that is compatible with data. By expanding on a Legendre basis instead of spherical harmonics, each multipole is determined by a single degree of freedom, making the interpretation of observations more straightforward. Finally, since the dipole of η is related to bulk velocity v_b, I estimate it for each sample, and find $v_b \approx 330 \pm 25$ km/s for the volume considered ($z < 0.05$ or $r < 150\ h^{-1}Mpc$). This value is consistent with other findings in the literature obtained through independent techniques.

In the fourth chapter, I present updated all-sky estimates of the η field obtained from state of the art public compilations of redshift independent distances: the Cosmicflows-4 (CF4) and Pantheon+ catalogs. The CF4 catalog enables extending estimates of the anisotropies in the expansion rate field to higher redshift, up to $z = 0.1$. Maps of η for redshifts up to $z = 0.05$ are quantitatively consistent with those from CF3 and Pantheon. I further divide this richer sample ($\sim 4\times$ its predecessor) into three subsamples: CF4SN (containing distance measurements using SNIa), CF4TF (containing distance measurements using the Tully-Fisher relation for spiral galaxies), and CF4FP (containing distance measurements using the Fundamental Plane method for elliptical galaxies). The results from these subsamples are consistent within the given uncertainties.

In the deepest redshift range explored, $0.05 < z < 0.1$, I also detect statistically significant evidence for dipolar and quadrupolar signals, each with an amplitude of $\sim 1 \times 10^{-2}$. These amplitudes are in tension with the predictions of the standard model of cosmology at this redshift. The tension observed in the dipole is consistent with independent findings from other researchers who analyzed the same CF4 sample using the FLRW model. These model-dependent analyses suggest that the bulk velocity over such a deep and large volume is inconsistent with standard model expectations. In addition to the unexpectedly large quadrupolar component, we also find equally perplexing evidence that the maxima of the dipole and quadrupole remain aligned along nearly the same axis as observed in the lower redshift shell. We further examined whether the expansion rate beyond the Shapley concentration exhibits axial symmetry around this privileged axis. To do so, I developed a more sophisticated method that leverages the properties of spherical harmonics. Specifically, if a spherical harmonic multipole ℓ is axially symmetric, rotating the coordinates such that the z-axis aligns with the axis of symmetry should cause all spherical harmonics, except for the $m = 0$ mode, to vanish. Notably, I found

that this rotation enhances the signal in the $m = 0$ modes while diminishing it in the others, thereby confirming the presence of axial symmetry. These findings suggest that the cosmic expansion rate is systematically and coherently perturbed on a scale exceeding $\sim 400h^{-1}$ Mpc. It is no longer just a matter of anomalous bulk flows. It is the whole complex structure of the expansion field around us that persists unchanged at least until $z = 0.1$, the highest redshift investigated.

In chapter 5, I review the covariant cosmographic approach to cosmology. This fully model-independent and non-perturbative framework allows for the interpretation of expansion rate data without assuming any specific spacetime metric $g_{\mu\nu}$. Its characteristic parameters, the covariant cosmographic parameters, are the coefficients of the redshift expansion of the luminosity distance in a generic spacetime. They depend on the geometric properties of space-time, but also on the speed at which the Earth observer moves relative to the frame of reference where matter is at rest. The exact functional form of this dependence was previously known only up to the third order. Motivated by evidence suggesting that this range may be insufficient to fully capture the expansion rate kinematics in a highly inhomogeneous local universe, I extend these results to the fourth order in redshift, incorporating the snap parameter $\mathbb{S}(\boldsymbol{n})$. I also demonstrate that the covariant Hubble parameter has multipoles up to the quadrupole ($\ell = 2$), while the independent multipoles of the deceleration parameter extend to the octupole ($\ell = 3$). The third-order expansion term, which includes the jerk and curvature parameters, has independent multipoles up to $\ell = 4$, and the snap parameter features independent multipoles up to $\ell = 5$.

The total number of degrees of freedom is 86 (with each multipole having $2\ell+1$ degrees of freedom), which is too large for meaningful data interpretation. However, I show that assuming axial symmetry and considering that matter particles move along geodesics reduces the number of degrees of freedom to 17. In addition, some multipoles involve spatial derivatives, which means that they are amplified by a factor equal to the ratio between the scale of the Hubble horizon and the scale of the perturbation that generates them. If we consider only these "boosted" multipoles, in addition to the monopoles, we end up with just 12 degrees of freedom, a fairly reduced number of degrees of freedom for statistical inference.

I then establish the relationship between the observable multipoles of η and the multipoles of the covariant cosmographic parameters under the assumption of axial symmetry. This lays the foundation for the data analysis and statistical inference presented in Chapter 7 of this thesis.

A key contribution of this section is the clarification and analytical quantification of the observer's motion on the amplitude of the cosmographic parameters. The datasets used in cosmological studies often provide measurements of redshift and distance relative to specific reference frames, typically the heliocentric frame or the Cosmic Microwave Background (CMB) frame, where the observer does not observe the CMB dipole. However, in theoretical calculations of cosmographic parameters, it is assumed that the observer is comoving with the cosmological matter fluid (the so called matter frame, which does not coincide with the heliocentric frame). While the matter and the CMB frames are indistinguishable in a perfectly uniform universe as described by the standard cosmological metric, they differ in arbitrary geometries. To address this issue, often overlooked in the literature, I introduce a new degree of freedom, the local relative velocity v_o between the theoretical matter frame and the observational frame in which measurements are analyzed. I show how, by incorporating this relative velocity into the analysis, we gain additional insight into the relative motion between the matter and CMB frames.

In Chapter 6 I test the formalism using axis-symmetric analytical models which simulate large-scale linear fluctuations in the redshift-distance relation in the local Universe. To this purpose I perturb an Einstein-de Sitter background with a spherically symmetric overdensity, considering two different sizes for the overdensity and assuming the observer is off-center with respect to the perturbation. This model is selected so that the observed multipoles of η and the bulk velocity are compatible with the values I inferred from data. I then discretely sample the model by trying to reproduce both the redshift distribution and the errors in distances expected from the Zwicky Transient Facility (ZTF) survey, a future and large survey of redshift independent distances.

This realistic model allows me to assess how the luminosity distance compares to the one reconstructed using the covariant cosmographic parameters, thereby evaluating the capabilities and limitations of our method. These analyses allow to find the redshift range where the given expansion of the distance is valid. In addition, it enables us to forecast the precision with which the covariant cosmographic parameters can be estimated. The results show that the estimation of the octupole of $\mathbb{Q}$ is biased if the snap is not included in the relations. Additionally, the multipole $\ell = 4$ of the jerk and $\ell = 5$ of the snap are biased, indicating that even higher-order expansion terms are necessary to accurately recover these multipoles. The other multipoles are not biased, and the velocity v_o is well reconstructed.

In the last chapter, I finally apply the covariant cosmography formalism to extract information from the CF4 and Pantheon+ samples. I estimate the multipoles of the cosmographic parameters (excluding the monopoles) in addition to the bulk velocity v_o directly from the measurements of the multipoles of expansion rate fluctuation field η (up to the multipole $\ell = 4$). I do not fit the monopole $\mathcal{M}$, which is related to the calibration of distance and can be biased given conflicting evidences of the literature. This is possible due to the η observable's inherent property of being independent of distance normalization. However, this comes with a trade-off: a degeneracy between the monopole of the jerk and curvature and the dipole and octupole of the snap. As a result, I can only estimate combinations of these parameters.

A second caveat is that, according to the formalism, if the theoretical expansion of distance accurately models the given sample up to a specified redshift, the best-fit cosmographic parameters should remain stable within their error bars as we vary the redshift interval of the analysis, especially its lower limit. However, I have found that stability holds systematically for all the different samples analyzed, but only up to a redshift cut of $z_{\rm cut} = 0.01$. Below this threshold, the parameters become unstable due to the influence of very local structures within this volume ($\lesssim 40$ Mpc), such as the Virgo cluster and the local void, which do not align with the average structure of the entire volume under study. This instability suggests that we are no longer in the fluid limit where covariant cosmography can be applied, and that discreteness effects are beginning to dominate over smoothness. Consequently, I apply this lower redshift cut to ensure the reliability of the estimated parameters.

For Pantheon+, I detect a statistically significant signal only for v_o. In CF4, signals are also observed in the quadrupole of $\mathbb{H}$ ($\sim (3\pm0.5)\%$ of the monopole), and in the dipole ($\sim 2 \pm 1$) and octupole ($\sim 1 \pm 0.5$) of $\mathbb{Q}$. The velocity v_o is found to be $\sim 170 \pm 30$ km/s in the direction of the dipole. Although no significant signals are found in the multipoles of the jerk, combinations of the dipole and octupole of the snap with the monopole of the jerk and curvature show significant signals. To further validate these findings, we also analyze the subsamples CF4SN, CF4TF, and CF4FP. The results from these subsamples

are consistent overall, with CF4SN showing no signal in the quadrupole of the Hubble parameter but confirming the robustness of the signals observed in the other parameters.

The positive quadrupole value of $\mathbb{H}$ suggests that the local cosmic fluid is being stretched along the axis of symmetry. I show that a single spherical "attractor" (over-density) located in the general direction of the Shapley Concentration can account for this effect. However, I also demonstrate that this same single-attractor model predicts opposite signs for the dipole and octupole of $\mathbb{Q}$, which contradicts observations. Interestingly, there is tentative evidence in the literature for the existence of a "repeller" (under-density), a large cosmic structure that could influence local dynamics. A model featuring a spherical attractor and repeller is only viable if the attractor, the observer, and the repeller are precisely aligned along a single axis to preserve axial symmetry in the expansion rate field. However I was no able to find any field configuration which could explain the observed multipoles of the covariant cosmographic parameters.

In conclusion, the model-independent, fully unperturbative approach developed in this thesis contributes to shed light on the complex structure of the local expansion rate field of the universe. This complexity shows no clear tendency to fade with distance, and the expansion rate to evolve towards an isotropic state. It thus motivates observational programs aimed at collecting redshift-independent distances beyond $z = 0.1$, so to gain physical insights on the nature and origin of the observed anisotropies.

The method also provides theoretical tools for a deeper investigation of key cosmological issues. Specifically, the constraints on covariant cosmographic parameters derived in this thesis will be crucial for accepting, rejecting, or refining specific metric models of the local universe's spacetime.

Looking ahead, there are many directions in which this preliminary analysis can be expanded.

In the immediate future, I plan to incorporate the information from the measurements of the monopole of the expansion rate field η into the analysis of the covariant cosmographic parameters. This will enhance the resolution of the fit and help break the degeneracies in determining these parameters.

Ideally, it would be beneficial to gain access to a larger, more densely populated, nearly all-sky sample of redshift-independent distances, such as the ZTF catalog currently being assembled. This would enhance the resolution with which covariant cosmographic models can be constrained.

Further investigation is also needed to identify which physical mass configurations are compatible with the polarity and alignment observed in the multipoles of the expansion rate field. This modeling will be instrumental in the long term for developing a suitable 4D metric for the local universe that explains the observed amplitude of the covariant cosmographic parameters. Exact metric models will enable analytical analyses that ultimately allow us to bypass the limitations of the standard approach, which relies on studying only small, linear, fluctuations around the FLRW background.

Regarding the Hubble tension, this work, rather than providing a solution as ambitiously intended at the beginning of this thesis, contributes additional problematic results to the already anomalous picture that are difficult to interpret within the framework of the standard model. It is therefore tempting to speculate that resolving the H_0 problem will necessitate the same new physical ingredients required to understand the puzzling kinematics observed in the expansion rate fluctuation field.

Appendices

Appendix A

Multipole expansions of $\mathbb{X}^{(3,4)}$ and $\mathbb{Y}^{(1,2)}$

$\mathbb{X}^{(1-4)}$ are defined in eqs. (5.16)–(5.19) and $\mathbb{Y}^{(1,2)}$ in eq. (5.20). Their multipoles are needed to obtain the multipole expansion of the covariant snap parameter.

Notation: Angled brackets on indices indicate the projected, symmetric, tracefree (PSTF) part of a tensor, relative to the matter 4-velocity u^μ. For a vector and a rank 2 tensor:

$$W_{\langle\mu\rangle} = h_\mu^{\ \nu} W_\nu \,, \quad W_{\langle\mu\nu\rangle} = \Big[h_\mu^{\ (\alpha} h_\nu^{\ \beta)} - \frac{1}{3} h_{\mu\nu} h^{\alpha\beta}\Big] W_{\alpha\beta} \,, \tag{A.1}$$

where $h_{\mu\nu} = g_{\mu\nu} + u_\mu u_\nu$. For the PSTF parts of higher-rank tensors, see [50]. Note that contraction of an arbitrary tensor with a PSTF tensor isolates the PSTF part:

$$V^\mu W_{\langle\mu\rangle} = V^{\langle\mu\rangle} W_{\langle\mu\rangle} \,, \quad V^{\mu\nu} W_{\langle\mu\nu\rangle} = V^{\langle\mu\nu\rangle} W_{\langle\mu\nu\rangle} \,, \tag{A.2}$$

and similarly for higher rank tensors.

The covariant multipoles of $\mathbb{X}^{(1-4)}$ and $\mathbb{Y}^{(1,2)}$ are all PSTF tensors. In order to simplify the expressions, we use the short-hand notation

$$W_{\mu_1\cdots\mu_n} \overset{\text{pstf}}{=} V_{\mu_1\cdots\mu_n} \quad \Leftrightarrow \quad W_{\langle\mu_1\cdots\mu_n\rangle} = V_{\langle\mu_1\cdots\mu_n\rangle} \,. \tag{A.3}$$

Multipoles of $\mathbb{X}^{(3)}$

$$\mathbb{X}^{(3)} = \langle\mathbb{X}^{(3)}\rangle + \mathbb{X}^{(3)}_\mu n^\mu + \mathbb{X}^{(3)}_{\mu\nu} n^{\langle\mu} n^{\nu\rangle} + \mathbb{X}^{(3)}_{\mu\nu\alpha} n^{\langle\mu} n^\nu n^{\alpha\rangle} + \mathbb{X}^{(3)}_{\mu\nu\alpha\beta} n^{\langle\mu} n^\nu n^\alpha n^{\beta\rangle} \,, \tag{A.4}$$

where

$$\langle\mathbb{X}^{(3)}\rangle = \frac{8}{5}\sigma_{\mu\nu}\sigma^{\nu\alpha}\sigma^{\mu}{}_{\alpha} + \frac{8}{5}\Theta\sigma_{\mu\nu}\sigma^{\mu\nu} + \frac{2}{9}\Theta^3 - \frac{2}{3}\Theta\dot{\Theta} - \frac{12}{5}\sigma^{\mu\nu}\dot{\sigma}_{\mu\nu} + \frac{1}{3}\ddot{\Theta} + \frac{2}{15}\nabla_\mu\nabla_\nu\sigma^{\mu\nu} + \frac{1}{9}\nabla^\mu\nabla_\mu\Theta + \frac{1}{9}u^\mu u^\nu\nabla_\mu\nabla_\nu\Theta\,, \tag{A.5}$$

$$\mathbb{X}^{(3)}_{\mu} \overset{\text{pstf}}{=} \frac{6}{5}\sigma^{\nu\alpha}\nabla_\mu\sigma_{\nu\alpha} + \frac{2}{3}\Theta\nabla_\mu\Theta + \frac{4}{5}\Theta\nabla_\nu\sigma_\mu{}^\nu - \frac{2}{3}u^\nu\nabla_\nu\nabla_\mu\Theta - \frac{2}{5}u^\nu\nabla_\nu\nabla_\alpha\sigma_\mu{}^\alpha + \frac{8}{15}\sigma_{\mu\nu}\nabla^\nu\Theta + \frac{6}{5}\sigma^{\nu\alpha}\nabla_\nu\sigma_{\alpha\mu} + \frac{6}{5}\sigma_{\mu\nu}\nabla_\alpha\sigma^{\nu\alpha} - \frac{2}{5}u^\nu\nabla_\alpha\nabla_\nu\sigma_\mu{}^\alpha\,, \tag{A.6}$$

$$\mathbb{X}^{(3)}_{\mu\nu} \overset{\text{pstf}}{=} \frac{32}{7}\sigma_\mu{}^\alpha\sigma_\nu{}^\beta\sigma_{\alpha\beta} + \frac{100}{21}\Theta\sigma_\mu{}^\alpha\sigma_{\nu\alpha} + \frac{4}{63}(29\Theta^2 - 21\dot{\Theta})\sigma_{\mu\nu} + \frac{1}{3}\nabla_\mu\nabla_\nu\Theta - \frac{46}{21}\Theta\dot{\sigma}_{\mu\nu} - \frac{48}{7}\sigma_\mu{}^\alpha\dot{\sigma}_{\nu\alpha} + \frac{2}{7}\nabla_\alpha\nabla_\mu\sigma_\nu{}^\alpha + \frac{1}{7}\nabla^\alpha\nabla_\alpha\sigma_{\mu\nu} + \frac{8}{7}u^\alpha u^\beta\nabla_\alpha\nabla_\beta\sigma_{\mu\nu} + \frac{2}{7}\nabla_\mu\nabla_\alpha\sigma_\nu{}^\alpha\,, \tag{A.7}$$

$$\mathbb{X}^{(3)}_{\mu\nu\alpha} \overset{\text{pstf}}{=} \frac{4}{3}\Theta\sigma_{\mu\nu}\nabla_\alpha + 2\Theta\nabla_\mu\sigma_{\nu\alpha} + 6\sigma_\mu{}^\beta\nabla_\nu\sigma_{\alpha\beta} - u^\beta\nabla_\mu\nabla_\nu\sigma_{\alpha\beta} - u^\beta\nabla_\beta\nabla_\mu\sigma_{\nu\alpha}\,, \tag{A.8}$$

$$\mathbb{X}^{(3)}_{\mu\nu\alpha\beta} \overset{\text{pstf}}{=} \frac{2}{3}\sigma_{\mu\nu}\sigma_{\alpha\beta}\Theta + \nabla_\mu\nabla_\nu\sigma_{\alpha\beta}\,. \tag{A.9}$$

Multipoles of $\mathbb{X}^{(4)}$

$$\mathbb{X}^{(4)} = \langle\mathbb{X}^{(4)}\rangle + \mathbb{X}^{(4)}_\mu n^\mu + \mathbb{X}^{(4)}_{\mu\nu} n^{\langle\mu}n^{\nu\rangle} + \mathbb{X}^{(4)}_{\mu\nu\alpha} n^{\langle\mu}n^\nu n^{\alpha\rangle} + \mathbb{X}^{(4)}_{\mu\nu\alpha\beta} n^{\langle\mu}n^\nu n^\alpha n^{\beta\rangle} + \mathbb{X}^{(4)}_{\mu\nu\alpha\beta\rho} n^{\langle\mu}n^\nu n^\alpha n^\beta n^{\rho\rangle}\,, \tag{A.10}$$

where

$$\begin{aligned}\langle\mathbb{X}^{(4)}\rangle = {}& \frac{8}{3}\sigma_{\mu\nu}\sigma^{\nu\alpha}\sigma_{\alpha\beta}\sigma^{\mu\beta} + \frac{172}{45}\Theta\sigma_{\mu\nu}\sigma^{\nu\alpha}\sigma^\mu{}_\alpha + \frac{2}{45}(53\Theta^2 - 6\dot{\Theta})\sigma_{\mu\nu}\sigma^{\mu\nu} + \frac{8}{27}\Theta^4 - \frac{34}{27}\Theta^2\dot{\Theta} + \frac{26}{27}\dot{\Theta}^2 \\ & - \frac{64}{9}\Theta\sigma^{\mu\nu}\dot{\sigma}_{\mu\nu} - \frac{52}{5}\sigma_{\mu\nu}\sigma^{\nu\alpha}\dot{\sigma}^\mu{}_\alpha + \frac{4}{3}\Theta\ddot{\Theta} - \frac{2}{15}u^\mu\nabla_\mu\nabla_\nu\nabla_\alpha\sigma^{\nu\alpha} - \frac{1}{9}u^\mu\nabla_\mu\nabla^\nu\nabla_\nu\Theta + \frac{8}{27}\nabla_\mu\Theta\nabla^\mu\Theta \\ & + \frac{1}{135}(30\dot{\Theta} - 43\Theta^2)u^\mu\nabla_\nu\sigma_\mu{}^\nu + \frac{2}{3}\nabla_\mu\Theta\nabla_\nu\sigma^{\mu\nu} + \frac{2}{5}\nabla_\mu\sigma^{\nu\alpha}\nabla^\mu\sigma_{\nu\alpha} + \frac{16}{5}u^\mu u^\nu\nabla_\mu\sigma^{\alpha\beta}\nabla_\nu\sigma_{\alpha\beta} \\ & + \frac{16}{45}\Theta\nabla_\mu\nabla_\nu\sigma^{\mu\nu} + \frac{8}{15}\sigma^{\mu\nu}\nabla^\alpha\nabla_\alpha\sigma_{\mu\nu} + \frac{64}{15}\sigma^{\mu\nu}u^\alpha u^\beta\nabla_\alpha\nabla_\beta\sigma_{\mu\nu} + \frac{32}{45}\sigma^{\mu\nu}\nabla_\nu\nabla_\mu\Theta + \frac{4}{9}\Theta\nabla^\mu\nabla_\mu\Theta \\ & - \frac{2}{9}\nabla^\mu\nabla_\mu\dot{\Theta} - \frac{2}{3}u^\mu u^\nu\nabla_\mu\nabla_\nu\dot{\Theta} + \frac{8}{15}\sigma^{\mu\nu}\nabla_\nu\nabla_\alpha\sigma_\mu{}^\alpha + \frac{11}{45}\Theta u^\mu u^\nu\nabla_\nu\nabla_\alpha\sigma_\mu{}^\alpha + \frac{7}{15}\sigma^{\alpha\beta}u^\mu u^\nu\nabla_\nu\nabla_\beta\sigma_{\mu\alpha} \\ & - \frac{49}{45}\Theta u^\mu\sigma^{\nu\alpha}\nabla_\alpha\sigma_{\mu\nu} + \frac{4}{45}(7\dot{\Theta} - 10\Theta^2)u^\mu u^\nu u^\alpha\nabla_\mu\sigma_{\nu\alpha} + \frac{2}{5}\nabla_\mu\sigma^{\mu\nu}\nabla_\alpha\sigma_\nu{}^\alpha - \frac{2}{15}u^\mu\nabla_\nu\nabla_\mu\nabla_\alpha\sigma^{\nu\alpha} \\ & + \frac{8}{15}\sigma^{\mu\nu}\nabla_\alpha\nabla_\nu\sigma_\mu{}^\alpha + \frac{11}{45}\Theta u^\mu u^\nu\nabla_\alpha\nabla_\nu\sigma_\mu{}^\alpha - \frac{2}{15}u^\mu\nabla_\nu\nabla_\alpha\nabla_\mu\sigma^{\nu\alpha} + \frac{2}{5}\nabla_\mu\sigma_{\nu\alpha}\nabla^\alpha\sigma^{\mu\nu} + \frac{5}{9}u^\mu u^\nu\nabla_\nu\sigma_{\mu\alpha}\nabla^\alpha\Theta \\ & + \frac{2}{45}u^\mu u^\nu\nabla_\alpha\sigma_{\mu\nu}\nabla^\alpha\Theta - \frac{14}{15}\sigma_\nu{}^\beta\sigma^{\nu\alpha}u^\mu\nabla_\beta\sigma_{\mu\alpha} + \frac{1}{5}u^\mu u^\nu\nabla_\alpha\sigma_\mu{}^\beta\nabla^\alpha\sigma_{\nu\beta} + u^\mu u^\nu\nabla_\nu\sigma_\mu{}^\alpha\nabla_\beta\sigma_\alpha{}^\beta \\ & + \frac{14}{5}u^\mu u^\nu u^\alpha u^\beta\nabla_\nu\sigma_\mu{}^\rho\nabla_\beta\sigma_{\alpha\rho} + \frac{7}{15}\sigma^{\alpha\beta}u^\mu u^\nu\nabla_\beta\nabla_\nu\sigma_{\mu\alpha} + \frac{34}{45}\Theta u^\mu u^\nu u^\alpha u^\beta\nabla_\beta\nabla_\alpha\sigma_{\mu\nu} \\ & + u^\mu u^\nu\nabla_\nu\sigma_{\alpha\beta}\nabla^\beta\sigma_\mu{}^\alpha + \frac{2}{45}\Theta u^\mu u^\nu\nabla^\alpha\nabla_\alpha\sigma_{\mu\nu}\,,\end{aligned} \tag{A.11}$$

$$
\begin{aligned}
\mathbb{X}^{(4)}_{\mu} \overset{\text{pstf}}{=}\ & \frac{344}{105}\Theta\sigma^{\nu\alpha}\nabla_\mu\sigma_{\nu\alpha} + \frac{1}{3}\Theta^2 u^\nu u^\alpha\nabla_\mu\sigma_{\nu\alpha} - \frac{4}{21}\dot\Theta u^\nu u^\alpha\nabla_\mu\sigma_{\nu\alpha} + \frac{24}{5}\sigma_\nu{}^\beta\sigma^{\nu\alpha}\nabla_\mu\sigma_{\alpha\beta} + \frac{122}{105}\sigma_{\nu\alpha}\sigma^{\nu\alpha}\nabla_\mu\Theta \\
& + \frac{191}{135}\Theta^2\nabla_\mu\Theta - \frac{1}{9}\Theta\nabla_\mu\dot\Theta - \frac{64}{35}\sigma^{\alpha\beta}u^\nu\nabla_\mu\nabla_\nu\sigma_{\alpha\beta} - \frac{1}{15}\Theta u^\nu\nabla_\mu\nabla_\alpha\sigma_\nu{}^\alpha + \frac{2}{35}\nabla_\mu\nabla_\alpha\nabla_\nu\sigma^{\nu\alpha} \\
& + \frac{1}{15}\nabla_\mu\nabla_\nu\nabla^\nu\Theta - \frac{1}{7}\sigma^{\alpha\beta}u^\nu\nabla_\mu\nabla_\beta\sigma_{\nu\alpha} - \frac{23}{105}\Theta u^\nu u^\alpha u^\beta\nabla_\mu\nabla_\beta\sigma_{\nu\alpha} + \frac{416}{315}\Theta^2\nabla_\nu\sigma_\mu{}^\nu - \frac{148}{105}\dot\Theta\nabla_\nu\sigma_\mu{}^\nu \\
& - \frac{96}{35}u^\nu\nabla_\mu\sigma^{\alpha\beta}\nabla_\nu\sigma_{\alpha\beta} - \frac{64}{35}\sigma^{\alpha\beta}u^\nu\nabla_\nu\nabla_\mu\sigma_{\alpha\beta} + \frac{2}{5}u^\nu\nabla_\nu\nabla_\mu\dot\Theta - \frac{124}{105}\Theta u^\nu\nabla_\nu\nabla_\alpha\sigma_\mu{}^\alpha - \frac{64}{35}\sigma^{\alpha\beta}u^\nu\nabla_\nu\nabla_\beta\sigma_{\mu\alpha} \\
& - \frac{64}{35}\sigma_\mu{}^\alpha u^\nu\nabla_\nu\nabla_\beta\sigma_\alpha{}^\beta + \frac{171}{35}\sigma_\mu{}^\alpha\sigma_{\nu\alpha}\nabla^\nu\Theta + \frac{1}{45}\sigma_{\mu\nu}\Theta\nabla^\nu\Theta - 2\sigma_{\mu\nu}\nabla^\nu\dot\Theta + \frac{356}{105}\sigma^{\nu\alpha}\Theta\nabla_\alpha\sigma_{\mu\nu} \\
& + \frac{509}{315}\Theta^2 u^\nu u^\alpha\nabla_\alpha\sigma_{\mu\nu} - \frac{116}{105}\dot\Theta u^\nu u^\alpha\nabla_\alpha\sigma_{\mu\nu} + \frac{356}{105}\sigma_\mu{}^\nu\Theta\nabla_\alpha\sigma_\nu{}^\alpha + \frac{593}{105}\sigma_\mu{}^\beta\Theta u^\nu u^\alpha\nabla_\alpha\sigma_{\nu\beta} \\
& + \frac{28}{5}\sigma_\mu{}^\beta\sigma_\beta{}^\rho u^\nu u^\alpha\nabla_\alpha\sigma_{\nu\rho} - \frac{1}{15}\Theta u^\nu\nabla_\alpha\nabla_\mu\sigma_\nu{}^\alpha + \frac{2}{35}\nabla_\alpha\nabla_\mu\nabla_\nu\sigma^{\nu\alpha} - \frac{124}{105}\Theta u^\nu\nabla_\alpha\nabla_\nu\sigma_\mu{}^\alpha \\
& + \frac{2}{35}\nabla_\alpha\nabla_\nu\nabla_\mu\sigma^{\nu\alpha} + \frac{2}{15}\nabla^\nu\nabla_\nu\nabla_\mu\Theta + \frac{4}{5}u^\nu u^\alpha\nabla_\alpha\nabla_\nu\nabla_\mu\Theta + \frac{2}{35}\nabla^\nu\nabla_\nu\nabla_\beta\sigma_\mu{}^\beta + \frac{16}{35}u^\nu u^\alpha\nabla_\alpha\nabla_\nu\nabla_\beta\sigma_\mu{}^\beta \\
& + \frac{16}{35}u^\nu u^\alpha\nabla_\alpha\nabla_\beta\nabla_\nu\sigma_\mu{}^\beta - \frac{13}{105}u^\nu\nabla_\mu\sigma_{\nu\alpha}\nabla^\alpha\Theta - \frac{148}{105}u^\nu\nabla_\nu\sigma_{\mu\alpha}\nabla^\alpha\Theta - \frac{2}{35}u^\nu\nabla_\alpha\sigma_{\mu\nu}\nabla^\alpha\Theta \\
& + \frac{14}{5}\sigma_\nu{}^\beta\sigma^{\nu\alpha}\nabla_\beta\sigma_{\mu\alpha} - \frac{4}{21}u^\nu u^\alpha u^\beta\nabla_\mu\Theta\nabla_\beta\sigma_{\nu\alpha} - \frac{9}{35}u^\nu\nabla_\alpha\sigma_\mu{}^\rho\nabla^\alpha\sigma_{\nu\rho} + \frac{14}{5}\sigma_\mu{}^\nu\sigma_\nu{}^\alpha\nabla_\beta\sigma_\alpha{}^\beta \\
& - \frac{9}{35}u^\nu\nabla_\mu\sigma_\nu{}^\alpha\nabla_\beta\sigma_\alpha{}^\beta - \frac{12}{7}u^\nu u^\alpha u^\beta\nabla_\mu\sigma_\nu{}^\rho\nabla_\beta\sigma_{\alpha\rho} - \frac{174}{35}u^\nu u^\alpha u^\beta\nabla_\nu\sigma_\mu{}^\rho\nabla_\beta\sigma_{\alpha\rho} - \frac{1}{7}\sigma^{\alpha\beta}u^\nu\nabla_\beta\nabla_\mu\sigma_{\nu\alpha} \\
& - \frac{23}{105}\Theta u^\nu u^\alpha u^\beta\nabla_\beta\nabla_\mu\sigma_{\nu\alpha} - \frac{64}{35}\sigma_\mu{}^\alpha u^\nu\nabla_\beta\nabla_\nu\sigma_\alpha{}^\beta - \frac{1}{15}\Theta u^\nu\nabla^\alpha\nabla_\alpha\sigma_{\mu\nu} - \frac{26}{21}\Theta u^\nu u^\alpha u^\beta\nabla_\beta\nabla_\alpha\sigma_{\mu\nu} \\
& - \frac{78}{35}\sigma_\mu{}^\rho u^\nu u^\alpha u^\beta\nabla_\beta\nabla_\alpha\sigma_{\nu\rho} + \frac{2}{35}\nabla_\beta\nabla^\nu\nabla_\nu\sigma_\mu{}^\beta + \frac{16}{35}u^\nu u^\alpha\nabla_\beta\nabla_\alpha\nabla_\nu\sigma_\mu{}^\beta - \frac{96}{35}u^\nu\nabla_\nu\sigma_{\alpha\beta}\nabla^\beta\sigma_\mu{}^\alpha \\
& - \frac{9}{35}u^\nu\nabla_\mu\sigma_{\alpha\beta}\nabla^\beta\sigma_\nu{}^\alpha + 4\sigma_\mu{}^\nu\sigma^{\alpha\beta}\nabla_\beta\sigma_{\nu\alpha} - \frac{4}{3}\dot\Theta\nabla_\mu\Theta - \frac{2}{35}u^\nu\nabla_\mu\Theta\nabla_\alpha\sigma_\nu{}^\alpha - \frac{9}{5}\Theta u^\nu\nabla_\nu\nabla_\mu\Theta \\
& + \frac{23}{7}\sigma_{\mu\nu}\Theta\nabla^\nu\Theta - \frac{64}{35}\sigma^{\alpha\beta}\,u^\nu\nabla_\beta\nabla_\nu\sigma_{\mu\alpha} - \frac{1}{7}\sigma_\mu{}^\rho u^\nu\nabla^\alpha\nabla_\alpha\sigma_{\nu\rho} + \frac{2}{35}\nabla^\nu\nabla_\beta\nabla_\nu\sigma_\mu{}^\beta \\
& - \frac{96}{35}u^\nu\nabla_\nu\sigma_\mu{}^\alpha\nabla_\beta\sigma_\alpha{}^\beta\,, \qquad\qquad (A.12)
\end{aligned}
$$

$$
\begin{aligned}
\mathbb{X}^{(4)}_{\mu\nu} \overset{\text{pstf}}{=}\ & 8\sigma_\mu{}^\alpha\sigma_\nu{}^\beta\sigma_\alpha{}^\rho\sigma_{\beta\rho} + \frac{256}{21}\Theta\sigma_\mu{}^\alpha\sigma_\nu{}^\beta\sigma_{\alpha\beta} + \frac{10}{21}\Theta\sigma_{\mu\nu}\sigma_{\alpha\beta}\sigma^{\alpha\beta} \\
& + \frac{2}{21}(81\Theta^2 - 76\dot\Theta)\sigma_\mu{}^\alpha\sigma_{\nu\alpha} + \frac{2}{189}\Theta(251\Theta^2 - 564\dot\Theta)\sigma_{\mu\nu} \\
& + \frac{1}{63}(30\dot\Theta - 43\Theta^2)u^\alpha\nabla_\mu\sigma_{\nu\alpha} - \frac{7}{3}\Theta\sigma_\mu{}^\beta u^\alpha\nabla_\nu\sigma_{\alpha\beta} + \frac{6}{7}\nabla_\mu\sigma^{\alpha\beta}\nabla_\nu\sigma_{\alpha\beta} + \frac{2}{21}u^\alpha u^\beta\nabla_\mu\Theta\nabla_\nu\sigma_{\alpha\beta} \\
& + \frac{3}{7}u^\alpha u^\beta\nabla_\mu\sigma_\alpha{}^\rho\nabla_\nu\sigma_{\beta\rho} + \frac{2}{3}\nabla_\mu\Theta\nabla_\nu\Theta + \frac{8}{7}\sigma^{\alpha\beta}\nabla_\mu\nabla_\nu\sigma_{\alpha\beta} + \frac{2}{21}\Theta u^\alpha u^\beta\nabla_\mu\nabla_\nu\sigma_{\alpha\beta} + \frac{8}{9}\Theta\nabla_\mu\nabla_\nu\Theta \\
& - \frac{2}{3}u^\alpha\nabla_\mu\nabla_\alpha\nabla_\nu\Theta - \frac{2}{7}u^\alpha\nabla_\mu\nabla_\alpha\nabla_\beta\sigma_\nu{}^\beta + \frac{8}{7}\sigma^{\alpha\beta}\nabla_\mu\nabla_\beta\sigma_{\nu\alpha} + \frac{11}{21}\Theta u^\alpha u^\beta\nabla_\mu\nabla_\beta\sigma_{\nu\alpha} + \frac{8}{7}\sigma_\mu{}^\alpha\nabla_\nu\nabla_\beta\sigma_\alpha{}^\beta \\
& - \frac{2}{7}u^\alpha\nabla_\mu\nabla_\beta\nabla_\alpha\sigma_\nu{}^\beta - \frac{34}{9}\Theta^2 u^\alpha\nabla_\alpha\sigma_{\mu\nu} + \frac{88}{21}\dot\Theta u^\alpha\nabla_\alpha\sigma_{\mu\nu} + \frac{15}{7}u^\alpha u^\beta\nabla_\mu\sigma_{\beta\rho}\nabla_\alpha\sigma_\nu{}^\rho + \frac{20}{21}\nabla_\mu\Theta\nabla_\alpha\sigma_\nu{}^\alpha \\
& - \frac{118}{7}\sigma_\mu{}^\beta\sigma_\beta{}^\rho u^\alpha\nabla_\alpha\sigma_{\nu\rho} - \frac{86}{7}\sigma_\mu{}^\beta\sigma_\nu{}^\rho u^\alpha\nabla_\alpha\sigma_{\beta\rho} + \frac{16}{7}\sigma_{\mu\nu}u^\alpha\nabla_\alpha\dot\Theta + \frac{16}{21}\Theta\nabla_\alpha\nabla_\mu\sigma_\nu{}^\alpha + \frac{8}{7}\sigma_\mu{}^\alpha\nabla_\alpha\nabla_\nu\Theta \\
& - \frac{2}{7}u^\alpha\nabla_\alpha\nabla_\mu\nabla_\beta\sigma_\nu{}^\beta - \frac{2}{7}u^\alpha\nabla_\alpha\nabla_\beta\nabla_\mu\sigma_\nu{}^\beta - \frac{1}{7}u^\alpha\nabla_\alpha\nabla^\beta\nabla_\beta\sigma_{\mu\nu} + \frac{20}{21}\nabla_\mu\sigma_{\nu\alpha}\nabla^\alpha\Theta + \frac{10}{21}\nabla_\alpha\sigma_{\mu\nu}\nabla^\alpha\Theta \\
& + \frac{6}{7}\nabla_\alpha\sigma_\mu{}^\beta\nabla^\alpha\sigma_{\nu\beta} + \frac{60}{7}u^\alpha u^\beta\nabla_\alpha\sigma_\mu{}^\rho\nabla_\beta\sigma_{\nu\rho} + \frac{12}{7}\nabla_\mu\sigma_\nu{}^\alpha\nabla_\beta\sigma_\alpha{}^\beta + \frac{15}{7}u^\alpha u^\beta\nabla_\mu\sigma_\nu{}^\rho\nabla_\beta\sigma_{\alpha\rho} \\
& + \frac{8}{7}\sigma_\mu{}^\alpha\nabla_\beta\nabla_\nu\sigma_\alpha{}^\beta + \sigma_\mu{}^\rho u^\alpha u^\beta\nabla_\beta\nabla_\nu\sigma_{\alpha\rho} - \frac{2}{7}u^\alpha\nabla_\beta\nabla_\mu\nabla_\alpha\sigma_\nu{}^\beta + \frac{8}{21}\Theta\nabla^\alpha\nabla_\alpha\sigma_{\mu\nu} + \frac{76}{21}\Theta u^\alpha u^\beta\nabla_\beta\nabla_\alpha\sigma_{\mu\nu}
\end{aligned}
$$

$$
\begin{aligned}
&+\frac{80}{7}\sigma_\mu{}^\rho u^\alpha u^\beta \nabla_\beta\nabla_\alpha\sigma_{\nu\rho}+\frac{2}{7}\sigma_{\mu\nu}\nabla^\alpha\nabla_\alpha\Theta-\frac{2}{7}u^\alpha\nabla_\beta\nabla_\alpha\nabla_\mu\sigma_\nu{}^\beta+\frac{12}{7}\nabla_\mu\sigma_{\alpha\beta}\nabla^\beta\sigma_\nu{}^\alpha-\frac{1}{7}u^\alpha\nabla^\beta\nabla_\alpha\nabla_\beta\sigma_{\mu\nu}\\
&-\frac{10}{7}u^\alpha u^\beta u^\rho\nabla_\rho\nabla_\beta\nabla_\alpha\sigma_{\mu\nu}-2\sigma_\mu{}^\beta\sigma_\beta{}^\rho u^\alpha\nabla_\nu\sigma_{\alpha\rho}+\frac{16}{21}\Theta\nabla_\mu\nabla_\alpha\sigma_\nu{}^\alpha+\sigma_\mu{}^\rho u^\alpha u^\beta\nabla_\nu\nabla_\beta\sigma_{\alpha\rho}\\
&-\frac{428}{21}\sigma_\mu{}^\beta\Theta u^\alpha\nabla_\alpha\sigma_{\nu\beta}-\frac{1}{3}u^\alpha\nabla_\alpha\nabla_\mu\nabla_\nu\Theta+\frac{10}{21}u^\alpha u^\beta\nabla_\mu\Theta\nabla_\beta\sigma_{\nu\alpha}+\frac{11}{21}\Theta u^\alpha u^\beta\nabla_\beta\nabla_\mu\sigma_{\nu\alpha}\\
&-\frac{1}{7}u^\alpha\nabla^\beta\nabla_\beta\nabla_\alpha\sigma_{\mu\nu}+\frac{8}{7}\sigma^{\alpha\beta}\nabla_\beta\nabla_\mu\sigma_{\nu\alpha}+\frac{8}{7}\sigma_\mu{}^\rho\nabla^\alpha\nabla_\alpha\sigma_{\nu\rho}\,,
\end{aligned}
\tag{A.13}
$$

$$
\begin{aligned}
\mathbb{X}^{(4)}_{\mu\nu\alpha}\overset{\text{pstf}}{=}\;&\frac{166}{27}\sigma_\nu{}^\beta\sigma_{\alpha\beta}\nabla_\mu\Theta+\frac{464}{81}\Theta\sigma_{\mu\nu}\nabla_\alpha\Theta+\frac{452}{27}\Theta\sigma_\mu{}^\beta\nabla_\alpha\sigma_{\nu\beta}+\frac{2}{81}(134\Theta^2-141\dot\Theta)\nabla_\alpha\sigma_{\mu\nu}\\
&+10\sigma_\mu{}^\beta\sigma_\nu{}^\rho\nabla_\alpha\sigma_{\beta\rho}-u^\beta\nabla_\nu\sigma_\mu{}^\rho\nabla_\alpha\sigma_{\beta\rho}-\frac{7}{27}\Theta u^\beta\nabla_\alpha\nabla_\nu\sigma_{\mu\beta}-\frac{5}{9}\sigma_\mu{}^\rho u^\beta\nabla_\alpha\nabla_\nu\sigma_{\beta\rho}+\frac{1}{3}\nabla_\mu\nabla_\nu\nabla_\alpha\Theta\\
&-\frac{26}{9}\Theta u^\beta\nabla_\alpha\nabla_\beta\sigma_{\mu\nu}-\frac{80}{9}\sigma_\mu{}^\rho u^\beta\nabla_\alpha\nabla_\beta\sigma_{\nu\rho}+\frac{2}{9}\nabla_\alpha\nabla_\beta\nabla_\nu\sigma_\mu{}^\beta+\frac{1}{9}\nabla_\alpha\nabla^\beta\nabla_\beta\sigma_{\mu\nu}+\frac{10}{9}u^\beta u^\rho\nabla_\alpha\nabla_\rho\nabla_\beta\sigma_{\mu\nu}\\
&-\frac{94}{27}u^\beta\nabla_\mu\Theta\nabla_\beta\sigma_{\nu\alpha}+\frac{4}{9}\Theta\sigma_{\mu\nu}\nabla_\beta\sigma_\alpha{}^\beta-\frac{40}{3}u^\beta\nabla_\nu\sigma_\mu{}^\rho\nabla_\beta\sigma_{\alpha\rho}-\frac{26}{9}\Theta u^\beta\nabla_\beta\nabla_\alpha\sigma_{\mu\nu}-\frac{80}{9}\sigma_\mu{}^\rho u^\beta\nabla_\beta\nabla_\alpha\sigma_{\nu\rho}\\
&+\frac{2}{9}\nabla_\beta\nabla_\alpha\nabla_\nu\sigma_\mu{}^\beta+\frac{8}{9}\sigma_{\mu\nu}\sigma_{\alpha\beta}\nabla^\beta\Theta+\frac{1}{9}\nabla^\beta\nabla_\alpha\nabla_\beta\sigma_{\mu\nu}+\frac{10}{9}u^\beta u^\rho\nabla_\rho\nabla_\alpha\nabla_\beta\sigma_{\mu\nu}+\frac{1}{9}\nabla^\beta\nabla_\beta\nabla_\alpha\sigma_{\mu\nu}\\
&+14\sigma_\mu{}^\beta\sigma_\beta{}^\rho\nabla_\alpha\sigma_{\nu\rho}+\frac{2}{9}\nabla_\alpha\nabla_\nu\nabla_\beta\sigma_\mu{}^\beta+\frac{4}{9}\Theta\sigma_\mu{}^\beta\nabla_\beta\sigma_{\nu\alpha}-4\sigma_{\mu\nu}u^\beta\nabla_\beta\nabla_\alpha\Theta+\frac{10}{9}u^\beta u^\rho\nabla_\rho\nabla_\beta\nabla_\alpha\sigma_{\mu\nu}\\
&-\frac{2}{9}u^\beta\nabla_\mu\Theta\nabla_\alpha\sigma_{\nu\beta}\,,
\end{aligned}
\tag{A.14}
$$

$$
\begin{aligned}
\mathbb{X}^{(4)}_{\mu\nu\alpha\beta}\overset{\text{pstf}}{=}\;&\frac{10}{3}\Theta\sigma_{\mu\nu}\sigma_\alpha{}^\rho\sigma_{\beta\rho}+\frac{2}{9}(13\Theta^2-9\dot\Theta)\sigma_{\mu\nu}\sigma_{\alpha\beta}+\frac{10}{3}\nabla_\mu\Theta\nabla_\beta\sigma_{\nu\alpha}+6\nabla_\nu\sigma_\mu{}^\rho\nabla_\beta\sigma_{\alpha\rho}\\
&+2\sigma_{\mu\nu}\nabla_\beta\nabla_\alpha\Theta-u^\rho\nabla_\beta\nabla_\alpha\nabla_\rho\sigma_{\mu\nu}-\,u^\rho\nabla_\beta\nabla_\rho\nabla_\alpha\sigma_{\mu\nu}-u^\rho\nabla_\rho\nabla_\beta\nabla_\alpha\sigma_{\mu\nu}-2\Theta\sigma_{\mu\nu}\dot\sigma_{\alpha\beta}\\
&+8\sigma_\mu{}^\rho\nabla_\beta\nabla_\alpha\sigma_{\nu\rho}+\frac{8}{3}\Theta\nabla_\beta\nabla_\alpha\sigma_{\mu\nu}\,,
\end{aligned}
\tag{A.15}
$$

$$
\mathbb{X}^{(4)}_{\mu\nu\alpha\beta\rho}\overset{\text{pstf}}{=}\;2\sigma_{\nu\alpha}\sigma_{\beta\rho}\nabla_\mu\Theta+2\Theta\sigma_{\mu\nu}\nabla_\rho\sigma_{\alpha\beta}+\nabla_\rho\nabla_\beta\nabla_\alpha\sigma_{\mu\nu}\,.
\tag{A.16}
$$

Multipoles of $\mathbb{Y}^{(1,2)}$

$$
\mathbb{Y}^{(1)}=\langle\mathbb{Y}^{(1)}\rangle+\mathbb{Y}^{(1)}_\mu\,n^\mu+\mathbb{Y}^{(1)}_{\langle\mu\nu\rangle}\,n^\mu n^\nu\,,
\tag{A.17}
$$

where

$$
\langle\mathbb{Y}^{(1)}\rangle=\frac{1}{3}R^\mu_\mu+\frac{4}{3}u^\mu u^\nu R_{\mu\nu}\,,
\tag{A.18}
$$

$$
\mathbb{Y}^{(1)}_\mu\overset{\text{pstf}}{=}-2u^\nu R_{\mu\nu}\,,
\tag{A.19}
$$

$$
\mathbb{Y}^{(1)}_{\mu\nu}\overset{\text{pstf}}{=}R_{\mu\nu}\,.
\tag{A.20}
$$

$$
\mathbb{Y}^{(2)}=\langle\mathbb{Y}^{(2)}\rangle+\mathbb{Y}^{(2)}_\mu\,n^\mu+\mathbb{Y}^{(2)}_{\langle\mu\nu\rangle}\,n^\mu n^\nu+\mathbb{Y}^{(2)}_{\langle\mu\nu\alpha\rangle}\,n^\mu n^\nu n^\alpha\,,
\tag{A.21}
$$

where

$$
\langle\mathbb{Y}^{(2)}\rangle=-\frac{1}{3}\dot R-\frac{2}{3}u^\mu\nabla_\nu R_\mu{}^\nu-2u^\mu u^\nu\dot R_{\mu\nu}\,,
\tag{A.22}
$$

$$\mathbb{Y}^{(2)}_{\mu} \overset{\text{pstf}}{=} \frac{6}{5}u^{\nu}u^{\alpha}\nabla_{\mu}R_{\nu\alpha} + \frac{1}{5}\,\nabla_{\mu}R + \frac{2}{5}\nabla_{\nu}R_{\mu}{}^{\nu} + \frac{12}{5}u^{\nu}\dot{R}_{\mu\nu}\,, \tag{A.23}$$

$$\mathbb{Y}^{(2)}_{\mu\nu} \overset{\text{pstf}}{=} -2u^{\alpha}\nabla_{\nu}R_{\mu\alpha} - \dot{R}_{\mu\nu}\,, \tag{A.24}$$

$$\mathbb{Y}^{(2)}_{\mu\nu\alpha} \overset{\text{pstf}}{=} \nabla_{\mu}R_{\nu\alpha}\,. \tag{A.25}$$

Appendix B

Light geodesics in Einstein de Sitter spacetime

Consider the FLRW metric

$$\mathrm{d}s^2 = -\mathrm{d}t^2 + a^2(t)\left[\mathrm{d}r^2 + r^2(\mathrm{d}\vartheta^2 + \sin^2\vartheta\,\mathrm{d}\phi^2)\right], \tag{B.1}$$

with an off-centre observer at a distance r_o from the center of the coordinates (at $r = 0$). We choose the Z-axis along this direction. The past pointing 4-wavevector of light is

$$k^\mu = \frac{\mathrm{d}x^\mu}{\mathrm{d}\lambda}, \tag{B.2}$$

where λ is an affine parameter. We determine the geodesic path by solving the geodesic equations

$$\frac{\mathrm{d}^2x^\mu}{\mathrm{d}\lambda^2} + \Gamma^\mu{}_{\nu\alpha}\frac{\mathrm{d}x^\nu}{\mathrm{d}\lambda}\frac{\mathrm{d}x^\alpha}{\mathrm{d}\lambda} = 0\,. \tag{B.3}$$

For the off-center observer, $k^3 = 0$ by symmetry. We choose the affine parameter as the physical distance measured by an observer at rest in the smooth background, with 4-velocity $\tilde{u}^\mu = \delta^\mu_0$, so that $\lambda = 0$ at the observer position and $(k^\mu\tilde{u}_\mu)_o = 1$. The initial conditions are

$$t(0) = t_0\,, \qquad r(0) = r_o\,, \qquad \vartheta(0) = 0\,, \quad \left.\frac{\mathrm{d}t}{\mathrm{d}\lambda}\right|_0 = -1\,, \qquad \left.\frac{\mathrm{d}r}{\mathrm{d}\lambda}\right|_0 = -\cos\theta\,, \qquad \left.\frac{\mathrm{d}\vartheta}{\mathrm{d}\lambda}\right|_0 = \frac{1}{r_o}\sin\theta\,, \tag{B.4}$$

where t_0 is the time of observation (today), and θ is the angle between the Z-axis and the direction the light ray measured by the observer $\tilde{u}^\mu$. The photon trajectory is thus

$$t(\lambda) = t_0\left(1 - \frac{5}{3}\frac{\lambda}{t_0}\right)^{3/5} \tag{B.5}$$

$$r(\lambda) = r_o\left\{1 + 6\cos\theta\frac{t_0}{r_o}\left[\left(1 - \frac{5}{3}\frac{\lambda}{t_0}\right)^{1/5} - 1\right] + 9\frac{t_0^2}{r_o^2}\left[\left(1 - \frac{5}{3}\frac{\lambda}{t_0}\right)^{1/5} - 1\right]^2\right\}^{1/2}, \tag{B.6}$$

$$\vartheta(\lambda) = \tan^{-1}(\cot\theta) - \tan^{-1}\left\{\cot\theta + 3\frac{t_0}{r_o}\left[\left(1 - \frac{5\lambda}{3t_0}\right)^{1/5} - 1\right]\csc\theta\right\}. \tag{B.7}$$

By using eq. (1.51) and eq. (1.53), we can then infer the value of the redshift and luminosity distance.

Bibliography

[1] Albert Einstein. "Cosmological Considerations in the General Theory of Relativity". In: *Sitzungsber. Preuss. Akad. Wiss. Berlin (Math. Phys.)* 1917 (1917), pp. 142–152.

[2] A. Friedman. "On the Curvature of space". In: *Z. Phys.* 10 (1922), pp. 377–386. DOI: 10.1007/BF01332580.

[3] E. P. Hubble. "Extragalactic nebulae." In: *ApJ* 64 (Dec. 1926), pp. 321–369. DOI: 10.1086/143018.

[4] Georges Lemaître. "Un univers homogène de masse constante et de rayon croissant, rendant compte de la vitesse radiale des nébuleuses extragalactiques". In: *Annales Soc. Sci. Bruxelles A* 47 (1927), p. 49. DOI: 10.1007/s10714-013-1548-3.

[5] Mario Livio. "Mystery of the missing text solved". In: *Nature* 479.7372 (2011), pp. 171–173. DOI: 10.1038/479171a.

[6] H. P. Robertson. "Kinematics and World-Structure". In: *Astrophys. J.* 82 (1935), pp. 284–301. DOI: 10.1086/143681.

[7] A. G. Walker. "On Milne's Theory of World-Structure". In: *Proc. Lond. Math. Soc. s* 2-42.1 (1937), pp. 90–127. DOI: 10.1112/plms/s2-42.1.90.

[8] Sunny Vagnozzi. "Seven Hints That Early-Time New Physics Alone Is Not Sufficient to Solve the Hubble Tension". In: *Universe* 9.9 (2023), p. 393. DOI: 10.3390/universe9090393. arXiv: 2308.16628 [astro-ph.CO].

[9] Chris Clarkson and Roy Maartens. "Inhomogeneity and the foundations of concordance cosmology". In: *Class. Quant. Grav.* 27 (2010), p. 124008. DOI: 10.1088/0264-9381/27/12/124008. arXiv: 1005.2165 [astro-ph.CO].

[10] C. L. Bennett et al. "Nine-year Wilkinson Microwave Anisotropy Probe (WMAP) Observations: Final Maps and Results". In: *ApJS* 208.2, 20 (Oct. 2013), p. 20. DOI: 10.1088/0067-0049/208/2/20. arXiv: 1212.5225 [astro-ph.CO].

[11] P. A. R. Ade et al. "Planck 2015 results. XVI. Isotropy and statistics of the CMB". In: *Astron. Astrophys.* 594 (2016), A16. DOI: 10.1051/0004-6361/201526681. arXiv: 1506.07135 [astro-ph.CO].

[12] Prakash Sarkar et al. "The scale of homogeneity of the galaxy distribution in SDSS DR6". In: *MNRAS* 399.1 (Oct. 2009), pp. L128–L131. DOI: 10.1111/j.1745-3933.2009.00738.x. arXiv: 0906.3431 [astro-ph.CO].

[13] C. Marinoni, J. Bel, and A. Buzzi. "The scale of cosmic isotropy". In: *JCAP* 2012.10, 036 (Oct. 2012), p. 036. DOI: 10.1088/1475-7516/2012/10/036. arXiv: 1205.3309 [astro-ph.CO].

[14] Stephen Appleby and Arman Shafieloo. "Testing isotropy in the local Universe". In: *JCAP* 2014.10, 070 (Oct. 2014), p. 070. DOI: 10.1088/1475-7516/2014/10/070. arXiv: 1405.4595 [astro-ph.CO].

[15] Carlos A. P. Bengaly et al. "Testing the cosmological principle in the radio sky". In: *JCAP* 2019.9, 025 (Sept. 2019), p. 025. DOI: 10.1088/1475-7516/2019/09/025. arXiv: 1905.12378 [astro-ph.CO].

[16] Suman Sarkar, Biswajit Pandey, and Rishi Khatri. "Testing isotropy in the Universe using photometric and spectroscopic data from the SDSS". In: *MNRAS* 483.2 (Feb. 2019), pp. 2453–2464. DOI: 10.1093/mnras/sty3272. arXiv: 1810.07410 [astro-ph.CO].

[17] Pierros Ntelis et al. "Cosmological constraints from cosmic homogeneity". In: *arXiv e-prints*, arXiv:1904.06135 (Apr. 2019), arXiv:1904.06135. arXiv: 1904.06135 [astro-ph.CO].

[18] Uendert Andrade et al. "Revisiting the statistical isotropy of GRB sky distribution". In: *Mon. Not. Roy. Astron. Soc.* 490.4 (2019), pp. 4481–4488. DOI: 10.1093/mnras/stz2754. arXiv: 1905.08864 [astro-ph.CO].

[19] Ethan Payne et al. "Searching for anisotropy in the distribution of binary black hole mergers". In: *Physical Review D* 102.10, 102004 (Nov. 2020), p. 102004. DOI: 10.1103/PhysRevD.102.102004. arXiv: 2006.11957 [astro-ph.CO].

[20] Biswajit Pandey and Suman Sarkar. "Testing homogeneity of the galaxy distribution in the SDSS using Renyi entropy". In: *JCAP* 2021.7, 019 (July 2021), p. 019. DOI: 10.1088/1475-7516/2021/07/019. arXiv: 2103.11954 [astro-ph.CO].

[21] Rodrigo S. Gonçalves et al. "Measuring the cosmic homogeneity scale with SDSS-IV DR16 Quasars". In: *JCAP* 03 (2021), p. 029. DOI: 10.1088/1475-7516/2021/03/029. arXiv: 2010.06635 [astro-ph.CO].

[22] Rong-Gen Cai et al. "Constraining the anisotropic expansion of the Universe". In: *Physical Review D* 87.12, 123522 (June 2013), p. 123522. DOI: 10.1103/PhysRevD.87.123522. arXiv: 1303.0961 [astro-ph.CO].

[23] Zhe Chang et al. "A tomographic test of cosmological principle using the JLA compilation of type Ia supernovae". In: *MNRAS* 478.3 (Aug. 2018), pp. 3633–3639. DOI: 10.1093/mnras/sty1120. arXiv: 1711.11321 [astro-ph.CO].

[24] Hua-Kai Deng and Hao Wei. "Null signal for the cosmic anisotropy in the Pantheon supernovae data". In: *European Physical Journal C* 78.9, 755 (Sept. 2018), p. 755. DOI: 10.1140/epjc/s10052-018-6159-4. arXiv: 1806.02773 [astro-ph.CO].

[25] Z. Q. Sun and F. Y. Wang. "Testing the anisotropy of cosmic acceleration from Pantheon supernovae sample". In: *MNRAS* 478.4 (Aug. 2018), pp. 5153–5158. DOI: 10.1093/mnras/sty1391. arXiv: 1805.09195 [astro-ph.CO].

[26] Uendert Andrade et al. "A Model-independent Test of Cosmic Isotropy with Low-z Pantheon Supernovae". In: *Astrophys. J.* 865.2 (2018), p. 119. DOI: 10.3847/1538-4357/aadb90. arXiv: 1806.06990 [astro-ph.CO].

[27] Dong Zhao, Yong Zhou, and Zhe Chang. "Anisotropy of the Universe via the Pantheon supernovae sample revisited". In: *MNRAS* 486.4 (July 2019), pp. 5679–5689. DOI: 10.1093/mnras/stz1259. arXiv: 1903.12401 [astro-ph.CO].

[28] J. P. Hu, Y. Y. Wang, and F. Y. Wang. "Testing cosmic anisotropy with Pantheon sample and quasars at high redshifts". In: *Astron. Astrophys.* 643 (2020), A93. DOI: 10.1051/0004-6361/202038541. arXiv: 2008.12439 [astro-ph.CO].

[29] W. Rahman et al. "New constraints on anisotropic expansion from supernovae Type Ia". In: *Mon. Not. Roy. Astron. Soc.* 514.1 (2022), pp. 139–163. DOI: 10.1093/mnras/stac1223. arXiv: 2108.12497 [astro-ph.CO].

[30] Dominik J. Schwarz and Bastian Weinhorst. "(An)isotropy of the Hubble diagram: Comparing hemispheres". In: *Astron. Astrophys.* 474 (2007), pp. 717–729. DOI: 10.1051/0004-6361:20077998. arXiv: 0706.0165 [astro-ph].

[31] A. Kashlinsky et al. "A measurement of large-scale peculiar velocities of clusters of galaxies: results and cosmological implications". In: *Astrophys. J. Lett.* 686 (2009), pp. L49–L52. DOI: 10.1086/592947. arXiv: 0809.3734 [astro-ph].

[32] I. Antoniou and L. Perivolaropoulos. "Searching for a Cosmological Preferred Axis: Union2 Data Analysis and Comparison with Other Probes". In: *JCAP* 12 (2010), p. 012. DOI: 10.1088/1475-7516/2010/12/012. arXiv: 1007.4347 [astro-ph.CO].

[33] Benedict Kalus et al. "Constraints on anisotropic cosmic expansion from supernovae". In: *Astron. Astrophys.* 553 (2013), A56. DOI: 10.1051/0004-6361/201220928. arXiv: 1212.3691 [astro-ph.CO].

[34] Mijin Yoon et al. "Dipolar modulation in number counts of WISE-2MASS sources". In: *Mon. Not. Roy. Astron. Soc.* 445 (2014), pp. L60–L64. DOI: 10.1093/mnrasl/slu133. arXiv: 1406.1187 [astro-ph.CO].

[35] Prabhakar Tiwari and Adi Nusser. "Revisiting the NVSS number count dipole". In: *JCAP* 03 (2016), p. 062. DOI: 10.1088/1475-7516/2016/03/062. arXiv: 1509.02532 [astro-ph.CO].

[36] B. Javanmardi et al. "Probing the Isotropy of Cosmic Acceleration Traced By Type Ia Supernovae". In: *Astrophys. J.* 810.1, 47 (Sept. 2015), p. 47. DOI: 10.1088/0004-637X/810/1/47. arXiv: 1507.07560 [astro-ph.CO].

[37] J. Colin et al. "High redshift radio galaxies and divergence from the CMB dipole". In: *Mon. Not. Roy. Astron. Soc.* 471.1 (2017), pp. 1045–1055. DOI: 10.1093/mnras/stx1631. arXiv: 1703.09376 [astro-ph.CO].

[38] K. Migkas et al. "Probing cosmic isotropy with a new X-ray galaxy cluster sample through the $L_X - T$ scaling relation". In: *Astron. Astrophys.* 636 (2020), A15. DOI: 10.1051/0004-6361/201936602. arXiv: 2004.03305 [astro-ph.CO].

[39] K. Migkas et al. "Cosmological implications of the anisotropy of ten galaxy cluster scaling relations". In: *Astron. Astrophys.* 649 (2021), A151. DOI: 10.1051/0004-6361/202140296. arXiv: 2103.13904 [astro-ph.CO].

[40] Nathan J. Secrest et al. "A Test of the Cosmological Principle with Quasars". In: *Astrophys. J. Lett.* 908.2 (2021), p. L51. DOI: 10.3847/2041-8213/abdd40. arXiv: 2009.14826 [astro-ph.CO].

[41] Thilo M. Siewert, Matthias Schmidt-Rubart, and Dominik J. Schwarz. "Cosmic radio dipole: Estimators and frequency dependence". In: *Astron. Astrophys.* 653 (2021), A9. DOI: 10.1051/0004-6361/202039840. arXiv: 2010.08366 [astro-ph.CO].

[42] Orlando Luongo et al. "Larger H0 values in the CMB dipole direction". In: *Phys. Rev. D* 105.10 (2022), p. 103510. DOI: 10.1103/PhysRevD.105.103510. arXiv: 2108.13228 [astro-ph.CO].

[43] Chethan Krishnan et al. "Hints of FLRW breakdown from supernovae". In: *Phys. Rev. D* 105.6 (2022), p. 063514. DOI: 10.1103/PhysRevD.105.063514. arXiv: 2106.02532 [astro-ph.CO].

[44] Maria Giovanna Dainotti et al. "On the Hubble constant tension in the SNe Ia Pantheon sample". In: *Astrophys. J.* 912.2 (2021), p. 150. DOI: 10.3847/1538-4357/abeb73. arXiv: 2103.02117 [astro-ph.CO].

[45] Kitty Ferguson. "The Glassmaker Who Sparked Astrophysics". In: *Nautilus* (Mar. 2014). Illustrated by Miko Maciaszek. URL: https://web.archive.org/web/20140323010729/http://nautil.us/issue/11/light/the-glassmaker-who-sparked-astrophysics.

[46] M. S. Longair. *The Cosmic Century: A history of astrophysics and cosmology*. Cambridge University Press, 2006.

[47] Steven Weinberg. *The First Three Minutes: A Modern View of the Origin of the Universe*. 2nd. Basic Books, 1993. ISBN: 9780465024377. URL: https://www.basicbooks.com/titles/steven-weinberg/the-first-three-minutes/9780465024377/.

[48] D. Scott Birney, Guillermo Gonzalez, and David Oesper. *Observational Astronomy 2'nd edition*. Cambridge University Press, 2006.

[49] Steven Weinberg. *Cosmology*. Oxford University Press Inc., 2008.

[50] Roy Maartens et al. "Covariant cosmography: the observer-dependence of the Hubble parameter". In: *JCAP* 09 (2024), p. 070. DOI: 10.1088/1475-7516/2024/09/070. arXiv: 2312.09875 [astro-ph.CO].

[51] R. Miles. "A light history of photometry: from Hipparchus to the Hubble Space Telescope". In: *Journal of the British Astronomical Association* 117 (Aug. 2007), pp. 172–186.

[52] G. F. R. Ellis. "Relativistic cosmology". In: *Proc. Int. Sch. Phys. Fermi* 47 (1971), p. 104. DOI: 10.1007/s10714-009-0760-7.

[53] G F R Ellis, R Maartens, and M A H MacCallum. *Relativistic Cosmology*. Cambridge: Cambridge University Press, 2012. ISBN: 9780511741005.

[54] International Astronomical Union. *IAU Press Release 1812*. [Accessed: August 27, 2024]. 2018. URL: https://www.iau.org/news/pressreleases/detail/iau1812/?lang.

[55] Patrick Peter and Jean-Philippe Uzan. *Primordial Cosmology*. Oxford Graduate Texts. Oxford University Press, Feb. 2013.

[56] Matt Visser. "Jerk, snap and the cosmological equation of state". In: *Class. Quant. Grav.* 21 (2004), pp. 2603–2616. DOI: 10.1088/0264-9381/21/11/006. arXiv: gr-qc/0309109.

[57] Steven Weinberg. *Gravitation and Cosmology: Principles and Applications of the General Theory of Relativity*. 685 pages. John Wiley & Sons, Inc., 1972. ISBN: 0471925675.

[58] Matt Visser. "Cosmography: Cosmology without the Einstein equations". In: *Gen. Rel. Grav.* 37 (2005). Ed. by D. E. McClelland and S. M. Scott, pp. 1541–1548. DOI: 10.1007/s10714-005-0134-8. arXiv: gr-qc/0411131.

[59] J. Kristian and R. K. Sachs. "Observations in cosmology". In: *The Astrophysical Journal* 143 (1966), p. 379. DOI: 10.1086/148522.

[60] J. B. Hartle. *Gravity: An Introduction to Einstein's General Relativity*. English. Addison-Wesley, 2003.

[61] P J Peebles. *The large-scale structure of the universe*. Princeton University Press, 1980.

[62] Lam Hui and Patrick B. Greene. "Correlated Fluctuations in Luminosity Distance and the (Surprising) Importance of Peculiar Motion in Supernova Surveys". In: *Phys. Rev. D* 73 (2006), p. 123526. DOI: 10.1103/PhysRevD.73.123526. arXiv: astro-ph/0512159.

[63] Ruth Durrer. *The cosmic microwave background*. Cambridge University Press, 2021.

[64] Camille Bonvin, Ruth Durrer, and M. Alice Gasparini. "Fluctuations of the luminosity distance". In: *Physical Review D* 73.2 (2006). DOI: 10.1103/physrevd.73.023523.

[65] Henrietta S. Leavitt and Edward C. Pickering. "Periods of 25 Variable Stars in the Small Magellanic Cloud". In: *Harvard Obs. Circ.* 173 (1912), pp. 1–3.

[66] Stephen Webb. *Measuring the Universe: The Cosmological Distance Ladder*. Springer London, 1999.

[67] Wendy L. Freedman et al. "The Carnegie-Chicago Hubble Program. VIII. An Independent Determination of the Hubble Constant Based on the Tip of the Red Giant Branch". In: *Astrophys. J.* 882 (2019), p. 34. DOI: 10.3847/1538-4357/ab2f73. arXiv: 1907.05922 [astro-ph.CO].

[68] R. B. Tully and J. R. Fisher. "A new method of determining distances to galaxies." In: *A&A* 54 (Feb. 1977), pp. 661–673.

[69] S. M. Faber and R. E. Jackson. "Velocity dispersions and mass-to-light ratios for elliptical galaxies." In: *ApJ* 204 (Mar. 1976), pp. 668–683. DOI: 10.1086/154215.

[70] Alan Dressler et al. "Spectroscopy and Photometry of Elliptical Galaxies. I. New Distance Estimator". In: *ApJ* 313 (Feb. 1987), p. 42. DOI: 10.1086/164947.

[71] John Tonry and Donald P. Schneider. "A New Technique for Measuring Extragalactic Distances". In: *AJ* 96 (Sept. 1988), p. 807. DOI: 10.1086/114847.

[72] R. Brent Tully et al. "Cosmicflows-4". In: *Astrophys. J.* 944.1 (2023), p. 94. DOI: 10.3847/1538-4357/ac94d8. arXiv: 2209.11238 [astro-ph.CO].

[73] Mario Hamuy and Philip A. Pinto. "Type II supernovae as standardized candles". In: *Astrophys. J. Lett.* 566 (2002), pp. L63–L65. DOI: 10.1086/339676. arXiv: astro-ph/0201279.

[74] Weidong Li et al. "Nearby supernova rates from the Lick Observatory Supernova Search – II. The observed luminosity functions and fractions of supernovae in a complete sample". In: *Monthly Notices of the Royal Astronomical Society* 412.3 (Apr. 2011), pp. 1441–1472. ISSN: 0035-8711. DOI: 10.1111/j.1365-2966.2011.18160.x. eprint: https://academic.oup.com/mnras/article-pdf/412/3/1441/17326749/mnras0412-1441.pdf. URL: https://doi.org/10.1111/j.1365-2966.2011.18160.x.

[75] S. Perlmutter et al. "Measurements of Ω and Λ from 42 High Redshift Supernovae". In: *Astrophys. J.* 517 (1999), pp. 565–586. DOI: 10.1086/307221. arXiv: astro-ph/9812133.

[76] Adam G. Riess et al. "Observational evidence from supernovae for an accelerating universe and a cosmological constant". In: *Astron. J.* 116 (1998), pp. 1009–1038. DOI: 10.1086/300499. arXiv: astro-ph/9805201.

[77] Dillon Brout et al. "The Pantheon+ Analysis: Cosmological Constraints". In: *Astrophys. J.* 938.2 (2022), p. 110. DOI: 10.3847/1538-4357/ac8e04. arXiv: 2202.04077 [astro-ph.CO].

[78] N. W. Boggess et al. "The COBE Mission: Its Design and Performance Two Years after Launch". In: *ApJ* 397 (Oct. 1992), p. 420. DOI: 10.1086/171797.

[79] C. L. Bennett et al. "First year Wilkinson Microwave Anisotropy Probe (WMAP) observations: Preliminary maps and basic results". In: *Astrophys. J. Suppl.* 148 (2003), pp. 1–27. DOI: 10.1086/377253. arXiv: astro-ph/0302207.

[80] N. Aghanim et al. "Planck 2018 results. I. Overview and the cosmological legacy of Planck". In: *Astron. Astrophys.* 641 (2020), A1. DOI: 10.1051/0004-6361/201833880. arXiv: 1807.06205 [astro-ph.CO].

[81] N. Aghanim et al. "Planck 2018 results. VI. Cosmological parameters". In: *Astron. Astrophys.* 641 (2020). [Erratum: Astron.Astrophys. 652, C4 (2021)], A6. DOI: 10.1051/0004-6361/201833910. arXiv: 1807.06209 [astro-ph.CO].

[82] Daniel J. Eisenstein et al. "Detection of the Baryon Acoustic Peak in the Large-Scale Correlation Function of SDSS Luminous Red Galaxies". In: *Astrophys. J.* 633 (2005), pp. 560–574. DOI: 10.1086/466512. arXiv: astro-ph/0501171.

[83] Dragan Huterer and Daniel L Shafer. "Dark energy two decades after: Observables, probes, consistency tests". In: *Rept. Prog. Phys.* 81.1 (2018), p. 016901. DOI: 10.1088/1361-6633/aa997e. arXiv: 1709.01091 [astro-ph.CO].

[84] Eleonora Di Valentino et al. "In the realm of the Hubble tension—a review of solutions". In: *Class. Quant. Grav.* 38.15 (2021), p. 153001. DOI: 10.1088/1361-6382/ac086d. arXiv: 2103.01183 [astro-ph.CO].

[85] Sunny Vagnozzi, Fabio Pacucci, and Abraham Loeb. "Implications for the Hubble tension from the ages of the oldest astrophysical objects". In: *JHEAp* 36 (2022), pp. 27–35. DOI: 10.1016/j.jheap.2022.07.004. arXiv: 2105.10421 [astro-ph.CO].

[86] C. Krishnan et al. "Is there an early Universe solution to Hubble tension?" In: *Phys. Rev. D* 102.10 (2020), p. 103525. DOI: 10.1103/PhysRevD.102.103525. arXiv: 2002.06044 [astro-ph.CO].

[87] Kenneth C. Wong et al. "H0LiCOW – XIII. A 2.4 per cent measurement of H0 from lensed quasars: 5.3σ tension between early- and late-Universe probes". In: *Mon. Not. Roy. Astron. Soc.* 498.1 (2020), pp. 1420–1439. DOI: 10.1093/mnras/stz3094. arXiv: 1907.04869 [astro-ph.CO].

[88] Hans Böhringer, Gayoung Chon, and Chris A. Collins. "Observational evidence for a local underdensity in the Universe and its effect on the measurement of the Hubble Constant". In: *Astron. Astrophys.* 633 (2020), A19. DOI: 10.1051/0004-6361/201936400. arXiv: 1907.12402 [astro-ph.CO].

[89] Richard Watkins et al. "Analysing the large-scale bulk flow using cosmicflows4: increasing tension with the standard cosmological model". In: *Mon. Not. Roy. Astron. Soc.* 524.2 (2023), pp. 1885–1892. DOI: 10.1093/mnras/stad1984. arXiv: 2302.02028 [astro-ph.CO].

[90] Abbé M. Whitford, Cullan Howlett, and Tamara M. Davis. "Evaluating bulk flow estimators for CosmicFlows–4 measurements". In: *Mon. Not. Roy. Astron. Soc.* 526.2 (2023), pp. 3051–3071. DOI: 10.1093/mnras/stad2764. arXiv: 2306.11269 [astro-ph.CO].

[91] David Camarena and Valerio Marra. "Impact of the cosmic variance on H_0 on cosmological analyses". In: *Phys. Rev. D* 98.2 (2018), p. 023537. DOI: 10.1103/PhysRevD.98.023537. arXiv: 1805.09900 [astro-ph.CO].

[92] Jonathan Carrick et al. "Cosmological parameters from the comparison of peculiar velocities with predictions from the 2M++ density field". In: *Mon. Not. Roy. Astron. Soc.* 450.1 (2015), pp. 317–332. DOI: 10.1093/mnras/stv547. arXiv: 1504.04627 [astro-ph.CO].

[93] Anthony Carr et al. "The Pantheon+ analysis: Improving the redshifts and peculiar velocities of Type Ia supernovae used in cosmological analyses". In: *Publ. Astron. Soc. Austral.* 39 (2022), e046. DOI: 10.1017/pasa.2022.41. arXiv: 2112.01471 [astro-ph.CO].

[94] Leandros Perivolaropoulos and Foteini Skara. "Challenges for ΛCDM: An update". In: *New Astron. Rev.* 95 (2022), p. 101659. DOI: 10.1016/j.newar.2022.101659. arXiv: 2105.05208 [astro-ph.CO].

[95] L. F. Secco et al. "Dark Energy Survey Year 3 results: Cosmology from cosmic shear and robustness to modeling uncertainty". In: *Phys. Rev. D* 105.2 (2022), p. 023515. DOI: 10.1103/PhysRevD.105.023515. arXiv: 2105.13544 [astro-ph.CO].

[96] Marika Asgari et al. "KiDS-1000 Cosmology: Cosmic shear constraints and comparison between two point statistics". In: *Astron. Astrophys.* 645 (2021), A104. DOI: 10.1051/0004-6361/202039070. arXiv: 2007.15633 [astro-ph.CO].

[97] Oliver H. E. Philcox and Mikhail M. Ivanov. "BOSS DR12 full-shape cosmology: ΛCDM constraints from the large-scale galaxy power spectrum and bispectrum monopole". In: *Phys. Rev. D* 105.4 (2022), p. 043517. DOI: 10.1103/PhysRevD.105.043517. arXiv: 2112.04515 [astro-ph.CO].

[98] Elcio Abdalla et al. "Cosmology intertwined: A review of the particle physics, astrophysics, and cosmology associated with the cosmological tensions and anomalies". In: *JHEAp* 34 (2022), pp. 49–211. DOI: 10.1016/j.jheap.2022.04.002. arXiv: 2203.06142 [astro-ph.CO].

[99] G. F. R. Ellis and J. E. Baldwin. "On the expected anisotropy of radio source counts". In: *Monthly Notices of the Royal Astronomical Society* 206.2 (Jan. 1984), pp. 377–381. ISSN: 0035-8711. DOI: 10.1093/mnras/206.2.377. eprint: https://academic.oup.com/mnras/article-pdf/206/2/377/18187025/mnras206-0377.pdf. URL: https://doi.org/10.1093/mnras/206.2.377.

[100] Ashok K. Singal. "Large peculiar motion of the solar system from the dipole anisotropy in sky brightness due to distant radio sources". In: *Astrophys. J. Lett.* 742 (2011), p. L23. DOI: 10.1088/2041-8205/742/2/L23. arXiv: 1110.6260 [astro-ph.CO].

[101] James J. Condon et al. "The NRAO VLA Sky survey". In: *Astron. J.* 115 (1998), pp. 1693–1716. DOI: 10.1086/300337.

[102] Edward L. Wright et al. "The Wide-field Infrared Survey Explorer (WISE): Mission Description and Initial On-orbit Performance". In: *Astron. J.* 140 (2010), p. 1868. DOI: 10.1088/0004-6256/140/6/1868. arXiv: 1008.0031 [astro-ph.IM].

[103] Eleonora Di Valentino, Alessandro Melchiorri, and Joseph Silk. "Planck evidence for a closed Universe and a possible crisis for cosmology". In: *Nature Astron.* 4.2 (2019), pp. 196–203. DOI: 10.1038/s41550-019-0906-9. arXiv: 1911.02087 [astro-ph.CO].

[104] Yehuda Hoffman et al. "The Dipole Repeller". In: (Feb. 2017). DOI: 10.1038/s41550-016-0036. arXiv: 1702.02483 [astro-ph.CO].

[105] Pavan Kumar Aluri et al. "Is the observable Universe consistent with the cosmological principle?" In: *Class. Quant. Grav.* 40.9 (2023), p. 094001. DOI: 10.1088/1361-6382/acbefc. arXiv: 2207.05765 [astro-ph.CO].

[106] Jun Koda et al. "Are peculiar velocity surveys competitive as a cosmological probe?" In: *Mon. Not. Roy. Astron. Soc.* 445.4 (2014), pp. 4267–4286. DOI: 10.1093/mnras/stu1610. arXiv: 1312.1022 [astro-ph.CO].

[107] Michael A. Strauss and Jeffrey A. Willick. "The Density and peculiar velocity fields of nearby galaxies". In: *Phys. Rept.* 261 (1995), pp. 271–431. DOI: 10.1016/0370-1573(95)00013-7. arXiv: astro-ph/9502079.

[108] P. B. Lilje, A. Yahil, and B. J. T. Jones. "The Tidal Velocity Field in the Local Supercluster". In: *ApJ* 307 (Aug. 1986), p. 91. DOI: 10.1086/164395.

[109] Hélène M. Courtois et al. "Three-dimensional Velocity and Density Reconstructions of the Local Universe with Cosmicflows-1". In: *ApJ* 744.1, 43 (Jan. 2012), p. 43. DOI: 10.1088/0004-637X/744/1/43. arXiv: 1109.3856 [astro-ph.CO].

[110] S. L. Parnovsky and A. S. Parnowski. "Yet another sample of RFGC galaxies". In: *Astrophys. Space Sci.* 343 (2013), pp. 747–754. DOI: 10.1007/s10509-012-1267-3. arXiv: 1210.0895 [astro-ph.CO].

[111] Suhail Dhawan et al. "The quadrupole in the local Hubble parameter: first constraints using Type Ia supernova data and forecasts for future surveys". In: (May 2022). arXiv: 2205.12692 [astro-ph.CO].

[112] Basheer Kalbouneh, Christian Marinoni, and Julien Bel. "Multipole expansion of the local expansion rate". In: *Phys. Rev. D* 107.2 (2023), p. 023507. DOI: 10.1103/PhysRevD.107.023507. arXiv: 2210.11333 [astro-ph.CO].

[113] George F. R. Ellis. "Relativistic cosmology (republication of 1969 lectures)". In: *General Relativity and Gravitation* 41.3 (2009), pp. 581–660. DOI: 10.1007/s10714-009-0760-7.

[114] M. A. H MacCallum and G. F. R Ellis. "A class of homogeneous cosmological models". In: *Communications in Mathematical Physics* 19.1 (1970), pp. 31–64. DOI: 10.1007/bf01645496.

[115] C. A. Clarkson. "On the Observational Characteristics of Inhomogeneous Cosmologies: Undermining the Cosmological Principle". PhD Thesis. University of Glasgow, Dec. 2000. URL: arxiv.org/abs/astro-ph/0008089.

[116] Chris Clarkson and Roy Maartens. "Inhomogeneity and the foundations of concordance cosmology". In: *Classical and Quantum Gravity* 27.12 (2010), p. 124008. DOI: 10.1088/0264-9381/27/12/124008.

[117] Asta Heinesen. "Multipole decomposition of the general luminosity distance Hubble Law — a new framework for observational cosmology". In: *Journal of Cosmology and Astroparticle Physics* 05.05 (2021), p. 008. DOI: 10.1088/1475-7516/2021/05/008.

[118] Krzysztof M. Gorski. "On Determining the spectrum of primordial inhomogeneity from the Cobe DMR sky maps. 1. Method". In: *Astrophys. J. Lett.* 430 (1994), p. L85. DOI: 10.1086/187444. arXiv: astro-ph/9403066.

[119] K. M. Górski et al. "HEALPix - A Framework for high resolution discretization, and fast analysis of data distributed on the sphere". In: *Astrophys. J.* 622 (2005), pp. 759–771. DOI: 10.1086/427976. arXiv: astro-ph/0409513.

[120] Kathryn P. Drake and Grady B. Wright. "A Fast and Accurate Algorithm for Spherical Harmonic Analysis on HEALPix Grids with Applications to the Cosmic Microwave Background Radiation". In: *J. Comput. Phys.* 416 (2020), p. 109544. DOI: 10.1016/j.jcp.2020.109544. arXiv: 1904.10514 [math.NA].

[121] Daniel J. Mortlock, Anthony D. Challinor, and Michael P. Hobson. "Analysis of cosmic microwave background data on an incomplete sky". In: *Mon. Not. Roy. Astron. Soc.* 330 (2002), p. 405. DOI: 10.1046/j.1365-8711.2002.05085.x. arXiv: astro-ph/0008083.

[122] Basheer Kalbouneh, Christian Marinoni, and Roy Maartens. "Cosmography of the local Universe by multipole analysis of the expansion rate fluctuation field". In: *JCAP* 09 (2024), p. 069. DOI: 10.1088/1475-7516/2024/09/069. arXiv: 2401.12291 [astro-ph.CO].

[123] Robert Braun. "The Interstellar Medium of M31. I. A Survey of Neutral Hydrogen Emission". In: *ApJS* 72 (Apr. 1990), p. 755. DOI: 10.1086/191431.

[124] Abdurro'uf et al. "The Seventeenth Data Release of the Sloan Digital Sky Surveys: Complete Release of MaNGA, MaStar, and APOGEE-2 Data". In: *The Astrophysical Journal Supplement Series* 259.2 (Mar. 2022), p. 35. DOI: 10.3847/1538-4365/ac4414. URL: https://dx.doi.org/10.3847/1538-4365/ac4414.

[125] Alan Dressler et al. "Spectroscopy and Photometry of Elliptical Galaxies: A Large-Scale Streaming Motion in the Local Universe". In: *ApJL* 313 (Feb. 1987), p. L37. DOI: 10.1086/184827.

[126] R. Brent Tully. *Nearby galaxies catalog*. 1988.

[127] Jeffrey A. Willick et al. "Homogeneous velocity-distance data for peculiar velocity analysis. 3. The Mark III Catalog of Galaxy Peculiar Velocities". In: *Astrophys. J. Suppl.* 109 (1997), p. 333. DOI: 10.1086/312983. arXiv: astro-ph/9610202.

[128] R. Brent Tully et al. "Our Peculiar Motion Away from the Local Void". In: *Astrophys. J.* 676 (2008), pp. 184–205. DOI: 10.1086/527428. arXiv: 0705.4139 [astro-ph].

[129] R. Brent Tully, Hé lène M. Courtois, and Jenny G. Sorce. "COSMICFLOWS-3". In: *The Astronomical Journal* 152.2 (Aug. 2016), p. 50. DOI: 10.3847/0004-6256/152/2/50. URL: https://doi.org/10.3847%2F0004-6256%2F152%2F2%2F50.

[130] D. M. Scolnic et al. "The Complete Light-curve Sample of Spectroscopically Confirmed SNe Ia from Pan-STARRS1 and Cosmological Constraints from the Combined Pantheon Sample". In: *ApJ* 859.2, 101 (June 2018), p. 101. DOI: 10.3847/1538-4357/aab9bb. arXiv: 1710.00845 [astro-ph.CO].

[131] J. Guy et al. "The Supernova Legacy Survey 3-year sample: Type Ia supernovae photometric distances and cosmological constraints". In: *A&A* 523, A7 (Nov. 2010), A7. DOI: 10.1051/0004-6361/201014468. arXiv: 1010.4743 [astro-ph.CO].

[132] Mathew Smith et al. "The SDSS-II Supernova Survey: Parameterizing the Type Ia Supernova Rate as a Function of Host Galaxy Properties". In: *ApJ* 755.1, 61 (Aug. 2012), p. 61. DOI: 10.1088/0004-637X/755/1/61. arXiv: 1108.4923 [astro-ph.CO].

[133] Masao Sako et al. "The Data Release of the Sloan Digital Sky Survey-II Supernova Survey". In: *Publ. Astron. Soc. Pac.* 130.988 (2018), p. 064002. DOI: 10.1088/1538-3873/aab4e0. arXiv: 1401.3317 [astro-ph.CO].

[134] Adam G. Riess et al. "BVRI Light Curves for 22 Type IA Supernovae". In: *AJ* 117.2 (Feb. 1999), pp. 707–724. DOI: 10.1086/300738. arXiv: astro-ph/9810291 [astro-ph].

[135] Saurabh Jha et al. "UBVRI Light Curves of 44 Type Ia Supernovae". In: *AJ* 131.1 (Jan. 2006), pp. 527–554. DOI: 10.1086/497989. arXiv: astro-ph/0509234 [astro-ph].

[136] Malcolm Hicken et al. "Improved Dark Energy Constraints from ~100 New CfA Supernova Type Ia Light Curves". In: *ApJ* 700.2 (Aug. 2009), pp. 1097–1140. DOI: 10.1088/0004-637X/700/2/1097. arXiv: 0901.4804 [astro-ph.CO].

[137] Malcolm Hicken et al. "CfA3: 185 Type Ia Supernova Light Curves from the CfA". In: *ApJ* 700.1 (July 2009), pp. 331–357. DOI: 10.1088/0004-637X/700/1/331. arXiv: 0901.4787 [astro-ph.CO].

[138] Malcolm Hicken et al. "CfA4: Light Curves for 94 Type Ia Supernovae". In: *ApJS* 200.2, 12 (June 2012), p. 12. DOI: 10.1088/0067-0049/200/2/12. arXiv: 1205.4493 [astro-ph.CO].

[139] Carlos Contreras et al. "The Carnegie Supernova Project: First Photometry Data Release of Low-Redshift Type Ia Supernovae". In: *AJ* 139.2 (Feb. 2010), pp. 519–539. DOI: 10.1088/0004-6256/139/2/519. arXiv: 0910.3330 [astro-ph.CO].

[140] Steven A. Rodney et al. "Type Ia Supernova Rate Measurements to Redshift 2.5 from CANDELS: Searching for Prompt Explosions in the Early Universe". In: *AJ* 148.1, 13 (July 2014), p. 13. DOI: 10.1088/0004-6256/148/1/13. arXiv: 1401.7978 [astro-ph.CO].

[141] O. Graur et al. "Type-Ia Supernova Rates to Redshift 2.4 from CLASH: The Cluster Lensing And Supernova Survey with Hubble". In: *ApJ* 783.1, 28 (Mar. 2014), p. 28. DOI: 10.1088/0004-637X/783/1/28. arXiv: 1310.3495 [astro-ph.CO].

[142] Adam G. Riess et al. "Type Ia Supernova Distances at Redshift ¿1.5 from the Hubble Space Telescope Multi-cycle Treasury Programs: The Early Expansion Rate". In: *ApJ* 853.2, 126 (Feb. 2018), p. 126. DOI: 10.3847/1538-4357/aaa5a9. arXiv: 1710.00844 [astro-ph.CO].

[143] Adam G. Riess et al. "New Hubble Space Telescope Discoveries of Type Ia Supernovae at z ¿= 1: Narrowing Constraints on the Early Behavior of Dark Energy". In: *ApJ* 659.1 (Apr. 2007), pp. 98–121. DOI: 10.1086/510378. arXiv: astro-ph/0611572 [astro-ph].

[144] N. Suzuki et al. "The Hubble Space Telescope Cluster Supernova Survey. V. Improving the Dark-energy Constraints above z ¿ 1 and Building an Early-type-hosted Supernova Sample". In: *ApJ* 746.1, 85 (Feb. 2012), p. 85. DOI: 10.1088/0004-637X/746/1/85. arXiv: 1105.3470 [astro-ph.CO].

[145] R. Brent Tully et al. "The Laniakea supercluster of galaxies". In: *Nature* 513.7516 (2014), p. 71. DOI: 10.1038/nature13674. arXiv: 1409.0880 [astro-ph.CO].

[146] D. J. Fixsen et al. "The Cosmic Microwave Background spectrum from the full COBE FIRAS data set". In: *Astrophys. J.* 473 (1996), p. 576. DOI: 10.1086/178173. arXiv: astro-ph/9605054.

[147] R. Brent Tully et al. "Our Peculiar Motion Away from the Local Void". In: *Astrophys. J.* 676 (2008), pp. 184–205. DOI: 10.1086/527428. arXiv: 0705.4139 [astro-ph].

[148] Christian Marinoni et al. "Galaxy Distances in the Nearby Universe: Corrections for Peculiar Motions". In: *ApJ* 505.2 (Oct. 1998), pp. 484–505. DOI: 10.1086/306183. arXiv: astro-ph/9805081 [astro-ph].

[149] Supranta S Boruah, Michael J Hudson, and Guilhem Lavaux. "Cosmic flows in the nearby Universe: new peculiar velocities from SNe and cosmological constraints". In: *Monthly Notices of the Royal Astronomical Society* 498.2 (Aug. 2020), pp. 2703–2718. DOI: 10.1093/mnras/staa2485. URL: https://doi.org/10.1093%2Fmnras%2Fstaa2485.

[150] Tao Hong et al. "2MTF – IV. A bulk flow measurement of the local Universe". In: *Monthly Notices of the Royal Astronomical Society* 445.1 (Sept. 2014), pp. 402–413. DOI: 10.1093/mnras/stu1774. URL: https://doi.org/10.1093%2Fmnras%2Fstu1774.

[151] Stephen J. Turnbull et al. "Cosmic flows in the nearby universe from Type Ia Supernovae". In: *Mon. Not. Roy. Astron. Soc.* 420 (2012), pp. 447–454. DOI: 10.1111/j.1365-2966.2011.20050.x. arXiv: 1111.0631 [astro-ph.CO].

[152] Adi Nusser and Marc Davis. "The cosmological bulk flow: consistency with ΛCDM and $z \approx 0$ constraints on σ_8 and γ". In: *Astrophys. J.* 736 (2011), p. 93. DOI: 10.1088/0004-637X/736/2/93. arXiv: 1101.1650 [astro-ph.CO].

[153] Morag I. Scrimgeour et al. "The 6dF Galaxy Survey: Bulk Flows on $50 - 70h^{-1}$ Mpc scales". In: *Mon. Not. Roy. Astron. Soc.* 455.1 (2016), pp. 386–401. DOI: 10.1093/mnras/stv2146. arXiv: 1511.06930 [astro-ph.CO].

[154] Dong Zhao, Yong Zhou, and Zhe Chang. "Anisotropy of the Universe via the Pantheon supernovae sample revisited". In: *Mon. Not. Roy. Astron. Soc.* 486.4 (2019), pp. 5679–5689. DOI: 10.1093/mnras/stz1259. arXiv: 1903.12401 [astro-ph.CO].

[155] Jonathan Carrick et al. "Cosmological parameters from the comparison of peculiar velocities with predictions from the 2M++ density field". In: *Monthly Notices of the Royal Astronomical Society* 450.1 (Apr. 2015), pp. 317–332. ISSN: 0035-8711. DOI: 10.1093/mnras/stv547. eprint: https://academic.oup.com/mnras/article-pdf/450/1/317/18510270/stv547.pdf. URL: https://doi.org/10.1093/mnras/stv547.

[156] Stephen Appleby, Arman Shafieloo, and Andrew Johnson. "Probing bulk flow with nearby SNe Ia data". In: *Astrophys. J.* 801.2 (2015), p. 76. DOI: 10.1088/0004-637X/801/2/76. arXiv: 1410.5562 [astro-ph.CO].

[157] Charles L. Steinhardt, Albert Sneppen, and Bidisha Sen. "Effects of Supernova Redshift Uncertainties on the Determination of Cosmological Parameters". In: *ApJ* 902.1, 14 (Oct. 2020), p. 14. DOI: 10.3847/1538-4357/abb140. arXiv: 2005.07707 [astro-ph.CO].

[158] Dale D. Kocevski and Harald Ebeling. "On the origin of the local group's peculiar velocity". In: *Astrophys. J.* 645 (2006), pp. 1043–1053. DOI: 10.1086/503666. arXiv: astro-ph/0510106.

[159] Dan Scolnic et al. "The Pantheon+ Analysis: The Full Data Set and Light-curve Release". In: *Astrophys. J.* 938.2 (2022), p. 113. DOI: 10.3847/1538-4357/ac8b7a. arXiv: 2112.03863 [astro-ph.CO].

[160] G. Paturel et al. "An extragalactic database. I. The catalogue of principal galaxies." In: *AAPS* 80 (Nov. 1989), pp. 299–315.

[161] Francesco Sorrenti, Ruth Durrer, and Martin Kunz. "The dipole of the Pantheon+SH0ES data". In: *JCAP* 11 (2023), p. 054. DOI: 10.1088/1475-7516/2023/11/054. arXiv: 2212.10328 [astro-ph.CO].

[162] Maria Lopes et al. "Bulk Flow Motion Detection in the Local Universe with Pantheon+ Type Ia Supernovae". In: *Astrophys. J.* 967.1 (2024), p. 47. DOI: 10.3847/1538-4357/ad3735. arXiv: 2405.11077 [astro-ph.CO].

[163] Richard Watkins and Hume A. Feldman. "Large-scale bulk flows from the Cosmicflows-2 catalogue". In: *Mon. Not. Roy. Astron. Soc.* 447.1 (2015), pp. 132–139. DOI: 10.1093/mnras/stu2414. arXiv: 1407.6940 [astro-ph.CO].

[164] R. Brent Tully et al. "Cosmicflows-2: The Data". In: *Astron. J.* 146 (2013), p. 86. DOI: 10.1088/0004-6256/146/4/86. arXiv: 1307.7213 [astro-ph.CO].

[165] S. L. Parnovsky and A. S. Parnowski. "Yet another sample of RFGC galaxies". In: *Astrophys. Space Sci.* 343 (2013), pp. 747–754. DOI: 10.1007/s10509-012-1267-3. arXiv: 1210.0895 [astro-ph.CO].

[166] Francesco Sorrenti, Ruth Durrer, and Martin Kunz. "The low multipoles in the Pantheon+SH0ES data". In: (Mar. 2024). arXiv: 2403.17741 [astro-ph.CO].

[167] Hume A. Feldman, Richard Watkins, and Michael J. Hudson. "Cosmic Flows on 100 Mpc/h Scales: Standardized Minimum Variance Bulk Flow, Shear and Octupole Moments". In: *Mon. Not. Roy. Astron. Soc.* 407 (2010), pp. 2328–2338. DOI: 10.1111/j.1365-2966.2010.17052.x. arXiv: 0911.5516 [astro-ph.CO].

[168] Yehuda Hoffman et al. "The large scale velocity field from the Cosmicflows-4 data". In: (Nov. 2023). arXiv: 2311.01340 [astro-ph.CO].

[169] Robert P. Kirshner. *The Extravagant Universe: Exploding Stars, Dark Energy, and the Accelerating Cosmos*. p. 71. Princeton University Press, 2002.

[170] M. L. Humason, N. U. Mayall, and A. R. Sandage. "Redshifts and magnitudes of extragalactic nebulae." In: *AJ* 61 (Jan. 1956), pp. 97–162. DOI: 10.1086/107297.

[171] C. J. Trendowski. "Senior Thesis". Princeton University, 1967.

[172] G. F. R. Ellis, D. R. Matravers, and R. Treciokas. "Anisotropic solutions of the Einstein-Boltzmann equations: I. General formalism". In: *Annals of Physics* 150 (1983), p. 455. DOI: 10.1016/0003-4916(83)90023-4.

[173] G. F. R. Ellis et al. "Ideal observational cosmology." In: *Physics Reports* 124.5 (Jan. 1985), pp. 315–417. DOI: 10.1016/0370-1573(85)90030-4.

[174] P J Peebles. *Physical Cosmology*. Princeton University Press, 1971.

[175] Wolfgang Hasse and Volker Perlick. "On spacetime models with an isotropic Hubble flow". In: *Class. Quant. Grav.* 16 (1999), p. 2559.

[176] O Umeh. *The influence of structure formation on the evolution of the Universe*. University of Cape Town: PhD thesis, 2013.

[177] Julian Adamek et al. "Towards Cosmography of the Local Universe". In: *Open J. Astrophys.* 7 (2024), p. 001c.118782. DOI: 10.33232/001c.118782. arXiv: 2402.12165 [astro-ph.CO].

[178] Suhail Dhawan et al. "The quadrupole in the local Hubble parameter: first constraints using Type Ia supernova data and forecasts for future surveys". In: *Mon. Not. Roy. Astron. Soc.* 519.4 (2023), pp. 4841–4855. DOI: 10.1093/mnras/stac3812. arXiv: 2205.12692 [astro-ph.CO].

[179] Jessica A. Cowell, Suhail Dhawan, and Hayley J. Macpherson. "Potential signature of a quadrupolar hubble expansion in Pantheon+supernovae". In: *Mon. Not. Roy. Astron. Soc.* 526.1 (2023), pp. 1482–1494. DOI: 10.1093/mnras/stad2788. arXiv: 2212.13569 [astro-ph.CO].

[180] R. K. Sachs. "Gravitational waves in general relativity. 6. The outgoing radiation condition". In: *Proc. Roy. Soc. Lond. A* 264 (1961), pp. 309–338. DOI: 10.1098/rspa.1961.0202.

[181] Jerome Kristian and Rainer K. Sachs. "Observations in cosmology". In: *Astrophys. J.* 143 (1966), pp. 379–399. DOI: 10.1086/148522.

[182] Robert M. Wald. *General Relativity*. Chicago, USA: Chicago Univ. Pr., 1984. DOI: 10.7208/chicago/9780226870373.001.0001.

[183] Sean M. Carroll. *Spacetime and Geometry: An Introduction to General Relativity*. Cambridge University Press, July 2019. DOI: 10.1017/9781108770385.

[184] Eric Poisson. *A Relativist's Toolkit: The Mathematics of Black-Hole Mechanics*. Cambridge University Press, Dec. 2009. DOI: 10.1017/CBO9780511606601.

[185] Chris Clarkson et al. "(Mis-)Interpreting supernovae observations in a lumpy universe". In: *Mon. Not. Roy. Astron. Soc.* 426 (2012), pp. 1121–1136. DOI: 10.1111/j.1365-2966.2012.21750.x. arXiv: 1109.2484 [astro-ph.CO].

[186] Pierre Fleury. "Light propagation in inhomogeneous and anisotropic cosmologies". PhD thesis. Paris U., VI, IAP, 2015. arXiv: 1511.03702 [gr-qc].

[187] Basheer Kalbouneh et al. "Expanding covariant cosmography of the local Universe: incorporating the snap and axial symmetry". In: (Aug. 2024). arXiv: 2408.04333 [astro-ph.CO].

[188] M. A. MacCallum and G. F. Ellis. "A class of homogeneous cosmological models". In: *Commun. Math. Phys.* 19 (1970), pp. 31–64. DOI: 10.1007/bf01645496.

[189] Asta Heinesen and Hayley J. Macpherson. "A prediction for anisotropies in the nearby Hubble Flow". In: *Journal of Cosmology and Astroparticle Physics* 2022.03 (2022), p. 057. DOI: 10.1088/1475-7516/2022/03/057.

[190] Lam Hui and Patrick B. Greene. "Correlated fluctuations in luminosity distance and the importance of peculiar motion in Supernova surveys". In: *Physical Review D* 73.12 (2006). DOI: 10.1103/physrevd.73.123526.

[191] Nick Horstmann, Yannic Pietschke, and Dominik J. Schwarz. "Inference of the cosmic rest-frame from supernovae Ia". In: *Astron. Astrophys.* 668 (2022), A34. DOI: 10.1051/0004-6361/202142640. arXiv: 2111.03055 [astro-ph.CO].

[192] Jacques Colin et al. "A response to Rubin \& Heitlauf: "Is the expansion of the universe accelerating? All signs still point to yes"". In: (Dec. 2019). arXiv: 1912.04257 [astro-ph.CO].

[193] David Rubin and Jessica Heitlauf. "Is the expansion of the universe accelerating? All signs still point to yes a local dipole anisotropy cannot explain dark energy". In: *Astrophys. J.* 894.1 (2020), p. 68. DOI: 10.3847/1538-4357/ab7a16. arXiv: 1912.02191 [astro-ph.CO].

[194] Suhail Dhawan et al. "The quadrupole in the local Hubble parameter: First constraints using type Ia supernova data and forecasts for future surveys". In: *Monthly Notices of the Royal Astronomical Society* 519.4 (2022), pp. 4841–4855. DOI: 10.1093/mnras/stac3812.

[195] Christian Marinoni et al. "Galaxy distances in the nearby Universe: Corrections for Peculiar Motions". In: *The Astrophysical Journal* 505.2 (1998), pp. 484–505. DOI: 10.1086/306183.

[196] R. Brent Tully et al. "COSMICFLOWS-3: Cosmography of the local void". In: *The Astrophysical Journal* 880.1 (2019), p. 24. DOI: 10.3847/1538-4357/ab2597.

[197] Melissa Amenouche. "Probing local anisotropies with Type Ia Supernovae from the Zwicky Transient Facility". PhD Thesis. Université Clermont Auvergne, Dec. 2022. URL: theses.hal.science/tel-04165406.

[198] Suhail Dhawan et al. "A uniform type Ia supernova distance ladder with the Zwicky Transient Facility: Absolute calibration based on the tip of the red giant branch method". In: *The Astrophysical Journal* 934.2 (2022), p. 185. DOI: 10.3847/1538-4357/ac7ceb.

[199] Adi Nusser. "On methods of estimating cosmological bulk flows". In: *Monthly Notices of the Royal Astronomical Society* 455.1 (2015), pp. 178–184. DOI: 10.1093/mnras/stv2099.

[200] D. J. Fixsen et al. “The Cosmic Microwave Background Spectrum from the Full COBE FIRAS Data Set”. In: *ApJ* 473 (Dec. 1996), p. 576. DOI: 10.1086/178173. arXiv: astro-ph/9605054 [astro-ph].